ABSTRACT

NUCLEAR SPECTROSCOPIC STUDIES OF NEUTRON-DEFICIENT, ODD-MASS RARE EARTHS NEAR THE N=82 CLOSED SHELL

By

Richard Earl Eppley

The decay schemes of Gd^{149}, Gd^{145g+m} and Sm^{141g+m} have been studied by γ- and β-ray spectroscopy in an effort to elucidate their nuclear properties. Also, a search for Dy^{147g+m} has been conducted, although no decay scheme can be proposed.

γ-ray spectroscopic techniques including Ge(Li) singles, Ge(Li)-NaI(Tl) coincidence, and Ge(Li)-Ge(Li) megachannel, 2-dimensional coincidence techniques have been employed. Where appropriate, electron spectra have been obtained by use of Si(Li) surface barrier detectors.

Twenty-five γ rays have been attributed to the electron-capture decay of 9.4-day Gd^{149} and incorporated in a decay scheme having 13 levels with energies of 0, 149.6, 459.9, 496.2, 574.2, 666.0, 748.2, 794.8, 812.4, 875.8, 933.3, 939.1, and 1097.3 keV. The isomeric decay of Gd^{145m} has been characterized as having a half-life of 85±3 seconds and an $M4$ transition of 721.4±0.4 keV. A direct ε/β^+ branch has also been determined as accounting for 4.7% of the decay from this level. Gd^{145g} is reported to have 38 γ rays associated with its decay, 26 of which (accounting for ≈97% of the total γ intensity) are incorporated into the decay scheme. This

decay scheme has 19 levels placed at 0, 329.5, 808.5, 953.4, 1041.9, 1567.3, 1599.9, 1757.8, 1845.4, 1880.6, 2203.3, 2494.8, 2642.2, 2672.6, 3236.0, 3259.6, 3285.6, 3623.8, and 4411.3 keV. Sm^{141g} and Sm^{141m} appear to have 9 and 32 associated γ rays, respectively. Levels in Sm^{141g} have been placed at 0, 196.6, 403.9, 728.3, 858.5, 1292.7, 1495.6, and 2005.0 keV. Levels in Sm^{141m} have been placed at 0, 196.6, 628.6, 804.5, 837.1, 974.0, 1108.1, 1167.2, 1313.2, 1414.8, 1834.0, 1983.1, 2063.5, 2091.6, 2119.2, and 2702.4 keV. The half-lives of Sm^{141g} and Sm^{141m} have been measured to be 11.3±0.3 and 22.1±0.3 minutes respectively.

Spin and parity assignments for the nuclear levels encountered in this investigation are based on log ft values, relative γ intensities, and transition multipolarities (where internal-conversion-electron intensities were available). Two intense transitions in Eu^{145}, which account for ≈72% of the β decay from Gd^{145g}, are interpreted as being three-quasiparticle states. Also, there are 6 states in Pm^{141}, lying between the energies of 1414.8 and 2702.4 keV, which appear to be three-quasiparticle states analogous to those reported recently for Pr^{139}. Mechanisms are suggested for these three-quasiparticle types of decay in terms of simple shell-model transitions and nucleon rearrangements.

Several families of nuclear isomers are compared with each other in terms of their level energies and reduced $M4$ transition probabilities. These include the Z=82, N=81, N=79, Z=50, Z=49, and N=49 families. High multipolarity electromagnetic transitions from these isomers are considered to be quite "pure" single-particle

transitions. The experimentally measured transition probabilities are compared to these single particle predictions in an effort to determine the degree to which this is true. Finally, levels in the odd-mass N=82 and Z=63 nuclides are traced as far as possible in an effort to understand nuclear behavior in this region better.

NUCLEAR SPECTROSCOPIC STUDIES OF NEUTRON-DEFICIENT, ODD-MASS RARE EARTHS NEAR THE N=82 CLOSED SHELL

By

Richard Earl Eppley

A THESIS

Submitted to
Michigan State University
in partial fulfillment of the requirements
for the degree of

DOCTOR OF PHILOSOPHY

Department of Chemistry

1970

ACKNOWLEDGEMENTS

I wish to thank Dr. Wm. C. McHarris not only for suggesting this region of study but also for guidance and help in all phases of the ensuing investigation, including the preparation of this thesis.

I also wish to thank Dr. W. H. Kelly for his help and advice. His suggestions on the performance of experiments and analysis of data are greatly appreciated.

Dr. H. G. Blosser and Mr. H. Hilbert have assisted with the operation of the Michigan State University sector-focused cyclotron. As with any large, complicated machine, it had its temperamental moments at which times their special touch was necessary for a successful run.

The members of our research group have all contributed in one way or another to the successful completion of this thesis research. Dr. D. Beery, Mr. J. Black, Mr. W. Chaffee, Mr. J. Cross, Mr. R. Doebler, Mr. R. Firestone, Mr. G. Giesler, Mr. R. Goles, Mr. K. Kosanke, Mr. R. Todd, and Dr. R. Warner have all helped in this work. I particularly wish to thank Dr. D. Beery for his help in the early stages of this project. Mr. R. Todd and Dr. R. Warner have shared jointly in the Sm^{144} research. In addition they have provided me with many hours of discussion on the research and other things philosophical.

Dr. P. Plauger, Mr. R. Au, Mr. and Mrs. W. Merritt and the cyclotron computer staff have been helpful in the writing of programs and with the operation of the computer.

Help has also been given by Mr. R. N. Mercer and his staff in the cyclotron machine shop, and by Mr. W. Harder in the cyclotron electronics shop.

I also wish to thank Mrs. Ina Samra for her help with the typing of this thesis as well as the typing of several reports for publication.

The National Science Foundation, U. S. Atomic Energy Commission and Michigan State University have provided much of the financial assistance for this research.

Finally, I thank my wife Sara for her help and encouragement during these past few years. I also thank her for just plain putting up with me during this hectic time.

TABLE OF CONTENTS

LIST OF TABLES

LIST OF FIGURES

Figure

Figure

Page

Figure

CHAPTER I

INTRODUCTION

"...In the development of atomic physics the interaction of atoms with electromagnetic radiation has been of paramount importance for the understanding of atomic structure. In the case of nuclei the interaction has not been so important a tool, since, unlike the atomic case, the wavelengths of interest are so short that they cannot be measured by the usual optical devices. The rather indirect methods which must be employed make the energy determination quite inaccurate compared with spectroscopic standards, and the available resolution is low. Furthermore, in most cases the radiation process is only one of many competing processes (such as particle emission or sometimes even beta-decay) and its probability is correspondingly lower.

For these reasons the study of gamma-rays from nuclei has remained on a rather rudimentary level..." (Blat52).

This was written in 1952, not so very long ago in terms of years but a very long time ago in terms of technological development. This thesis has been possible precisely because such a statement about γ-ray spectroscopy is no longer valid.

In the early 1960's, when solid state detectors became available, energy resolution was dramatically improved to the point where, for the first time, individual transitions could be resolved

in complex γ-ray spectra. Needless to say, a whole new dimension was then opened for the study of nuclear properties. γ-ray spectroscopy immediately became an important tool for these investigations.

The present investigation is a good example of the unpredictableness of scientific research. One begins a research project looking for answers to predetermined questions and, as in the present case, finds a few answers and many more unanswered questions. Also, one is apt to end up investigating certain phenomena which were unrealized at the outset of the study. The topics of this thesis evolved in just such a manner.

The original intent was to study a sequence of neutron-deficient odd-mass rare earth isotopes in an effort to elucidate their decay schemes in as much detail as possible. This information would be of great value for the testing of existing nuclear models as well as possibly suggesting a means of, at least semi-emperically, being able to describe in a uniform fashion the change in the various levels as one goes from permanently deformed nuclei to spherical nuclei near closed shells. Gadolinium was chosen as an element satisfying this criterion, as well as possessing neutron-deficient isotopes in the desired spherical region which would be obtainable with our energy limitations (p_{max} = 45 MeV and He^3_{max} = 70 MeV).

With this intent work was completed on the decay schemes of Gd^{149}, Gd^{145m}, and Gd^{145g}. However, with our discovery of an 85-

second isomer in Gd^{145}, we became interested in studying other N=81 isotones (six of which were already known). Preliminary calculations, based on the known $M4$ N=81 isotones, indicated that Dy^{147m} should be of a half-life that we could handle by our counting techniques. Thus, a series of experiments was initiated at Yale University in an effort to identify this species.

At about this same time, states were observed in Nd^{139m} (McH69j,Bee69d) which were characterized as three-quasiparticle states. These states are quite uncommon but where found to be very useful for determining nuclear properties of relatively high-lying states. Out of the Nd^{139m} work came predictions for similar states in Sm^{141m} and Nd^{137m}.

Consequently, the nuclear species studied during the course of this thesis work were Gd^{149}, Gd^{145g}, Gd^{145m}, Sm^{141g}, Sm^{141m}, and Dy^{147}.

Chapter II describes the many types of experimental set-ups used during the course of this work. The latter part of the chapter also describes three chemical techniques, used primarily for Gd^{149}, for separating the Gd fraction of the target material from contaminents of Eu and Sm.

Since we are fortunate in having two computers at our disposal, an SDS Sigma-7 and a DEC PDP-9, data analysis could be accomplished both in the quantity and in the quality needed for this work. Three of the most useful data reduction codes used in this laboratory are described in Chapter III.

The heart of this thesis, the experimental results, comprise Chapter IV. During this work, certain "discoveries" proved to be particularly interesting. As already mentioned, this investigation began with Gd^{149}. The fairly complete study we made of the Eu^{149} levels populated by the decay of this species will undoubtedly prove valuable for any future theoretical considerations of this region. Eu^{149} is in the twilight zone. In § 4.1. we report the observation of more levels than can be incorporated in a simple shell model picture, while, at the same time, the levels are such that they cannot be fit into rotational structures as would be expected of a permanently deformed nucleus. There is presently no nuclear model which can adequately account for such a situation.

As opposed to higher mass Gd isotopes, Gd^{145g} decays primarily to two states at 1757.8 and 1880.6 keV. These states, in turn, decay predominantly directly to the ground state of Eu^{145}. We report over 30 γ transitions accompanying the decay of Gd^{145g} with the above mentioned two transitions accounting for $\approx$63% of the total γ intensity. This anomaly occurs, most likely, because the $s_{1/2}$ state drops down to become the ground state (replacing the $d_{3/2}$ state). Another interesting facet of this work was the observation of an $\varepsilon/\beta+$ branch from the isomeric decay of Gd^{145}. Of the N=81 isomers which have been studied previously, only Sm^{143} appears to have a β-decay branch. From such branchings one can directly arrive at occupation probabilities for the state involved.

In apparent confirmation of the three-quasiparticle predictions discussed above, Sm^{141m} does exhibit 6 β-allowed states lying

between 1414.8 keV and 2702.4 keV. These states have properties similar to those in Nd^{139m} with one notable exception. The three-quasiparticle states in Nd^{139m} have a plethora of interconnecting transitions; these states in Sm^{141m} have not a single observed interconnecting transition. Five of these six states in Pm^{141} decay principally to an $11/2^-$ state at 628.6 keV. The sixth state, however, completely bypasses the $11/2^-$ state, preferring to decay to the ground and 1st excited state instead. In § 4.4.11. a mechanism will be proposed for this three-quasiparticle type of decay.

The decay of Sm^{141g} still remains as a partly unsolved problem. There are two intense transitions, at 403.9 keV and 438.2 keV, neither of which can be ruled out as belonging to this ground state decay. The puzzle is that one of them, the 403.9-keV state, exhibits a half-life of 11.3 minutes, while the other level has a measured half-life of 10.0 minutes. We have evidence both for and against both of these transitions being from levels in Pm^{141}. Other than this the decay of Sm^{141g} seems to be straightforward, decaying largely to the Pm^{141} ground state.

The identification of Dy^{147g} and Dy^{147m} still remains a challenging problem. We began a search (primarily for the Dy^{147m} species) after our experimental determination of the decay properties of Gd^{145m}. The only feasible means of producing this species is with a C^{12} beam on either a Nd^{142} or a Sm^{144} target. Because of the beam requirement we repaired to Yale University where their heavy ion linear accelerator was made available for our use. §4.5. will describe our results to date. We have evidence from several types of experiments

which indicates that we do produce Dy^{147}. We do have seemingly conclusive evidence that there is no Dy^{147m} *M4* transition (at least not in our useable half-life range) with a measurable internal-conversion intensity. This could well mean that Dy^{147m} de-excites predominantly via an ε/β^+ branch.

Chapter V sketches the derivation of the single-particle transition probability expressions for various multipole transitions, beginning with the Maxwell equations. These expressions, first expressed by Weisskopf, are by far the most frequently used estimates against which to compare experimentally measured transition half-lives. The purpose of the chapter is not to present a mathematically rigorous derivation but rather to give a beginner a feeling for what is invloved in such a derivation.

The final chapter, Chapter VI, is primarily concerned with the trends in families of nuclear isomers, both neutron and proton, around the 50 and 82 closed shells. For example, the N=79 and N=81 isotones show marked energy dependence on Z while the isomers of the lead isotopes (Z=82) are quite similar in energy and consequently show a constancy in their reduced transition probabilities. The trends of other isomeric families will be compared to these two seemingly different types of behavior.

Inasmuch as possible the energy levels of nuclei in the Gd-Eu-Sm region will be traced as functions of energy. The available information on much of this region is quite sketchy and few conclusions can be drawn.

CHAPTER II

EXPERIMENTAL EQUIPMENT AND PROCEDURES

All of the nuclear species studied in the present investigation decay by positron emission and/or electron capture. A variety of techniques, discussed in this chapter, were used to construct decay schemes based on the study of these decay characteristics.

This chapter is divided into three main parts. The first, consisting of § 2.1. through § 2.3, describes the electronics set-ups for the γ-ray and conversion-electron data taken at Michigan State University. The apparatus used at Yale University, in conjunction with the Dy^{147} experiments, is briefly described in § 2.4. § 2.5 describes the chemical separation techniques used principally for the isolation of the Gd^{149} activity.

2.1. γ-Ray Spectrometers

As mentioned in Chapter I, the Ge(Li) γ-ray detector has been principally responsible for the resurgence of the study of complex nuclear structures by measurements of the γ-ray de-excitations. Hand in hand with the development of these solid state detectors has been the development of vastly improved electronics. In just the approximately $3\frac{1}{2}$ years since the beginning of this study, we have gone from a γ-ray spectrometer system having a resolution of ≈5.6 keV FWHM for the 1333-keV γ of Co^{60}, a detector efficiency of <<1%, and an analyzer having 1024 channels of memory to our present system: a detector resolution of 1.9 keV FWHM for Co^{60}, a detector efficiency of 3.6% (relative to a 3×3-in. NaI(Tl) detector 25 cm. from a Co^{60} source), and the capability of obtaining spectra up to 8192 channels in length.

2.1.1. Ge(Li) Singles Spectrometer

Our γ-ray spectrometer is really a "system" that includes, besides the Ge(Li) detector and bias supply, a charge sensitive FET preamplifier, a spectroscopy amplifer, an analog to digital converter (ADC), and some type of memory or storage unit and associated spectrum readout. The majority of the electronic equipment is modular so that equipment from various manufacturers can be used together for a particular experiment.

A typical spectroscopy charge-sensitive preamplifer integrates and shapes the charge output from the detector and presents a tail pulse (rise time ≈25 nsec, decay time ≈50 μsec) to the main amplifier.

The spectroscopy amplifiers which we use have considerable versatility. Shaped unipolar or bipolar output pulses with 0.25-μs widths are available for timing purposes or for input to an ADC. These amplifiers have highly linear amplification responses and include such features as adjustable pole-zero cancellation and base-line restoration.

The pole-zero feature permits precise elimination of undershoots on the amplifier pulse after the first differentiation. This becomes important at high counting rates, since if the undershoot saturates, the amplifier will be blocked not only for the time of the primary pulse, but also for the duration of the undershoot. Also, succeeding pulses which may fall into the undershoot will have an apparent area smaller than the actual area, thus causing a loss in resolution.

Base-line restoration also improves resolution at high count rates by restoring the undershoot of the amplifier signals to a DC baseline after all other shaping has been accomplished. The improved resolution is accomplished by the reduction of pile-up distortion caused by undershoot.

In this laboratory spectra can be collected in a variety of analyzers. Of principle use for the present research has been a Nuclear Data ND-2200 4096-channel analyzer, a PDP-9 computer interfaced to a Northern Scientific NS-625 dual 4096-channel ADC, and our Sigma 7 computer interfaced to four Northern Scientific 8096-channel ADC's. The NS-625 has a 40-MHz digitizing rate and the NS-629 has a 50-MHz digitizing rate.

2.1.2. Ge(Li)-NaI(Tl) Coincidence Spectrometers

Coincidence spectra have played an important role in the present research. Since the vast majority of nuclear excited states have very short half-lives as compared with our ability to measure them, coincidence units with resolving times on the order of nanoseconds can be used to study those transitions which are in fast or "prompt" coincidence with one another. In this manner, coincidence spectra are a useful tool for determining the relationships of the observed γ-transitions and their interconnections with the deduced nuclear energy levels.

Several types of single parameter coincidence spectra have proved to be useful. Both prompt and delayed coincidence spectra have been used, utilizing a Ge(Li) detector for one leg of the timing circuit. In addition, anti-coincidence spectra and 511-511-keV (pair) coincidence spectra have been obtained by use of a Ge(Li) detector in conjunction with an 8×8-in. split annulus. Each of these will be described in the following sections.

2.1.2.A. Coincidence Spectrometer using Ge(Li) *vs* 3×3-in. NaI(Tl)

Before the advent of Ge(Li)-Ge(Li) coincidence techniques, which will be described in § 2.1.2.C, NaI(Tl) scintillators coupled to photomultiplier tubes provided the principle means of obtaining timing pulses for coincidence spectra. Such a set-up is shown in Figure 1. In addition to the equipment needed for the collection of a singles spectrum, equipment is needed to provide timing information. As shown in this figure, a 3×3-in. NaI(Tl) detector was used for this purpose. The pulses from the photomultiplier were fed to a spectroscopy

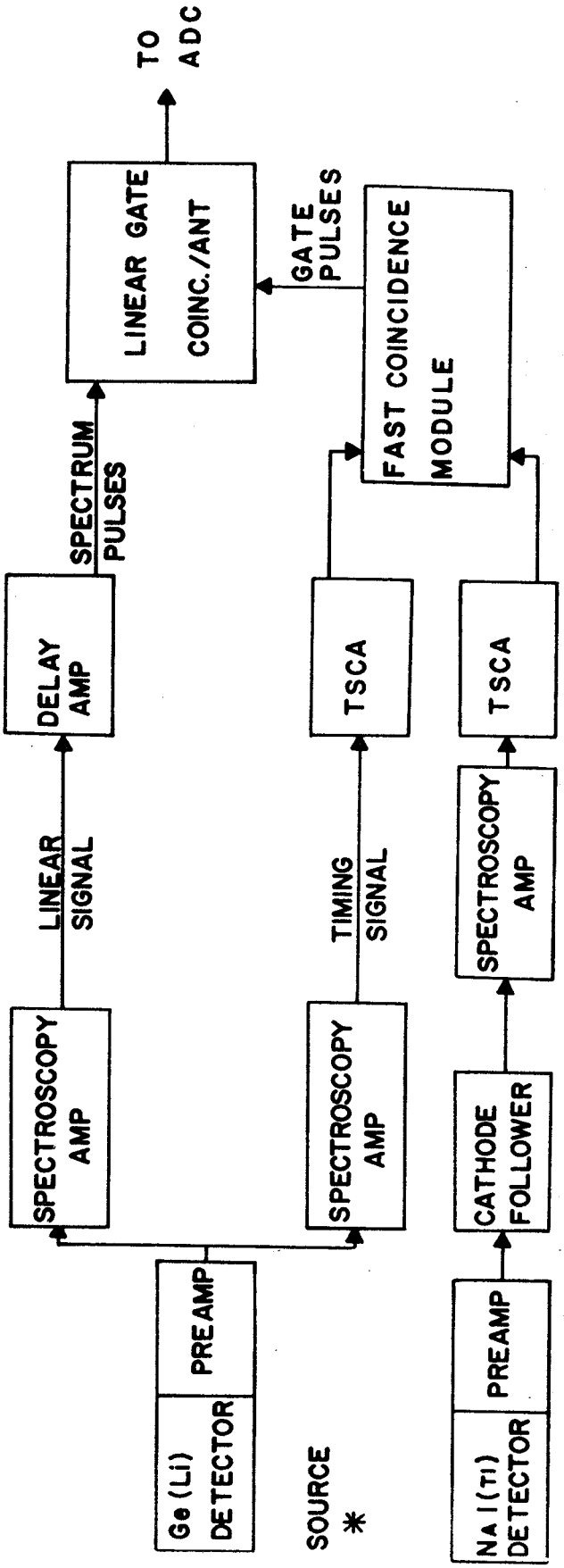

Figure 1. Schematic illustration of the Ge(Li)-Nai(Tl) coincidence apparatus.

amplifer through a cathode follower, which is used simply as a buffer for impedance mismatch between the photomultiplier and amplifier. The NaI(Tl) signals are then presented to a timing single channel analyzer (TSCA). The TSCA, in turn, is used first to determine the energy gate and then to output a logic pulse to a fast coincidence unit. In this manner timing pulses are output only for pulses which fall in the voltage range selected by the TSCA.

Similarly, a timing signal must be derived from the Ge(Li) linear signal. This is accomplished by the use of a second TSCA which outputs a logic signal to the coincidence unit. The function of the fast coincidence unit is to output a logic signal only when a Ge(Li) and NaI pulse arrive within a specified time interval of one another. For most of our coincidence work this resolving time (2τ) was set at 100 nsec.

The majority of coincidence runs utilized an external linear gate. A logic pulse from the fast coincidence unit opens the gate for a pre-determined length of time, allowing any linear signal present at the input during that time to pass through the open gate and on to the ADC. In this manner, only pulses from γ-ray transitions occurring within the specified resolving time are allowed to pass through the linear gate and be digitized by the ADC. The delay amplifier shown in Figure 1 is solely for the purpose of delaying the linear signal to compensate for the delay incurred by the timing signals while they are proceeding through the coincidence circuits. The delay can be adjusted to insure that the linear singnals and coincidence timing signals arrive simultaneously at the gate.

2.1.2.B. Ge(Li) vs 8×8-in. NaI(Tl) Split Annulus

Several types of coincidence experiments can be carried out using the split annulus for one of the detectors. One-half of the annulus can be used as a simple NaI(Tl) detector. In addition to the usual prompt and delayed coincidence and anti-coincidence experiments that can be accomplished with the annulus are Compton suppression experiments. The annulus can also be used as a pair spectrometer for obtaining β^+ feedings and double escape spectra. For the present research, the annulus was used primarily for anti-coincidence experiments and as a pair spectrometer.

While coincidence spectra show the relationship of γ-rays which are related to each other, anti-coincidence spectra enhance those transitions which are either transitions to the ground state from levels populated primarily by electron capture with little or no γ-ray feeding from above, or transitions from a level with a half-life considerably longer than the resolving time of the apparatus, i.e., transitions from isomeric levels. The electronics set-up using the annulus in an anti-coincidence experiment is shown in Figure 2. A 3×3-in. NaI(Tl) detector is positioned in the top of the annular tunnel in order to increase the solid angle subtended by the detectors. The Ge(Li) detector is positioned in the bottom of the annular tunnel, facing the 3×3-in. NaI(Tl) detector at the top. The source is placed between these two detectors, approximately in the middle of the tunnel. The electronics used is very similar to that used in the coincidence experiments which have been described in § 2.1.2.A. above The main difference is that now there are three timing signals

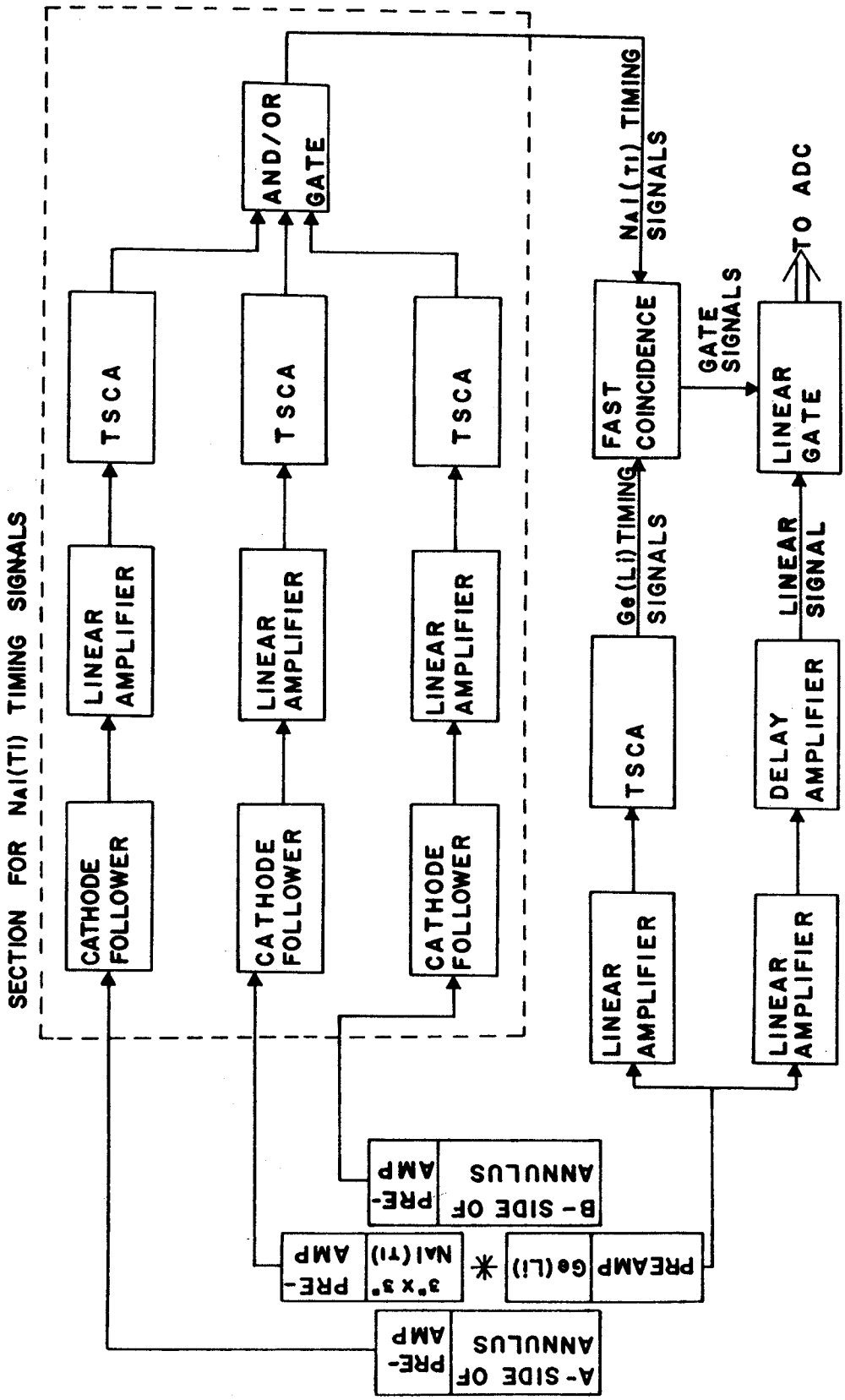

Figure 2. Schematic illustration of the anticoincidence apparatus. This same apparatus is used for obtaining pair spectra after the elimination of the 3×3-in. NaI(Tl) detector leg and AND/OR gate.

necessary instead of just one. These timing signals must be combined in some way so that the fast coincidence unit is presented with a single logic pulse (no matter whether a signal is present in only one leg or a combination of the legs). For this purpose we have used an ORTEC universal coincidence module, shown in Figure 2 as an AND/OR gate. The number of coincidence requirements is set to 1 on this module to effect the desired single, well shaped output pulse. In this mode, resolving time for the unit has no meaning and does not have to be set. The only relevant resolving time consideration is that associated with the fast coincidence module, which was commonly set to 100 nsec for these experiments.

Another use for the annulus was as a pair spectrometer for determining the β^+ feeding of levels. In this mode of operation the resulting spectra show enhancement of those γ-rays involved in prompt coincidence with levels which are fed by β^+ emission. Of course, double-escape peaks are also greatly enhanced in these spectra. The apparatus shown in Figure 2 can be employed, with the exception that the 3×3-in. NaI(Tl) detector and associated electronics are not used. Since we are now interested in a triple coincidence requirement, i.e., a coincidence output pulse only when a timing signal from the Ge(Li) detector and both halves of the annulus occur within the resolving time of the fast coincidence module, the AND/OR gate is not needed. Signals from each half of the annulus, as well as the Ge(Li) timing signals, are routed directly to the fast coincidence unit, which is set for the triple-coincidence requirement. With these exceptions and different settings of the linear gate, the experimental set-up remains the same as for the anticoincidence experiment.

2.1.2.C. Ge(Li)-Ge(Li) Megachannel, 2-Dimensional Coincidence Spectrometer

With the availability of larger volume Ge(Li) detectors came the technique of 2-dimensional coincidence experiments. The ultimate aim of such experiments is to obtain coincidence data for any and all peaks or regions with a single run. (In practice the data obtained usually fall somewhat short of this goal.)

Even though Ge(Li) detectors are still quite inefficient with respect to available NaI(Tl) detectors, they compensate for this in other ways. Due to the Ge(Li) resolution, peak to Compton ratio, etc., good coincidence data can be obtained with fewer counts per channel than necessary with NaI(Tl). The electronics used in this laboratory for the 2-dimensional coincidence experiments is diagrammed in Figure 3. This is a double coincidence set-up where we want the linear signal to be recorded from each of the detectors, hence the fast coincidence unit transmits a logic pulse to two linear gates, one for each detector. The two detectors presently used for these runs have efficiencies of 2.5% and 3.6%.

Coincidence events are collected on magnetic tape by use of a task called EVENT which runs under the JANUS monitor system of our Sigma-7 computer. The data obtained under this system are a 2-dimensional integral coincidence array.

Each linear gate transmits a linear signal when opened by a coincidence event. These two linear signals are input to separate ADC's, operated in a synchronous mode, which are interfaced to the computer. The encoded coincidence pair is then stored on magnetic

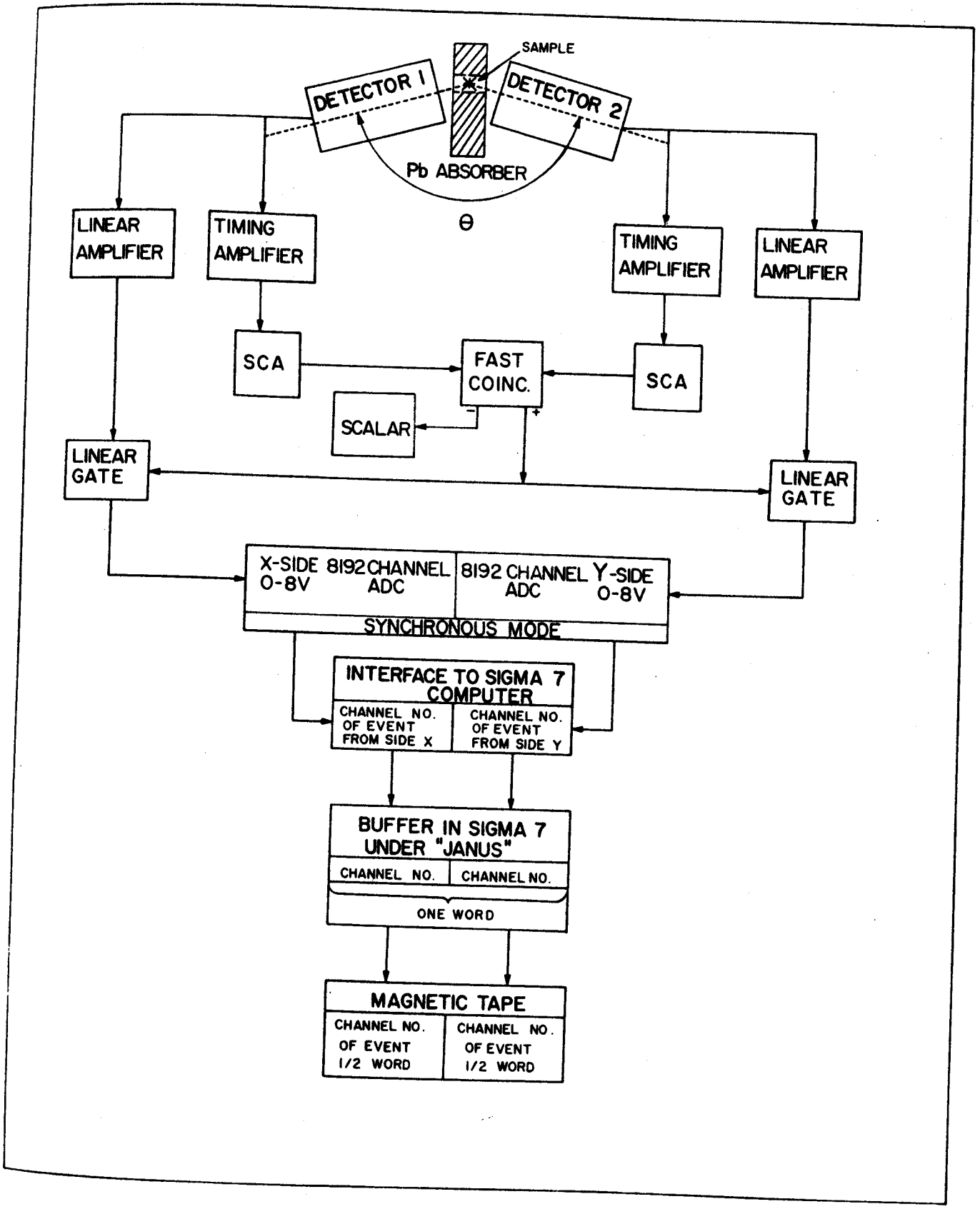

Figure 3. Schematic diagram of the megachannel 2-dimensional apparatus.

tape as one word, the first half of the word being the address from detector 1 and the second half of the word being the address associated with detector 2. The lead absorber shown in the diagram between the detectors is used to reduce γ-ray scattering between the two detectors. Without the absorber spurious peaks appear in the coincidence spectra. These scattering phenomena are discussed in (Gie70)

The data thus stored on the magnetic tape represent information on all peaks in coincidence with all other peaks. All that remains is to strip these 2-dimensional data by taking the appropriate slice representing a particular peak on energy region. These gated specta are recovered off-line on the Sigma-7 computer through use of the program EVENT RECOVERY (event). This code allows us to search the tape for a miximum of 10 gates per single pass of the tape. Background subtraction can be effected for any or all of the gates on the same pass.

All coincidence runs used in the present work utilize a 4096×4096 array. The system operates satisfactorily at counting rates up to ≈2000 coincidence events per second.

2.2. Conversion-Electron Spectrometer

For the conversion electron spectra of Gd^{145m} we utilized a 100-μ thick Si(Li) detector. This detector was mounted in the usual γ-ray cryostat and cooled to methanol-dry ice temperature (≈77°C) for operation. A 1/4-mil Havar window was used for this detector. A 200-V bias was used for operation of the detector. A typical resolution of ≈5 keV on the Cs^{137} *K*-conversion peak was obtained, thus allowing

separation of the *K*- and *L*- conversion electron peaks. In addition to the required bias supply, an ORTEC 109A preamplifier and 451 spectroscopy amplifier were used in conjunction with an analyzer. To utilize this detector for the determination of internal conversion coefficients required the simultaneous counting of the source with both the conversion-electron detector and Ge(Li) γ-ray detector. Normalization between the detectors (efficiency corrections) was obtained through the counting of standards having known (and measurable) conversion coefficients, Cs^{137} and Bi^{203} being the most suitable. Conversion electron spectra of Gd^{145m} are shown in the experimental section.

2.3. X-Ray Spectrometer

X-ray spectra also provide a powerful method of studying nuclear decay. With the resolution presently available it is possible to determine unambiguously which elements are present in particular sources. Coincidence experiments using an x-ray detector will be discussed in § 2.4. The x-ray detector in use at Michigan State is a Si(Li) detector with a 150 Å gold surface barrier contact. This ORTEC detector has a warranted resolution of 275 eV at 6.4 keV, counting through a 5 mil Be window The detector active diameter is 6mm, with a sensitive depth of 3mm. This detector is operated at a bias of 1500 V at liquid N_2 temperature. An integral part of the detector is an ORTEC model 117 preamplifier with a cooled FET first stage. The preamp is directly attached to the cryostat to reduce capacitance.

The useful efficiency range of the x-ray detector is from about 5 keV to <100 keV. This type of detector is also quite sensitive

to charged particles such as electrons and positrons. This is both an advantage and a disadvantage when obtaining spectra with high positron fluxes, such as the spectra obtained in this research. These charged particles cause detector output pulses of a much higher voltage than the x-ray pulses under consideration. As a consequence, the positron pulses are badly clipped by the amplifier, which cause a great deal of ringing on the pulses, and present a complex problem for the ADC. The ill effect of this situation shows up as a high noise background below approximately 10 keV. This problem can be partly alleviated by running the experiment in a self-gated coincidence mode. This allows the single channel analyzer to stop all pulses above the window level. This produces a cleaner spectrum but is not completely satisfactory since the problem is still present in the detector and can still have the adverse effect of lowering the system resolution.

A few attempts have been made at using various sized magnets for deflecting the positrons before they reach the detector. Unfortunately, no improvement has been realized. In addition, using a magnet requires removing the source to a greater distance from the detector. Due to the already extremely low efficiency of the detector, this becomes impractical.

2.4. Special Equipment for the Dy^{147} Experiments

The Dy^{147} experiments, described in Chapter 4, were carried out at Yale University using their Heavy Ion Linear Accelerator. While the detectors and electronics used for these experiments were standard items, most of the equipment was not the same as used for the other experiments reported in this thesis.

Four types of experiments were accomplished at Yale: electron singles, γ-ray singles, x-ray singles, and γ-ray versus x-ray coincidence experiments.

The search for the predicted *M*4 transition in Dy^{147} included looking for the expected conversion electrons. This was accomplished with the electron detector described in § 2.2. A 400-channel RIDL analyzer and an ORTEC 410 amplifier were used in conjunction with this detector.

For the γ-ray and x-ray experiments, the data were taken with a PDP-8/I computer interfaced to a dual Northern Scientific ADC.

γ-ray spectra were obtained with a Princeton Gamma-Tech Ge(Li) detector having a 2.3-keV resolution on the 1.33 MeV peak of Co^{60} and an efficiency of 6.5%. The detector was coupled to a Tennelec TC-137 preamplifier, ORTEC 451 amplifier, and the PDP-8/I.

The x-ray spectra were obtained with a Nuclear Equipment Corporation x-ray detector and preamplifier. The remainder of the system was the same as for the γ-ray detector.

X-ray versus γ-ray coincidence spectra were obtained using the x-ray and γ-ray detectors described above in conjunction with a standard fast coincidence circuit. Representative spectra collected at Yale are shown in § 4.5.

2.5. Chemical Separations

The rare earth group of elements (Z=57 through Z=71), in general, pose a real challenge for separation. These elements differ from one another mainly in the filling of inner 4*f* shell of electrons,

the outer electronic configuration being very similar for all of the members of this group. Consequently, they exhibit similar oxidation states and oxidation potentials - hence, the separation difficulty. All rare earth elements exhibit the characteristic +3 oxidation state. Only cerium has a relatively stable +4 oxidation state, with samarium, europium, thulium, and ytterbium exhibiting semi-stable +2 oxidation states.

For the present research, we needed separations of gadolinium from samarium and from gross amounts of europium. Gd^{149} was the only radioactive species involved in the present investigation with a half-life long enough to make some sort of chemical separation feasible. For the separation of Gd^{149} three different techniques were tried, two of them successfully. Two of these techniques utilized the fact that europium and samarium have 2+ oxidation states, while gadolinium exhibits only the 3+ state under the same conditions.

The first technique was that of HCl-Zn reduction. The second was an attempt at forming the 2+ europium species by use of hypophosphorous acid as the reducing agent. The third was that of ion-exchange. These are described in more detail below.

2.5.1. Zn-HCl Reduction

This procedure is similar to the one reported by R. N. Keller (Kel61). Targets usually consisted of about 100 mg of $Eu_2{}^{151}O_3$. After bombardment, these samples were dissolved in 3*M* HCl, keeping the volume to about 10-15 ml. This dissolution takes anywhere from a few minutes to an hour. Heating helps to speed up the process. The dissolved sample was then heated to boiling in a water bath and powdered

zinc added, nitrogen being bubbled through the solution during this entire period to prevent oxidation. The mixture was allowed to react in this manner for one hour.

At this point a few drops of H_2SO_4 was introduced to the solution for precipitation of $SmSO_4$ and $EuSO_4$, and the solution was allowed to cool. While cooling, the N_2 gas was still bubbled through the solution. When cool the mixture was centrifuged, the supernate decanted, and reduced in volume to allow transfer to a small glass vial for counting. This resulting solution should be free of europium and samarium contaminants. This solution could be used to run through the separation procedure a second time if itwas found that a complete separation was not obtained. We have found that one pass does separate Eu and Gd to the extent necessary to obtain a "clean" Gd γ-ray spectrum. The first separtion takes 2-3 hours, with each succeeding cycle requiring an additional 1 1/2 hours.

2.5.2. Hypophosphorous Acid Reduction

The HCl-Zn reduction technique discussed in the last section takes a minimum of two to three hours to perform, as does the ion-exchange method discussed in §2.5.3. A method was sought which would allow separation of species with shorter half-lives. Again, a reduction technique was sought which would allow the formation of Eu^{++} and Sm^{++} in the presence of Gd^{+++}. The relevant oxidation potentials are given in Table 1.

Hypophosphorous acid was tried as the reducing agent. Since H_3PO_2 is hygroscopic as well as being unstable, it must be prepared as needed. The method chosen for the production and purification of

Table 1. Oxidation Potentials*

$Gd(s) \leftrightarrow Gd^{+3}(aq) + 3e^-$	+2.40
$Eu(s) \leftrightarrow Eu^{+3}(aq) + 3e^-$	+2.41
$Sm(s) \leftrightarrow Sm^{+3}(aq) + 3e^-$	+2.41
$Eu^{+2}(aq) \leftrightarrow Eu^{+3}(aq) + 1e^-$	+0.43
$Sm^{+2}(aq) \leftrightarrow Sm^{+3}(aq) + 1e^-$	+1.55
$H_3PO_2 + H_2O \leftrightarrow H_3PO_3 + 2H^+ + 2e^-$	+0.59

* T. Moeller, *The Chemistry of the Lanthanides*, Reinhold Publishing Corp., New York, 1963.

H_3PO_2 is that of Klement (Kle49). This method employs the reaction,

$$NaH_2PO_2 + HCl \rightarrow H_3PO_2 + NaCl.$$

The NaH_2PO_2 was passed through the H^+ form of a cation exchange column (Dowex 50x4). The resulting solution of H_3PO_2 was dehydrated by evaporation on a water bath and then placed in a vacuum chamber over P_2O_5 and kept there until all of the water was removed. The acid was then recrystallized. This method yields a product with a purity of approximately 98%. It was found that the H_3PO_2 could be kept for a long period of time by keeping it in a closed container at dry ice temperature.

We were primarily interested in separating Gd from the europium target material. That is, we attemped to reduce Eu^{+++} to Eu^{++}, the appropriate reaction being

$$2Eu^{+++} + H_3PO_2 + H_2O \rightleftarrows 2Eu^{++} + H_3PO_3 + 2H^+$$

The addition of H_2SO_4 to this reaction mixture would precipitate $EuSO_4$, thus effecting the desired separation.

The half reactions for the reduction step are

$$2Eu^{+++} + 2e^- \leftrightarrow 2Eu^{++}$$

and

$$H_3PO_3 + 2H^+ + 2e^- \leftrightarrow H_3PO_2 + H_2O$$

therefore,

$$E^o_{cell} = E^o_{red} - E^o_{ox} = 0.16V.$$

For europium,

$$E_{Eu} = E^{o}_{Eu} + \frac{RT}{nF} \ln\left(\frac{a^2_{Eu^{+3}}}{a^2_{Eu^{+2}}}\right),$$

and for H_3PO_2,

$$E_{Acid} = E^{o}_{Acid} + \frac{RT}{nF} \ln\left(\frac{a_{H_3PO_3}}{a_{H_3PO_2}}\right) \cdot a^2_{H^+}$$

$$= E^{o}_{Acid} + \frac{RT}{nF} \ln\left(\frac{a_{H_3PO_3}}{a_{H_3PO_2}}\right) - 0.0591\ (pH).$$

Consequently, the cell reaction can be written as

$$E_{cell} = (E^{o}_{Eu} - E^{o}_{Acid}) + 0.0591\ (pH) + \frac{RT}{2F} \ln\left(\frac{a^2_{Eu^{+3}} \cdot a_{H_3PO_2}}{a^2_{Eu^{+2}} \cdot a_{H_3PO_3}}\right).$$

Finally,

$$E_{cell} = 0.16 + 0.0591\ (pH) + 0.0591 \ln\left(\frac{a^2_{Eu^{+3}} \cdot a_{H_3PO_2}}{a^2_{Eu^{+2}} \cdot a_{H_3PO_3}}\right)$$

As a result of this analysis, it is seen that as the pH increases, there is a better chance for the reaction to take place, all else being constant.

A reduction attempt was first carried out at a low pH ($\simeq$1), with a solution containing equal parts of Eu and Gd. H_2SO_4 was added in order to precipitate any Eu^{++} that might be formed. However, no precipitate was visible, indicating that the reduction had not taken place. Reductions were attempted by raising the pH in small increments. Up to a pH of about 4, no precipitation occurred.

However, a complicating factor was that as the *p*H was raised above 4, hydroxide precipitation of the rare earths began to occur. Both Gd and Eu began to precipitate at the same *p*H and at that point the reduction process could no longer be checked.

At this point attempts of Eu reduction by this method were terminated. Further study is needed to determine whether the hydroxide formation can be repressed or whether the apparent activation energy can be reduced in a manner to allow the reaction to proceed at a lower *p*H.

2.5.3. Ion-Exchange Separations

Ion-exchange is probably the single most powerful, and most used, technique for the separation of the rare earth elements. Even a casual inspection of the literature reveals literally hundreds of separation techniques, each tailored to specific separations and conditions. There are numerous review articles, one of the best being that of Stevenson and Nervik (Stev60). The abundance of articles proves, at least in part, that a technique must be developed for the particular separation of interest. There is no one single method for the separation of all rare earth mixtures. Many factors influence the separation, including the column size, the resin particle size and degree of cross-linkage, the flow rate through the column, the column temperature, and the mass of the sample.

Cation-exchange techniques all involve two steps. The first is to adsorb the rare-earth mixture onto the resin. The second step then involves the desorbtion of specific elements by the appropriate

eluting agent. For the separation of Gd and Eu target material, we have chosen α-hydroxyisobutyric acid as the eluant. This eluant was first used for the separation of actinide elements by Choppin, Harvey, and Thompson (Cho56a) and later adapted to the separation of the rare earth elements by Choppin and Silva (Cho56b).

The column bed was composed of Dowex 50x8 (200-400 mesh), a cation-exhange resin. Dowe 50 is a sulfonated styrene-divinylbezene compound. The x "*n*" designation indicates the degree of divinylbenzene cross-linking. The lower the cross-linking, the more porous the structure. All else being constant, very little cross linking is desirable, inasmuch as this produces a greater surface area per volume. However, a resin with a small amount of cross linking, say x1, has the unfortunate property of greatly changing volume as the solution acidity changes. Thus, a compromise must be reached, and in our case we chose a x8 resin.

Our apparatus, shown in Figure 4, is similar to that described by Thompson, Harvey, Choppin, and Seaborg (Thom54). The column dimensions are 5cm × 2mm, with the column being surrounded by a liquid jacket used to maintain a constant temperature throughout the procedure. For our purpose, boiling trichloroethylene allowed us to maintain the column at 87°C.

The resin bed was composed of Dowex 50x8 (200-400 mesh), which has been described earlier. 8*N* HCl was used to wash the resin. After thoroughly mixing the resin in the acid, only the resin still suspended after about 30 seconds was used to pack the column. This allowed a very densely packed column having a high resin surface area.

Figure 4. Ion-exchange apparatus. This was used principally for the separation of Gd^{149}. The side arm contains the ion-exchange resin. Trichloroethylene vapor (87°C) passes through the jacket surrounding the resin bed to keep it at this constant temperature. The Trichloroethylene vapor and condensate then passes out the top of the heating jacket and returns to the boiling flask. At the top of the apparatus is a water cooled condenser to insure that there is no escape of the "heatant" to the atmosphere. It was generally necessary to use a pressure head at the inlet of the resin bed to regulate the flow rate through the bed.

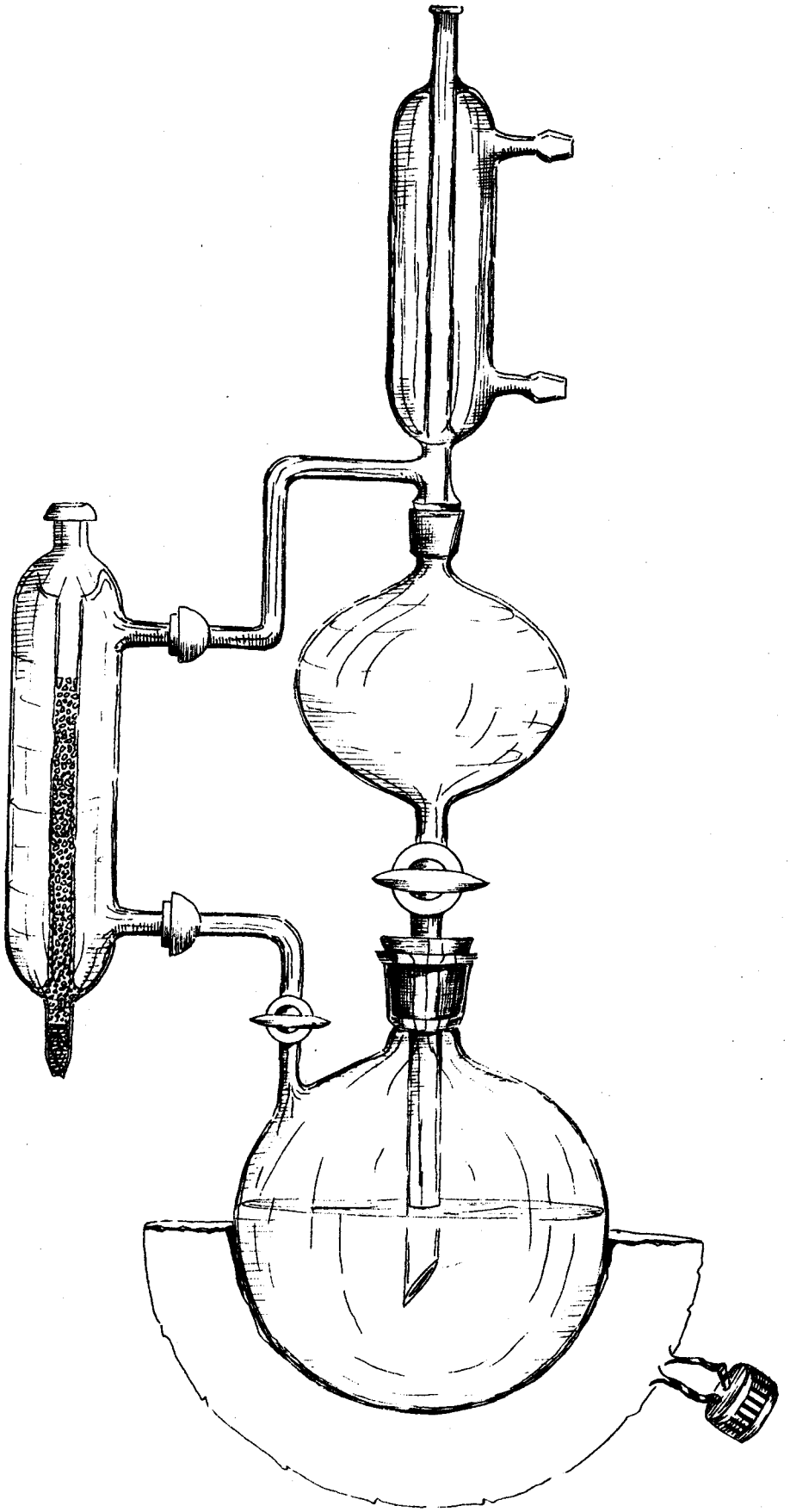

The eluant is prepared by first making a 0.2 *M* solution of ammonium α-hydroxyisobutrate solution, to which HCl is added dropwise to adjust the *p*H to 4.00. The time necessary to remove a particular rare-earth element from the column is highly dependent on the *p*H of the eluent. Choppin and Silva found that a *p*H of 4.0 was optimum for lutetium-ytterbium-thulium separations and a *p*H of 4.6 was optimum for neodymium-praseodymium-cerium-lanthanum separations. Rather than lower the *p*H below 4.2, they found it more desirable to increase the α-hyroxyisobutrate concentration to 0.3 *M* or 0.4 *M*. Reference (Stev60) shows the time versus *p*H relationship for Am, Cm, and Cf. Since the elements are eluted in reverse order, lowering the *p*H to a value less than 4.0 can cause the lower mass elements of a series to remain on the column for such a long time that the separation becomes impractical.

Flow rate has a great effect on the degree of separation, also. An optimum flow rate was found to be 0.5 drop/min.

The target material was dissolved in 1-2 *M* HCl and diluted to obtain a final solution 0.05 *M* in HCl. Eluant was allowed to flow through the column, at 87°C, until bubbles no longer formed in the resin bed. At this point the flow of eluant was stopped and the space above the resin bed was cleared of any remaining solution. This space was then washed with hot water to insure removal of all traces of eluant. Two drops of the water was allowed to flow through the bed. This procedure was then repeated using hot 0.05 *M* HCl. The top cavity (above the bed) was then cleared of all remaining HCl.

Two drops of the solution, (adjusted to 0.05 *M* Hcl), prepared from the target was then introduced to the top of the resin bed and allowed to flow through the bed. Two drops of H_2O was then used to wash down the top cavity. This cavity was then filled with the hot α-hydroxyisobutrate solution and a pressure head connected. The pressure was then adjusted, by the height of the water bulb, to obtain an eluant flow rate of 0.5 drop/min.

Drops were collected on small aluminum planchets, two drops each and dried. They were then counted and a graph prepared of counts per channel versus drop number. An elution curve is shown in Figure 5 for a separation of Gd and Eu, using the above method. The target material ($Eu_2^{151}O_3$ + Gd^{149}) was doped with $Eu^{152,154}$ so that the Eu peak could be identified. The separation is not complete for various reasons, one of the most important being the necessity of having to separate minute quantities of Gd from a gross amount of target material. Running the Gd fraction through a second exchange procedure would greatly enhance the separation.

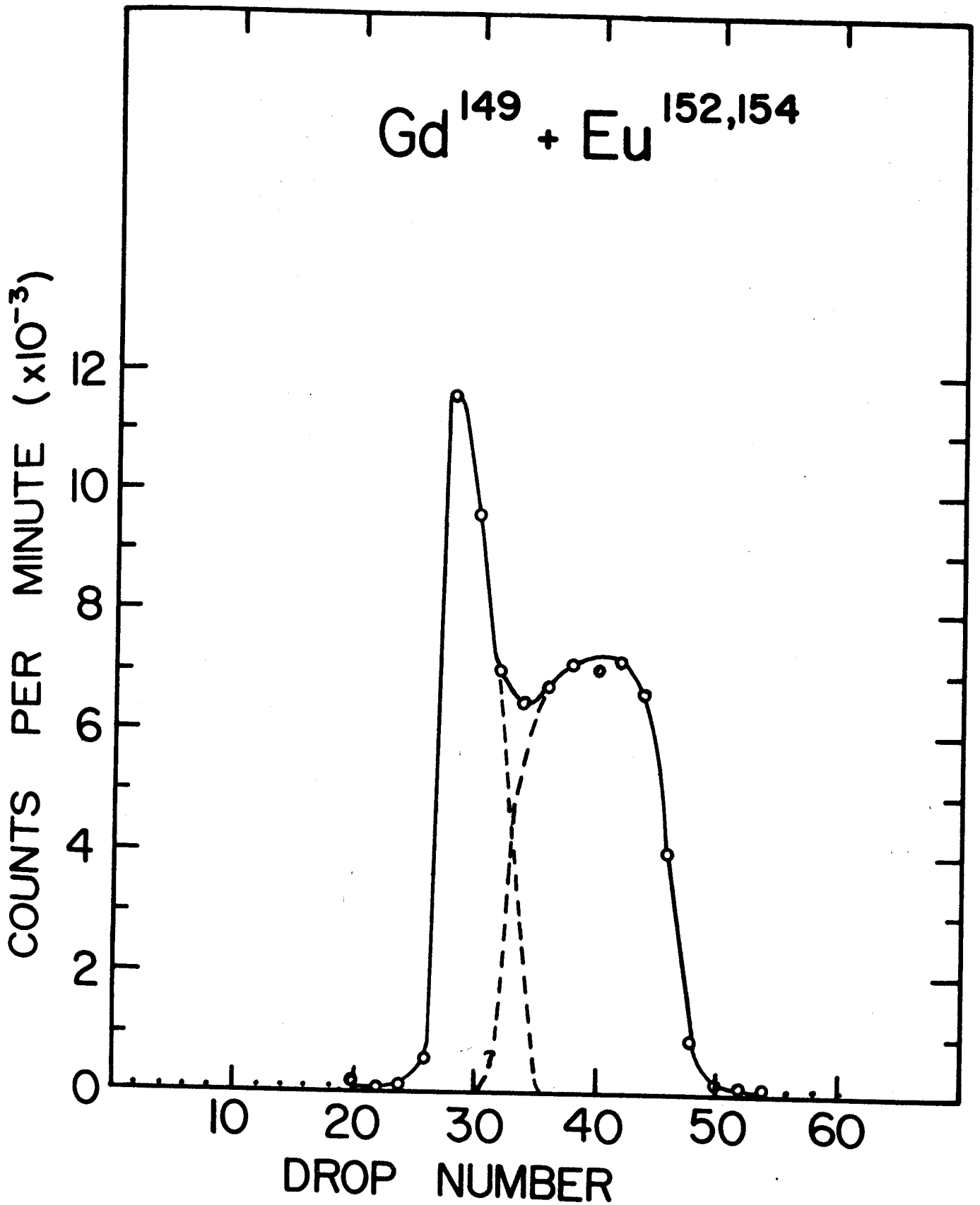

Figure 5. Elution curve for Gd^{149}-$Eu^{152,154}$ using Dowex 50×8 resin and α-hydroxyisobutyric acid as the eluant.

CHAPTER III

DATA REDUCTION

At Michigan State University we have a wealth of computer programs to assist us with the analysis of spectra, ranging from relatively simple programs for determining energy and efficiency curves to quite complex programs which automatically scan a given spectrum, pick out peaks, and determine their energies and relative intensities. Once the fundamental parameters of energies and intensities are determined for the decay of a particular nuclear species, they must fit together in a coherent fashion to arrive at a decay scheme.

In addition to the various coincidence and anticoincidence techniques used to place nuclear levels and γ transitions in a decay scheme, we have programs which look systematically at sums of γ transitions to determine whether certain energy sums equal other energies or energy sums. For example, a sum of two energies could be compared in turn to each single γ-ray energy. If these agree to within a predetermined limit, the computer prints the results. In like manner, three can be compared to one, etc. The results of such a program cannot be used alone with any degree of confidence, but prove to be helpful when used in conjunction with experimental coincidence data.

One of the more tedious jobs necessary for the construction of a decay scheme is that of determining the β feeding

to each of the daughter levels, and ultimately to arrive at a reduced transition probability, or log ft, to each level. This involves a considerable amount of arithmetic, particularly with decay schemes possessing many levels, and is easily adaptable to a computer operation.

This chapter singles out three quite useful computer programs, MOIRAE, SAMPO, and SCHEME and gives a brief description of each one. Also included in § 3.3.3. is a step by step description of the operation of our PDP-9 computer and its usefulness for FORTRAN programming.

3.1. Gamma Ray Energy and Intensity Determinations

3.1.1. Program MOIRAE

MOIRAE (Moir) could be described as a computerized "graphical" method of spectral analysis. This program, as with all programs currently in use in this laboratory, is based on the analysis of photopeaks only. This method of analysis is desirable for several reasons. For example, while total response functions are known for NaI(Tl) crystals and are quite reproducible for all detectors of a given size, they do not reproduce well in going from one Ge(Li) detector to another. Also, using total response functions to strip a γ-ray spectrum results in an error accumulation that is proportional to the complexity of the spectrum being analyzed. Using only photopeaks for the analysis limits any errors from one part of the spectrum from having any effect on the analysis of other parts of the spectrum.

All analysis by means of MOIRAE is performed by instructions to the computer via interfaced sense switches arranged below the display oscilloscope. This equipment is shown in Figure 6. The oscilloscope provides a live display of the spectrum as well as a display of the fitted background curve, channel marker, centroid position of analyzed peak, and provision for displaying the net spectrum that results after subtraction of all events below the background curve. Output is provided by the line printer and/or punched cards, all controlled by the sense switches.

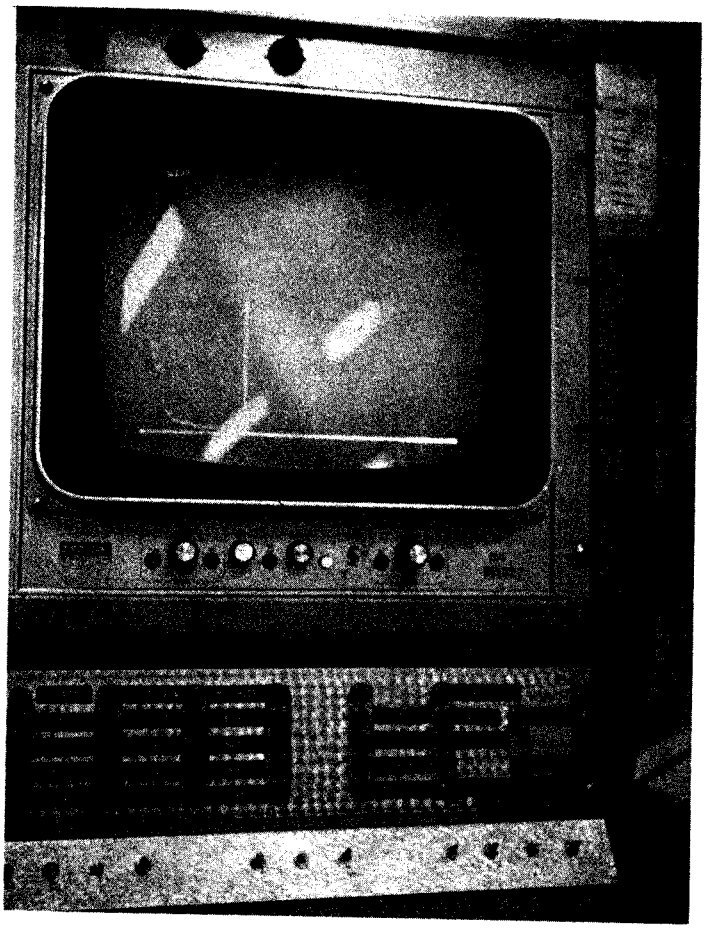

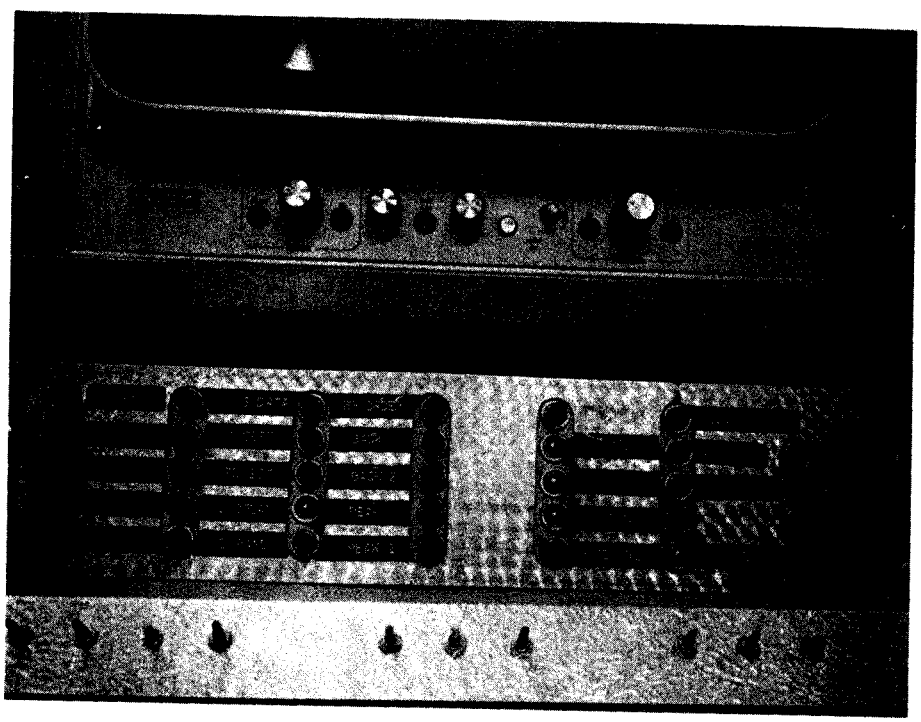

Figure 6. Oscilloscope and sense switches used for program MOIRAE.

MOIRAE is used predominantly for the calculation of centroids and net peak areas of γ-ray spectra. No provision is currently available for γ-ray energy and γ-ray intensity calibrations within the program. These conversions must be made with one of several available auxiliary programs.

Another disadvantage of MOIRAE is its inability to strip individual peaks in a multiplet. These must either be done by hand or by SAMPO (to be described in the next section). Also, MOIRAE requires the constant attention of the user, since all operations are manually controlled by visual reference. A complete γ-ray analysis by use of MOIRAE can take 2-3 hours for complex spectra. Figure 7 shows photographs of a segment of the Gd^{149g} γ-ray spectrum in various stages of analysis. These will be referred to in the following description.

Generally, the first order of business when using MOIRAE is to expand the spectrum horizontally to display only a segment that can be conveniently displayed on the scope. Figure 7a shows an expanded segment of the Gd^{145g} singles γ-ray spectrum, including the 808.5-keV transition (middle peak). The end peaks are the double escape peaks from the 1757.8-keV and 1880.6-keV transitions. The same horizontal expansion is usually kept throughout the entire analysis, the spectrum being "walked" across the scope by use of a sense switch. The vertical display is adjusted for a good view of the background level and is readjusted as necessary.

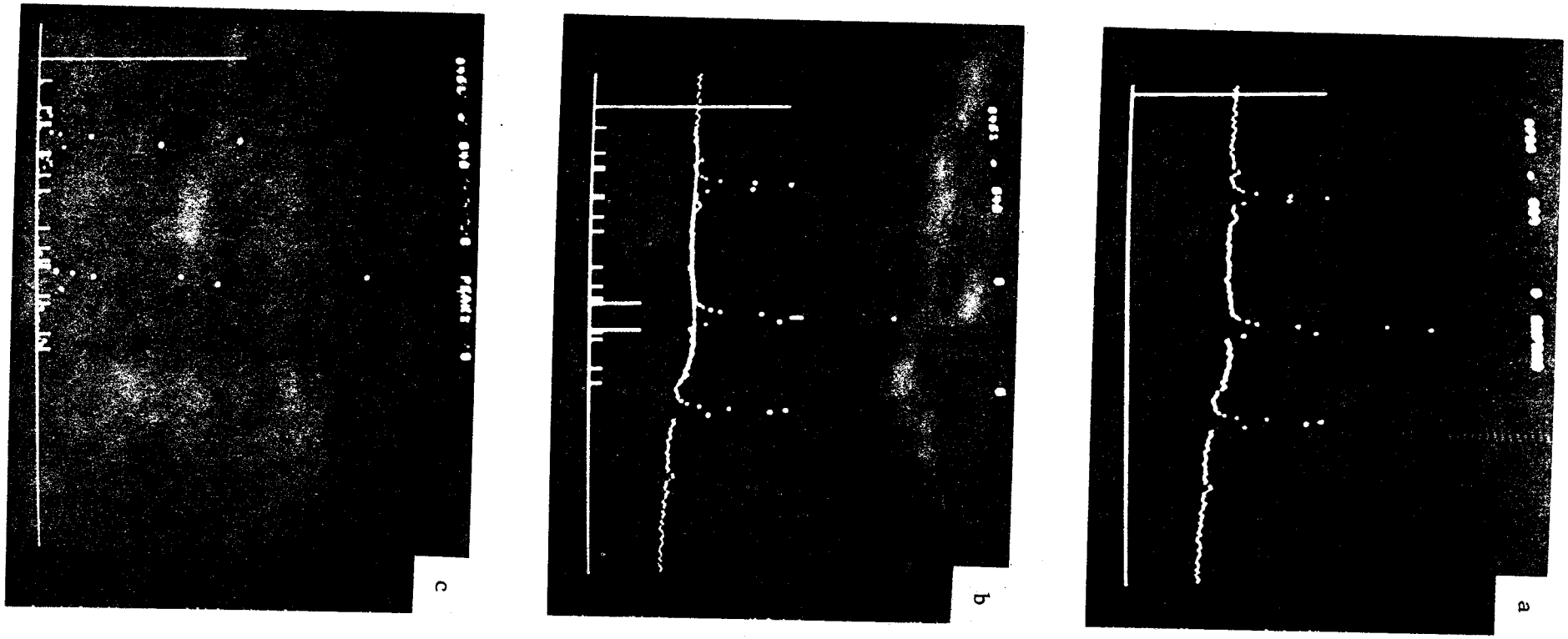

Figure 7. Oscilloscope displays generated by program MOIRAE. 7a shows an expanded segment of the Gd^{145g} γ-ray spectrum which is ready to be analyzed. 7b shows the same segment with a cubic-least-squares curve fitted through the background points. The centroid of the center peak is also marked on this photograph. 7c displays the same region after subtraction of all counts falling under the background curve.

Background can then be fit over all or any portion of the displayed spectral segment. Channels are selected which are to be included in a polynomial least-squares fit, 1*st* through 10*th* order being available at the discretion of the operator. Figure 7b shows the background fit to a 5*th* order polynomial. The large vertical line at the left of the display is the marker used for choosing channels to be used in the analysis. The shortest vertical lines along the bottom of the display are markers showing those channels used in the least-squares background determination. The background curve can then be modified as seems appropriate after inspection.

Once the background under a given peak is properly fitted (in the operator's judgment), the vertical marker is used to designate the upper and lower channels to be considered as end points for the peak. A center of gravity calculation is then performed over the channels which fall beetween the markers to determine the centroid for that peak. This feature is shown in Figure 7b. The two tallest vertical lines under the 808.5-keV peak (middle peak) mark the beginning and ending channels used in the centroid calculation. Notice that the centroid is also marked on the display.

Figure 7c is a display of the same region after subtraction of all counts falling under the background curve shown in Figure 7b, and can be used as another means of checking the "goodness" of fit for the background curve.

In this manner all resolvable peaks in the spectrum are analyzed. The results for each peak are stored on a computer disk and are output together at the end of the analysis. At that point all results are output on the line printer and/or punched cards. Figure 8 shows a sample of the line-printer output from MOIRAE. Beginning at the top of the figure, the raw data are presented for the spectral segment which was displayed on the scope. The center portion of the figure shows the counts per channel for the segment actually used in the background determination. Notice the "smoothness" of this curve. This gives a visual indication of any unexpected fluctuations in the background curve. The bottom portion of Figure 8 shows the counts in the spectral segment after subtraction of the background. Also included is the listing of the analyzed parameters. In particular, the "difference between raw data and background" is the net peak area used in the determination of the γ-intensity, the "centroid" is later used for the energy determination, the "sum of raw data and background" is the raw data count of the peak, the "square root of above" is the square root of the raw data, and the "end points used" are the beginning and ending channels used for the centroid and net area determinations.

The results obtained from MOIRAE are only as good (or bad) as the user's judgment of the analysis as based on the observation of the scope display. Net peak areas can change drastically for peaks situated on Compton edges or other bad-background regions.

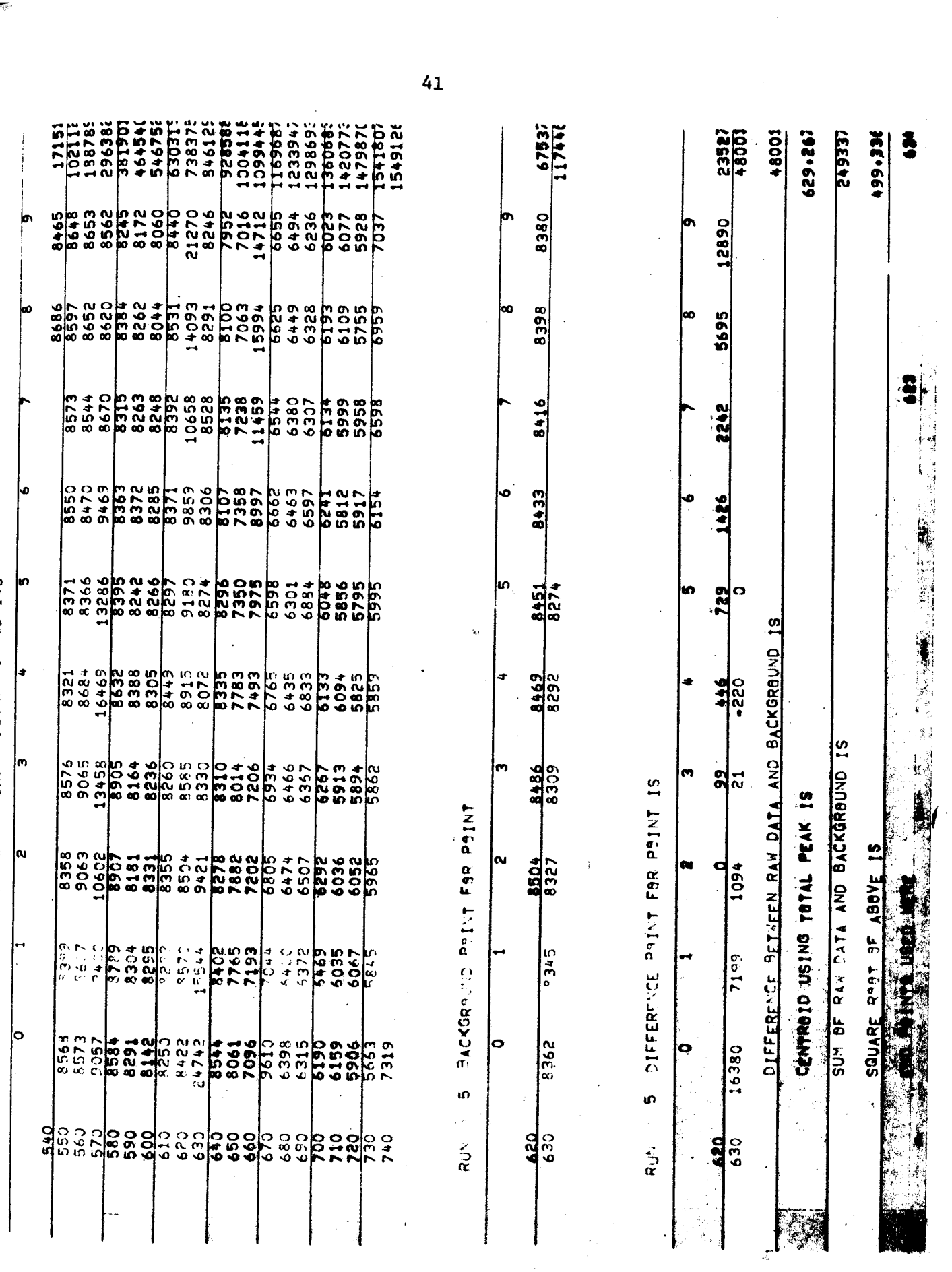

Figure 8. Sample of line-printer output from program MOIRAE.

The results depend on ones judgement as to the shape of the background underlying the peak itself. Since a polynomial background fit can be performed for any size spectral segment, questions arise as to the "best" way to perform this fit. In particular: How large a segment should be fit at one time and what polynomial approximation should be used? Unfortunately, there is no single answer. There is always the unanswerable question of the shape of the Compton background under a peak. For an ideal peak of high intensity situated on a smooth, horizontal background, a straight-line approximation for the background would seem appropriate. For peaks situated on Compton edges, etc., the answer is not so clear cut and must be left to individual judgement. However, if any rule of thumb is valid, it could be said that when the actual Compton shape is not known, a straight-line approximation is as suitable as any other approximation. With this in mind, it seems reasonable that any size interval can be fit to a single polynomial curve as long as the background is fit smoothly and appromixmates the desired background shape under each of the peaks included in the interval. Background fitting over a region is easily accomplished with MOIRAE since the operator is always in visual control. The great advantage of fitting a whole region at one time rather than just over individual peaks is the time saved in the analysis.

It is fortunate that even in the midst of a somewhat uncertain placement of the underlying background, the peak centroid changes only slightly with the different background choices that might be made.

One other very useful feature of MOIRAE should be mentioned. This is the ability to study easily the changes of a single transition through many spectra in a convenient manner. Ordinarily one would have to read in a spectrum, adjust the vertical and horizontal gains by means of the sense switches, and move through the spectrum to the peak of interest. MOIRAE alleviates this bottleneck in that any particular peak or spectral region, once displayed on the scope, can be followed through as many as 20 spectra for such purposes as determining transition half-lives.

3.1.2. Program SAMPO

This computer program was first described by Routti and Prussin (Rou69). It utilizes the photopeak method of analysis, with each experimental peak being fit to a Gaussian function having exponential tails. The program used at Michigan State University is an abbreviated version of this program. At present we have no scope display or light pen capability with this program.

SAMPO performs several analysis tasks including:

1. Fitting of photopeaks to an analytical function and determining the precise centroid for each peak.
2. Fitting and subtraction of background.
3. Calculation of energy and statistical error of the energy for each peak from an internally prepared calibration curve.

4. Calculation of net area and statistical error of the area for each peak and converting this net area to a relative intensity by way of an internally prepared detector efficiency calibration curve.

5. Stripping of multiplets and determining the parameters of steps 1-4 for each of the peaks in the multiplet.

The results of SAMPO analysis are output on the line printer, including plots of the raw data and accompanying fitted background and peak curves. Figure 9 shows a portion of SAMPO output for a Gd^{145g} spectrum. This figure will be referred to in the following description.

Peak centroids are determined by fitting the experimental peak with the Gaussian-exponential function whose parameters must be determined from "standard" peaks. The standard peaks should be chosen from single, well-shaped γ peaks spaced at regular intervals over the whole spectrum under consideration.

Shape parameters for fitting the experimental "standard" peaks with the mathematical function are determined by minimizing the function,

$$\chi^2 = \sum_{i=k-\ell}^{k+m} (n_i - f_i)^2 / n_i \quad ,$$

where i = channel number

n_i = counts in channel i ,

k = approximate channel of peak ,

ℓ, m = channels limiting the fitting interval ,

$$f_i = p_1 + p_2 (i-p_4) + p_3 \exp [-1/2(i-p_4)^2/p_5^2]$$

for $p_4 - p_6^2 \leq i \leq p_4 + p_7^2$,

$$f_i = p_1 + p_2 (i-p_4) + p_3 \exp [1/2\ p_6^2\ (2i-2p_4+p_6^2)/p_5^2]$$

for $i < p_4 - p_6^2$,

and

$$f_i = p_1 + p_2 (i-p_4) + p_3 \exp [1/2\ p_7^2\ (2p_4-2i + p_7^2)/p_5^2]$$

for $i > p_4 + p_7^2$,

and where the minimization process is carried out with respect to the p_i. The p_i are defined as follows:

p_1 = constant in the continuum approximation

p_2 = slope of the continuum approximation

p_3 = height of Gaussian

p_4 = centroid of a Gaussian

p_5 = width of the Gaussian

p_6 = distance in channels to lower Gaussian-exponential juncture.

p_7 = distance in channels to upper Gaussian-exponential juncture.

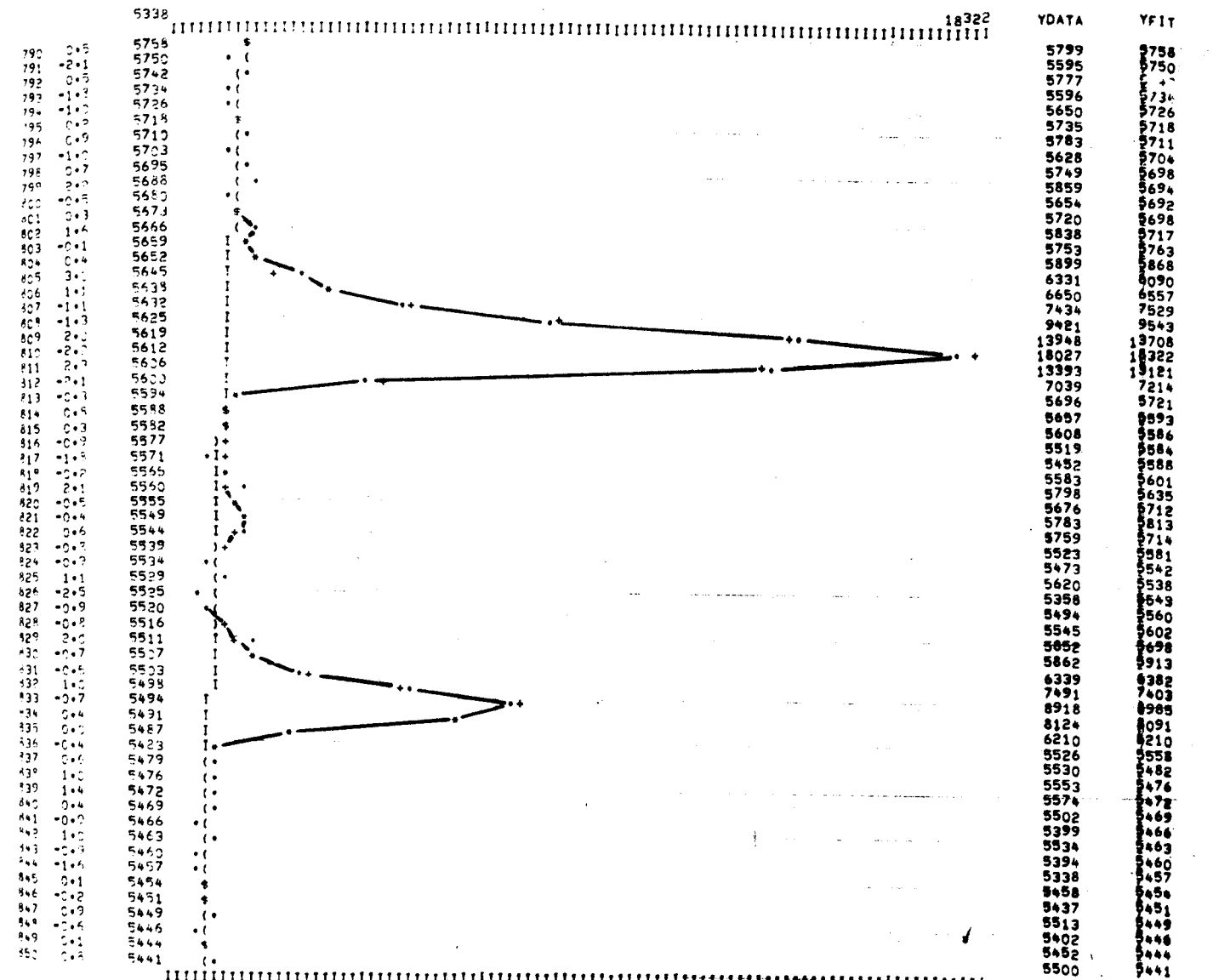

RESULTS FROM THE ABOVE FIT, BE CRITIICAL WITH THE ERROR ESTIMATES
REJECT IF CHISQUARE = 0.8947E+02 OR SIGMA = 1.312 IS UNACCEPTABLE, CHECK PLOT FOR MISSING PEAKS

CHANNEL	FIT-ERR-CH	ENERGY-KEV	CAL-ERR-KEV	EN-ERR-KEV	AREA-COUNTS	FIT-ERR-PC	INTENS-COUNT	CAL-ERR-PC	INT-ERR-PC
[illegible]	0.0032	1041.2006	0.4000	0.4000	0.3777E+05	0.6843	0.3777E+05	0.0000	0.6843
EFFICIENCY DATA NOT READ IN									
[illegible]	0.3143	1056.3315	0.4000	0.5722	0.7765E+03	21.8456	0.7765E+03	0.0000	21.8456
EFFICIENCY DATA NOT READ IN									
[illegible]	0.0253	1078.1460	0.4000	0.4013	0.1043E+05	1.8420	0.1043E+05	0.0000	1.8420

Figure 9. Sample output from the computer program SAMPO.

These shape parameters are part of the output from the program and can be used in subsequent analysis of γ-ray spectra taken under the same experimental conditions, thus affording a great saving in computer time.

The remainder of the peaks in the spectrum are fitted to the Gaussian-exponential function using shape parameters determined by a linear interpolation between values obtained for standard peaks.

An energy calibration curve is prepared from the centroids determined for the standard peaks and the energies given for these peaks. The usual calibration method is to perform a piecewise linear fit between succeeding standard points. Alternatively, higher order polynomials can be used to prepare the calibration curve. Figure 9 shows the results of such an analysis. The line printer plot alone shows a wealth of information. Beginning at the top of the figure,"YFIT" shows the counts per channel for the fitted peak and background curves, while "YDATA" is the actual counts per channel for the raw data. The three rows of numbers at the bottom of the plot show the counts per channel for the fitted background curve, the channel deviation between the raw data, the total calculated counts for each channel, and the channel numbers for each channel in the plot. The symbols used for the plot itself are given vertically on the right hand side of the plot. Further to the right are the results

of the analysis for the plotted segment. The background under each peak is determined by fitting it to a polynomial curve. The net area for a given peak is then determined as the area of the fitted function for the peak minus the area of the fitted background counts under the peak. Therefore, with SAMPO the net areas which are output are areas determined by the fitted functions and not areas determined directly from the raw data. These net peak areas can be transformed into relative transition intensities by means of a detector calibration curve prepared from intensity data supplied for the designated standard peaks. If no intensity data are input, only net peak areas and relative peak areas are output by the program.

The statistical error in an area determination is expressed as a percentage error. Such an error reflects the difference between the fitted analytical function and the raw experimental points for a given peak; therefore, such an error value partially reflects how well the peak shape matches the shapes of the bracketing standard peak shapes.

At this point a comment is in order on the use of higher order curves used for energy calibration. While such a curve may seem to fit the selected data points with a smaller standard deviation, when there is a significant nonlinearity in the system, oscillations can occur in the fitted curve which may cause significant errors in the peak energies determined between the fitting points. Consequently, in a system of unknown or marginal linearity the piecewise linear fit can be

a better approximation for the calibration curve. This is the procedure chosen for SAMPO.

Another point to be made is that under no circumstances should energies be sought from a calibration curve of higher than first order when the centroid to be converted is outside the range of standard centroids used in the preparation of the curve. Depending on the degree of curvature, energy values so obtained can actually be off by several keV.

All of the above described tasks can be performed by SAMPO in two modes, automatic or manual. Generally, a combination of both is used for the complete analysis of a γ-ray spectrum. First, peaks are picked which are to be used for energy and shape standards. SAMPO is then allowed to determine and shape parameters and energy calibration curve from this information. Next, SAMPO automatically searches the spectrum for all suspected peaks. Each candidate is screened for statistical significance as well as for possessing the proper shape before receiving SAMPO's seal of approval. Each peak passing the required tests is then fully analyzed as already described. In complex spectra there are always weak peaks which fall below the minimum statistical limit set for automatic analysis. The manual mode of operation is then used for the analysis of these peaks. In the manual mode, analysis is performed only on those peaks for which approximate centroids are input on FITS cards. Thus, it usually requires two passes of SAMPO through the computer to effect a complete analysis of a γ-ray spectrum, the second pass

being required for the manual analysis of the weak peaks and multiplets not recognized in the automatic analysis mode on the first pass. The analysis results, like the sample shown in Figure 9, are given again in summary form at the end of the lineprinter output. In this summary the results for all peaks are given in ascending centroid order.

One of the more powerful features of SAMPO is its ability to resolve, or strip, peaks belonging to multiplets. Using SAMPO in its manual mode is the most satisfactory procedure for this purpose. The approximate centroids for each peak in the multiplet are input on FITS cards, several cards generally being input at one time on which the centroids are varied slightly. SAMPO outputs the results for each card along with the chi-square calculation for each one. Most often, that analysis is chosen which has the lowest chi-square. In this regard SAMPO has proven itself able to determine accurately both energies and intensities for each peak in the multiplet. When more than one pass through the computer must be made for an analysis, or when analyses are to be performed on several γ-ray spectra taken under the same experimental conditions, the originally determined shape parameters can be input at the start of the program rather than requiring SAMPO to recalculate them. This results in less computer time being used for the analyses. A general rule of thumb is that the Sigma-7 computer can analyze a complex spectrum (say 50 peaks) in a period of about 15 minutes. This compares to the 2-3 hours necessary, under favorable conditions, for the same analysis by use of MOIRAE.

On a few occasions MOIRAE and SAMPO have been used for the analysis of the same spectrum. For the intense peaks the centroids agree to less than 0.1 channel, with an overall average of about 0.2 channel for all peaks in the analysis. As might be expected, the peak area determinations show a greater variation between the two methods of analysis. The variation is particularly pronounced on badly shaped, weak peaks. The better method for these "bad" cases must be determined on an individual basis. Area determinations for the majority of peaks, however, show agreement to usually better than ±10%.

3.2. PDP-9 Machine Operation for FORTRAN Programming

Being able to use the PDP-9 computer for running computer programs, as well as for spectra acquisition, is a great benefit. This is particularly true when, for one reason or another, the Sigma-7 is not available. The use of DECtape greatly simplifies the operation of the PDP-9 for this programming. To facilitate the use of the PDP-9 by future personnel in the laboratory, the following descriptions are offered.

Keyboard Monitor System

This is the monitor system furnished by DEC for use with the DECtape option. This allows all of the FORTRAN math library, editor, FORTRAN compiler, Macro assembler and loader, as well as the Monitor to be stored on a single DECtape. In addition, several other utility programs are stored on this same tape.

It is most useful to create and modify FORTRAN programs by use of the editor supplied by DEC. The description of this program

is found in the Utility Programs Manual for the Advanced Software System (UPM). The editor outputs the created FORTRAN program in ASCII code onto punched paper tape. This tape is then read into the computer under the control of the FORTRAN compiler program, which in turn outputs a binary coded paper tape in machine language to be used as the operational program. These binary object programs can be stored on DECtape and called through the Keyboard Monitor.

Several user programs, including SCHEME which is described in the next section, are available and are further described in (Ann69). All input and output communication with these programs is via the teletype.

A sequential guide for loading and using these FORTRAN programs is the following:

1. Mount SYSTEM TAPE on one of the transports. Set the transport address to 8. Set the remote-off-local switch to remote.
2. Mount the user tape on the other transport. Set the transport address to 2. Set the remote-off-local switch to remote.
3. Turn on the TTY.
4. Place the Advanced Monitor Bootstrap paper tape in the reader. Set the address switches to 17637. Press I/O Reset on the computer, then press Readin.

At this point the Bootstrap will be read, which in turn initiates the loading of the keyboard Monitor System into core. When the system is

ready, "Monitor V4B" will be typed on the TTY.

5. Type in load, then hit the carriage return. This will cause the Linking Loader to be brought into core. When accomplished, "Loader V3A" will be typed out.
6. Type the name of the program, followed by the name(s) of any user subroutines which the main program calls for. Each name is to be separated by a comma. Press Alternate Mode (not the carriage return).

The user program and subroutines will be loaded first, followed by all subroutines, functions, etc., from the system tape which are necessary for the operation of the user program. As each is loaded, the name and loading address will be output on the TTY. Any loading error encountered is noted by number of the TTY and can be looked up in one of the manuals (e.g. UPM). When the program is successfully loaded, a "control S" (↑S) is output on the TTY.

7. To initiate program operation, ↑S is typed on the TTY.

At this point control is turned over to the program. Program input parameters and formats are obtained from the appropriate program listing.

A program can be reinitialized at any time by simply typing ↑S. Also, control can be returned to the Monitor at any time by typing ↑C.

3.3. Determination of the Decay Scheme Parameters with Program Scheme

Program SCHEME is one of the available FORTRAN programs for use with the PDP-9 computer. This program relieves the user of some of the drudgery encountered on the way to obtaining log *ft* values for β decay. Utilizing the level energies and β feeding for the daughter states as the input information, it calculates EC(K)/EC(tot), EC(K)/β^+, and EC(tot)/β^+ decay to each level. The resulting electron- capture percentages are then used in the log *ft* calculations. To use this program one should have an understanding of the steps necessary for arriving at the log *ft* values.

3.3.1. Steps Necessary in the Determination of Log *ft* values for β Decay.

The following is a summary of the steps necessary for log *ft* determinations. These steps will vary to a degree depending on the nucleus under discussion.

1. Obtain total transition intensities for all electromagnetic transitions involved in the decay schems. This must include corrections to the γ-ray intensities for the internal-conversion process.
2. Total β decay to each daughter level is determined by subtracting the electromagnetic intensity to a level from the total intensity out of a level. β decay to the ground state presents a special

problem and can be arrived at by a variety of means, including determination by use of the annihilation peak, x-ray peaks, or through the positron intensity to the ground state as determined from a positron spectrum.

3. Obtain EC(K)/EC(tot) for each level, where EC(K)= K-electron capture intensity and EC(tot) = total electron capture intensity.
4. Obtain EC/β^+ for each level, where β^+ = positron intensity.

The parameters of steps 3 and 4 are obtained from graphs in the Table of Isotopes (TI67).

5. From steps 3 and 4 the ratio EC(tot)/β^+ is obtained for each level.
6. From steps 2 and 5 the total electron capture intensity to each level is obtained.
7. Calculate the log ft value for each level, based on the EC(total) decay to each level.

The log ft values are usually determined through the equation log ft = log $f_o t$ + log C + Δlog ft. All three terms on the right side of the equation can be read from graphs given in (TI67) or (NST59).

The above steps assume decay from a single parent level. If an isomeric level is present in the parent, which can decay by electromagnetic and β transitions, the procedure becomes more complicated.

3.3.2. A Short Look at the Log *ft* Equation

Retreating one step, to a paper by Moszkowski (Mosz51), we can take a look at the origin of the parameters involved in the above equation for arriving at log *ft* values. For β^+ decay, f_o is given by

$$f_o = \int_1^{W_o} W(W^2-1)\ (W_o-W)^2 dW \rightarrow$$

$$[W_o^4/30)-3/20)W_o^2-(2/15)][W_o^2-1)] \ + (2.302/4)W_o \log[W_o^2-1)\ ],$$

where W_o is the transition energy in units of mc^2. This rather complex expression reduces to $f_o = (W_o + E_K)^2$, in units of mc^2, for electron-capture. In this equation E_k is the k-binding energy for the parent species. From this expression, log $f_0 t$ is easily obtained. Note that t, the half-life, is the total half-life for the parent species. Log C is a factor arising as a Coulomb correction term. For EC decay this is a constant for a given Z and is most easily obtained from available graphs. Δ log *ft* is a correction term for a branch that consists of less than 100% of the total decay. It is simply Δ log *ft* = - log (p/100), where p is the percent electron-capture decay to the particular level. Note that to obtain this percentage, the electron-capture intensity to the level is normalized to the total intensity (both EC and β^+) to all levels, including the ground state.

To go through the procedure described in §3.3.1. once would be bad enough, but if it should happen that some number has to be changed along the way, say a change in a γ-ray intensity,

the whole procedure must be repeated since all parameters are related, and a change in one means a change in all of them. At this point one appreciates the convenience of letting the computer do all this busy work.

3.3.3. Description of Program SCHEME

The following is the computer listing of the program SCHEME and the required subroutine BRATE. The program requires the input of the total β intensity to each daughter level, including the ground state. The program assumes β decay from a single parent level. The following program listing for SCHEME contains comment statements as an aid in the use of the program. The parameters A, B, and C are the coefficients resulting from a least squares fit of EC(K)/β^+ values, over the appropriate energy range, from the graph in (TI67). This could not be incorporated into SCHEME because of memory limitations.

```
   *P
C      PROGRAM SCHEME
C      THIS PROGRAM IS FOR THE DETERMINATION OF EC/B+ RATIOS,
C      TOTAL EC INTENSITIES TO EACH LEVEL, PERCENT DECAY TO EACH
C      LEVEL AND THE LOG FT'S TO EACH LEVEL.
C      EC = ELECTRON CAPTURE ENERGY TO THE GROUND STATE.
C      AK1 = TO BE READ FROM THE GRAPHS(TABLE OF ISOTOPES,P.576)
C      BK = K BINDING ENERGY
C      BL1 = L1 BINDING ENERGY
C      S = L2 TO L1 RATIO
C      V = TOTAL(M+N+...) TO TOTAL L RATIO
C      EN(I) = LEVEL ENERGIES(INCLUDING 0.0)
C      ANTN(I) = TOTAL INTENSITY TO LEVELS(EC + B+).
C      CIN(I) = K-CAPTURE INTENSITIES TO LEVELS
C      A,B,C = COEFFICIENTS FROM LEAST SQUARED FIT OF EC(K)/B+
C              DATA FROM GRAPH IN THE TABLE OF ISOTOPES.
C      Z = LOG(C) FROM GRAPH FOR EC IN THE TABLE OF ISOTOPES.
C      HF = TOTAL HALF-LIFE IN SECONDS.
C
       DIMENSION DE(50),R(50),CAP(50),ANTN(40)
       DIMENSION CIN(40),FN(40),DELT(40)
       COMMON/C1/EN(40),RESULT(40)
     1 WRITE(1,100)
   100 FORMAT(27H PROGRAM SCHEME, ENTER DATA//)
       READ(2,220)N
   220 FORMAT(I2)
       READ(2,200)EC,AK1,BK,BL1,S,V
   200 FORMAT(E15.8)
       WRITE(1,140)
       READ(2,210)(EN(I),I=1,N)
   210 FORMAT(F10.2)
       WRITE(1,140)
       READ(2,210)(ANTN(I),I=1,N)
       WRITE(1,140)
       READ(2,200)A,B,C,HF,Z
C
C      FOR OBTAINING EC DECAY ENERGIES FOR EACH LEVEL.
C
       DO 300 I=1,N
       DE(I) = EC-EN(I)
   300 CONTINUE
C
C      R = L1 TO K RATIO FOR ALLOWED AND 1ST. FORBIDDEN TRANS.
C
       DO 310 I=1,N
       ANUM = (DE(I)-BL1)**2.0
       ADEN = (DE(I)-BK)**2.0
       R(I) = AK1*(ANUM/ADEN)
   310 CONTINUE
```

```
C       CALCULATION OF PERCENT DECAY BY K-CAPTURE
C
        SUM = 1.00+S
        DO 320 I=1,N
        CAP(I) = 1.0/(1.00+R(I)*SUM*(1.00+V))
  320   CONTINUE
        WRITE(1,110)
  110   FORMAT(1H0///)
        CALL BRATE(N,A,B,C,EC)
        WRITE(1,120)
  120   FORMAT(8X,7H ENERGY,8X,8HECL1/ECK,6X,13HEC(K)/EC(TOT),8X,
       18HEC(K)/B+/)
        DO 330 I=1,N
        WRITE(1,130)EN(I),R(I),CAP(I),RESULT(I)
  130   FORMAT(5X,F10.2,(3(5X,E12.6)))
  330   CONTINUE
        WRITE(1,140)
  140   FORMAT(1H0)
C
C       SECTION FOR DETERMINING EC(TOT)/B+ RATIOS
C
        DO 50 I=1,N
   50   RESULT(I) = (RESULT(I)/CAP(I))
C
C       FOR DETERMINING TOTAL EC TO EACH LEVEL.
C
        DO 51 I=1,N
        IF(ANTN(I).GT.0.0) GO TO 49
        CIN(I) = 0.0
        GO TO 51
   49   CIN(I) = (RESULT(I)*ANTN(I))/(1.00+RESULT(I))
   51   CONTINUE
        ADD = 0.00
        DO 52 I=1,N
        ADD = ADD+ANTN(I)
   52   CONTINUE
        DO 53 I=1,N
        ANTN(I) = (ANTN(I)/ADD)*100.0
        CIN(I) = (CIN(I)/ADD)*100.0
   53   ANTN(I) = (ANTN(I)-CIN(I))
```

```
C       SECTION FOR THE CALCULATION OF LOG FT VALUES
C
        DO 800 I=1,N
        F0 = ((DE(I)+BK)/511.0)**2.0
        FN(I) = ALOG10(F0*HF)
        IF(CIN(I).EQ.0.00) DELT(I) = 20.00
        IF(CIN(I).EQ.0.00) GO TO 800
        DELT(I) = -ALOG10(CIN(I)/100.00)
  800   CONTINUE
        WRITE(1,365)
  365   FORMAT(5X,7H ENERGY,5X,9H%EC DECAY,5X,9H%B+ DECAY,2X,6HLOG FT/
        DO 810 I=1,N
        VALU = FN(I)+Z+DELT(I)
        WRITE(1,370)EN(I),CIN(I),ANTN(I),VALU
  370   FORMAT(2X,F10.2,(2(2X,E12.5)),2X,F6.2)
  810   CONTINUE
        WRITE(1,140)
        WRITE(1,150)
  150   FORMAT(19H END OF CALCULATION)
C
C       MM USED FOR HALTING THE PROGRAM
C       PRESS CARRIAGE RETURN TO REINITIALIZE THE PROGRAM.
C
        READ(2,230)MM
  230   FORMAT(I1)
        GO TO 1
        STOP
        END
```

The following subroutine, necessary for the determination of the EC(K)/β^+ ratios, must be used with program SCHEME. These ratios are determined from a quadratic equation whose coefficients must be determined separately (due to memory limitations) from data given in (TI67).

```
C       SUBROUTINE BRATE
C       TO BE USED WITH PROGRAM SCHEME.
C       FOR THE DETERMINATION OF EC(K)/B+ RATIOS BASES ON THE
C       GRAPH IN THE TABLE OF ISOTOPES (P.575).
C       A,B,C = COEFFICIENTS FROM LEAST SQUARED RESULTS (LOG VALUES).
C       EC = ELECTRON CAPTURE DECAY ENERGY TO THE GROUND STATE.
C       N = NUMBER OF ENERGY LEVELS TO BE CONSIDERED.
C       EN = LEVEL ENERGIES.
C
        SUBROUTINE BRATE(N,A,B,C,EC)
        COMMON/C1/EN(40),RESULT(40)
        CONST = EC-1022.0
        WRITE(2,235)CONST
  235   FORMAT(2X,25H\TOTAL B+ DECAY ENERGY = ,F8.2//)
        DO 10 I=1,N
        ANUM = CONST-EN(I)
        IF(ANUM.GT.0.0) GO TO 2
        WRITE(2,230)I
  230   FORMAT(1X,7H LEVEL ,I2,33H IS GREATER THAN THE DECAY ENERGY/)
        RESULT(I) = 1.0E20
        GO TO 10
    2   RESULT(I) = ALOG10(ANUM)
   10   CONTINUE
        DO 15 I=1,N
        ANSW = A+B*(RESULT(I))+C*(RESULT(I)*RESULT(I))
        RESULT(I) = 10.0**ANSW
   15   CONTINUE
        RETURN
        END
```

Chapter IV

EXPERIMENTAL RESULTS

4.1. The Electron-Capture Decay of Gd^{149}

4.1.1. Introduction

Neutron-deficient Gd isotopes lie in a region of special interest for the testing of nuclear models. They and their Eu daughters range from nuclei that have large quadrupole moments, suggesting permanently deformed nuclei, through closed-shell nuclei that can be described by an extreme single-particle shell model. The heavier isotopes ($N \geq 90$) are permanently deformed and exhibit well-developed rotational bands and other features that have been described successfully by the Bohr-Mottelson unified model. Spherical nuclei appear as one approaches the closed neutron shell at $N=82$. It would be of considerable interest to be able to correlate the nuclear levels, especially in the odd-mass nuclei where single-particle states are most easily observed, as one moves from the spheriodal region into the spherical region, and we have embarked on a program to do this, primarily through the study of the radioactive decay of neutron-deficient GD isotopes. As Gd^{152}, Gd^{154}through Gd^{158}, and Gd^{160} are stable (Gd^{152} is slightly α active), Gd^{153} is the isotope nearest stability which permits the study of Eu states. And, because the decay schemes of Gd^{153} and Gd^{151} (refs. Alex 64 and Shir 63) are fairly well characterized, the logical place to begin the experimental investigation was with Gd^{149}.

9.4-d Gd^{149} was first discovered by Hoff, Rasmussen, and Thompson (Hoff 51) in 1951, who produced the isotope by the reactions, $Eu^{151}(p,3n)Gd^{149}$ and $Sm^{147}(\alpha,2n)Gd^{149}$. Since that beginning, several papers have been published on its partial decay scheme. Because of the complexity of the γ-ray spectrum, however, the earlier investigations (Hoff 51, Shir 57, Pras 62) that used NaI(Tl) detectors did not observe a number of the weaker and/or more closely spaced lines because of the inherently poor resolution of these detectors.

However, even in more recent investigations, in which Ge(Li) detectors (Jak 66, Adam 68) and conversion-electron detectors (Anto 58, Adam 58, Dah 59, Harm 66) were employed, discrepancies remain as to many of the Eu^{149} energy levels and also even with respect to which transitions properly follow Gd^{149} decay. In particular, there has been disagreement in the placement of transitions appearing at 993, 1013, and 1082 keV in the γ-ray spectrum. We undertook the present investigation to try to eliminate some of these uncertainties.

Gd^{149} decays almost exclusively by electron capture, although a small α branch of $4.6\pm1.5\times10^{-6}$ and an energy of 3.01±0.02 MeV has been reported (Siiv 65). We have been able to put an upper limit of $10^{-3}(\beta^{+}/K)$ on the positron branch (cf.§ 1.4). This means that the electromagnetic transitions become the exclusive tool for its study. Very good conversion electron data already existed, so we made use of these and have concentrated on the photon spectra and coincidence and anticoincidence experiments.

4.1.2. Source Preparation

Gd^{149} was prepared by the reaction, $Eu^{151}(p,3n)Gd^{149}$. Both natural europium oxide (47.82% Eu^{151}, 52.18% Eu^{153}) and separated isotope (96.83% Eu^{151}, 3.17% Eu^{153}) obtained from Isotopes Division, Oak Ridge National Lab., were used in the proton bombardments. The proton beam was furnished by the MSU Sector-Focused Cyclotron, using a beam energy of 28 MeV with a typical current of 2 μA. Typically, 100 mg targets were bombarded for periods of 1-2 h.

For the first few hours after the bombardments, several short-lived peaks were evident in the spectra. However, after these disappeared, essentially pure Gd^{149} remained. This happy circumstance results because other (p,xn) reactions that should be possible have product nuclei of long half-lives. Activity resulting from the decay of the daughter, Eu^{149} (t = 106 d), did not show up for several days. However, some spectra (particularly for the anti-coincidence runs and for the study of the 993-, 1013-, and 1082-keV peaks) were obtained after chemical separation of Gd from the target material. Two different methods of chemical separation were employed.

The first method was the utilization of Zn-HCl reduction, described in §II.5.1. Owing to a semi-stable Eu^{++} state, Eu can be separated from the reduction mixture by precipitation with H_2SO_4. This technique, carried out two successive times on the target material, yields quite pure (as to the radioactive components) Gd^{149}.

For γ-ray analysis, this was the only step necessary. When the source must be essentially "mass free", as for an electron source, the Zn^{++} must be removed. This can be accomplished by extraction of the Zn^{++} with methyl-isobutyl ketone (hexone).

The second method of separation used was cation-exchange, described in §2.5.3. The resin beds were composed of Dowex 50×8 resin (200-400 mesh) and were 4-5 cm in length and 2 mm in diameter. A trichloroethylene bath was used to maintain the column temperature at 87°C during the separation. The eluting agent was 0.4 *M* α-hydroxy-isobutyric acid with the *p*H adjusted to approximately 3.8-4.0 by the addition of NH_3 solution.

4.1.3. Gd^{149} Spectra

4.1.3.A. Singles Spectra

Two Ge(Li) detectors, both of which were manufactured in this laboratory, were used for all spectra. One was a 7-cm^3 5-sided coaxial detector, the other a 3-cm^3 planar detector. Both were mounted in dip-stick cryostats having aluminum housings 0.16-cm thick. The detectors were used with low-noise room-temperature FET preamplifiers, *RC* linear amplifiers having pole-zero compensation, and 1024- and 4096-channel analyzers.

The Gd^{149} sources were usually counted after having aged several days, but spectra were obtained at times varying from immediately after bombardment to several weeks after bombardment. This technique, together with the chemical separations, enabled us to identify impurity γ rays.

The γ-ray energies were determined by comparison with the standards listed in Table 2. The larger peaks were first determined by counting the Gd^{149} sources simultaneously with these standards. The weaker peaks, which would be obscured by the standards, were later determined by using the then well-determined stronger Gd^{149} peaks as internal standards. The centroids of the standard peaks were determined by using a computer program (Moir), described in §III.1.1. that first subtracts the background by performing a cubic least-squares fit to several channels on each side of the peak. The channels included in the peak are fit to a quadratic curve to determine the centroid, and the centroids of the peaks are fit to a least-squares nth degree curve, which

Table 2. γ-ray Energy Standards used for Gd^{149}.

Nuclide	γ-Ray energies (keV)	Reference
Am^{241}	50.545±0.031	a
Ce^{141}	145.43 ±0.02	b
Cm^{243}	209.85 ±0.06	c
	228.28 ±0.08	c
	277.64 ±0.02	c
Cs^{137}	661.595±0.076	d
Mn^{54}	834.85 ±0.10	e
Co^{60}	1173.226±0.040	f
	1332.483±0.046	f
Co^{56}	846.4 ±0.5	g
	1038.9 ±1.0	g
	1238.2 ±0.5	g
	1771.2 ±1.0	g
	D2598.5 ±0.5	g

[a]J. L. Wolfson, Can. J. Phys. 42, 1387 (1964).

[b]J. S. Geiger, R. L. Graham, I. Bergström, and F. Brown, Nucl. Phys. 68, 352 (1965).

[c]R. E. Eppley, unpublished results (1969).

[d]D. H. White and D. J. Groves, Nucl. Phys. A91, 453 (1967).

[e]W. W. Black and R. L. Heath, Nucl. Phys. A90, 650 (1967).

[f]G. Murray, R. L. Graham, and J. S. Geiger, Nucl. Phys. 63, 353 (1965).

[g]R. L. Auble, Wm. C. McHarris, and W. H. Kelly, Nucl. Phys. A91, 225 (1967).

becomes the calibration curve. This calibration curve, in turn, is used to determine the energies of the unknown peaks by a similar process.

The relative peak intensities were determined from the peak areas with the use of relative photopeak efficiency curves for both Ge(Li) detectors. The curves were obtained by the use of a set of standard γ-ray sources whose relative intensities have been carefully measured repeatedly with a NaI(Tl) detector.

We have identified 25 γ rays as resulting from the ε decay of Gd^{149}. Singles spectra are shown in Figure 10 (separated Eu^{151} target) and Figure 11 (natural Eu target). A list of the γ-ray energies and intensities is given in Table 3. These energies and intensities are average values from many runs in which various counting geometries, both detectors, and different combinations of associated electronics were used. The listed errors are the overall experimental errors determined as 1/2 of the range of the values obtained for all the runs included for each average value.

The *K* x-ray intensity was obtained by a direct comparison with Ce^{141}, of which 70% decays to the 145.4-keV state of Pr^{141}. The Gd^{149} x-ray spectrum is shown in Figure 12 along with x-ray spectrum of $Ce^{139,141}$. The gain of these spectra is such that the 149.6-keV γ-ray for Gd^{149} is included as are the 145.4-keV and 165.8-keV transitions for Ce^{141} and Ce^{139}, respectively.

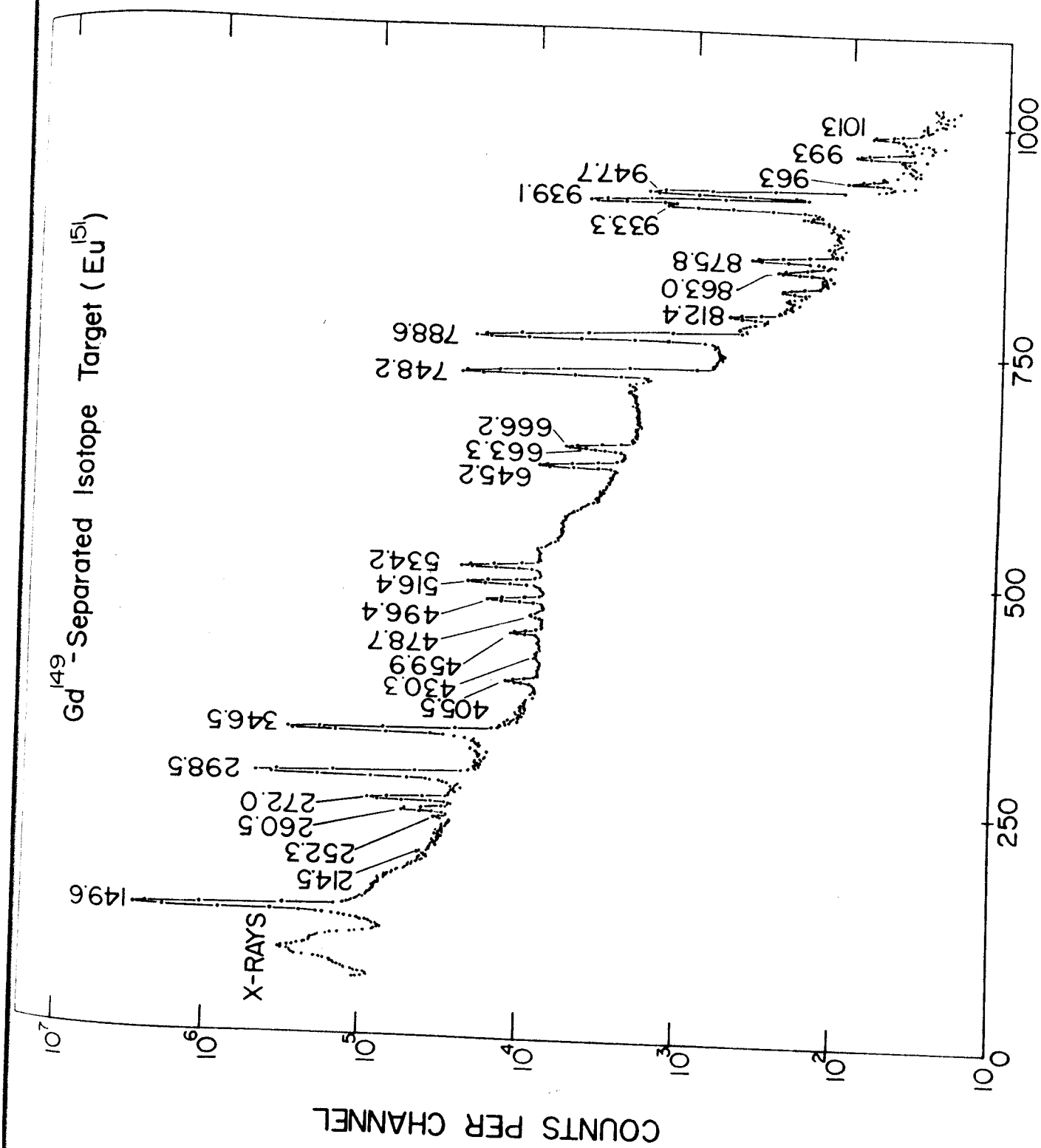

Figure 10. Gd^{149} singles γ-ray spectrum from a Eu^{151} separated isotope target.

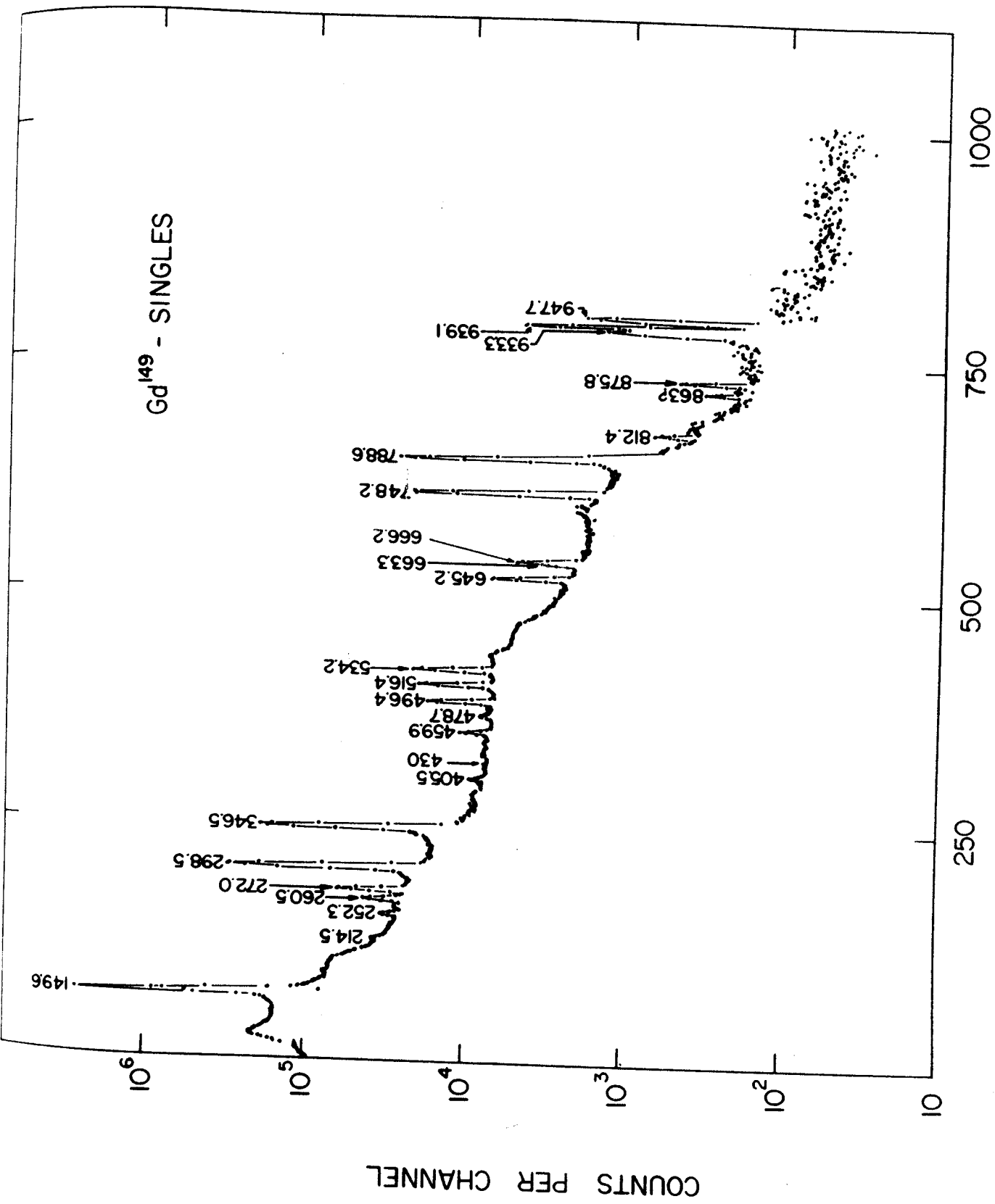

Figure 11. Gd^{149} singles γ-ray spectrum from a natural Eu target.

Table 3. Energies and relative intensities of γ rays from the decay of Gd^{149}.

This work		Jaklevic, Funk, and Mihelich[a]		Adam, Toth, and Meyer[b]	
Energy (keV)	Intensity	Energy (keV)	Intensity	Energy (keV)	Intensity[c]
K x-rays	468 ±100	*K* x-rays	487 ±35	–	–
149.6±0.2	233.4 ±10	150.0±0.5	197 ±20	149.8	258.9 ±20.0
–	–	–	–	184.8	0.23 ± 0.12
214.5±0.6	0.81± 0.10	216.0±0.5	1.6± 0.8	216	0.91 ± 0.40
–	–	–	–	230.4	0.65 ± 0.31
–	–	–	–	235.1	0.14 ± 0.07
252.3±0.7	1.08± 0.25	–	–	252.5	0.54 ± 0.15
260.5±0.3	5.80± 0.4	262.0±0.5	7.0± 0.7	260.9	4.70 ± 0.80
–	–	–	–	264.6	
–	–	–	–	267.8	0.061± 0.015
–	–	–	–	268.6	
272.0±0.2	14.6 ± 0.6	272.0±0.5	16.1±2	272.6	11.6 ± 1.0
298.5±0.2	126.7 ± 10	298.5±0.5	106 ±10	298.7	114.8 ± 4.9
346.5±0.3	≡100	347.0±0.5	100 ±10	346.8	100.0 ± 4.9
405.5±0.7	3.7 ± 1.5	–	–	404.0	0.70 ± 0.30
430 ±1[d]	0.33± 0.05	–	–	–	–
459.9±0.3	2.4 ± 0.2	461 ±1	2.3± 0.3	460.3	1.81 ± 0.30
478.7±0.3	0.95± 0.10	480 ±1	0.4± 0.1	478.3	1.80 ± 0.51
496.4±0.3	7.2 ± 0.4	497.0±0.5	7.2± 0.7	496.6	6.61 ± 1.00
516.4±0.3	11.1 ± 1.5	517.0±0.5	10.7± 1	516.8	10.30 ± 1.00
534.2±0.3	13.2 ± 0.6	534.0±0.5	12.5± 1.3	534.4	13.50 ± 1.00
645.2±0.3	5.9 ± 0.5	646.5±0.5	7.0± 0.7	645.2	6.20 ± 0.59
663.3±0.7	1.1 ± 0.2	–	–	663.4	4.51 ± 0.49
666.2±0.7	3.9 ± 0.6	666.5±0.5	6.0± 0.6	666.6	
748.2±0.3	34.6 ± 4.0	749.5±0.5	37.0± 4	749.1	34.1 ± 4.0
788.6±0.3	29.6 ± 3.0	790.5±0.5	34.8± 4	789.3	31.2 ± 4.0

Table 3 continued

812.4±0.5	0.55± 0.13	813 ±1	0.7±1	813.0	0.642± 0.149
863 ±1 ?	0.32± 0.10	865 ±1	0.3±0.05	-	-
875.8±0.4	0.90± 0.11	878 ±1	0.7±0.1	876.2	0.980± 0.201
933.3±0.5	2.2 ± 0.5	934 ±1	2.8±0.3	934	2.41 ± 0.30
939.1±0.4	9.0 ± 1.4	939.0±0.5	12.1±2	939.0	11.2 ± 2.0
947.7±0.5	3.7 ± 0.6	949.0±0.5	4.8±0.5	948.0	3.70 ± 0.70
-	-	993 ±1	1.5±0.2	-	-
-	-	1013 ±1	1.3±0.1	-	-
-	-	1082 ±1	0.8±0.1	-	-

[a](Jak66)

[b](Adam68)

[c]These intensities were obtained by normalizing the intensity (891±44) for the 346.5-keV γ as given in (Adam68) to 100, always retaining the original number of significant figures.

[d]This transition was not seen in the singles spectra but only in the 600-keV region gated spectrum.(Figure 18).

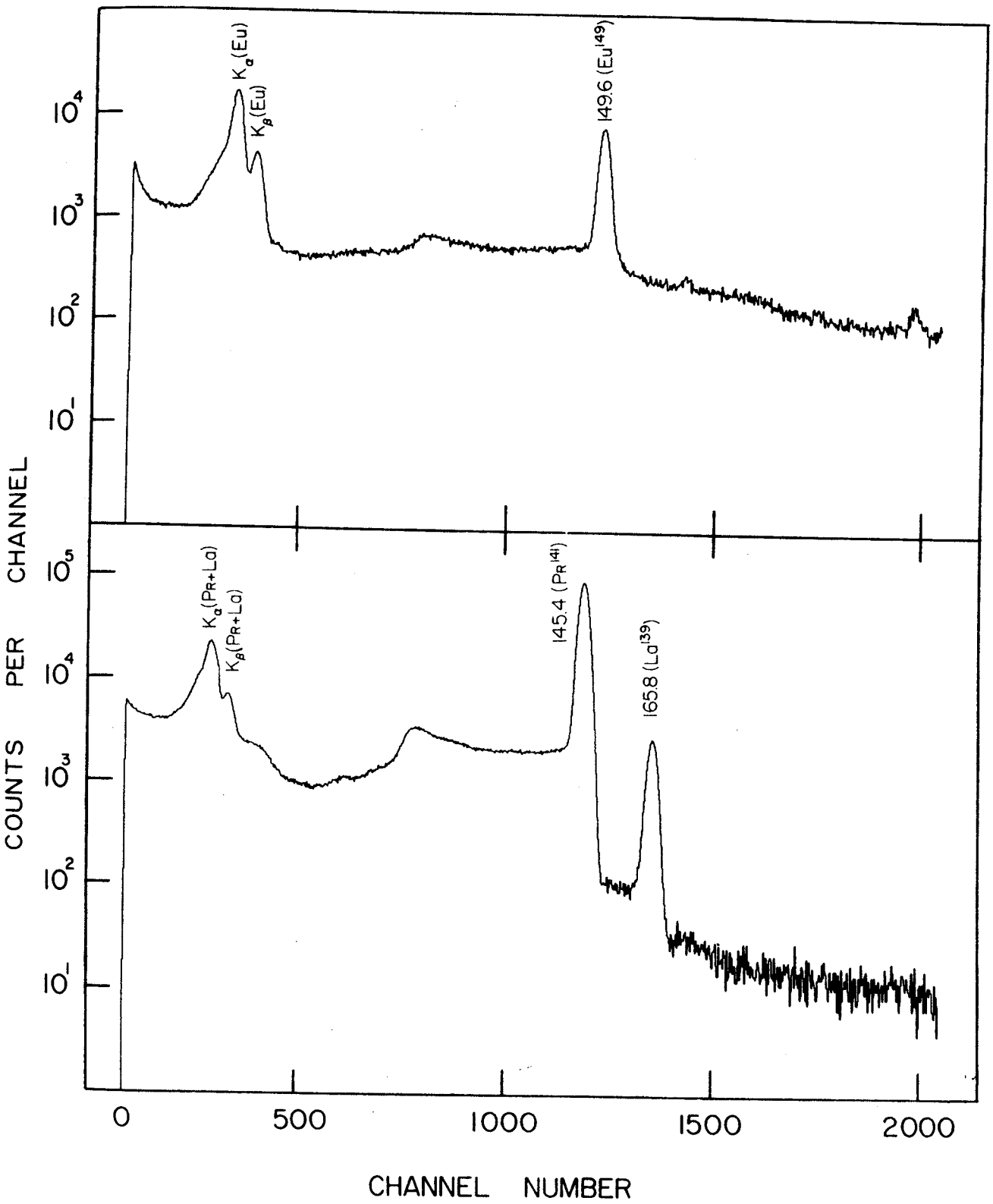

Figure 12. Gd^{149} x-ray spectrum compared to a $Ce^{139,141}$ spectrum.

Due to the presence of the contaminant Ce^{139}, the total Ce x-ray intensity had to be corrected appropriately in order to arrive at the experimental Ce^{141} *K* -x-ray intensity. This correction was accomplished by use of the *K*-shell fluorescent yield and I_γ/I_{K-X} (IC + EC) values reported by Donnelly and Wiedenbeck (Don 68). The total relative Ce^{139} *K* x-ray contribution, both electron capture and internal conversion, could then be calculated from knowing the intensity of the 165.8-keV γ ray accompanying the de-excitation of the Ce^{139}. The ratio of *K* x-rays to 145.6-keV γ's in Ce^{141} has been measured (Nem 61) to be 0.341±0.010. The area ratio [*K* x-ray/149.6-keV γ] for Gd^{149} was measured to be 2.45. When corrected for efficiency by the Ce^{141} ratio, this becomes 2.01. The errors involved should be quite small even though the efficiency curves are changing rapidly in this region, because the energies of the Gd^{149} and Ce^{141} x-rays and γ-rays are so similar.

As can be seen from the singles spectrum resulting from the bombardment of separated Eu^{151} (Figure 10), peaks are present at 963, 993, and 1013 keV in addition to those at lower energies. These three "high-energy" peaks were also seen in many of the bombardments using natural Eu, and they have been reported previously (Jak 66) as belonging to the decay of Gd^{149}. We questioned this because, as can be seen in Figure 11, a spectrum taken from an older source (in this case using natural Eu target) no longer contains these transitions. An excitation function

was run using a natural europium oxide target with proton beams from 10 MeV to 35 MeV at 5 MeV intervals. The characteristic Gd^{149} peaks first appeared in the 20 MeV spectrum as expected (Q = -16.9 MeV) and had all but vanished by 35 MeV, thus exhibiting an excitation function with a width typical of a compound nuclear reaction. Of the three peaks (961, 993, and 1013 keV) only the 961 keV peak was in evidence in any of these runs. However, it first appeared in the 10-MeV spectrum and continued to be present in all of the higher energy spectra. It was accompanied by peaks at 121 keV and 841 keV, these three transitions being characteristic of the decay of the 9.3-h isomeric level of Eu^{152}. This activity could easily be made by the $Eu^{151}(n,\gamma)Eu^{152m}$ reaction. The peaks at 993 keV and 1013 keV did not appear in any of the excitation function spectra; however, the statistics were such that very weak peaks at these energies would not be observed. When observed in other singles spectra these two peaks do appear to decay with a half-life similar to, but less than, that of Gd^{149}, although no specific half-life determination has been made. It should be noted that, when present, these peaks do remain with the Gd fraction after separation in an ion-exchange process.

4.1.3.B. Prompt Coincidence Spectra

Both prompt and delayed spectra were obtained by a variety of methods. The 7-cm^3 Ge(Li) detector was normally used for recording spectra, with a 3×3-in. NaI(Tl) detector setting the gates. For some of the spectra, however, the Ge(Li) detector was placed at one end inside the tunnel of an 8×8-in. NaI(Tl) split annulus (Aub167). The source was placed on top of the Ge(Li) detector inside the annulus. For an anticoincidence spectrum a 3×3-in. NaI(Tl) detector was placed at the other end of the annulus tunnel in order to subtend a greater solid angle from the source, thereby further reducing the Compton background, in particular the Compton edges resulting from backscattering from the Ge(Li) detector. For all of the coincidence experiments a standard fast-slow coincidence circuit was used and the lower discriminators of the single-channel analyzers were adjusted to accept only pulses with energies greater than those of the *K* x-rays. For the coincidence runs the resolving time (2τ) of the fast coincidence unit was ≈100 nsec, while for the anticoincidence run it was ≈200 nsec. These experimental set-ups are described in more detail in §II.1.2.

The anticoincidence and integral or "any" coincidence spectra are shown in Figures 13 and 14. These spectra complement each other in helping to elucidate the decay scheme. The enhancement of a peak in the anticoincidence spectrum implies a ground-state

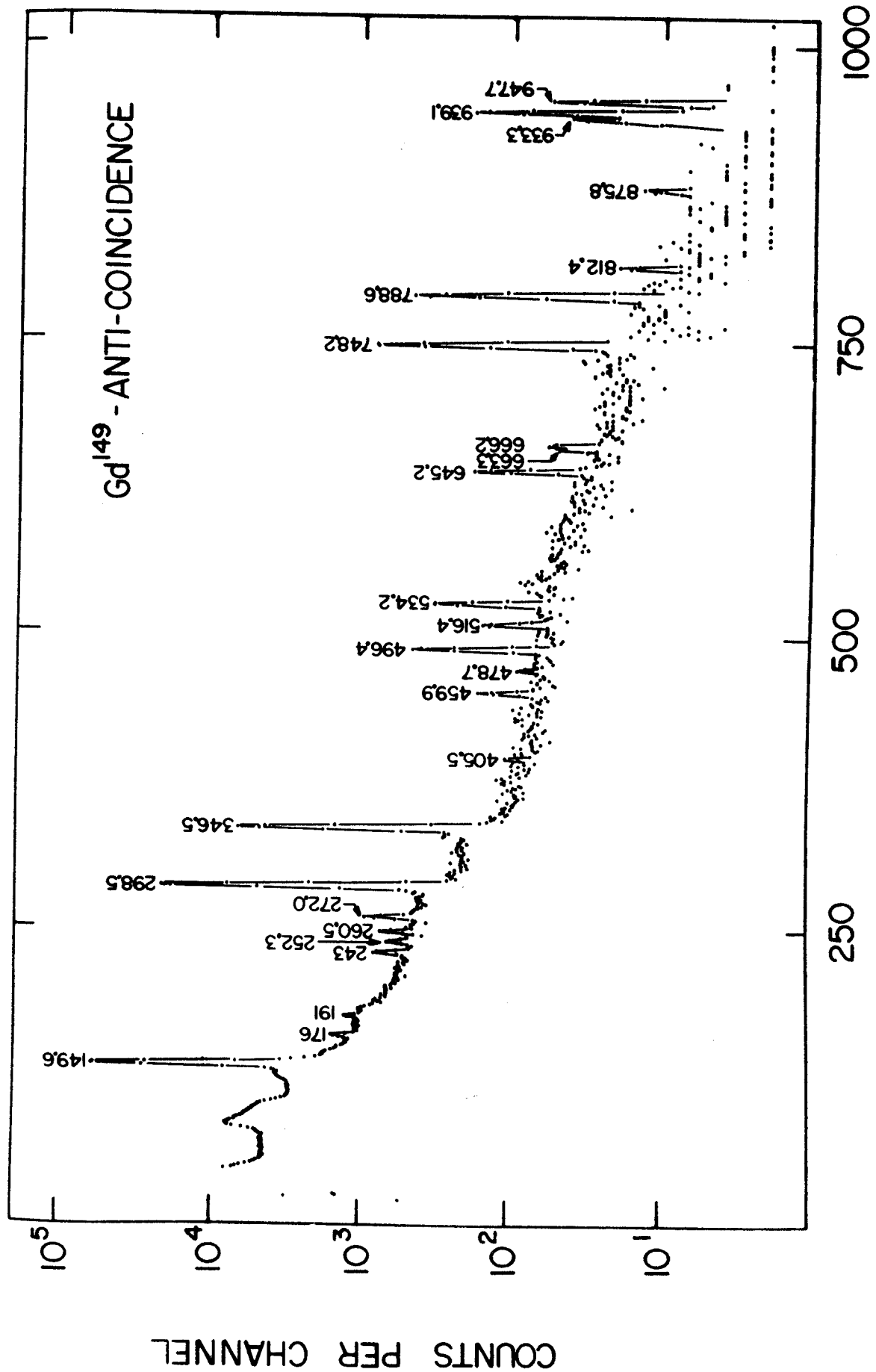

Figure 13. Anticoincidence spectrum of Gd^{149}.

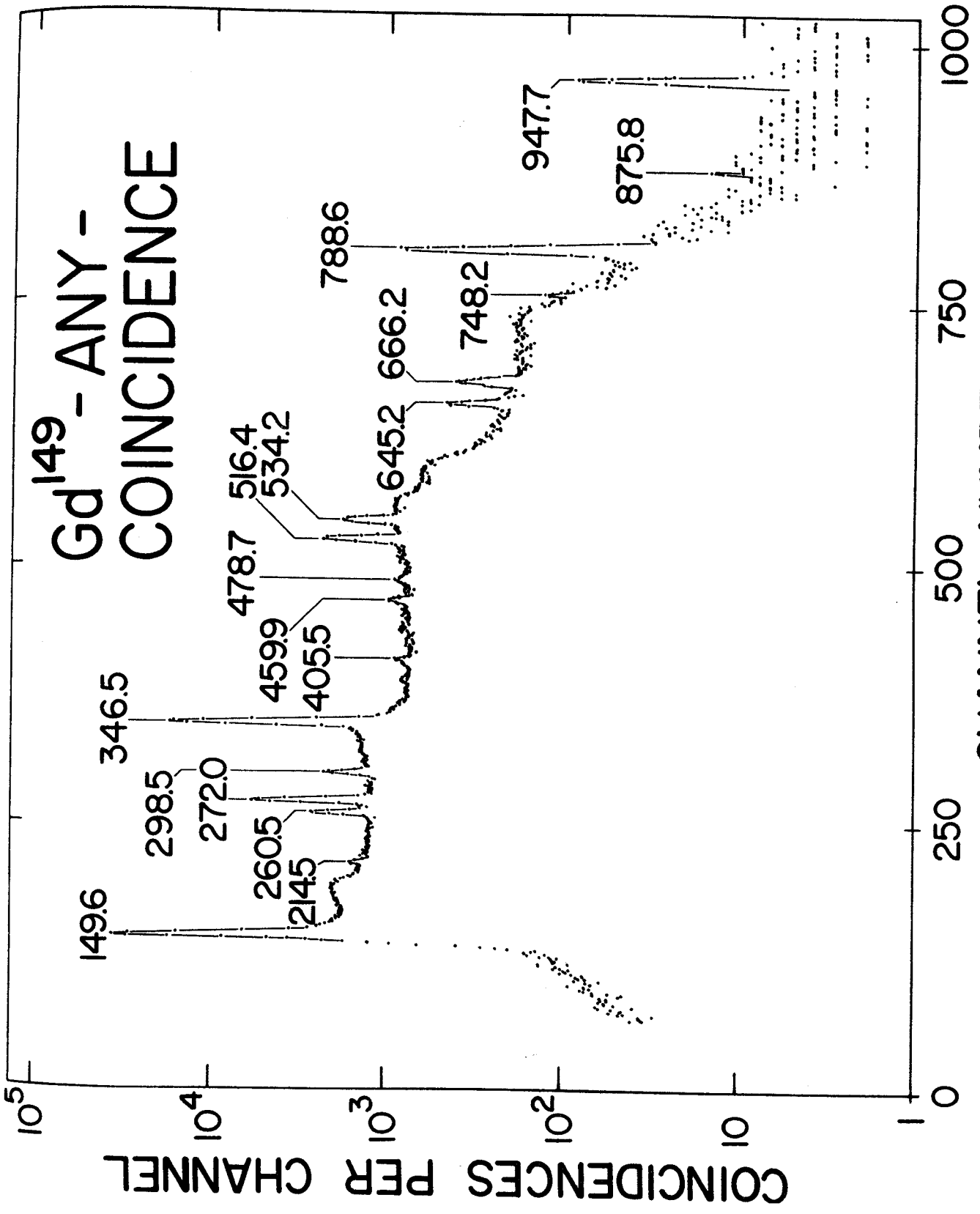

Figure 14. Integral-coincidence spectrum of Gd^{149}.

transition either from a level fed primarily by direct ε decay or from a level with a half-life long compared with the resolving time; examples are the 748.2- and 496.4-keV γ's. In the integral coincidence spectrum such transitions should be either absent or reduced in intensity. The integral coincidence spectrum also confirms much of the information gained from the individually-gated spectra below. The relative intensities of peaks in the coincidence runs are given in Table 4 and a summary of our inferences from them is given in Table 5.

Other useful coincidence spectra were obtained by gating on the 149.6-, 346.5-, and 534.2-keV peaks and on the 600- and 900-keV regions. These are shown in order in Figures 15-19. Tables 4 and 5 again summarize the relevant information from these spectra, but we defer any detailed discussion until §1.5, where points essential to our construction of the decay scheme will be covered.

Table 4. Intensities of Gd^{149} γ rays in coincidence experiments.

E_γ (keV)	Relative Intensity							
	Singles	Anti-coincidence	Integral coincidence	149.6-keV gate	346.5-keV gate[a]	534.2-keV gate	600-keV gate	900-keV gate
149.6±0.2	233.4 ±10	-	48.4	-	≡233.4	1.10	5.02	only peak in spectrum
214.5±0.6	0.81± 0.10	1.37	0.78	-	-	0.68	-	-
252.3±0.7	1.08± 0.25	1.30	-	-	-	-	-	-
260.5±0.3	5.80± 0.40	1.43	5.03	2.88	6.03	≡5.80	0.79	-
272.0±0.2	14.6 ± 0.6	2.78	18.1	33.3	14.5	6.21	≡14.6	-
298.5±0.2	126.7 ±10	109.2	4.71	15.7	25.9	0.43	-	-
346.5±0.3	≡100	63.7	≡100	272.5	4.93	0.21	-	-
405.5±0.7	3.7 ± 1.5	-	1.67	-	-	0.87	0.12	-
430 ±1	-	-	-	-	-	-	0.33	-
459.9±0.3	2.4 ± 0.2	1.41	2.80	-	-	0.38	0.11	-
478.7±0.3	0.95± 0.10	-	1.63	-	-	-	0.089	-
496.4±0.3	7.2 ± 0.4	≡7.2	-	-	-	-	-	-
516.4±0.3	11.1 ± 1.5	1.89	23.0	≡11.1	14.1	0.054	0.19	-
534.2±0.3	13.2 ± 0.6	6.53	14.9	2.36	5.82	0.062	0.13	-
645.2±0.3	5.9 ± 0.5	3.83	6.1	6.22	-	-	-	-
663.3±0.7	1.1 ± 0.2	{1.81	{ 6.34	1.11	-	-	-	-
666.2±0.7	3.9 ± 0.6							
748.2±0.3	34.6 ± 4.0	31.1	0.35	-	-	0.048	-	-
788.6±0.3	29.6 ± 3.0	18.7	28.1	16.3	-	-	-	-
812.4±0.5	0.55± 0.13	0.46	-	-	-	-	-	-
863.1±1.0	0.32± 0.10	-	-	-	-	-	-	-
875.8±0.4	0.90± 0.11	-	-	-	-	-	-	-

Table 4 continued

933.3±0.4	2.2 ± 0.5	2.55	-	-	-	-	-	-
939.1±0.6	9.0 ± 1.4	9.90	-	-	-	-	-	-
947.7±0.5	3.7 ± 0.6	2.41	-	-	-	-	-	-

[a]Nothing appears to be in prompt coincidence with the 346.5-keV γ except the 149.6-keV γ, and its intensity should be diminished in this spectrum because it is fed by many other γ rays in addition to the 346.5-keV γ. Thus, all the intensities in this column should be regarded as upper limits originating from chance or instrumental effects.

Table 5. Summary of Coincidence Data

Gate energy (keV)	Peaks in coincidence (keV)	Figure no.
Integral gate	149.6, 214.5, 260.5, 272.0, 346.5, 405.5, 459.9, 478.7, 516.4, 534.2, 645.2, 663.3, 666.2, 788.6, 947.7	14
149.6	272.0, 346.5, 516.4, 645.2, 663.3, 788.6, 947.7	15
346.5	149.6	16
534.2	214.5, 260.5, 405.5	17
600 region	149.6, 272.0, 430.3	18
900 region	149.6	19
149.6 delayed coincidence	252.3, 298.5	20

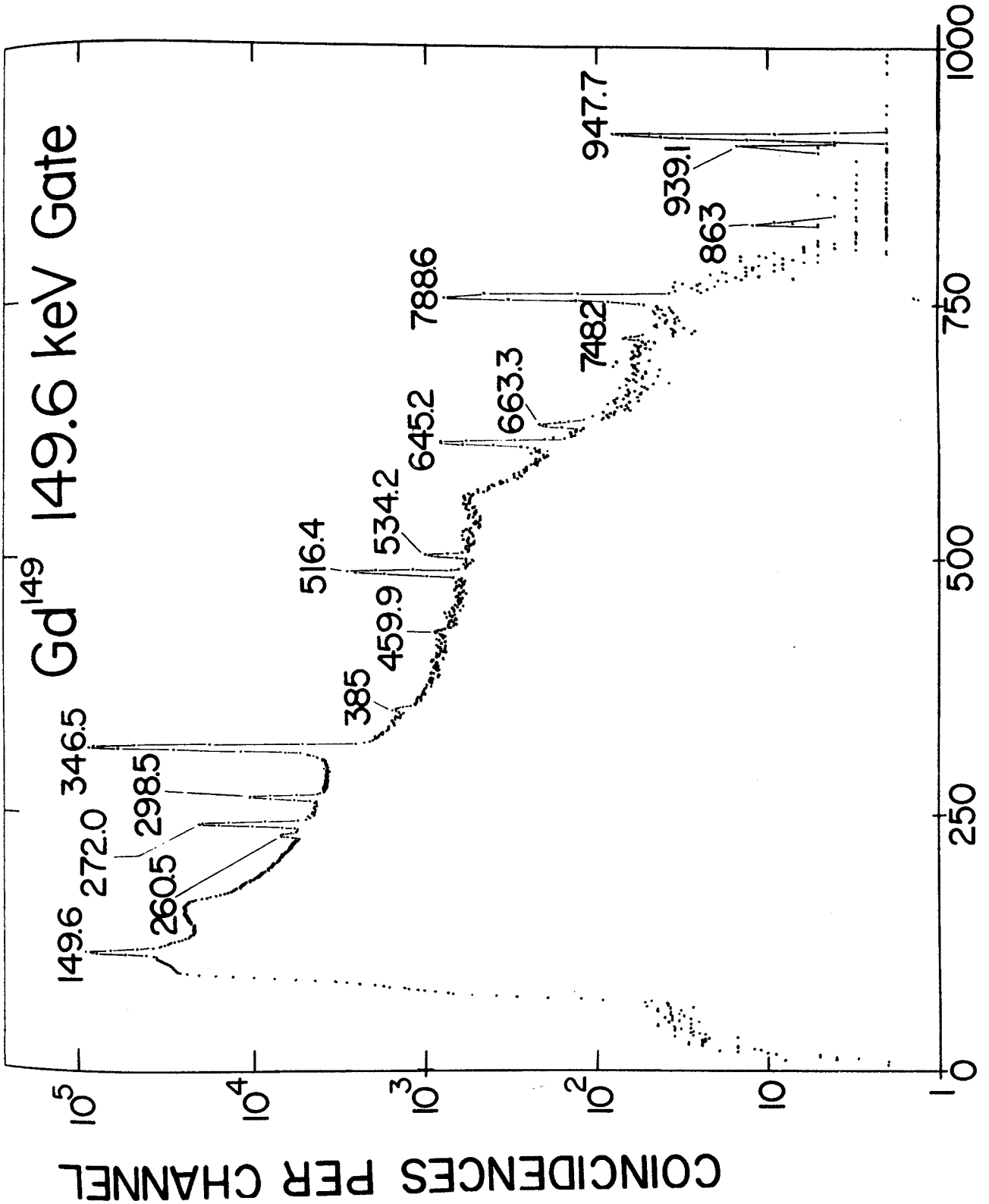

Figure 15. Spectrum of γ rays from Gd^{149} decay observed in coincidence with the 149.6-keV transition.

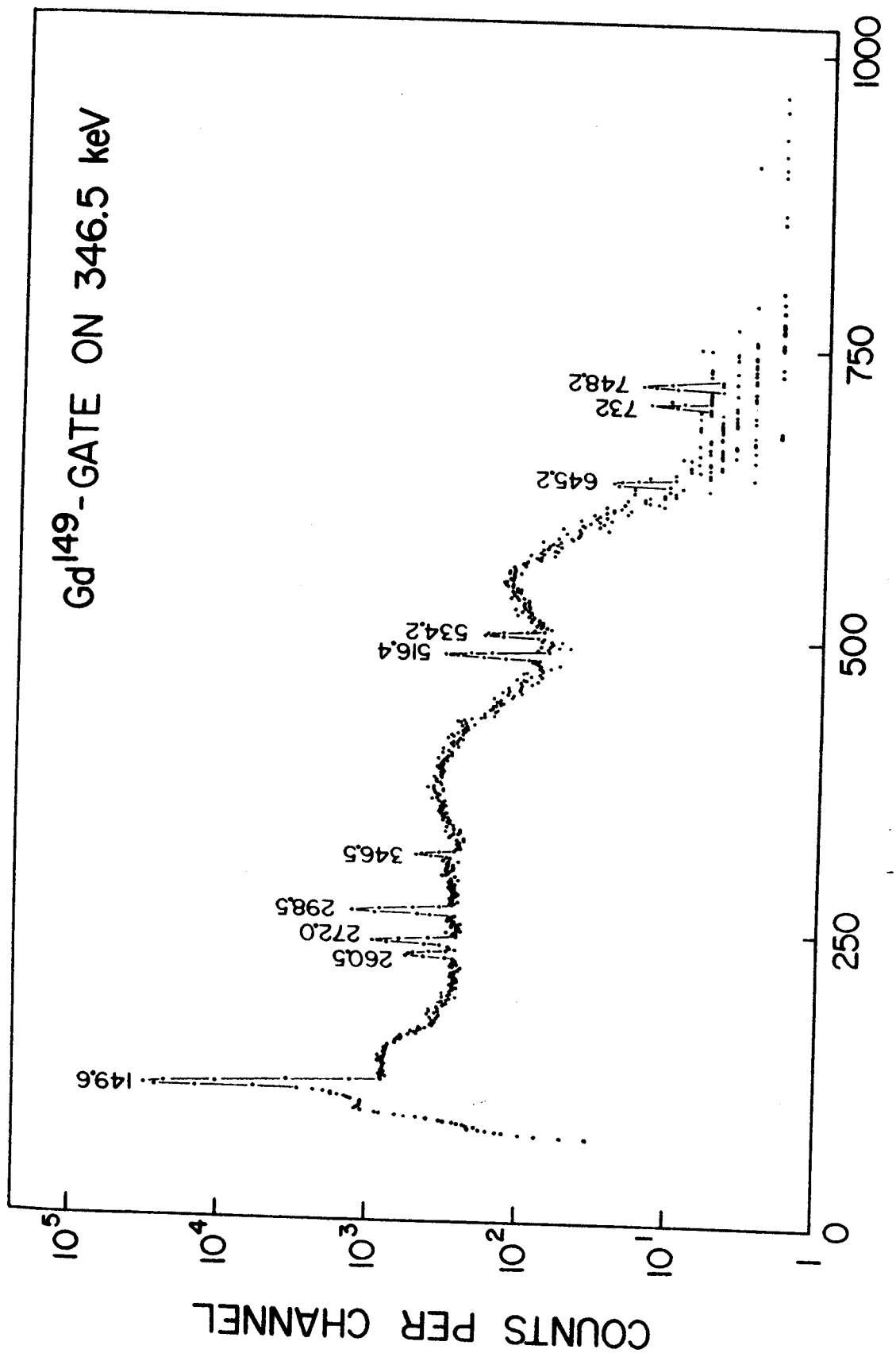

Figure 16. Gd^{149} coincidence spectrum taken with a prompt gate on the 346.5-keV transitions.

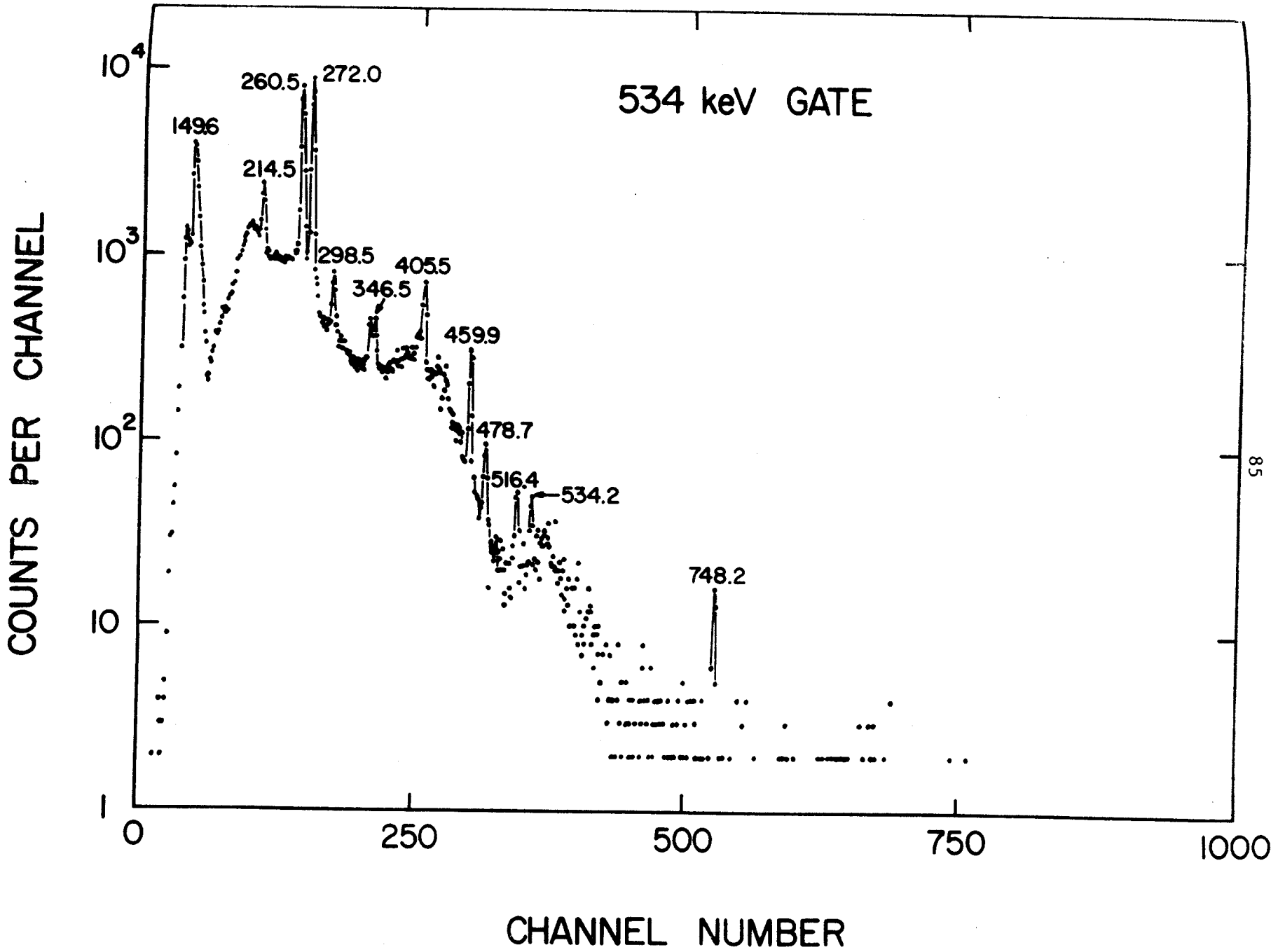

Figure 17. Coincidence spectrum of Gd^{149} with the gate on the 534.2-keV transitions.

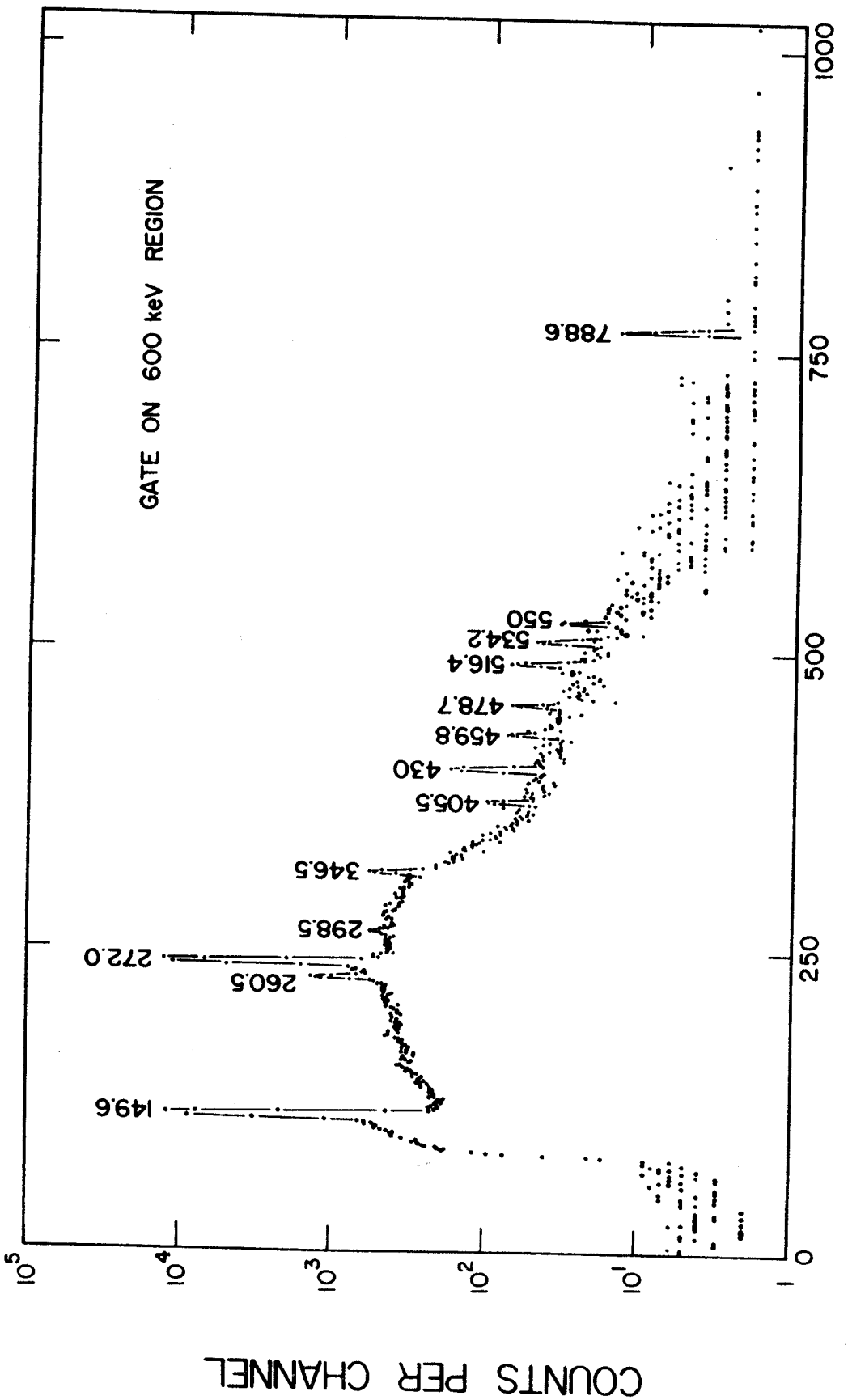

Figure 18. Gd^{149} coincidence spectrum with the gate set on the 600-keV region.

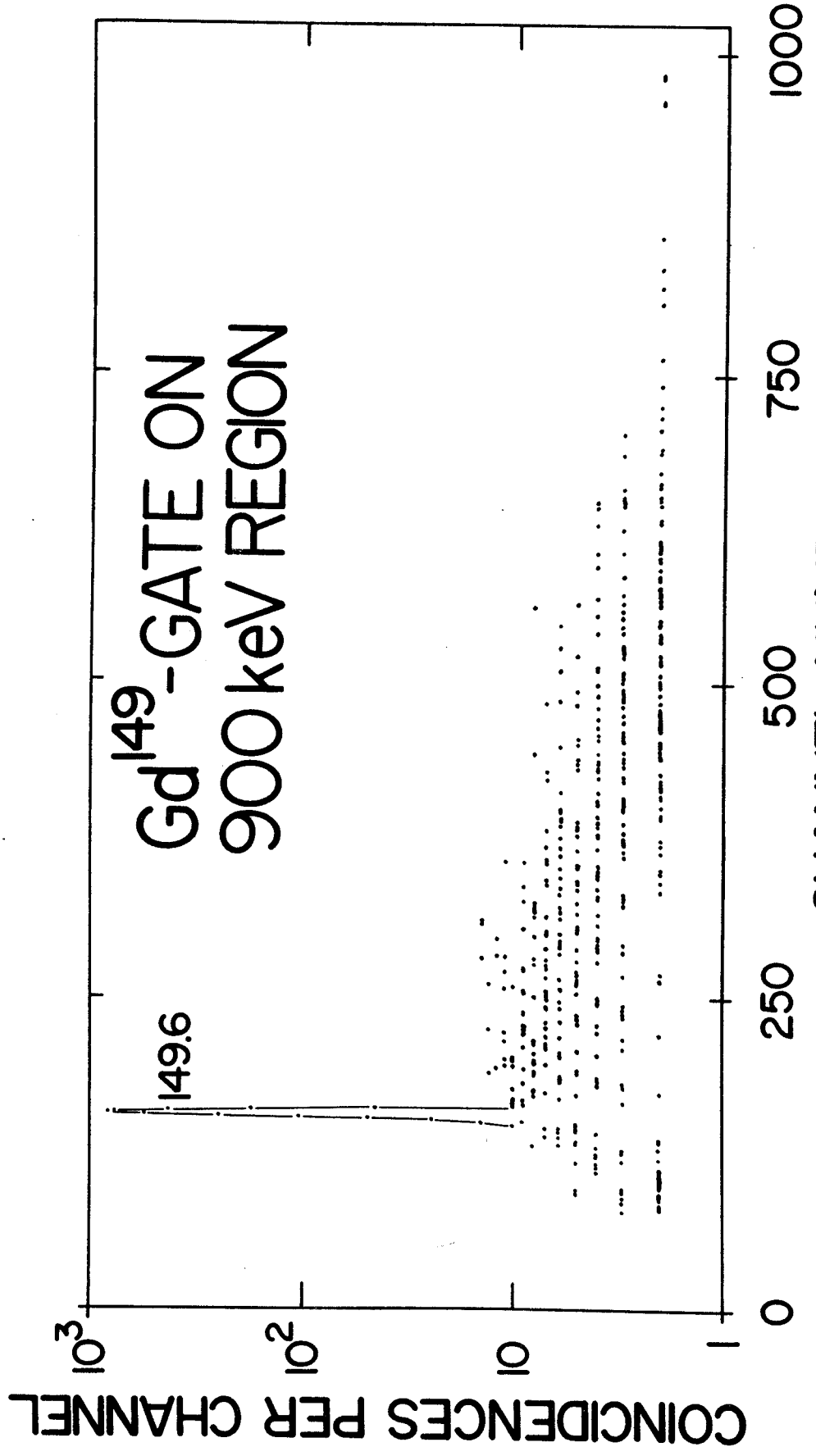

Figure 19. Gd^{149} coincidence spectrum with the gate set on the 900-keV region.

4.1.3.C Delayed Coincidence Studies

Many nuclei in this region have an $h_{11/2}$ isomeric state, and Eu^{149} is no exception. The 496.4-keV state was first suggested to be isomeric by Shirley, Smith, and Rasmussen (Shir 57), who assigned the 346.7-keV transition as *M2* on the basis of its conversion ratios. The half-life of the state was later measured by Berlovich, et al. (Berl 61), to be $2.48\pm0.05\times10^{-6}$ sec. In several previous studies (Pras 62, Jak 66) delayed-coincidence experiments were performed to determine the feeding of the 346.7-keV state from above, but we obtain somewhat different results from these.

We used a 3×3-in NaI(Tl) detector to gate on the 346.5-keV γ and on the 149.6-keV γ that is in coincidence with it (cf. the decay scheme in Figure 23 below). The 7-cm^3 Ge(Li) detector signal was delayed relative to these gates by inserting passive delays ranging from 0.25 to 0.50 μsec, depending on the particular run. The fast resolving time (2τ) again was set at ≈100 nsec. The spectrum resulting from the 149.6-keV delayed gate is shown in Figure 20 and the intensities of peaks in this spectrum are compared with their intensities in the corresponding prompt spectrum in Table 6. A summary of the conclusions is also included in Table 5. The spectrum resulting from the 346.5-keV gate produced essentially the same results so is not shown.

In all the delayed spectra the 298.5-keV γ was enhanced, indicating that it does indeed feed the 496.4-keV level. There was

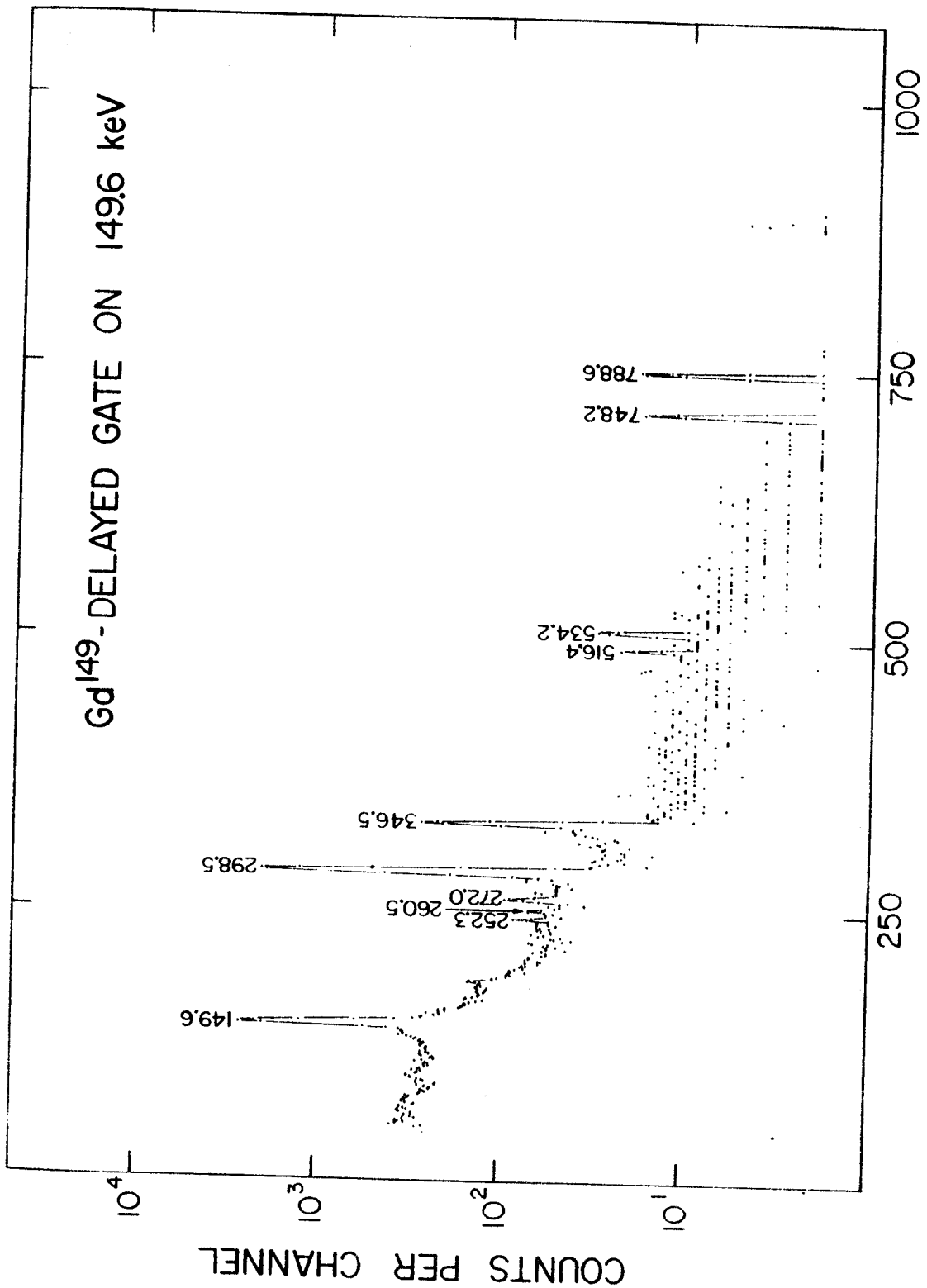

Figure 20. Gd^{149} delayed coincidence spectrum.

Table 6. Intensities of Gd^{149} γ rays in delayed and prompt coincidence.

E_γ (keV)	Relative Intensity (normalized to singles intensity)	
	149.6-keV delayed	149.6-keV prompt
149.6±0.2	4.78	-
252.3±0.7	0.85	-
260.5±0.3	0.86	2.88
272.0±0.2	2.08	33.3
298.5±0.2	≡126.7	15.7
346.5±0.3	18.2	272.5
496.4±0.3	1.17	-
516.4±0.3	1.51	≡11.1
534.2±0.3	2.73	2.36
645.2±0.3	-	6.22
663.3±0.7	{ -	1.11
666.2±0.7		
748.2±0.3	5.37	-
788.6±0.3	5.68	16.3

also some evidence for enhancement of the 252.3-keV γ. However, the 459.9-keV γ, which had previously been reported (Pras 62, Jak 66) as feeding the 496.4-keV level, is completely missing from Figure 20. This, and other evidence which will be discussed in §4.1.5., leads us to the conclusion that the 459.9-keV γ does not proceed to the 496.4-keV level but instead depopulates a newly proposed 459.9-keV level.

4.1.3.D. Internal Conversion Coefficients

For the determination of internal conversion coefficients we used the electron intensities reported by Harmatz and Handley, (Harm 66) who reported extensive values for K electrons along with some values for L_I and M_I electrons. These values were obtained with flat-field permanent magnet spectrographs using photographic plates and have reported uncertainties of ≈15% for the most prominent lines. For purposes of normalization we assumed the 346.5-keV transition to be pure *M2* and used the theoretical value of α_K from Hager and Seltzer (Hag 68).

Multipolarities or possible multipolarities were assigned for all transitions where K-electron intensities were available. The experimental α_K's, theoretical α_K's of Hager and Seltzer (Hag68), and assigned multipolarities are listed in Table 7. Where necessary, (logarithmic) quadratic interpolation was made between the tabular theoretical values. As our lowest energy was 149.6 keV, this method yielded satisfactory results. These theoretical values were used to construct the smooth curves in Figure 21, upon which we have superimposed the experimental points along with their estimated errors (ranging between 15 and 30%).

Usually $K/L_{(tot)}$ and $K/M_{(tot)}$ ratios can be used as indicators of transition multipolarities. For the present case only a few L_I and M_I values are reported (Harm66). Where possible the L_I conversion values were used with the experimental K-conversion values to determine experimental values for K/L_I ratios. These values are compared in Table 8 with theoretical values based on

Table 7. Experimental and theoretical internal conversion coefficients for Gd^{149} transitions.

Energy (keV)	Exp. ICC (K) [b]	Theoretical ICC (K-Shell)[a]						Assigned Multipolarity
		$E1$	$E2$	$E3$	$M1$	$M2$	$M3$	
149.6	0.54(0)	0.811(-1)	0.371(0)	0.144(1)	0.507(0)	0.326(1)	-	$M1$
214.5	-	0.319(-1)	0.122(0)	0.398(0)	0.193(0)	0.936(0)	0.359(1)	-
252.3	0.13(0)	0.225(-1)	0.874(-1)	0.277(0)	0.133(0)	0.624(0)	0.225(1)	$M1$
260.5	0.26(-1)	0.196(-1)	0.736(-1)	0.238(0)	0.116(0)	0.523(0)	0.191(1)	$E1$
272.0	0.12(0)	0.158(-1)	0.552(-1)	0.182(0)	0.933(-1)	0.391(0)	0.146(1)	$M1$
298.5	0.85(-1)	0.128(-1)	0.436(-1)	0.139(0)	0.743(-1)	0.300(0)	0.106(1)	$M1$
346.5	≡0.20(0)	0.938(-2)	0.310(-1)	0.911(-1)	0.532(-1)	0.202(0)	0.644(0)	$M2$
405.5	0.90(-2)	0.607(-2)	0.190(-1)	0.569(-1)	0.333(-1)	0.118(0)	0.372(0)	$E1$
459.9	0.30(-1)	0.460(-2)	0.130(-1)	0.334(-1)	0.248(-1)	0.780(-1)	0.210(0)	$M1(E3)^c$
478.7	0.12(-1)	0.423(-2)	0.119(-1)	0.308(-1)	0.225(-1)	0.704(-1)	0.188(0)	$E2$
496.4	0.33(-1)	0.395(-2)	0.113(-1)	0.296(-1)	0.207(-1)	0.654(-1)	0.176(0)	$E3$
516.4	0.19(-1)	0.365(-2)	0.106(-1)	0.281(-1)	0.188(-1)	0.600(-1)	0.162(0)	$M1$
534.2	0.19(-1)	0.338(-2)	0.971(-2)	0.254(-1)	0.173(-1)	0.541(-1)	0.144(0)	$M1(E3)^c$
645.2	0.30(-2)	0.221(-2)	0.576(-2)	0.135(-1)	0.107(-1)	0.297(-1)	0.698(-1)	$E1$
663.3	0.15(-1)	0.211(-2)	0.560(-2)	0.133(-1)	0.100(-1)	0.283(-1)	0.672(-1)	$(M1,E3)^c$
666.2	0.66(-2)	0.210(-2)	0.557(-2)	0.133(-1)	0.993(-2)	0.280(-1)	0.668(-1)	$E2(M1)$
748.2	0.20(-2)	0.168(-2)	0.448(-2)	0.107(-1)	0.754(-2)	0.211(-1)	0.495(-1)	$E1$
788.6	0.51(-2)	0.145(-2)	0.359(-2)	0.790(-2)	0.649(-2)	0.168(-1)	0.363(-1)	$E2,M1$
812.4	-	0.135(-2)	0.322(-2)	0.682(-2)	0.598(-2)	0.150(-1)	0.311(-1)	-
875.8	0.46(-2)	0.118(-2)	0.281(-2)	0.592(-2)	0.502(-2)	0.125(-1)	0.256(-1)	$M1(E3)^c$
933.3	-	0.108(-2)	0.267(-2)	0.584(-2)	0.440(-2)	0.113(-1)	0.239(-1)	-
939.1	0.49(-2)	0.107(-2)	0.266(-2)	0.582(-2)	0.434(-2)	0.112(-1)	0.237(-1)	$M1(E3)^c$
947.7	0.17(-2)	0.105(-2)	0.263(-2)	0.579(-2)	0.425(-2)	0.110(-1)	0.234(-1)	$(E1)$

[a](Hag68)

[b]No precise error estimates could be assigned to these conversion coefficients. Harmatz and Handley (Harm66) assigned intensity errors as being ±15% for their most prominent lines. Our γ-ray intensity errors are given in Tables 3 and 9.

[c]These transitions are probably *M*1's; the closeness of the *M*1 and *E*3 conversion coefficients makes a decision based on these alone difficult, but *M*1 assignments are consistent with the remainder of the decay scheme.

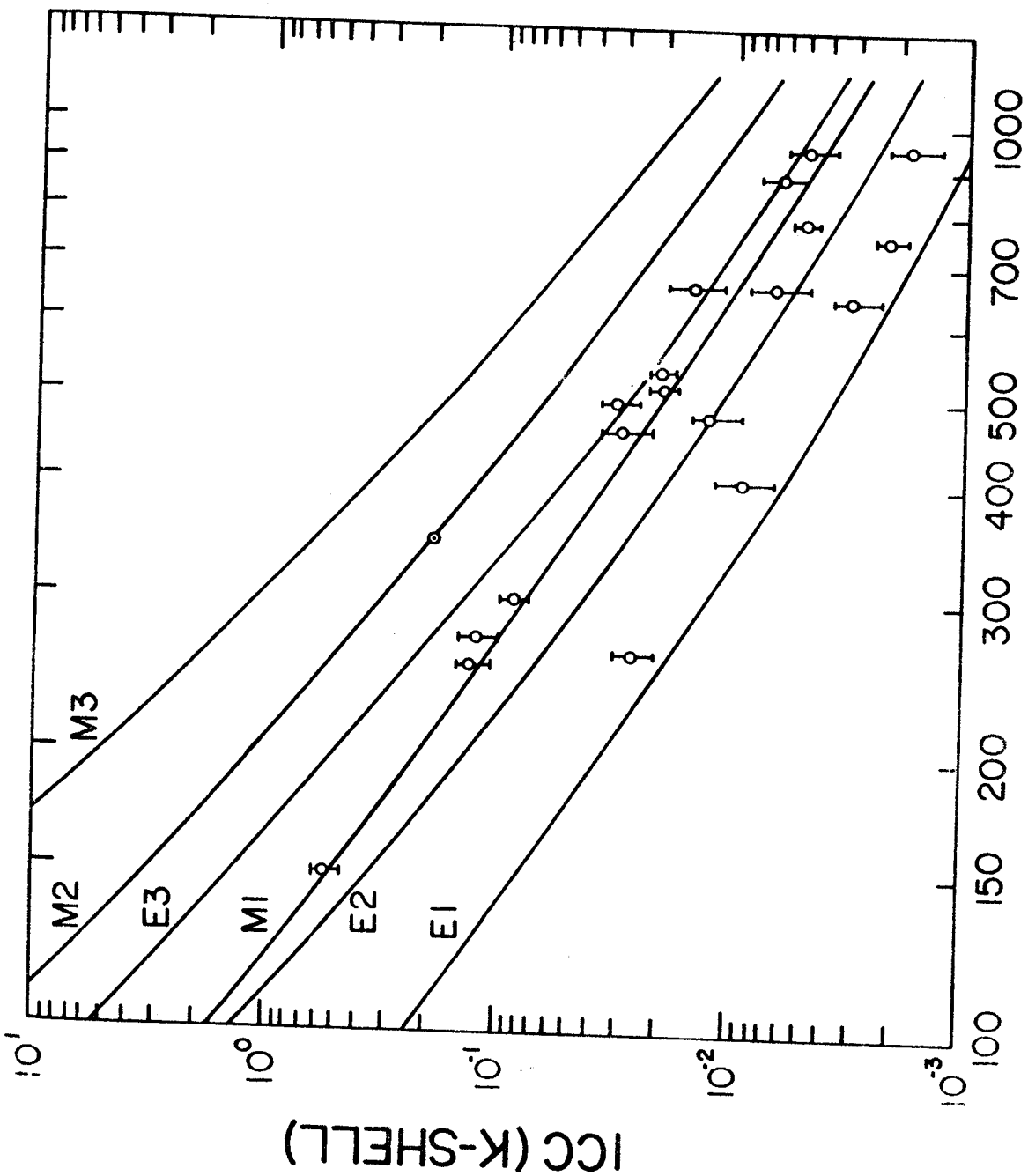

Figure 21. Experimental and theoretical conversion coefficients for the transitions in Eu^{149} following the decay of Gd^{149}.

Table 8. Experimental and Theoretical K/L_I ICC Ratios for Gd^{149} Transitions.

Energy (keV)	Exp. K/L_I [b]	Theoretical K/L_I Ratios[a]						Indicated Multipolarity[c]
		E1	E2	E3	M1	M2	M3	
149.6	8.5	9.3	9.9	9.5	7.6	5.7	--	E1,M1
272.0	8.7	8.2	8.0	7.7	7.3	5.9	4.9	E1
298.5	8.5	8.3	8.0	7.5	7.4	6.1	5.1	E1
346.5	7.3	8.9	9.3	8.9	8.0	7.2	6.2	M2
496.4	6.5	8.5	8.1	7.5	7.8	6.9	6.1	M2 or M3
516.4	7.2	8.7	9.1	9.0	7.9	7.6	7.2	M3
534.2	9.0	8.8	9.5	9.7	8.0	7.9	7.7	E1
939.1	8.4	8.6	8.9	8.9	8.0	8.0	8.0	E1

[a] (Hag 68)

[b] Based on values given in (Harm 66).

[c] These multipolarities are indicated by the theoretical ratios given here. They are not necessarily the adopted values determined from other experimental evidence.

the tables of Hager and Seltzer (Hag 68). As is easily seen, the ratios are so similar and vary so slowly they are only of marginal use for multipolarity assignments. The indicated multipolarities, based on comparison of the experimental and theoretical ratios, are also shown in Table 8. These values were not used as the primary factor in assigning transition multipolarities.

4.1.4. Electron-Capture Energy

Because there is no measureable β^+ emission from the decay of Gd^{149}, a direct measurement of its decay energy is not possible. Various estimates of Q_ε range all the way from 1.220 MeV (Avot 7) to 2.275 MeV (Harm 11). As an alternative to an arbitrary adoption of one of the several published values, we made a graphical estimate of Q_ε, using a method similar to that suggested by Way and Wood (Way 54) and previously used by Grover (Grov 59).

A plot (Figure 22) was made of all experimentally known decay energies vs Z for pairs of nuclei having the same neutron numbers as the pair for which the decay energy is to be determined. Both electron-capture and β^- decay pairs were plotted, and for our particular graph, as Q_ε is chosen to be positive and Q_{β^-} negative, the abscissa for the former is Z_{parent} and for the latter $Z_{daughter}$. For example, in estimating Q_ε for Gd^{149}, the experimental decay energies of all pairs with N=85→86 or N=86→85 were plotted. As can be seen from Figure 22, these points all fall on a straight line, and Q_ε for Gd^{149} can be read from the same line. Using this method we estimate Q_ε as 1.320 MeV. The plots for Gd^{145}, Gd^{147}, and Gd^{151} have also been included for reference. As read from the graph, Q_ε for these isotopes is 4.9, 2.2, and 0.56 MeV, respectively. These compare with previous estimates of 5, 1.8 and 0.4 MeV (refs. Grov 59, Mat 65 and Alex 64, respectively).

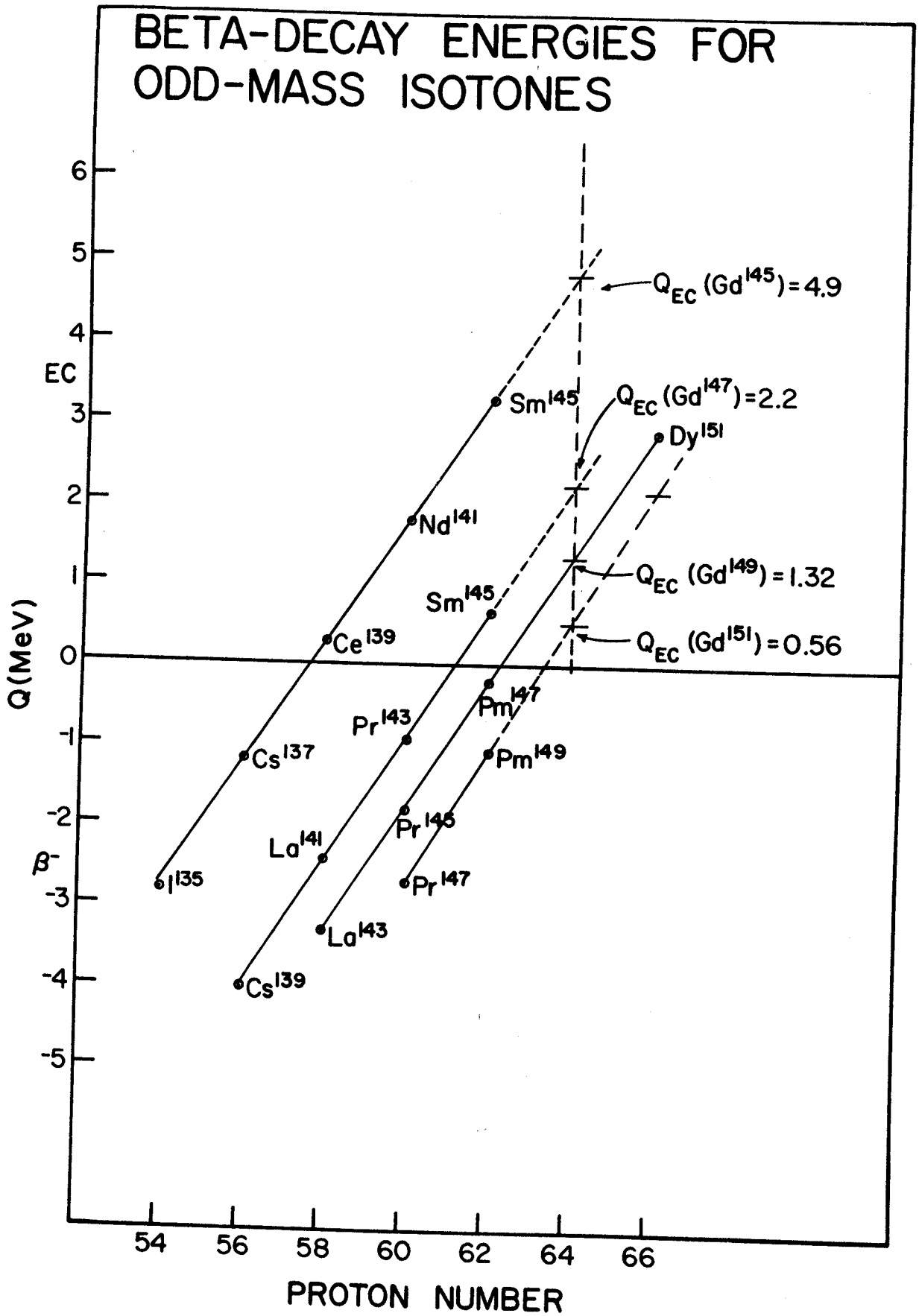

Figure 22. Graphical estimates for the electron-capture decay energies for several odd-mass Gd isotopes, including Gd^{149}.

In essence, this method involves taking the difference between two parabolas cutting across the mass surface and assumes that there are no appreciable bumps or ridges to distort the surface in the region involved. Had we chosen to make a similar plot based on proton pairs rather than neutron pairs, it is easy to see that the N=82 shell would have introduced a serious distortion. Although there is no formal justification for the plot we did make, the fact that no major proton shells or subshells are likely to be encountered means that such estimates for Q_ε should be reasonably reliable.

4.1.5. Proposed Decay Scheme

On the basis of the foregoing coincidence, delayed coincidence, and anti-coincidence spectra, aided by energy sums and intensity balances, we have placed excited states in Eu^{149} as indicated by our decay scheme, presented in Figure 23. The results of our γ-ray energy and intensity measurements, conversion coefficients, and assigned transition multipolarities are summarized in Table 9. Unfortunately, as we have intimated earlier, the preparation of clean Gd^{149} sources, free from subtle contaminants, is not a trivial task, and many incorrect transitions and states have accrued in the literature. Thus, we have included in our decay scheme only those states that were actually indicated by *experiments* in our laboratory. To ameliorate this inflexible position somewhat, we have included in Figure 23, to the side of our decay scheme, some placements that we could neither confirm nor deny and which appear to be reasonable. For the most part these originate from the conversion-electron work of Harmatz and Handley (Harm 66), who observed a number of transitions too weak to be detectable in γ-ray spectra.

Specific evidence for our placing of each level and its associated transitions follows:

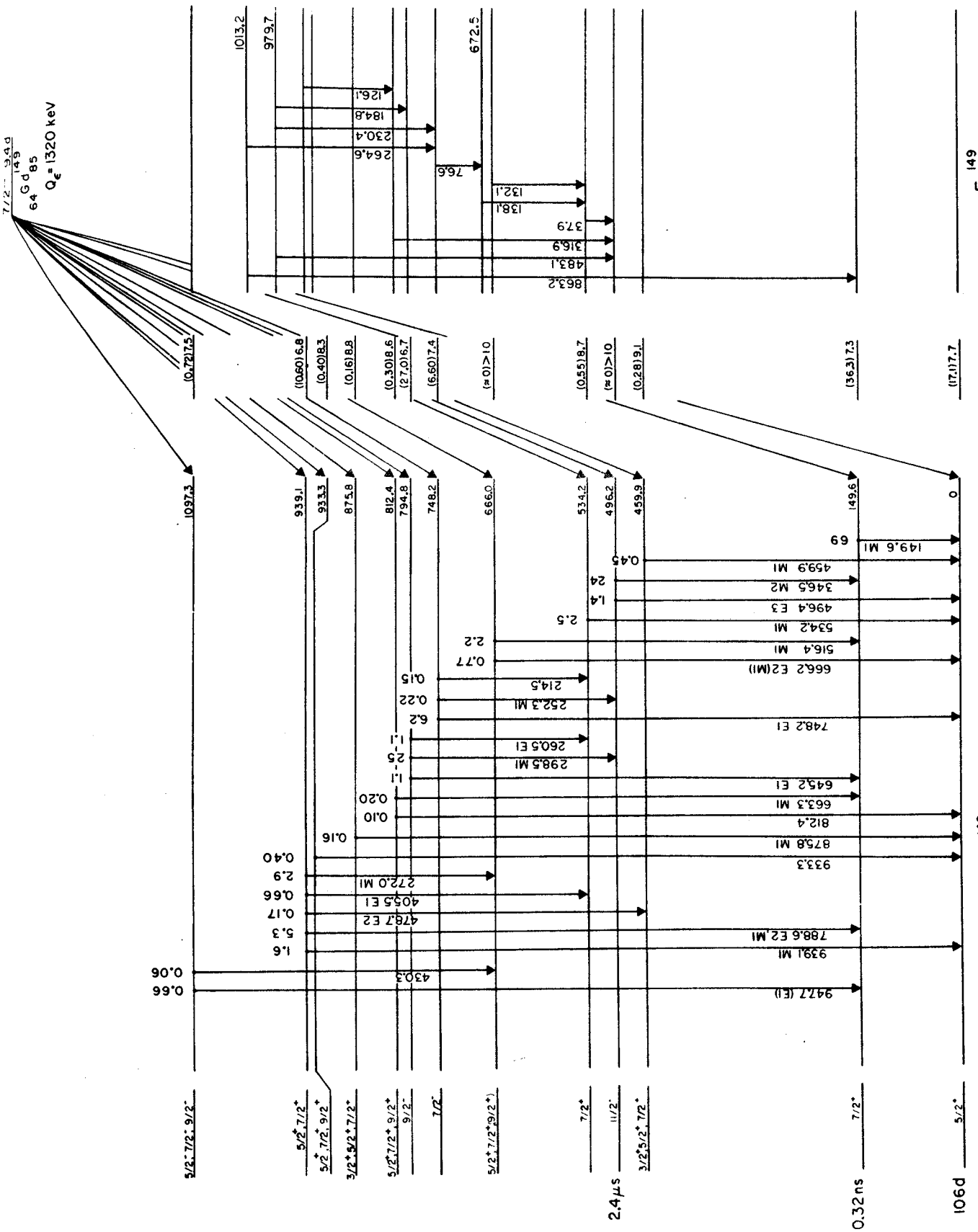

Figure 23. Decay scheme for Gd^{149}.

Table 9. Transition data for Gd^{149}.

Energy	Photon Intensity	*K*-Conversion Intensity[a,b,c]	Total Intensity	Exp. α_K	Multipole Order
K x-rays	468 ±100	-	-	-	-
149.6±0.2	233 ±10.0	124.9	377	0.54	*M*1
214.5±0.6	0.81± 0.1	-	0.84	-	-
252.3±0.7	1.1 ± 0.2	0.14	1.23	0.13	*M*1
260.5±0.3	5.8 ± 0.4	0.15	5.92	$2.6\ 10^{-2}$	*E*1
272.0±0.2	14.6 ± 0.6	1.75	16.3	$1.2\ 10^{-1}$	*M*1
298.5±0.2	127 ± 10	10.75	138	8.5	*M*1
346.5±0.3	≡100	20.0	123	0.20	*M*2
405.5±0.7	3.7 ± 1.5	0.033	3.7	$9.0\ 10^{-3}$	*E*1
430	0.33± 0.05	-	0.33	-	-
459.9±0.3	2.4 ± 0.19	0.073	2.49	$3.0\ 10^{-2}$	*M*1
478.7±0.3	1.0 ± 0.1	0.011	0.96	$1.2\ 10^{-2}$	*E*2
496.4±0.3	7.2 ± 0.35	0.238	7.49	$3.3\ 10^{-2}$	*E*3
516.4±0.3	11.1 ± 1.5	0.213	11.3	$1.9\ 10^{-2}$	*M*1
534.2±0.3	13.2 ± 0.55	0.256	13.5	$1.9\ 10^{-2}$	*M*1
645.2±0.3	5.9 ± 0.5	0.018	5.9	$3.0\ 10^{-3}$	*E*1
663.3±0.7	1.1 ± 0.2	0.016	1.10	$1.5\ 10^{-2}$	*M*1
666.2±0.7	3.9 ± 0.6	0.026	4.0	$6.6\ 10^{-3}$	*E*2
748.2±0.3	34.6 ± 4.0	0.071	34.7	$2.0\ 10^{-3}$	*E*1
788.6±0.3	29.6 ± 3.0	0.15	29.8	$5.1\ 10^{-3}$	*M*1+*E*2
812.4±0.5	0.55± 0.1	-	0.55	-	-
863[e] ?	0.32± 0.1	weak	-	-	-
875.8±0.4	0.90± 0.1	0.0041	0.91	$4.6\ 10^{-3}$	*M*1
933.3±0.	2.2 ± 0.5	-	2.2	-	-
939.1±0.	9.0 ± 1.4	0.044	9.0	$4.9\ 10^{-3}$	*M*1
947.7±0.5	3.7 ± 0.6	0.0062	3.7	$1.7\ 10^{-3}$	(*E*1)

[a]Intensities from (Harm66).

[b]Intensities renormalized such that the α_K (346.5 keV) $\equiv$ 0.20.

[c]Errors in the relative intensities are reported as being 15% for the most intense peaks and increasing for the weaker ones.

[d]For the purpose of arriving at total intensity values, theoretical *L* and *M* conversion coefficients were used for the indicated multipolarities. Interpolated values from Hager and Seltzer (Hag68).

[e]Not included in the decay scheme.

149.6-keV level. The 149.6-keV peak is by far the most intense transition in the γ-ray spectrum. If this were not a ground-state transition, we should see other transitions of comparable intensity that would de-excite the level fed by the strong 149.6-keV transition. Therefore, in agreement with all previous workers, we place the first excited state near 150 keV, specifically, at 149.6 keV. This is also consistent with an overwhelming mass of systematics showing that odd-proton nuclei with $51 \leq Z \leq 63$ have 5/2+ or 7/2+ ground states or first-excited states separated by an energy rarely greater than 150 keV.

The coincidence experiment having its gate on the 149.6-keV peak (Figure 15) showed enhanced peaks at 272.0, 346.5, 516.4, 645.2, 663.3, 788.6, and 947.7 keV. These results agree with those of Jaklevic, Funk, and Mihelich (Jak 66), with the exception of the 663.3-keV peak, which they did not see in a coincidence spectrum. All of these transitions can thus be considered as feeding the 149.6-keV level, and it will be shown later that, with the exception of the 272.0-keV γ, all feed it directly.

The 149.6-keV coincidence spectrum, in conjunction with the singles spectra, made it possible to determine the energies of the peaks in the 663.3- 666.2-keV doublet more precisely than before. As only the 663.3-keV γ was in coincidence with the 149.6-keV γ, its energy and intensity could be determined directly from the coincidence spectrum. These values were then used to subtract the 663.3-keV peak from the singles doublet, leaving the 666.2-keV peak quite well determined by the difference.

459.9-keV level. Owing to the results of the delayed coincidence spectra (Figure 20), the 459.9-keV γ can no longer be considered to be feeding the 496.4-keV level, as had been concluded by previous workers. (Pras 62, Jak 66, Adam 68). Also, as seen in Figure 13 and Table 4, this γ ray is enhanced in the anti-coincidence spectrum but is absent from most of the prompt coincidence spectra. From this evidence, we place the 459.9-keV γ as emanating from a level of this same energy.

On the basis of energy sums, the 478.7-keV γ could be placed connecting the 459.9-keV level with the well-established 939.1-keV level (see below). Other evidence for this placement comes from the 534-keV gated spectrum (Figure 17). While the 459.9-keV peak is less intense than in the singles spectra, it is still present -- most likely due to some of the 478.7-keV γ in the relatively wide NaI(Tl) gate. The fact that it is present to more than a very small extent implies that it does not feed the 496.4-keV level, which has a half-life of 2.48 μsec. In Figure 7 the 459.9- and 478.7-keV γ's have the same intensity relative to each other as they do in the singles spectra, suggesting again that they are related as above.

496.2-keV level. This is the relatively well-known 11/2- isomeric state, again a characteristic of odd-Z nuclei in this region. Its half-life has been measured (Ber 161) to be 2.48±0.05 μsec. As a result of this half-life, the transitions

to and from this level must be studied by means of delayed coincidence techniques. From the results of such experiments (§4.1.3.d., Figure 20 and Table 6), only the 252.3- and 298.5-keV γ's are placed as proceeding to the 496.2-keV level. It is depopulated by the 496.4-keV γ to the ground state (cf. Figure 13) and by the 346.5-keV γ to the 149.6-keV level (Figure 15 and §4.1.3.D.). The adopted energy, as for all of the excited states to be discussed, is a weighted average of these γ rays.

534.2-keV level. In the 534-keV gated coincidence spectrum (Figure 17) the 214.5- and 260.5-keV peaks are most obviously enhanced. Other relatively intense peaks are those at 272.0, 405.5, 459.9, and 478.7 keV, all of which are more intense than can be ascribed to chance coincidences. We have already dealt with the 459.9- and 478.7-keV peaks, and the 272.0-keV peak can be explained from the 516.4-keV γ falling within the gate. This leaves the 405.5-keV γ as feeding the 534.2-keV level, although its coincidence intensity is somewhat less than expected. This coincidence spectrum does not rule out its feeding the 748.2-keV level, which in turn feeds the 534.2-keV level. From energy sums and differences, however, it is one of 5 γ rays that depopulate the 939.1-keV state, and this is the only placement consistent with our proposed decay scheme.

666.0-keV level. The three primary peaks included in the gate for the "600-keV region" coincidence spectrum (Figure 18) lie at 645.2, 663.3, and 666.2 keV. We have already discussed

how the 666.2-keV γ appears to be a ground-state transition (above, in the section on the 149.6-keV level), implying the existence of a level at this energy. The peaks in Figure 18 are those at 149.6, 272.0, 430.3, and perhaps 516.4 keV (crossover timing jitter cut down on the intensity of the latter). That these transitions are involved in cascades is corroborated by the integral-coincidence spectrum. The 149.6-keV coincidence spectrum shows the 516.4-keV γ to feed the 149.6-keV level; if we try to place it as feeding this level indirectly through some higher level, we obtain no consistency whatever with the remainder of the decay scheme and very quickly exceed the available decay energy. Thus, it depopulates the 666.0-keV level.

The 272.0- and 430.3-keV γ's feed into the 666.0-keV level from the 933.3- and 1097.3-keV levels, respectively. These placements are the only ones supported by energy sums.

748.2- and 812.4-keV levels. The 748.2- and 812.4-keV γ's were indicated to be ground state transitions by the anti-coincidence spectrum. In addition, the 534.2-keV coincidence (Figure 17) and the delayed coincidence (Figure 20) spectra indicated our placement of the 214.5- and 252.3-keV γ's, making the level at 748.2 keV reasonably certain. Similarly, the enhancement of the 663.3-keV γ in the 149.6-keV gated spectrum adds confidence to the placement of a level at 812.4 keV, which had not been adduced by previous workers (the 812.4-keV γ had been variously assigned).

794.8-keV level. There are no transitions to the ground state from this level, probably because of the proposed high spin of the state. However, each of the transitions leading from it was enhanced in the appropriate coincidence spectrum -- 260 keV in Figures 14 and 17, 298.5 keV in Figure 20, and 645.2 keV in Figures 14 and 15.

875.8-keV level. Perhaps the least certain level in our decay scheme, this placement rests solely on the enhancement of the 875.8-keV γ in the anti-coincidence spectrum and its suppression in all of the coincidence experiments. Also, there is no other position consistent with the remainder of the decay scheme in which to put it.

933.3-, 939.1-, and 1097.3-keV levels. In the "900-keV region" gated coincidence spectrum (Figure 19), the only peak present is the one at 149.6 keV. From the integral, 149.6-keV gated, and anti-coincidence spectra, it is evident that the 947.7-keV γ is the only one in coincidence. It indicates a level at 1097.3 keV, which is corroborated by the enhancement of the 430.3-keV γ to the 666.0-keV level, as discussed above. The 933.3-keV level is placed on the basis of its sole transition to the ground state. The 939.1-keV level, on the other hand, depopulates by 5 γ rays, all of which are confirmed by coincidence spectra, as discussed above under the sections concerning the levels to which each feeds.

4.1.6. Discussion

$_{63}Eu^{149}_{86}$, with four neutrons above the N=82 closed shell, must have its structure interpreted cautiously. Although the closed shell is only four neutrons away in one direction, well-defined rotational structure makes its appearance (Alex 64) at Eu^{153}, only four neutrons in the other direction. This means that when discussing states in Eu^{149} one must be careful not to draw arbitrary conclusions from the spherical shell model and must be prepared to accept collective effects and the fractionation of single-particle strengths over many states.

That Eu^{149} should be very soft toward vibrational deformations is borne out by the fact that Sm^{148}, its even-even core, has a 2+ one-phonon vibrational state (Baba 63) at only 551 keV, a 3- (octupole?) state at 1162 keV, and a 4+ (from the two-phonon vibrational triplet?) at 1181 keV.

The simple shell model predicts that above Z=50 the available proton orbits are $g_{7/2}$ and $d_{5/2}$ lying close together, then, after a gap of a few hundred keV, $h_{11/2}$, $s_{1/2}$, and $d_{3/2}$. The parent, Gd^{149}, should have eight $g_{7/2}$ and six $d_{5/2}$ protons (or some distribution of proton pairs in these nearly degenerate orbits) outside the Z=50 closed shell. Its last three neutrons should lie in $h_{9/2}$ and/or $f_{7/2}$ orbits, the unpaired neutron being in the $f_{7/2}$ orbit, similar to many other $I\pi$=7/2- nuclei above N=82. [This neutron assignment involves somewhat circular logic connected with the Gd^{149} ε decay properties, but no other assignment gives any sort of consistent picture.]

Similarly, the ground state of Eu^{149} can be characterized as $(g_{7/2})^8(d_{5/2})^5$ protons above Z=50 and $(h_{9/2})^4$ or $(f_{7/2})^4$ (or some combination) neutrons above N=82. This 5/2+ configuration is well established from its ε decay (Harm 61) and again is consistent with many odd-Z nuclei in this region. The first-excited state undoubtedly has a $g_{7/2}$ proton hole as a major component in its configuration, i.e., $(g_{7/2})^7(d_{5/2})^6$, again in agreement with many other odd-Z nuclei in the region. These assignments are consistent with the 0.32-nsec half-life (Berl 62) of the 149.6-keV state, a half-life quite in line with ℓ-forbidden $M1$ transitions between $g_{7/2}$ and $d_{5/2}$ states.

The ε decay to the ground and 149.6-keV states demonstrates quite clearly that they are separate single-particle states and not members of a K=5/2 rotational band. From our above assignments the ε decay can be pictured as $\pi d_{5/2} \rightarrow f_{7/2}$ for the ground state and $\pi g_{7/2} \rightarrow \nu f_{7/2}$ for the 149.6-keV state. The observed branchings (and log ft's), 17.1% (7.7) and 36.3% (7.3) are perfectly consistent with such transitions. On the other hand, if the 149.6-keV state were the 7/2+ member of a K=5/2 rotational band, the relative ε population should be predictable by the ratio of the squares of the following vector-coupling coefficients,

$$\frac{\langle I_i K_i \ell (K_f - K_i) | I_i \ell I_f K_f \rangle^2_{\text{excited}}}{\langle I_i K_i \ell (K_f - K_i) | I_i \ell I'_f K_f \rangle^2_{\text{ground}}} = \frac{\langle 7/2\ 7/2\ 1\ -1 | 7/2\ 1\ 7/2\ 5/2 \rangle^2}{\langle 7/2\ 7/2\ 1\ -1 | 7/2\ 1\ 5/2\ 5/2 \rangle^2}$$

$$= 1/3 \ .$$

This is clearly in the wrong direction even before the energy dependence has been included.

The only other simple single-particle state that can be clearly identified is the $h_{11/2}$ state at 496.2 keV. The measured $M2$ and $E3$ multipolarities of the 346.5- and 496.4-keV transitions indicate the 11/2- assignment, as does the 2.48±0.05-μsec half-life of the state. Single-particle estimates (Mosz 53) for the half-lives of the $M2$ and $E3$ are 3.8×10^{-8} and 8.2×10^{-5} sec, respectively, to be compared with the measured partial half-lives of 2.7×10^{-6} and 3.6×10^{-5} sec. The $M2$ is retarded by a factor of approximately 70, but, then, $M2$'s are commonly retarded by such factors. More surprising, the $E3$ is enhanced by a factor of about 2.3 over its single-particle estimate, and most $E3$'s are also retarded. However, there are three other known enhanced $E3$ transitions (Bee 69, Hise 67) in La^{137}, Pr^{139}, and Eu^{147}, all nuclei just above or below $N=82$ and all involving an $h_{11/2}$ state. A cursory attempt (Hise 67) has been made to explain the enhancements on the basis of octupole-coupled admixtures of the ground states in the $h_{11/2}$ states, but at this point meaningful quantitative calculations cannot be made. However, the assignment of the 496.2-keV state as an $h_{11/2}$ state is warranged, and its receiving no direct ϵ population from Gd^{149} is consistent with this assignment.

A number of spin and parity assignments can be made for the other states, but deciding much about their internal structures

is quite difficult. Many of the states are undoubtedly core-coupled, e.g., the 459.9- and 534.2-keV states, but most conclusions at this point would be somewhat arbitrary. Unfortunately, theoretical studies of this region are all but nonexistent, and even useful experimental systematics are scarce. We are currently studying other nearby Gd isotopes and hope to be able to say more about the structures of states in the various nuclei in this region at the conclusion of these studies. Meanwhile, in this paper we confine ourselves to a more or less straightforward discussion of the spins and parities per se, as they can be deduced from the γ transitions. The ε decay itself yields little information, for most of the log ft values lie in the range which indicates either first-forbidden or allowed transitions, and it will be necessary to know more about the internal structures of the states before drawing serious conclusions from these values.

The 459.9-keV state can be assigned 3/2+, 5/2+, or 7/2+ because of the $M1$ character of its ground-state γ-ray transition. The log ft value of 9.1 seems to imply a first-forbidden unique transition. However, if one considers this state to arise from core-coupling to the one-phonon 551-keV state in Sm^{148}, the log ft value would be expected to be larger than normal. With this in mind, the ε decay could in fact be a normal first-forbidden transition. Consequently, the spin assignment for the 459.9-keV state cannot be narrowed down from the above. And if the $d_{5/2}$ ground state were the single-particle component of

the core-coupled state, this could easily explain the absence of a transition to the 149.6-keV state.

The 534.2-keV state can also be assigned 3/2+, 5/2+, or 7/2+ because of the *M*1 character of its ground-state transition. It is also tempting to think of this state as the $d_{5/2}$ ground state coupled to the 2+ quadrupole vibrational state. We shall see below that the assignment for the 534.2-keV state can be narrowed down to 7/2+.

The 666.0-keV state is limited to 5/2+, 7/2+, or 9/2+ by the *M*1 transition to the 149.6-keV state. If, as it appears, the 666.2-keV transition to the ground state does have appreciable *M*1 admixing in its *E*2 character, the 9/2+ possibility is eliminated.

Assignments for the next two states, at 748.2 and 794.8 keV, can be much more specific because of the many γ-ray branches proceeding from them. The 748.2-keV *E*1 γ implies a spin of 3/2-, 5/2-, or 7/2- for the 748.2-keV state. The 252.3-keV γ to the 11/2- state appears to be an *M*1, which is inconsistent with the 748.2-keV γ being an *E*1. However, assuming the 252.3-keV γ to be really an *E*2 narrows the choice for the 748.2-keV state to 7/2-. The log ft of 7.4 is somewhat high for an allowed transition, but, remembering that the 748.2-keV state undoubtedly has a complex structure, one would expect a β transition to it to be hindered. With a 7/2- assignment, the 214.5-keV γ to the 534.2-keV state allows the narrowing of assignments for the latter down to 5/2+ or 7/2+.

The strong 298.5-keV *M*1 transition from the 794.8-keV state to the 496.4-keV state suggests the possibilities 9/2-, 11/2-, or 13/2- for the upper state. The 645.2-keV *E*1 transition to the 149.6-keV state limits the choice to 9/2-. The log ft for ε decay to this state is the lowest for decay to any state, implying that this transition, if any, is allowed, again consistent only with the 9/2- assignment. The 260.5-keV *E*1 γ then allows the assignment for the 534.2-keV state to be narrowed further to 7/2+.

If we may be forgiven a little speculation at this point, a word about one component of the wave function of the 794.8-keV state might perhaps be in order. Consider the two facts: 1) a relatively simple mechanism must exist for populating the state so readily from Gd^{149}, and 2) the abnormally large intensity of the transition to the 496.4-keV state indicates a similarity to that state. Now, there is ample indication (Fel 70, Wild 70a) that,below $N=82$ at least, there is appreciable $h_{11/2}$ character in the proton pairs of the Gd isotopes, and this should also be true here. Any ε transitions from Gd^{149} involving $g_{7/2}$ or $d_{5/2}$ protons would not be expected to proceed at all rapidly to the available final neutron states, nor would they lead to 9/2- overall final states. On the other hand, a $\pi h_{11/2} \rightarrow \nu h_{9/2}$ transition not only would proceed relatively quickly, but also it would lead to the final configuration, $(\pi h_{11/2})(\nu h_{9/2})(\nu f_{7/2})$, which could

furnish a 9/2- state among its couplings. Similar cases, resulting in three-particle final states are known (Bee 69d and McH 69a) in the N=82 region, although the three-particle states lie considerably higher than 794.8 keV. Thus, although we do not suggest this as the primary component of the 794.8-keV state, such an admixture would account satisfactorily for the ε decay.

The state at 812.4 keV is assigned 5/2+, 7/2+, or 9/2+ on the basis of its ground-state γ transition and the 663.3-keV $M1$ transition to the 149.6-keV state. A possible 3/2+ assignment for this state is ruled out on the argument that the large log ft is probably a result of internal complexities in the state necessitating multi-particle rearrangement during the ε decay rather than the ε decay being first-forbidden unique.

The single γ transition of 875.8 keV emanating from the state of this energy is assigned an $M1$ multipolarity. This limits the state spin to 3/2+, 5/2+, or 7/2+, assignments that are compatible with the ε decay to this state.

Harmatz and Handley (Harm 66) do not report conversion-electron intensity values for the 933.3-keV transition. Therefore, we cannot make a definite spin assignment to the 933.3-keV state on the basis of this transition. From the log ft value of 8.3, assuming this again to be a hindered first-forbidden transition, the spin could be 5/2+, 7/2+, or 9/2+.

The 939.1-keV *M*1 ground-state transition suggests 3/2+, 5/2+, or 7/2+ for the 939.1-keV state. The 788.6-keV transition (if it really contains an appreciable *M*1 admixture) eliminates the 3/2+ possibility, as does the relatively low log *ft* value of 6.8. Neither the 478.7- nor the 272.0-keV γ's allow this to be narrowed further. It should be noted that an *E*1 multipolarity for the 405.5-keV transition, while experimentally indicated is incompatible with the other assignments. A three-particle final state component can also be invoked here to explain the ε decay, this time a $\pi g_{7/2} \rightarrow \nu h_{9/2}$ transition resulting in $(\pi g_{7/2})^{-1}$ $(\nu h_{9/2})(\nu f_{7/2})$ as a component of the final state.

The 947.7-keV *E*1 transition implies 5/2-, 7/2-, or 9/2- for the 1097.3-keV state. The log *ft* is compatible with any of these possibilities, but other than this, little can be deduced about the state.

4.2. The Decay of Gd^{145m}

4.2.1. Introduction

Gadolinium isotopes cover a wide range of nuclear types, extending from permanently deformed nuclei to spherical single closed-shell nuclei at $N = 82$. As a result, systematic studies of their decay properties and structures should prove quite rewarding, for here is one of the few regions in the nuclidic chart where one can follow trends in nuclear states when moving from one extreme nuclear type to another. Gd^{145m} was our second invesigation of the Gd isotopes; an isotope on the neutron-deficient side of the $N = 82$ closed shell. In this region the Gd isotopes have not been very well characterized until quite recently, although their decays present some interesting anomalies, such as the peculiar ground-state decay of Gd^{145} into what appear to be three-quasiparticle states in its Eu^{145} daughter, the subject of which forms § 4.3. On the neutron-deficient side of $N = 82$, a systematic study of the odd-mass isotones also appears well worthwhile because of the appearance of long series of nuclear isomers having quite different and distinct decay properties. The longest series of these isomers, in the $N = 81$ nuclei, extended from Te^{133} to Sm^{143}, and it seemed reasonable that Gd^{145}, as the next nucleus in line, should also exhibit isomeric states.

We subsequently observed the metastable state in Gd^{145} and its isomeric transition. The energy of the transition was found to be 721±0.4 keV and the half-life of the state, 85±3 sec. These values were consistent with our predictions based on the systematics of the other $N = 81$ isotones, and they were first reported in November 1968

(Epp70B). Since that time, Jansen, Morinaga, and Signorini (Jan69) have published results in very good agreement with our γ-ray energy and half-live values. Since our first preliminary report we have also observed the conversion electrons from the isomeric transition, clearly identifying it to be of *M*4 multipolarity, and we have observed a β^+/ε branch from Gd^{145m} directly to states in Eu^{145}.

Even by 1951 some 77 nuclear isomers had been classified by Goldhaber and Sunyar (Gold51). Since then, of course, isomers have been one of the prominent nuclear properties used to test the validity of nuclear models. In particular, *M*4 transitions are of interest for testing the extreme single-particle model. If such a thing as a "pure" single-particle transition exists, these transitions are good candidates for that distinction. The *M*4 transitions observed in the $N = 81$ nuclei are thought to proceed from $h_{11/2}$ to $d_{3/2}$ states, and the $h_{11/2}$ state should be particularly pure owing to its being the only odd-parity, high-spin state at low excitations. We discuss the properties of these *M*4 transitions in § 4.2.3.

4.2.2. Experimental Results

We produced Gd^{145m} in this laboratory by both the $Sm^{144}(\tau,2n)Gd^{145m}$ and the $Sm^{144}(\alpha,3n)Gd^{145m}$ reactions. The calculated Q-values for these reactions were -10.4 and -30.9 MeV, respectively (Myer65). For all of these experiments separated isotope Sm^{144} (95.10%, obtained from Oak Ridge National Laboratory) in the form of Sm_2O_3 was used as the target material. The τ and α beams, typically 20 MeV and 40 MeV, respectively, were furnished by the Michigan State University Sector-Focused Cyclotron. Excitation functions were run to determine the energy for maximum Gd^{145m} yield in each case. Most of our experiments were performed with the τ beam, and typically a 10-mg or smaller target would be bombarded with a 0.5-μA beam for 1 min. Because of the short half-life of Gd^{145m}, no chemical separations could be carried out. Fortunately, they proved to be unnecessary, owing to the cleanness of the reactions. After most bombardments it took less than 2 min to retrieve the target and transport it to the counting area.

We also produced Gd^{145m} in a set of confirming experiments performed at the Yale University Heavy-Ion Accelerator. C^{12} beams ranging between 70 and 120 MeV were used, and the reactions of interest were $Nd^{142}(C^{12},\alpha 5n)Gd^{145m}$ and $Sm^{144}(C^{12},2\alpha 3n)Gd^{145m}$. The latter was discovered quite by accident and has an unexpectedly large cross section. It must proceed by a combination of cluster stripping and compound nucleus formation.

The γ-ray energies were determined by simultaneous counting with the standards listed in Table 10. A γ-ray singles spectrum is shown in Figure 24. The peaks appearing in this spectrum without

Table 10. γ-ray energy standards used for Gd^{145m}.

Nuclide	γ-ray energies (keV)	Reference
Ce^{141}	145.43±0.02	a
Cm^{243}	209.85±0.06	b
	228.28±0.08	b
	277.64±0.02	b
Co^{56}	846.4 ±0.5	c
	1038.9 ±1.0	c
	1238.2 ±0.5	c

[a] J. S. Geiger, R. L. Graham, I. Bergström, and F. Brown, Nucl. Phys. 68, 352 (1965).

[b] R. E. Eppley, unpublished results (1969).

[c] R. L. Auble, Wm. C. McHarris, and W. H. Kelly, Nucl. Phys. A91, 225 (1967).

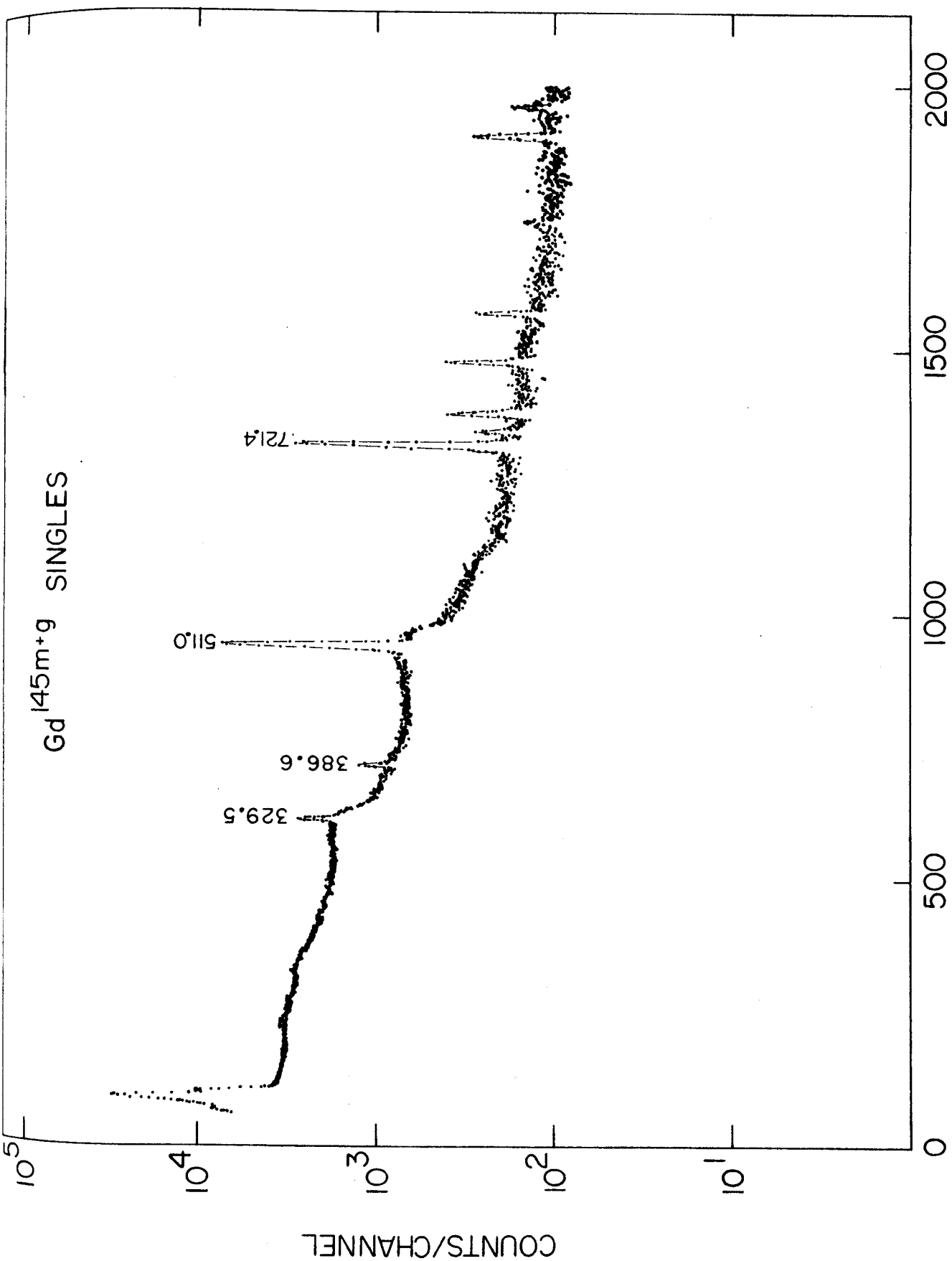

Figure 24. Singles γ-ray spectrum from 85-second Gd^{145m}.

energy assignments listed come from the decay of the ground state of Gd^{145} (see § 4.3). The detector used was a five-sided trapezoidal Ge(Li) detector fabricated in this laboratory. It had an active volume of ≈7-cm^3 and a resolution of 2.9 keV FWHM for the Co^{60} 1.333-MeV γ. The γ rays associated with the decay of Gd^{145m} had energies of 721.4±0.4, 386.6±0.3, and 329.5±0.3 keV, as determined from the averages of a number of experiments.

The Gd^{145m} half-life was determined with the help of a computer code called GEORGE (Geor). This code allows us to accumulate data through an 8192-channel ADC interfaced to the MSU Cyclotron Laboratory Sigma-7 computer. We can dump segments of the spectrum in successive time intervals: counting can be stopped, the spectrum segment dumped onto a Rapid Access Disc (for punching on cards at a later time), the memory erased, and the counting resumed, all in considerably less than one second of elapsed time. In the present case the spectra were dumped at 15-sec intervals. A pulser peak was included in each spectrum for later determination of the proper dead-time corrections. The net peak areas, corrected for dead time, then yielded the half-life information in the usual manner. A plot of a Gd^{145m} decay curve, corrected for dead time, is shown in Figure 25. The reported half-life is an average of three such least-squared decay curves.

A listing of our E_γ and half-life values is given in Table 11, where they are compared with those of Jansen, Morinaga, and Signorini.

The electron spectra were obtained by use of a 1000-μ thick Si(Li) surface barrier detector, cooled to methanol-dry ice temperature and operating with a bias of +200 V. The resolution of this

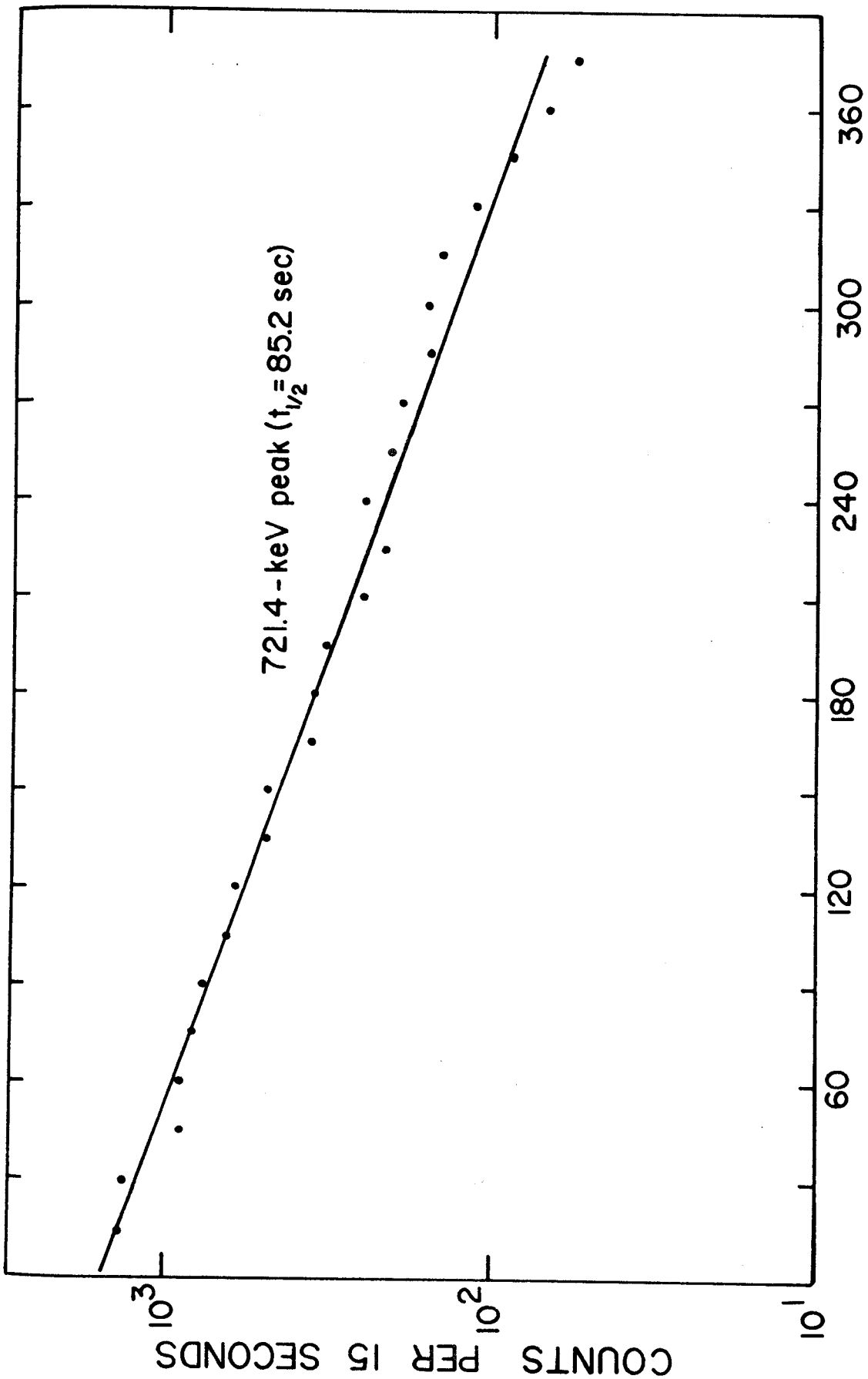

Figure 25. Half-life curve for Gd^{145m}.

Table 11. Transition data summary for Gd^{145m}

	This work	Jansen, Morinaga, and Signorini[a]
$E_\gamma(M4)$	721.4±0.4 keV	721.3±0.7 keV
$E_\gamma(M2)$[b]	386.6±0.3 keV	---
$E_\gamma(M1)$[b]	329.5±0.3 keV	---
$t_{\frac{1}{2}}$	85±3 sec	85±7 sec

[a](Jan69).

[b]These transitions occur in Eu^{145} and result from the direct feeding of the $h_{11/2}$ state in that nucleus by Gd^{145m}. The multipolarities are assumed from the properties of the states as determined from Gd^{145g} decay and scattering. Cf. refs. §4.3. and (New70).

detector was typically 5 keV FWHM in the 600-keV region, the electrons having passed through a 0.25-mil HAVAR window. A resulting electron spectrum is shown in Figure 26.

In order to arrive at a value for the conversion coefficient of the isomeric transition, the γ-ray and electron spectra were measured simultaneously from the same source, which was placed in a fixed, reproducible geometry. Again, owing to the short half-life, "mass-free" sources could not be made. However, as can be seen from the electron spectrum, our "thick" sources led to a minimum of straggling. For calibrating the detector efficiencies and the geometry corrections, a Cs^{137} source was used as a standard. A value of 0.094 was used for the α_K of its 661.6-keV transition; this is an average of the values given in (Dan62 and Hult 61).

Two separate experiments, made at widely differeng times, were performed to determine the Gd^{145m} K- and L-internal-conversion coefficients. The results, compared with theoretical values for various multipolarities, are shown in Table 12. The logarithms of the theoretical values were interpolated from a quadratic least-squares fit to the tabulated values of Hager and Seltzer (Hag68). The experimental α_K value definitely shows the isomeric transition to be $M4$ in character. The measured K/L ratio places it as being either $M3$ or $M4$. The former is a more sensitive test, however, and an $M4$ assignment fits in quite well with the systematics of transition probabilities in the $N = 81$ isotones, as we shall see in the next section.

We shall see later that the 386.6- and 329.5-keV γ's fit between known (§ 4.3 and New70) states and imply that 4.7% of the decay

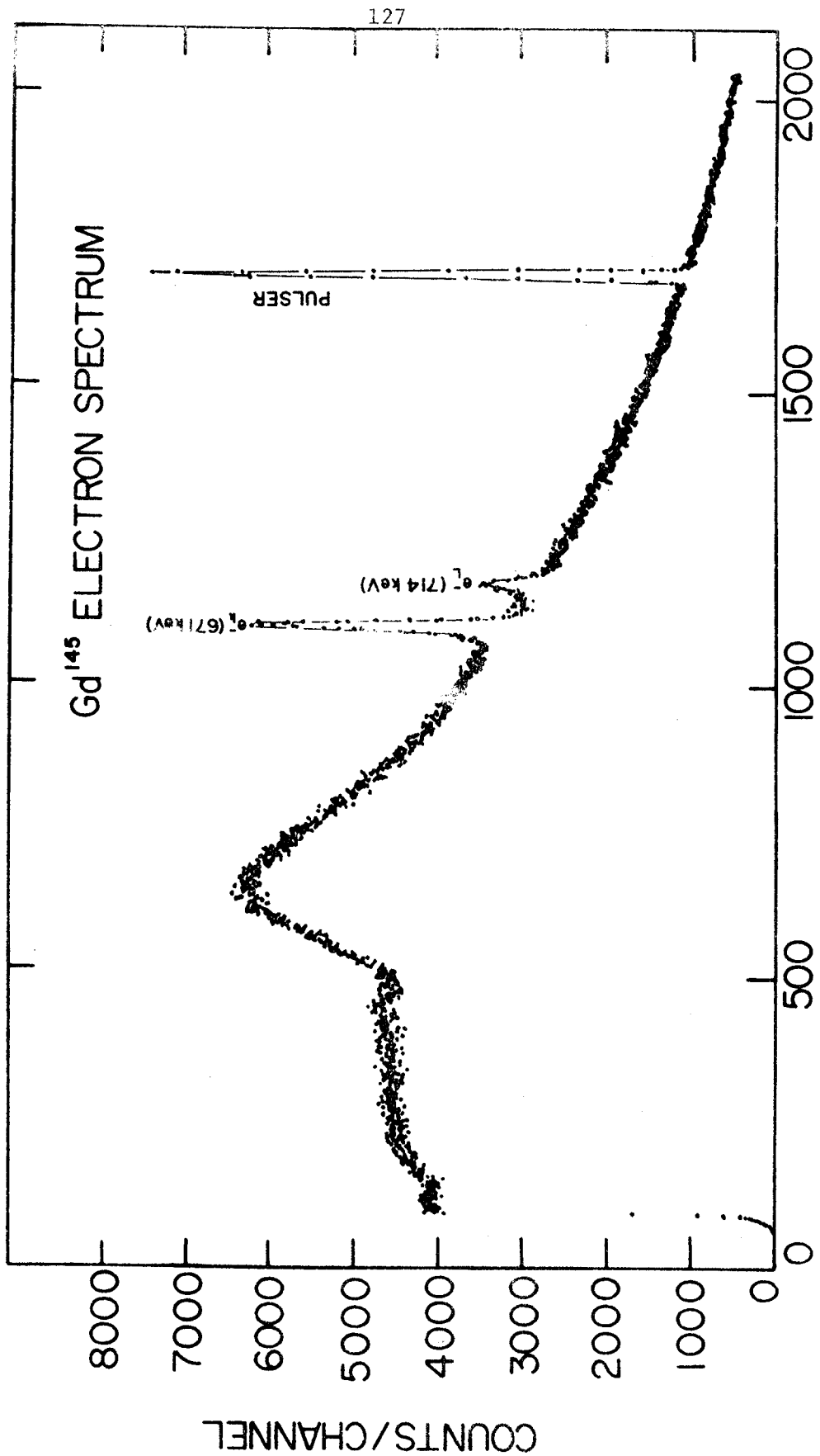

Figure 26. Electron spectrum showing conversion lines from the 721.4-keV M4 isomeric transition in Gd^{145}.

Table 12. Conversion coefficients for the isomeric transition in Gd^{145}.

	Experimental	Theoretical[a]			
		*E*3	*E*4	*M*3	*M*4
α_K	0.12±0.2	0.011	0.024	0.054	0.118
α_K/α_L	5.4±0.7	3.50	3.53	5.77	4.88

[a](Hag68).

of Gd^{145m} goes via a direct β^+/ε branch to an $h_{11/2}$ state in Eu^{145}, the other 95.3% going via the isomeric transition. The 4.7% branch was determined by correcting the 386.6-/721.4-keV photon ratio (found to be 0.048) for conversion, again using the conversion coefficients of Hager and Seltzer and assuming the 386.6-keV transition to be a pure *M*2 transition. The 329.5-keV γ results also from the decay of the ground state of Gd^{145}, so no quantitative information about its intensity could be obtained from these experiments.

4.2.3. Gd^{145m} and $N = 81$ Isomers

Figure 27 shows our decay scheme for Gd^{145m}. While the other known $N = 81$ odd-mass isotones have been assigned $d_{3/2}$ ground-state configurations, there is some evidence (see § 4.3) that in Gd^{145} the $s_{1/2}$ state has replaced the $d_{3/2}$ state as the ground state, which may account partly for the peculiar ground-state decay of Gd^{145}. Newman, et al., (New70) also came to this conclusion when interpreting their scattering data from the $Sm^{144}(\tau,d)Eu^{145}$ reaction in conjunction with their Gd^{145g} decay data. If the $s_{1/2}$ assignment is correct, the *M*4 isomeric transition in Gd^{145} does not proceed directly to the ground state but to a state ΔE in energy above the ground state. This excited $d_{3/2}$ state would then decay to the ground state via a predominatly *M*1 transition.

In search for a low-energy *M*1 transition, we have utilized a Si(Li) x-ray detector, which is useful in the 5-100-keV energy region for γ rays and is also sensitive to charged particles. No peaks that are in evidence in any of our spectra in the 10-100-keV range can be attributed to the decay of Gd^{145m}. The high positron flux, primarily from Gd^{145g} decay, contributed to a high background problem below 10

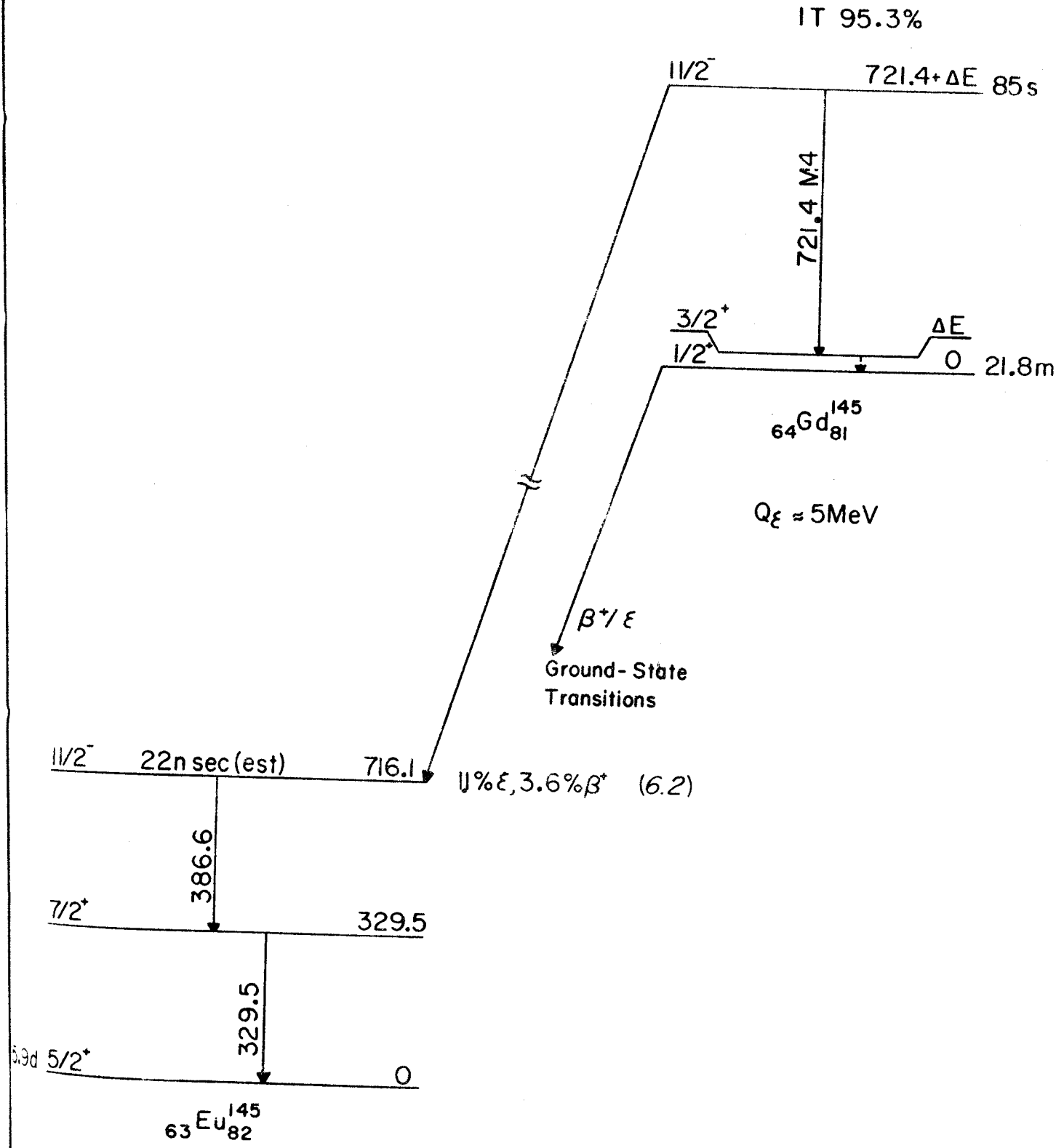

Figure 27. Decay scheme for Gd^{145m}.

keV and ruled out observing a transition in that region. Assuming such a low-energy transition to be present, most likely $M1$ in character, it would be converted primarily in the L_I shell, with α_{L_I} having a value of 4.5 at 46 keV and increasing to 246 at 9.38 keV (Hag68). Consequently, assuming the transition to be low in energy, say, 20 keV or less, would preclude observing the photons. However, we should have been able to see the L_I conversion line if the energy were above 10 keV. The radial matrix elements for the $M4$ transitions in the $N = 81$ odd-mass isotones were calculated using Moszkowski's (Mosz53) approximations for a single neutron hole,

$$T^{SP}_{(ML)} = \frac{2(L+1)}{L[(2L+1)!!]^2}\,\omega\frac{e^2}{\hbar c}\left[\frac{R_o}{c}\right]^{2L}\left[\frac{\hbar}{mcR_o}\right]^2 (\mu_N L)^2 |M|^2 S(j_i, L, j_f),$$

where L is the multipolarity of the transition, R_o is the effective nuclear radius, $S(j_i, L, j_f)$ is a statistical factor (i.e., angular momentum portion of the matrix element), which for $11/2 \rightarrow 3/2$ transitions has the value 15/11, and μ_N is the dipole moment of the neutron. Symbolically, $|M|^2$ has the form,

$$|M|^2 = \left(\int_0^\infty R_f \left[\frac{r}{R_o}\right]^{L-1} R_i r^2 dr \right)^2 .$$

Our results are plotted in Figure 28, where we also show the differences in energy between the $h_{11/2}$ and $d_{3/2}$ states.

The resulting transition probabilities are consistently smaller than the approximation of a constant wave function,

$$|M|^2 = \left[\frac{3}{L+2}\right]^2 (\mu_N L)^2 = 14.6,$$

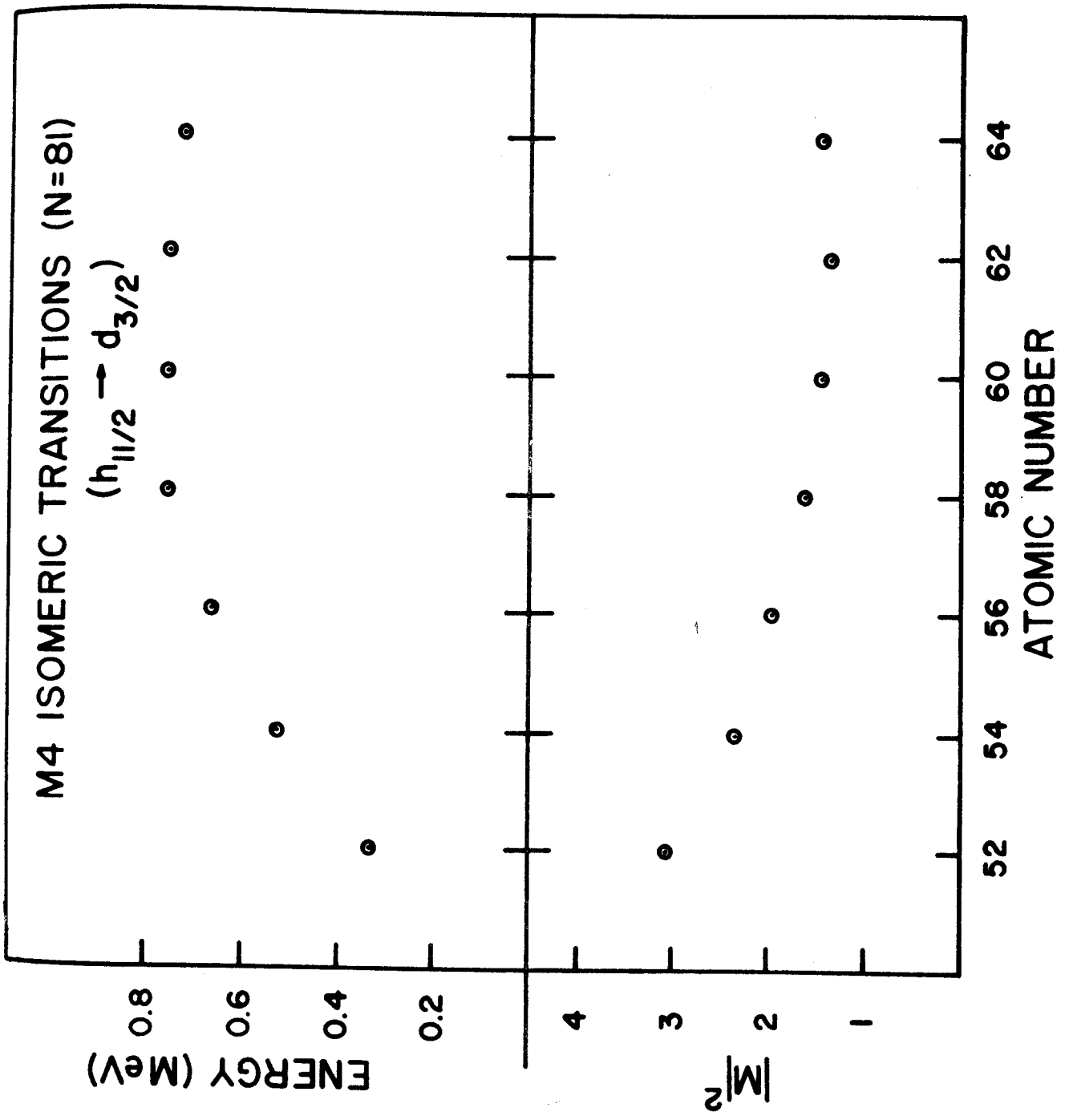

Fig. 4

Figure 28. Plots of the $h_{11/2} \rightarrow d_{3/2}$ energy differences and of the squares of the radial matrix elements for the *M*4 isomeric transitions that connect these states in the *N* = 81 odd-mass isotones.

but this fact should not concern us particularly, for $M4$ transitions are customarily retarded over such estimates and one needs much more detailed information about the nuclear wave functions in order to make detailed comparisons meaningful. What is of more importance is the fact that the values of $|M|^2$ are not constant but show a definite trend in this series of isotones. [It is unusual for $|M|^2$ not to be constant over such a series. For example, in the odd-mass neutron-deficient lead isotopes, $|M|^2$ was constant to the point that an apparent 15% discrepancy at Pb^{203} suggested that an unobserved transition was competing with the $M4$ isomeric transition, and this competing transition was subsequently discovered (Doeb68)]. Other isomeric series will be discussed in Chapter VI.

The complete answer as to why the discrepancy in magnitude and in trend exists between the experimental and theoretical values is still not forthcoming. Kotajima (Kot63) summarizes several effects that could contribute to these deviations: 1) cancellation of the magnetic moments because of the mesonic effect, 2) configuration mixing or spin polarization, or 3) the use of too crude an approximation for the radial wave functions. In the same paper he explores the usefullness of applying a more realistic function for these radial wave functions, but the matrix elements were remarkably insensitive to changes in these wave functions. This effect, then, by itself could not explain even the deviations in magnitude, much less the "bowing" of the curve as seen in Figure 28.

More recently, Jansen, Morinaga, and Signorini (Jan69) have also sought to better the experimental-theoretical agreements. In a

calculation similar to that used by Kotajima, they recalculated the radial matrix elements using a potential function consisting of a Woods-Saxon part and a spin-orbit part. In this manner they recalculated the radial part of the Schrödinger equation for these nuclei. In addition to this refinement, they took account of configuration mixing by utilizing the results of Horie and Oda (Hor64). In this manner, much of the Z dependence was removed. However, the experimental values are still lower than the theoretical ones for all reasonable values of R_o. For an R_o of 1.22 f, the experimental -to-theoretical ratio hovers around 0.5.

An alternate attack on this problem might prove to be useful. Recasting the problem in a quasi-particle framework would allow a simplified picture, the transition probabilities depending only on the particle-hole character of the states involved. Stripping and pick-up reactions are just now beginning to be carried out on nuclei in this region, so occupation numbers may very well become available from these before long. As soon as such information is available, this type of formulation can be explored more fully.

Finally, it should be noted that as Z increases there is an increase in the direct β^+/ε decay to the $h_{11/2}$ states in the daughter nuclei. On the neutron-deficient side of the N = 81 odd-mass isotones, Ce^{139m} does not have sufficient decay energy to populate such a state in La^{139}, but the decay is energetically possible for Nd^{141m}, Sm^{143m}, and Gd^{145m}. We have made a careful search for direct population of the $h_{11/2}$ state in Pr^{141} by Nd^{141m} decay (Bee68) and have been able to set an upper limit of 0.01% on any such population. This results

in a log ft greater than 7. From Sm^{143m} decay, however, Feldsteiner and Rosner (Feld70) were able to detect a direct branch of 0.2% to the state in Pm^{143}, implying a log ft of 6.7. And we find a direct branch of 4.7% from Gd^{145m} decay, resulting in a log ft of only 6.2. We consider this to be an indication of the increased occupation of the $h_{11/2}$ orbit by proton pairs as one moves up the series. This is an aspect of the decay of the N = 81 series that is still under investigation.

4.3. The Strange Case of Gd^{145g}

4.3.1. Preamble

This investigation continues our overall studies of the neutron-deficient Gd isotopes, the decay of Gd^{149} (§ 4.1.) and the characterization of the isomer, Gd^{145m} (§4.2), having been reported previously.

Although several earlier papers speculated on Gd^{145}, Grover (Grov59) 1959 seems to have been the first to characterize this nuclide to any degree of clarity. It was also reported at about the same time by Olkowsky, et al. (Olk59). Both sets of results, having been obtained with NaI(Tl) detectors, were incomplete. A good example is the fact that the two intense transitions at 1757.8 and 1880.6 keV were previously unresolved. The NaI(Tl) data showed these as a composite peak reported to be 1.75 MeV (Olk59), although with considerable insight Grover (Grov59) decided that there were two transitions in the peak but did not elucidate further.

As far as we have been able to determine, no conversion electron studies have ever been made on Gd^{145g} decay, and, indeed its short half-life (21.8 m, cf. § 4.3.3.C. below) and the high energies of its stronger transitions make such experiments impracticable. And until the recent paper of Newman, et al. (New70) no high resolution, e.e., Ge(Li), γ-ray studies had been reported. The lack now and in the forseeable future of electron data cripples one in trying to assemble a complete decay scheme, for he has to work without direct information on the multipolarities of the transitions. However, the spins and parities of a number of the lower states in

the daughter Eu^{145} were determined by Newman, et al., through an analysis of the $Sm^{144}(\tau,d)Eu^{145}$ reaction. This reaction tends to discriminate against complex states, though, and, as will be seen later in this paper, we have reason to believe that the primary states populated by the decay of Gd^{145g} are complex. Our work has proceeded in parallel with the work of Newman, et al., and, indeed, there has been exchange of information between the groups (Toth69). They concentrated on the (τ,d) studies, however, taking only single γ-ray spectra, whereas we have concentrated on γ-ray studies, using various coincidence and anticoincidence techniques. Their experiments thus excite and explain many of the more straightforward lower-lying states that we see only weakly or not at all. We, on the other hand, see evidence of a number of higher-lying states populated or depopulated by weaker γ-rays, and we think we can explain what we call "the strange case" of Gd^{145g} decaying overwhelmingly to the two states at 1757.8 and 1880.6 keV. Here, then, is an excellent case where β-γ spectroscopy from one laboratory and the reactions spectroscopy from another laboratory supplement and complement each other.

By "the strange case" we mean the abrupt break in the decay properties of the odd-mass N=81 isomer pairs (§ 4.2.), that occurs at Gd^{145g}. By now there is a known series of seven N=81 isomer pairs, the ground state in each case presumably being a single $d_{3/2}$ neutron hole in the N=82 shell and the metastable state being an $h_{11/2}$ neutron hole. The metastable state decays exlusively to the ground state via an $M4$ transition in the lighter mass isotones, although recently some direct branching has been observed from Sm^{143m} decay

and from Gd^{145m} decay. More germane, on the netron-deficient side of the N=81 series, the $(\nu d_{3/2})^{-1}$ ground states of $_{58}Ce^{139}$, $_{60}Nd^{141}$ and $_{62}Sm^{143}$ (Geig65,Bee68 and DeF68, respectively) all decay in a very straightforward fashion to the $\pi d_{5/2}$ states in their daughter nuclei. A priori there was no reason to expect the decay of $_{64}Gd^{145g}_{81}$ to behave otherwise, yet it was soon discovered that there is essentially no decay to the $\pi d_{5/2}$ ground state of Eu^{145} - its unhindered decay populates the two aforementioned high-lying states. We now think we have a reasonable explanation for this, involving: 1) a crossing of the $\nu d_{3/2}$ and $\nu s_{1/2}$ orbits so that the ground state of Gd^{145} is really $(\nu s_{1/2})^{-1}$, coupled with 2) a shift downward in energy of the $\pi h_{11/2}$ orbits, allowing an appreciable $(\pi h_{11/2})$ component in the Gd^{145} wave function. There is now indirect evidence (§ 4.2. and New70) for both of these, and if they be true, the Gd^{145} can be described as a "straightforward" decay into high-lying three-quasiparticle states, somewhat analogous to the decay (Bee69d) of Nd^{139m}. This will be discussed in § 4.3.5. below.

4.3.2. Source Preparation

Gd^{145g} sources were prepared primarily by the $Sm^{144}(\tau,2n)Gd^{145}$ reaction, which has a Q value of -10.6 MeV (Myer65). 20-MeV τ beams (the threshold for Gd^{144} production), furnished by the Michigan State University sector-focused cyclotron, were used to bombard enriched targets of $Sm_2^{144}O_3$ (95.10% Sm^{144}, obtained from the Isotopes Division, Oak Ridge National Laboratory). Typically, 25-mg targets were bombarded for 1-2 minutes with 0.5-μA of beam current. We also used the $Sm^{144}(\alpha,3n)Gd^{145}$ reaction (Q = -30.9 MeV) to prepare a few sources, bombarding similar targets with 40-MeV α's.

It is interesting to note the competing reactions that can accompany $(\tau,\times n)$ reactions. After a bombardment at MSU to produce Gd^{143} by the $Sm^{144}(\tau,4n)Gd^{143}$ reaction (Q = -31.2 MeV) using 40-MeV τ's, we found that we had produced quite a pure source of Sm^{141m+g} (see § 4.4), most likely by a $Sm^{144}(\tau,\alpha 2n)Sm^{141}$ reaction (Q = -9.8 MeV). Also, on attempting to produce Dy^{147} by the $Nd^{142}(C^{12},7n)Dy^{147}$ reaction (Q = -74.9 MeV) using 70-120-MeV C^{12} beams from the Yale University Heavy-Ion Accelerator, we found a sizable amount of Gd^{145} to be present, presumably through the competing $Nd^{142}(C^{12},\alpha 5n)Gd^{145}$ reaction (Q = -56.2 MeV). And, as a climax we found we were also able to produce Gd^{145} by the $Sm^{144}(C^{12},2\alpha 3n)Gd^{145}$ reaction (Q = -38.4 MeV) which has an unexpectedly large cross section. It must proceed by a combination of cluster stripping and compound nucleus formation. The low binding energies of α's in these neutron-deficient nuclei below N=82 makes for large cross sections for evaporating α's as well as n's. Not only does this cause a large number of different nuclides

to be made in most bombardments, thus complicating the task of analysis, but also it may set a practical limit to the production of nuclei farther from stability in this region by standard bombarding techniques. Our bombardments by the 20-MeV τ beam did, however, produce quite pure sources of Gd^{145g}. Here, apparently, the bombarding energy was too low for any competing $(\tau,\alpha xn)$ reaction. The next higher mass nuclide, Gd^{146}, which should still have an appreciable formation cross-section at this energy has a half-life of 48 d and thus posed no problem. In addition, Eu^{145} has a half-life of 5.9 d and a well worked-out decay scheme (Adam68a), so we did not have to worry about contamination of the spectra by daughter transitions.

Each source was counted within 2-3 minutes of the end of the bombardment and counted for varying intervals of time up to a maximum of 80 minutes, approximately 4 half-lives. The γ rays attributed to Gd^{145g} decay all retained their constant relative intensities over this period.

4.3.3. Experimental Data

4.3.3.A. Singles γ-Ray Spectra.

Two separate Gd(Li) detectors were used to obtain the Gd^{145g} γ-ray spectra. One was a 7-cm^3 active volume 5-sided coaxial detector ($\approx$0.5% efficient for the Co^{60} 1333-keV γ, compared with a 3×3-in. NaI(Tl) detector at 25 cm) manufactured in this laboratory, the other a 2.6% efficient detector manufactured by Nuclear Diodes, Inc. The best resolution we obtained was 2.3 keV FWHM for the Co^{60} 1333-keV

peak. Both detectors were used with room-temperature FET preamplifiers, linear amplifiers having near-Gaussian pulse shaping and 4096-channel analyzers or ADC's interfaced to computers.

The γ-ray energies were determined by counting the spectra simultaneously with the standards listed in Table 2. The larger peaks in the spectrum were first calibrated by use of the standards. These calibrated peaks, in turn, were used to determine the energies of the weaker peaks in spectra taken without the standards. The centroids and net peak areas were determined with the aid of the computer code SAMPO, as described in § 3.1.2. The backgrounds were first subtracted and the centroids then determined by fitting the peaks to Gaussian functions having exponential tails on both the upper and lower sides of the peaks. The specific peak shapes were determined by comparisons with reference peaks specified at intervals throughout the spectrum. The energies were then determined by fitting the centroids to a quadratic calibration equation. Peak areas are then converted to γ-ray intensities through curves previously determined in this laboratory for each detector. These curves were obtained by using a set of standard γ-ray sources whose relative intensities had been carefully measured with a 3×3-in. NaI(Tl) detector.

A word about the energies of the higher-energy γ-rays (E_γ > 1880.6 keV): Because of the weakness of these peaks it was not possible to observe them in spectra when standards were counted simultaneously. Thus, we had to resort to an extrapolation of our calibration curves up into this region. Various polynomial extrapolations were tried and discarded, for we found that a linear

extrapolation gave the best agreement between the energies of the photopeak and those determined from double-escape peaks falling within our well-calibrated energy range. One should be somewhat wary, however, of systematic errors in the energies of these γ rays.

After taking spectra from and following the decay of at least 15 different Gd^{145g} sources prepared at widely differing times, we have identified 38 γ rays as resulting from the β^+/ε decay of Gd^{145g}. A singles spectrum taken with the 7-cm^3 detector is shown in Figure 29. A list of these γ rays and their relative intensities is given in Table 13, where they are compared with the results of Newman, et al. (New70). All values from our work are the averages from many determinations, with the quoted errors reflecting the statistical fluctuations found among the different runs.

4.3.3.B. Coincidence Spectra

1. Anticoincidence spectra. One of the most convenient "first steps" in elucidating a complex decay scheme such as that of Gd^{145g} is to determine which transitions are ground-state transitions, especially the primarily ε-fed ground-state transitions. To obtain such information we performed an anticoincidence experiment between the 7-cm^3 Ge(Li) detector and an 8×8-in. NaI(Tl) split annulus. This setup has been described in § 2.1.2.B., but in brief it works as follows: The Ge(Li) detector is operated in an anticoincidence mode (resolving time, $2\tau \approx 200$ nsec) with either (optically isolated) half of the annulus or the 3×3-in. detector. Thus, the system serves both as a Compton-suppression and, more important, as a cascade-

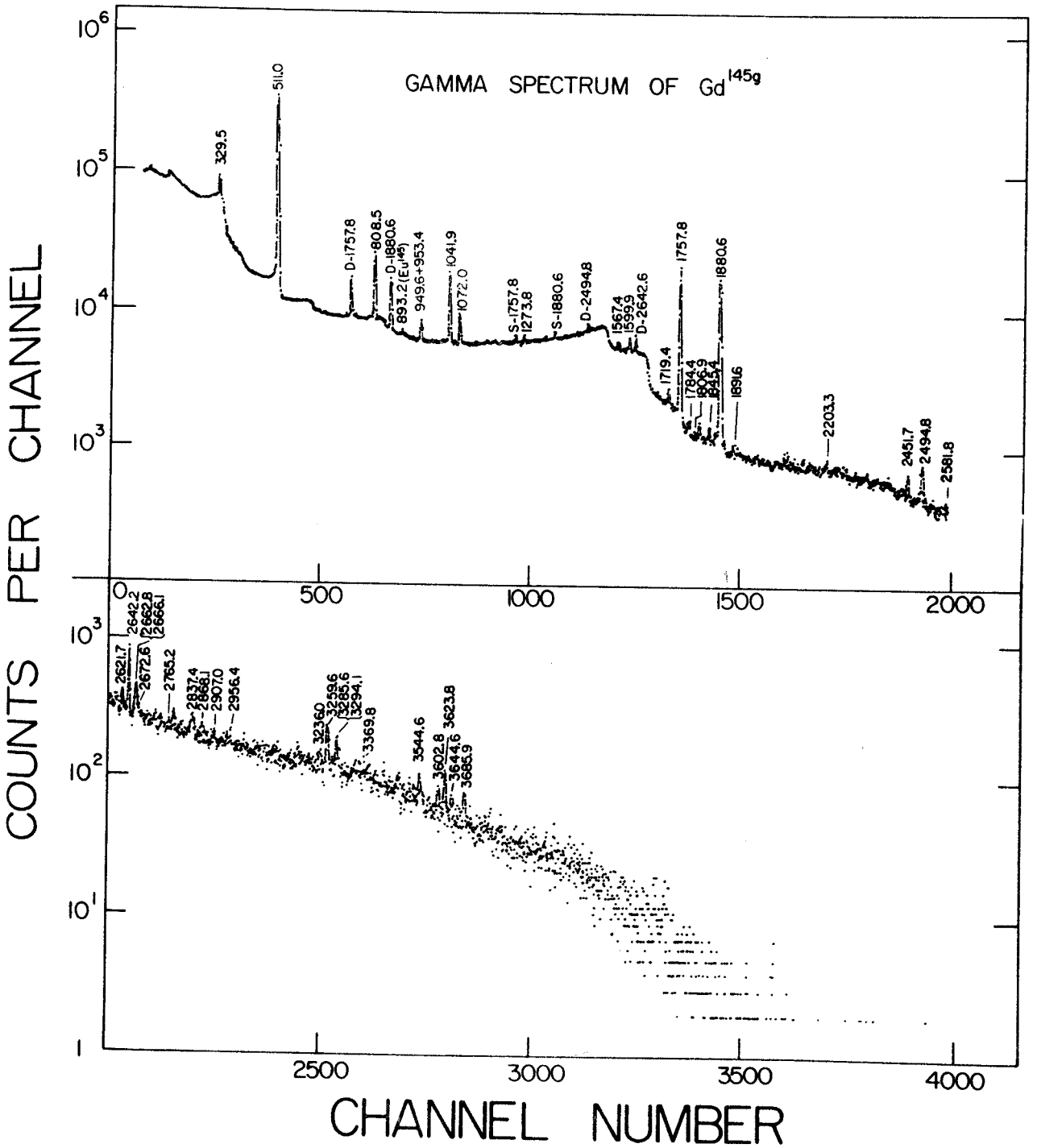

Figure 29. Singles γ-ray spectrum from Gd^{145g}.

Table 13. Energies and Relative Intensities of γ rays from the decay of Gd^{145g}

This work		E. Newman, et al.[a]	
Energy(keV)	Intensity[b]	Energy(keV)	Intensity[c]
329.5±0.2	30.8±2.0	330.1	31
808.5±0.2	≡100	808.4	≡100
949.6±0.3	8.6±0.3	949.4	5.9
953.4±0.3	15.8±0.3	953.7	11.8
1041.9±0.2	112±4.0	1041.9	107
1072.0±0.4	31±1.0	1072.2	17.6
1567.4±0.2	10.4±0.2	1567	10.2
1599.9±0.2	20±0.4	1599.9	19.6
1719.4±0.2	13.3±0.1	1719.5	11.8
1757.8±0.3	380±10	1757.9	392
1784.4±0.4	4.8±0.2		
1806.9[d]±1.0	2.7±0.3		
1845.4±0.4	6.3±0.1	1844.7	4.7
1880.6±0.5	364±10	1880.6	384
1891.6±0.3	4.9±0.2		
2203.3±0.2	2.2±0.1	2202.8	7.1
2451.7±0.5	3.6±0.2		
2494.8±0.5	14.5±0.5	2494.3	15.3
2581.8±0.4	3.0±0.2		
2642.2±0.5	21.6±0.2	2642.9	25.9
2662.8[d]±0.4	6.7±0.7	2663.2	3.5

Table 13, continued

Our Work		E. Newman, et al.[a]	
Energy(keV)	Intensity[b]	Energy	Intensity[c]
2666.1±0.4[d]	7.2±0.1		
2672.6±0.9	1.8±0.2	2674.0	2.4
2765.2±1.5	1.9±0.1		
2837.4±0.3	4.6±0.4	2837.7	9.8
2868.1±0.7	1.3±0.1		
2907.0±0.4	1.2±0.1		
2956.4±0.2[d]	1.5[e]		
3236.0±0.5	1.6±0.2		
3259.6±0.6	2.2±0.2		
3285.6±0.5	1.7±0.1		
3294.1±0.5[d]	1.4[e]		
3369.8±0.5[d]	0.8[e]		
3544.6±0.5[d]	1.6[e]		
3602.8±0.5[d]	1.0[e]		
3623.8±0.5[d]	2.1[e]		
3644.6±0.5[d]	0.9[e]		
3685.9±1.6[d]	1.4[e]		
		781.3[f]	3.1
		914.6[f]	2.7
		1070.2[f]	9.8
		1781.9[f]	7.1

[a](New70). [b]The errors given on the intensities reflect only the statistical scatter about the average over many runs. The absolute uncertainties will be larger, perhaps ±10% for the more intense peaks and correspondingly greater for the less intense peaks. [c]The intensities given in (New70) were renormalized so that the 808.5 keV $\gamma \equiv 100$.
[d]These γ rays show up only weakly (but consistently) in the spectra, so we place them only tentatively as originating from Gd^{145g} decay.
[e]These intensities may well be off by as much as a factor of 2.
[f]Transitions reported in (New70) for which we found no corresponding transitions. See the text for a discussion of these transitions.

suppression spectrometer. An anticoincidence spectrum is shown in Figure 30 and the relative intensities of the γ rays in this spectrum are compared with those in the singles spectra in Table 14.

2. Megachannel coincidence spectra. Our two-dimensional "megachannel" coincidence experiment utilized two Ge(Li) detectors, the Nuclear Diodes 2.5% detector and an ORTEC 3.6% detector. A block diagram of the electronics is shwon in Figure 3. The experiment was much like a standard fast-slow coincidence experiment, except that both the x and y events were processed each time a fast coincident event was detected. The x and y addresses were stored in the two halves of a single (32-bit) word in a dedicated buffer in the MSU Cyclotron Laboratory Sigma-7 computer. When the buffer was filled, events were collected in a second, similar buffer while the contents of the first were written on magnetic tape. The spectra were recovered later off-line by a program that allowed one to obtain gated "slices" with or without a linearly interpolated background subtraction.

The short half-life of Gd^{145g}, coupled with the fact that there just are not too many coincidences associated with its decay, makes it difficult to obatin "pretty" coincidence spectra. In order to record as many coincidence events as possible during a limited counting time, we used a 180° geometry for the detectors, although this can cause serious complications because of Compton scattering between the detectors (Gie70). With repeated bombardments during a 1-d period we were able to collect 1.8×10^6 coincidence events, which

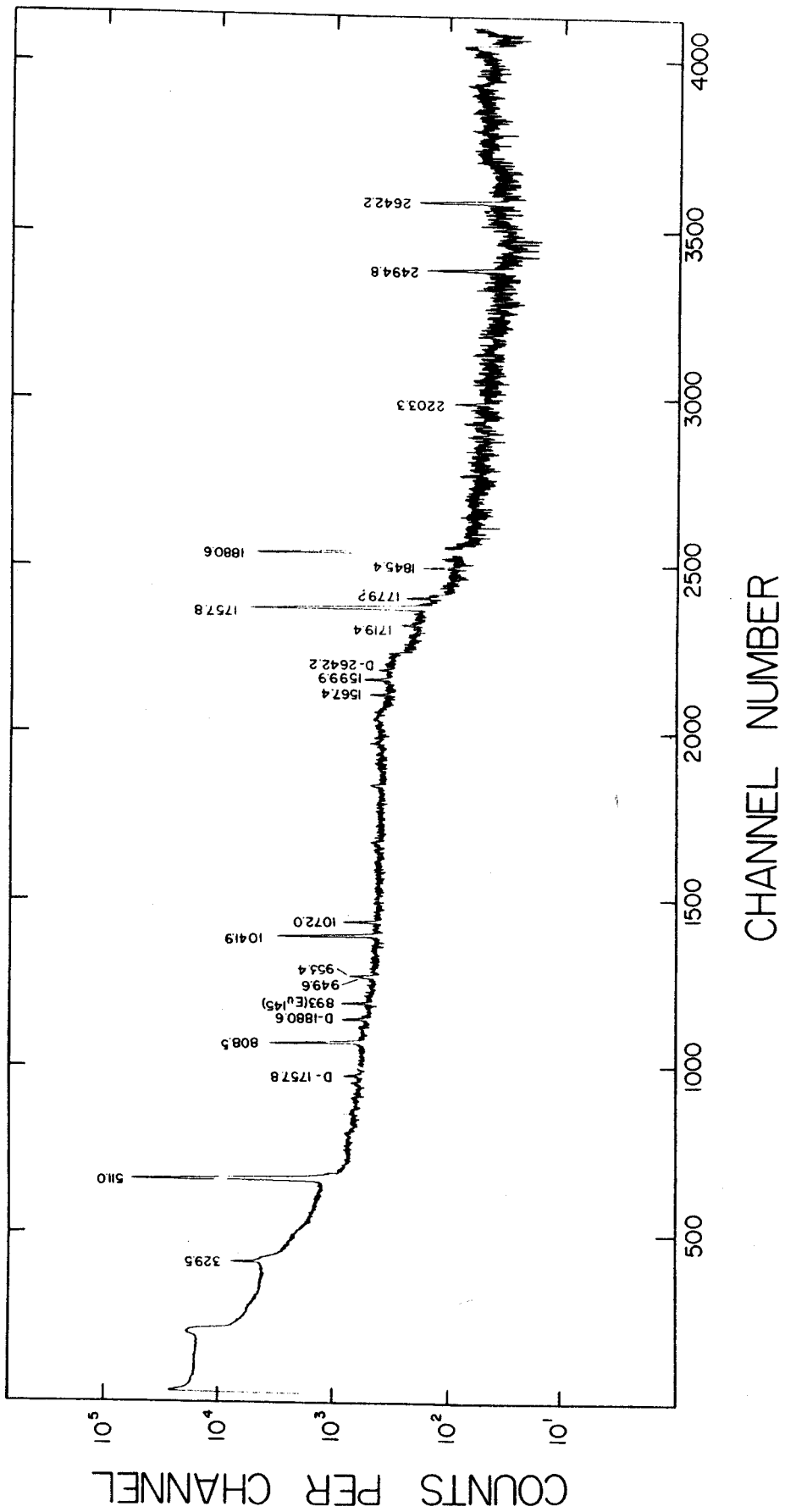

Figure 30. Anticoincidence spectrum of Gd^{145} decay.

Table 14. Relative Intensities of Gd^{145g} γ rays in Coincidence Experiments.

Energy [a] (keV)	Relative Intensities			
	Singles	Integral Coinc.	511-511 Coinc.	Anti-Coinc.
329.5	30.8	60		24
808.5	≡100	≡100	≡100	86
949.6	8.6	18.4		5.5
153.4	15.8	19.3		11
1041.9	112	85.6	28.0	112
1072.0	31	35.6		21
1567.4	10.4			11
1599.9	20		0.64	21
1719.4	13.3	13.5		6.6
1757.8	380	214	100	507
1784.4	4.8			
1806.9	2.7			
1845.4	6.3			7.9
1880.6	364	171	86.8	497
1891.6	4.9			
2203.3	4.4			5.6
2451.7	3.6			
2494.8	14.5		1.5	20
2581.8	3.0		1.1	
2642.2[b]	21.6			30

[a]The errors for these γ-ray energies are given in Table I.

[b]No coincidence information was obtained above this energy.

were then analyzed. The integral coincidence spectra for the x (2.5%) and y (3.6%) detectors, and six gated spectra (gates on x, display from y), including background subtraction, are shown in Figures 31 and 32. Of the slices taken, these were the only ones that contained substantially useful information. Relative intensities from the integral coincidence spectra are included in Table 14, and the results of the megachannel coincidence experiment are summarized in Table 15.

An important gate that is missing from Figure 31 and 32 are the ones on the 329.5-keV γ, which depopulates the first-excited state in Eu^{145}. Because of its position atop the intense $\gamma\pm$ Compton edge, coincidence spectra gated on it, with or without intricate or nonintricate background subtraction, could not be "unconfused" from spectra indicating β^+ feeding! Unfortunately, this has ramifications on the construction of the decay scheme, as will be shown in §4.3.4.

3. Pair Spectra. The two halves of the 8×8-in. NaI(Tl) split annulus were used in conjunction with the 7-cm^3 Ge(Li) detector to determine the relative amounts of β^+ feeding to the various levels in Eu^{145}. Each half of the annulus was gated on the 511-keV $\gamma\pm$ peak and a triple coincidence (resolving time, $2\tau \approx 100$ nsec) was required among these and the Ge(Li) detector. A resulting spectrum is shown in Figure 33. Note that double-escape peaks are also enhanced in this spectrum. A discussion

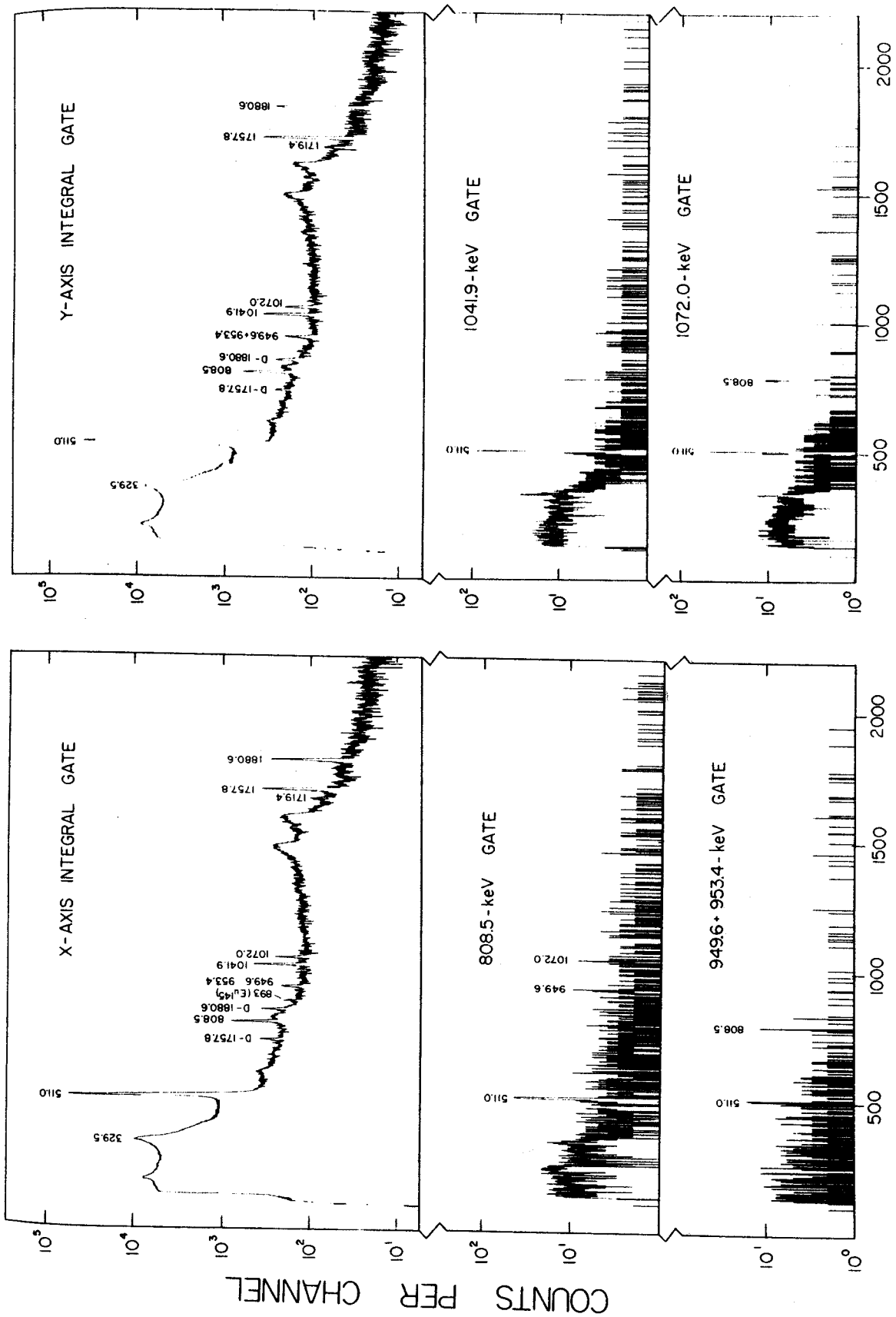

Figure 31. 2-dimensional coincidence spectra for the decay of Gd^{145g}.

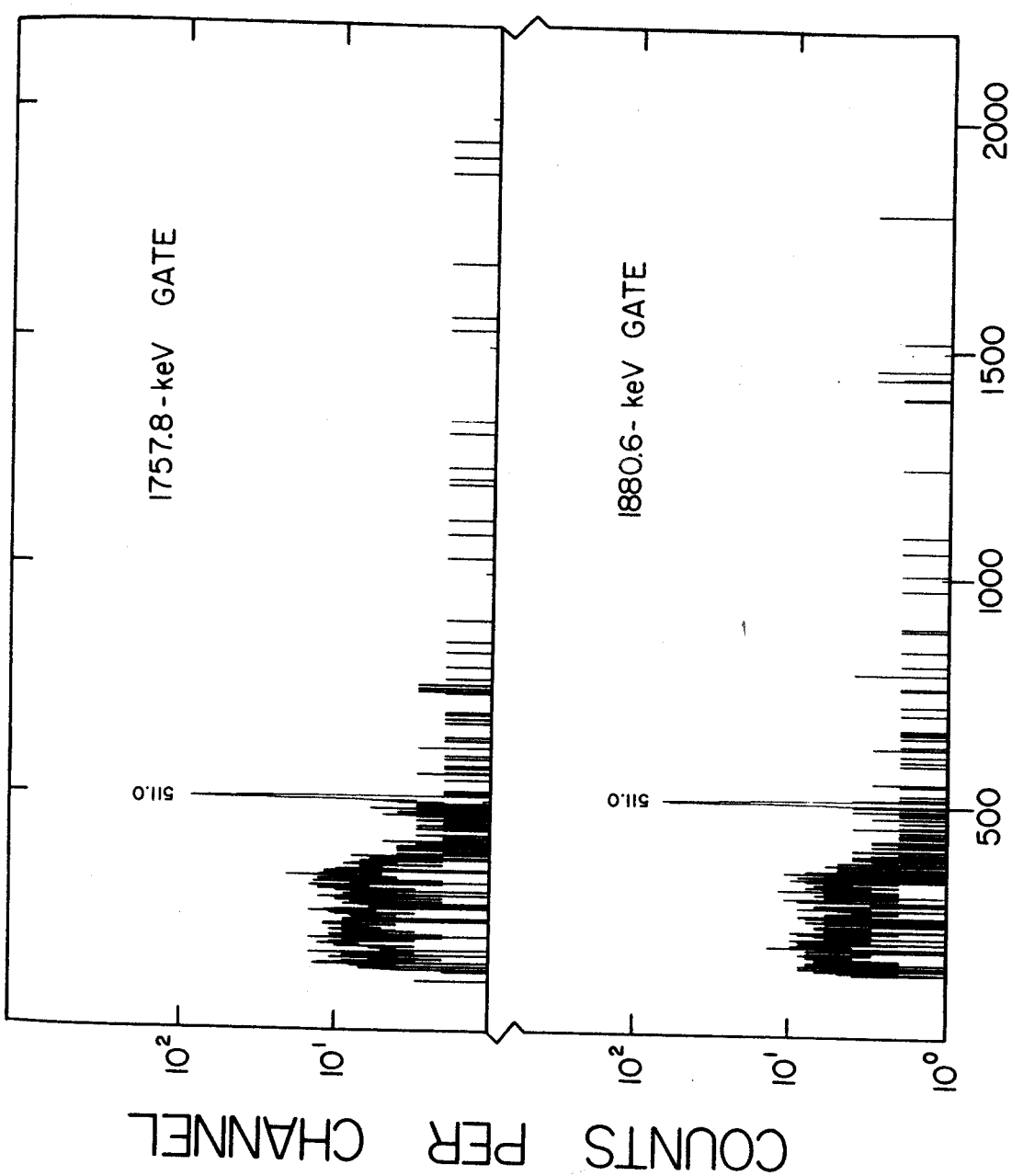

Figure 32. Additional gated spectra for the 2-dimensional run.

Table 15. Summary of γ-ray Coincidences in Gd^{145g}.

Gate Energy (keV)	γ's Enhanced (keV)
Integral	329.5, 808.5, 949.6, 953.4, (1041.9)[a], 1072.0, 1719.4
808.5	949.6, 1072.0
949.6	808.5
953.4	
1041.9	(329.5)[b], (893.2)[c]
1072.0	(329.5)[b], 808.5
1757.8	$\gamma^{\pm}$
1880.6	$\gamma^{\pm}$
511-511	808.5, 1041.9, 1757.8, 1880.6 2494.8[d], 2642.2[d]
Anti	1041.9, 1567.4, 1599.9, 1757.8, 1845.4, 1880.6, 2203.3, 2494.8, 2642.2

[a]As seen in Table II, the intensity for this transition is less than in singles. This is reasonable since it is only weakly fed by two γ transitions and β^+.

[b]This transition appears weakly in the gated spectrum.

[c]From Eu^{145} decay.

[d]This peak is very weak in the 511-511-keV spectrum.

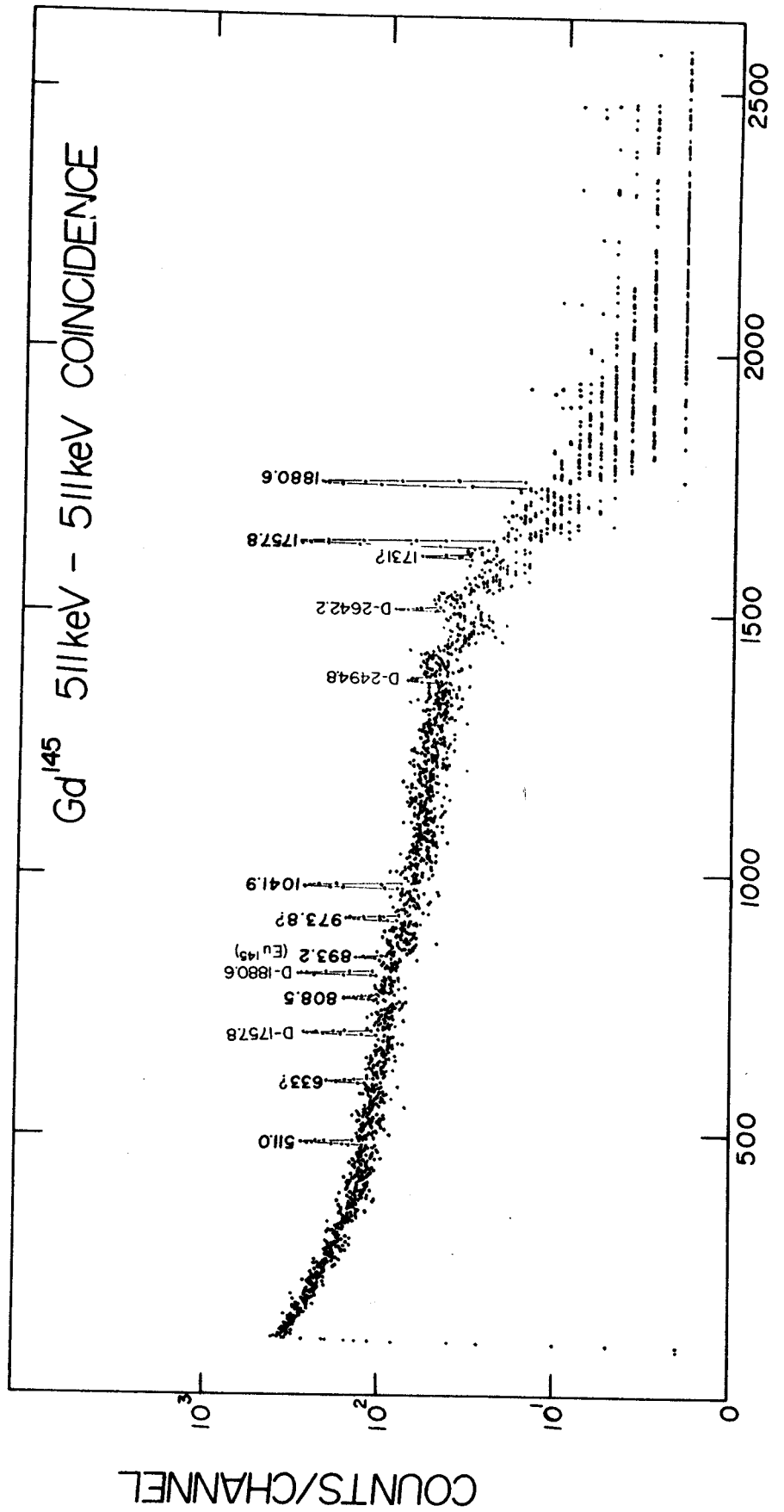

Figure 33. Gd^{145g} coincidence spectrum gated on 511-511-keV.

of the β^+ feedings extracted from this experiment is deferred until §4.3.5., where they are presented in Table 16.

4.3.3.C. Half-Life Determination for Gd^{145g}. The half-life of Gd^{145g} was determined by following the net peak areas of the 1757.8- and 1880.6-keV peaks as a function of time. We used a 50-MHz ADC interfaced to the MSU Cyclotron Laboratory Sigma-7 computer for this experiment. A code called GEORGE (GEOR) allowed us to take data, have a live display on an 11-in. scope, and dump the displayed data onto the computed disc at precise intervals that were determined at the beginning of the run. The sequence of events: count for the predetermined length of time, stop the counting, dump the spectrum onto the disc, erase the memory and begin counting again. The entire dumping process takes significantly less than 1 sec. The spectra can be punched on cards later as they are removed from the disc, thereby making the start and stop times of data acquistion independent of the card punching time. A pulser peak was included in each spectrum so that dead-time corrections could be properly applied to the data. In this manner the half-life can be measured independently for any or all of the peaks in the entire spectrum.

Forty consecutive spectra were obtained for each of the two peaks at 1757.8 and 1880.6 keV, each one representing a 2-minute time span. After background subtraction and dead-time corrections the points were least-squared to straight lines (semilog). From an

average of these calculations we determined the half-life of Gd^{145g} to be 21.8±0.6 minutes, to be compared with the less precise value of 25 minutes obtained by Grover (GRO59). Figure 34 shows the half-life curve obtained by observing the decay of the 1757.8-keV peak in one series of spectra.

4.3.4. Proposed Decay Scheme

Our proposed decay scheme for Gd^{145g} is shown in Figure 35. It is larely in agreement with the level scheme proposed by Newman, et al (New70), the main differences being our omission of their proposed levels at 2112.0, 2662.5, and 3167.2 keV and our addition of nine new levels at 953.4, 1567.3, 2203.3, 2642.2, 3236.0, 3259.6, 3285.6, 3623.8, and 4411.3 keV. Of the 38 γ rays listed in Table 13, 26 have been placed in the decay scheme accounting for over 97% of the total γ-ray intensity. It is entirely possible that many of the remaining γ rays proceed from levels that decay via single transition. These γ rays were all too weak to have been seen in any of our coincidence work, so, with no further evidence for their placement, we have omitted them entirely.

The assigned spins and parities, discussed in §4.3.5., represent a combination of deductions from our work and also the conclusions of Newman, et al., for the states observed via the $Sm^{141}(\tau,d)Eu^{145}$ reaction. The results of the two studies are in good agreement for most states. We calculated (see §4.1.4.) the total ε-decay to be $\simeq$ 5 MeV. The β^+/ε ratios displayed on Figure 35

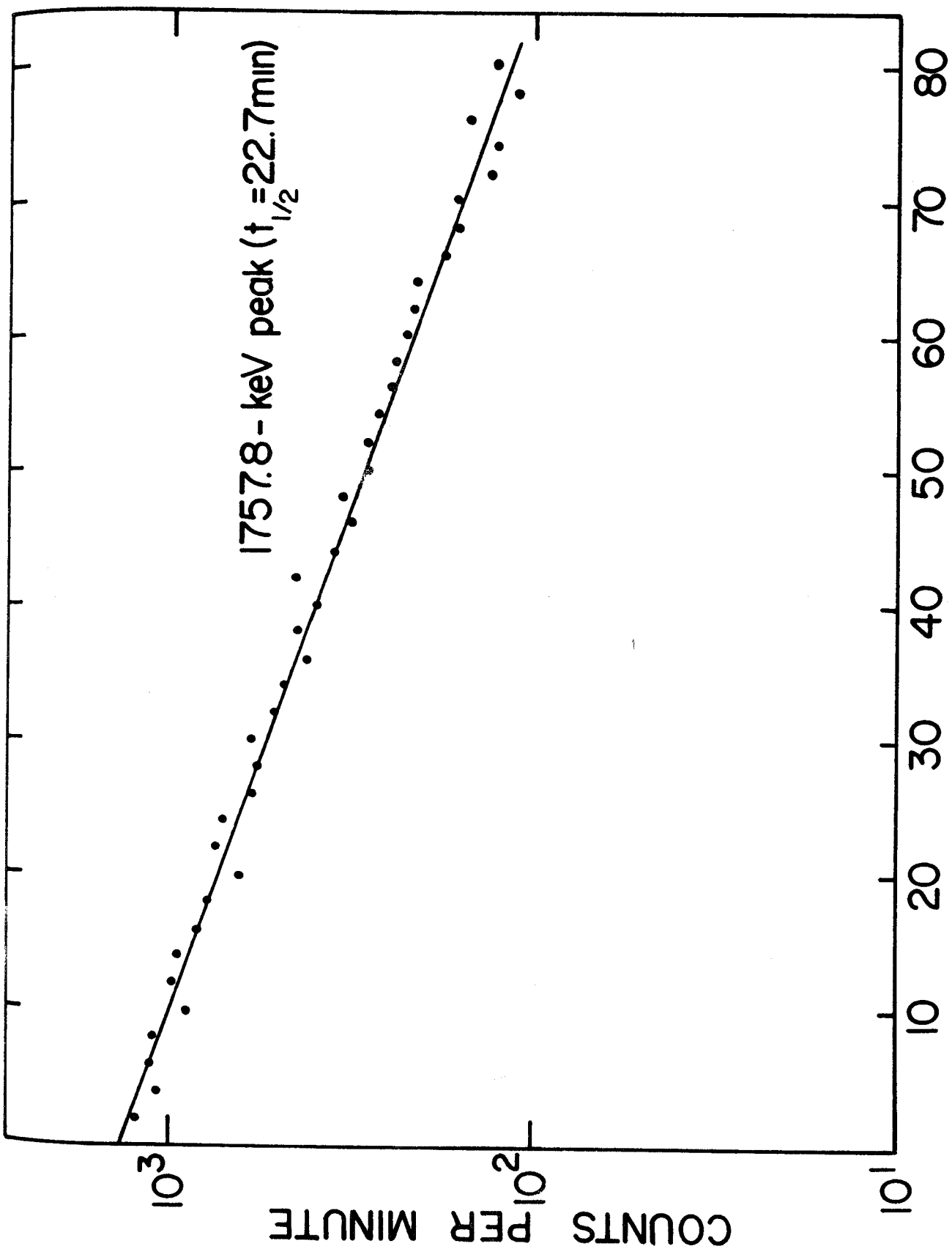

Figure 34. Half-life curve for Gd^{145g}.

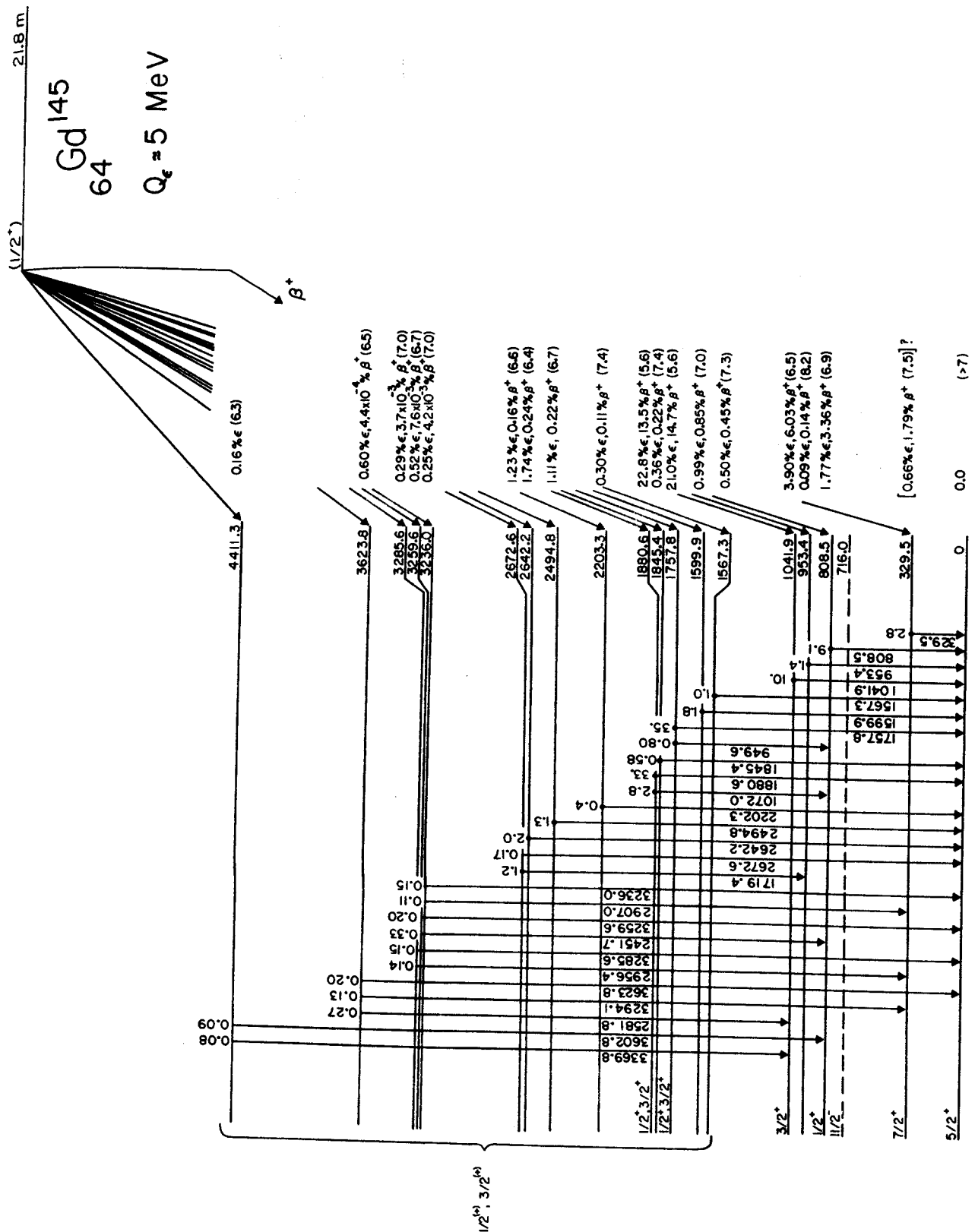

Figure 35. Decay scheme for Gd^{145}.

are calculated values using the methods of Zweifel (Zwei57). We shall see later (cf. Table 16) that our experimentally deduced ratios for some of the more hindered transitions do not agree with these values. However, we do not have experimental values for many of the states, and to be consistent we have used the calculated values. This does not alter any significant conclusions presented on the decay scheme.

The relative γ-ray intensities listed in Tabele 13 were based on a value of 100 for the 808.5-keV γ. The relative x-ray intensity was not measured. Thus, the intensities given on the decay scheme are based on the assumption that there is no direct β decay to the $Eu^{145}(d_{5/2})$ ground state. This seems to be a good assumption in several respects. First, in light of good evidence (§4.2 and New70) for the ground state of Gd^{145} being predominantly an $s_{1/2}$ state, a direct transition to the Eu^{145} ground state would be a second-forbidden transition. Also, Newman, et al., determined that the ≈25-minute component of the $\gamma^{\pm}$ could be accounted for by assuming no β^+ decay to the ground state, based on the β^+/K x-ray value of 0.6 obtained by Grover.

Specific evidence for the placement of levels and transitions in the decay scheme is given as follows:

Ground, 329.5-, 716.0-, 808.5-, and 1041.9-keV States. These states were all populated strongly by the $Sm^{144}(\tau,d)Gd^{145}$ reaction and appear to be essentially single-particle states, viz., the $d_{5/2}$, $g_{7/2}$, $h_{11/2}$, $s_{1/2}$, and $d_{3/2}$ in that order. We also see

specific evidence for the 329.5-, 808.5-, and 1041.9-keV levels. The 716.0-keV state is the $\pi h_{11/2}$ isomeric state, which is not populated by the decay of Gd^{145m} but is populated by the decay (§4.2) of Gd^{145g}.

As seen in the integral coincidence spectra of Figure 31, the $\gamma^{\pm}$ Compton background peaks near the 329.5-keV γ, so no reliable information can be obtained from a gate on this γ ray. That it is indeed involved in cascades is indicated by the anticoincidence spectrum (Figure 30), where its intensity is diminished. The four transitions into the 329.5-keV state were placed strictly on the basis of energy differences. From the intensity balances, we deduce that the 329.5-keV state receives 0.55% ε and 1.5% β^+ feeding. Also, the $\gamma^{\pm}$ coincidence spectrum (Figure 33) shows the 329.5-keV γ. However, this much β^+/ε feeding implies a log ft of 7.5, which is much lower than reasonable considering that the transition to this state would most likely be a $1/2^+ \rightarrow 7/2^+$, i.e., second forbidden, transition. And, although the 329.5 lies in a particularily bad place for a precise intensity determination, we do not think that our intensity value (or that of Newman, et al.) can be wrong enough to give us this low log ft value artificially. In addition, although we could have missed placing several γ rays that feed into the 329.5-keV level from above, the overall intensity of the unplaced γ rays is rather small, so it would be difficult to alter the intensity balance by placing them. We are left with a β^+/ε feeding that we do not

believe but cannot explain away easily.

The placement of the 808.5-keV γ as proceeding from a level of the same energy is consistent with our coincidence and anticoincidence data. The 949.6- and 1072.0-keV γ's can be seen to be in coincidence with the 808.5-keV γ in Figure 31. The 2451.7- and 3602.8-keV γ's are too weak to be picked up in our coincidence spectra and were placed purely by energy differences. As we shall see in §4.3.5, the 808.5-keV state is a $1/2^+$ state, which is consistent with its depopulating only to the ground state. The log *ft* of 6.9 is somewhat high for an allowed transition, but it falls within a reasonable range, and we shall see that the transition involved a multi-particle rearrangement, so it would be expected to be slow.

The 1041.9-keV γ can also be seen to be a ground-state transition, as it is enhanced in the anticoincidence spectrum. There are no strong coincidences in the 1041.9-keV gated spectrum (Figure 31), again suggesting direct decay to the ground state. The 2581.8- and 3369.8-keV γ's, too weak to be seen in our coincidence spectra, were placed solely on the basis of energy differences. The log *ft* for β^+/ε population of the 1041.9-keV state is quite in line with an allowed transition, consistent with the assignment of this state as $3/2^+$ by Newman, et al.

1757.8- and 1880.6-keV States. The two intense γ rays at 1757.8 and 1880.6 keV dominate the entire Gd^{145g} γ-ray spectrum. They are enhanced in the anticoincidence spectrum and depressed in

the integral coincidence spectra, and the spectra gated on them (Figures 31 and 32) show nothing other than $\gamma^{\pm}$. Thus, they are well established as ground-state transitions from levels having the same energies. Further, the 808.5-keV gated spectrum showed that each of these two states decays additionally through the 808.5-keV level. Together, these two states receive 71.9% of the total β^+/ε population from Gd^{145g}. The low log ft (5.6 for each) values certainly suggest allowed transitions, and, assuming the $1/2^+$ ground state assignment for Gd^{145g}, this means that the states are $1/2^+$ or $3/2^+$. This is consistent both with their decaying directly to the ground state and through the $1/2^+$ 808.5-keV state. The 1757.8-keV state appears to be excited only slightly in the $Sm^{144}(\tau,d)Gd^{145g}$ reaction (New70) and it is not clear whether the 1880.6-keV state is excited or not (it falls too close to the peak from the 1843-keV state). Needless to say, neither state appears to be simple in structure, and we shall explain both of them as three-quasiparticle states in the next section.

953.4- and 2672.6-keV Levels. These levels were placed on the basis of moderately convincing, although by no means airtight, coincidence results. Both the 953.4- and the 1719.4-keV γ's were enhanced in the integral coincidence spectra, neither was enhanced in the anticoincidence spectrum, and neither could be detected in the pair spectrum, implying that β^+ feeding could not account for their appearance in the coincidence spectra. Unfortunately, both are weak enough that the gated spectrum on the 949.6-953.4-

keV region proved inconclusive. Additionally, the sum, 953.4 + 1719.4 = 2672.8 keV, so we place levels at 953.4 and 2672.6 keV, the order of the two transitions being chosen because of their relative intensities.

1567.3-, 1599.9-, 1845.4-, 2203.3-, 2494.8- and 2642.2-keV Levels. These levels were placed on the basis of their respective ground-state transitions being enhanced in the anticoincidence spectrum. Newman, et al., also observed states at 1843 and 2480 (doublet) keV excited by the (τ,d) reaction.

The Remaining Levels: 3236.0, 3259.6, 3285.6, 3623.8, and 4411.3 keV. Because of the weakness of the γ rays, no coincidence data of any significance could be obtained above the line at 2642.2 keV. Thus, these four levels had to be placed solely on the basis of sums and must be considered as tentative. Under "normal" circumstances we would not venture to suggest levels on just this basis, but here there are mitigating circumstances. First, the precision of the sums is quite good, considering the energies and intensities involved: 0.5, 0.6, 0.3, 0.2 and 0.5 keV for the five levels, respectively. Second, the states are spaced rather widely apart in the nucleus with the γ rays having reasonably disparate energies. In addition, each level does account for at least two γ transitions to lower, well founded levels. Such would tend to make accidental agreements less probable than under normal circumstances; yet it must be remembered that these are by no means random numbers, and there may be some subtle, insidious relations not recognized. Thus, bear in mind: Tentative.

4.3.5. Discussion.

Some twenty states have now been placed, with varying degrees of confidence, in Eu^{145}. In some respects, then this nucleus finds itself among the better known members of the $N = 82$ series. All five major proton orbits between $Z = 50$ and 82 lie reasonably close together, resulting in relatively low-lying single-particle states that are not so fragmented as in the lighter $N = 82$ isotones. Also, the peculiar decay properties of Gd^{145g} give us some information about what appear to be three-quasiparticle states.

4.3.5.A. Single-Particle States. The five states at 0, 329.5, 716.0, 808.5 and 1041.9 keV comprize the major components of all of the single-proton orbits between $Z = 50$ and 82, viz., $d_{5/2}$, $g_{7/2}$, $h_{11/2}$, $s_{1/2}$ and $d_{3/2}$, respectively. This was amply demonstrated by Newman, et al. (New70), in their (τ,d) scattering reaction, where their spectroscopic factors indicated precisely the occupations expected for adding a proton to a $Z = 62$ nucleus.

The $5/2^+$ nature of the ground state is also corroborated by the decay properties (Adam68a) of Eu^{145} itself. The primary component of its wave function appears to be just what one might expect from a simple shell-model picture, $(\pi g_{7/2})^8 (\pi d_{5/2})^5$ above the closed $Z = 50$ shell. Note, now, that there is little or no β^+/ε decay ($\log ft \geq 7$) from the Gd^{145g} to this $\pi d_{5/2}$ ground state. Herein lies the first half of the Gd^{145g} "strange case", for both Nd^{141g} and Sm^{143g} decay (Bee68) quite readily ($\log ft \simeq 5.3$) to the $\pi d_{3/2}$

ground states of their respective daughters, in simple shell model terms this decay being $(\pi g_{7/2})^8(\pi d_{5/2})^2(\nu d_{3/2})^{-1} \rightarrow (\pi g_{7/2})^8(\pi\ _{5/2})$ for Nd^{141g} and $(\pi g_{7/2})^8(\pi d_{5/2})^4(\nu d_{3/2})^{-1} \rightarrow (\pi g_{7/2})^8(\pi d_{5/2})^3$ for Sm^{143g}. There are many ways in which one could explain away a milder retardation of the Gd^{145g} decay to the Eu^{145} ground state, but the only reasonable explanation that we find for the experimental fact (hindered by at least a factor of 100 and probably much more) is that the ground state of Gd^{145} is not a $(\nu d_{3/2})^{-1}$ state but instead a $(\nu s_{1/2})^{-1}$ state. Newman, et al., also came to this conclusion. Some reasonable indirect evidence for this is available, viz., the $(\nu s_{1/2})^{-1}$ state does progress to lower energies with increasing Z in the N=81 nuclei: it lies at 281 keV (Bir63) in Ba^{137}, at 250 keV (Bir63 and Yap70) in Ce^{139}, and at 195 keV (Wild70) in the Nd^{141}. Thus, it might be expected to have replaced the $(\nu d_{3/2})^{-1}$ state by Gd^{145}. However, in our study (§ 4.2.) of Gd^{145m} we were neither able to confirm nor to deny this. Thus, it must be admitted that there is only indirect for this $s_{1/2}$ assignment, but more will be said about it in the next section.

The $(\pi g_{7/2})^{-1}$ state (actually a $(\pi g_{7/2})^7(d_{5/2})^{2n}$...state - more about the dots and the pairing force in the next section) at 329.5 keV is well-established, but, quite surprisingly, it may receive a small amount of β^+/ε population, with the log ft being ≈7.5. Actually, we do not believe this, and, considering the uncertainty in the intensity of the 329.5-keV γ because of its position in the spectrum, perhaps most of the feedings can be attributed to experimental difficulties. The results, however, are duly recorded on Figure 35.

As expected the $h_{11/2}$ state at 716.0 keV is not populated by Gd^{145g} decay, although we noted (§4.2.) its being populated directly by 4.7% the Gd^{145m} decays. The log ft was found to be 6.2. The fact that such a direct decay takes place implies some population of the $h_{11/2}$ orbit by proton pairs in Gd^{145}. This, as we shall see in the next section, is the second clue toward explaining the "strange case" of Gd^{145g}.

The β^+/ε decay to the $s_{1/2}$ 808.5- and $d_{3/2}$ 1041.9-keV states, with respective log ft's of 6.9 and 6.5, appear to be allowed transitions. However, note that these are somwhat high log ft values for allowed transitions especially, when compared with the log ft's for decay to the 1757.8- and 1880.6-keV states. The implication could be that they are not altogether straightforward transitions. Also, as can be seen in Table 16, the $\varepsilon(tot)/\beta^+$ ratios for decay to these states are large compared with the predicted (Zwei57) ratios for straightforward allowed transitions. Often such squelching of the β^+ branch is also indicative of complexities in the decay process. This, then, is the third clue.

4.3.5.B. Three-Quasiparticle States

The fourth and most obvious clue, of course, is the strong decay of Gd^{145g} to the states at 1757.8 and 1880.6 keV. These two states account for 72% of the Gd^{145g} decay, and the low log ft's, both 5.6, clearly indicate non-hindered allowed transitions. Now, the state at ≈1757 keV populated by an ℓ=2 transfer (transfer (implying $I^{\pi}= 3/2^+$) in the (τ,d) experiment of Newman, et al., may

or may not be the same as the 1757.8-keV state populated by Gd^{145g} decay. In any event, the extracted spectroscopic factor (C^2S) was only 0.02, indicating the structure of that state to be more complicated (or at least different) that what could be attained by a simple dropping of a proton into a vacant or semi-vacant Sm^{144} orbit. The 1880.6-keV state may or may not have been populated (Wild70) (cf. Fig. 3 of New70) in the (τ,d) experiment, but if populated at all it was only to the slightest extent. Also, in their shell-model calculations using a very truncated basis set (proton states above considered, $g_{7/2}$ and $d_{5/2}$ orbits deginerate and occupied by pairs, and the only allowed states resulting from the single odd proton moving from orbit to orbit with or without the breaking of a single additional pair, but never more than one proton to be promoted into the $h_{11/2}$, $s_{1/2}$, or $d_{3/2}$ orbit region), Newman, et al., were unable to construct states corresponding to the 1757.8- and 1880.6-keV states. Our inference here is that perhaps these states involve the promotion of more than one proton into the $h_{11/2}$, $s_{1/2}$, and $d_{3/2}$ region or, considering that they lie well above the pairing gap, they involve broken neutron pairs.

We have arrived at a simple shell-model picture that, qualitatively at least, explains all four clues, or effects, quite well: 1) no β^+/ε population ot the Eu^{145} ground state, 2) some direct population of the 716.0-keV state by Gd^{145m}, 3) hindered transitions to the $s_{1/2}$ and $d_{3/2}$ states, and 4) fast transitions to the 1757.8- and 1880.6-keV states - meaning that these last go by

major components of the wave functions and not minor admixtures. Our model is outlined in stylized form in Figure 36 and involves two assumptions: 1) the ground state of Gd^{145} is indeed a $(\nu s_{1/2})^{-1}$ state and 2) there is appreciable population of the $h_{11/2}$ orbit by proton pairs in both Gd^{145g} and Gd^{145m}. Both have already been implicitly discussed and 2) has been directly proven by the population of the 716.0-keV $h_{11/2}$ state by Gd^{145m} (cf. the appropriate transition in Figure 36). [Also, compare the rapid drop in positon of the $h_{11/2}$ state from 1.1 MeV in Pr^{141} to 716.0 keV in Eu^{145}. It should lie even lower in Gd^{145}, and the pairing force should insure its partial occupation simply by virtue of its large degeneracy.]

Lack of appreciable population to the Eu^{145} ground state comes about naturally if Gd^{145g} is $(\nu s_{1/2})^{-1}$. Protons in the occupied orbits, $g_{7/2}$, $d_{5/2}$, and to some extent $h_{11/2}$, should have little tendency to transform into an $s_{1/2}$ neutron. Even the most favorable case, $\pi d_{5/2} \rightarrow \nu s_{1/2}$, should be slow.

Now, there are well-documented cases of β^+/ε decay into high-lying three-quasiparticle states from the nearly nuclei Nd^{139m} (Bee68 and McH69a) and Sm^{141m} (§4.5), both of which follow quite straightforwardly from simple shell-model considerations. Looking about for analogons transitions in the present case, one is immediately struck by the availability of the $\nu h_{9/2}$ orbit - by a crude extrapolation from the lead-bismuth region we would predict it to lie some 1.5-2.5 MeV higher than the $s_{1/2}$ or $d_{3/2}$ orbits. Thus, the primary decay of Gd^{145g} can be represented as $\pi h_{11/2} \rightarrow \nu h_{9/2}$, or more

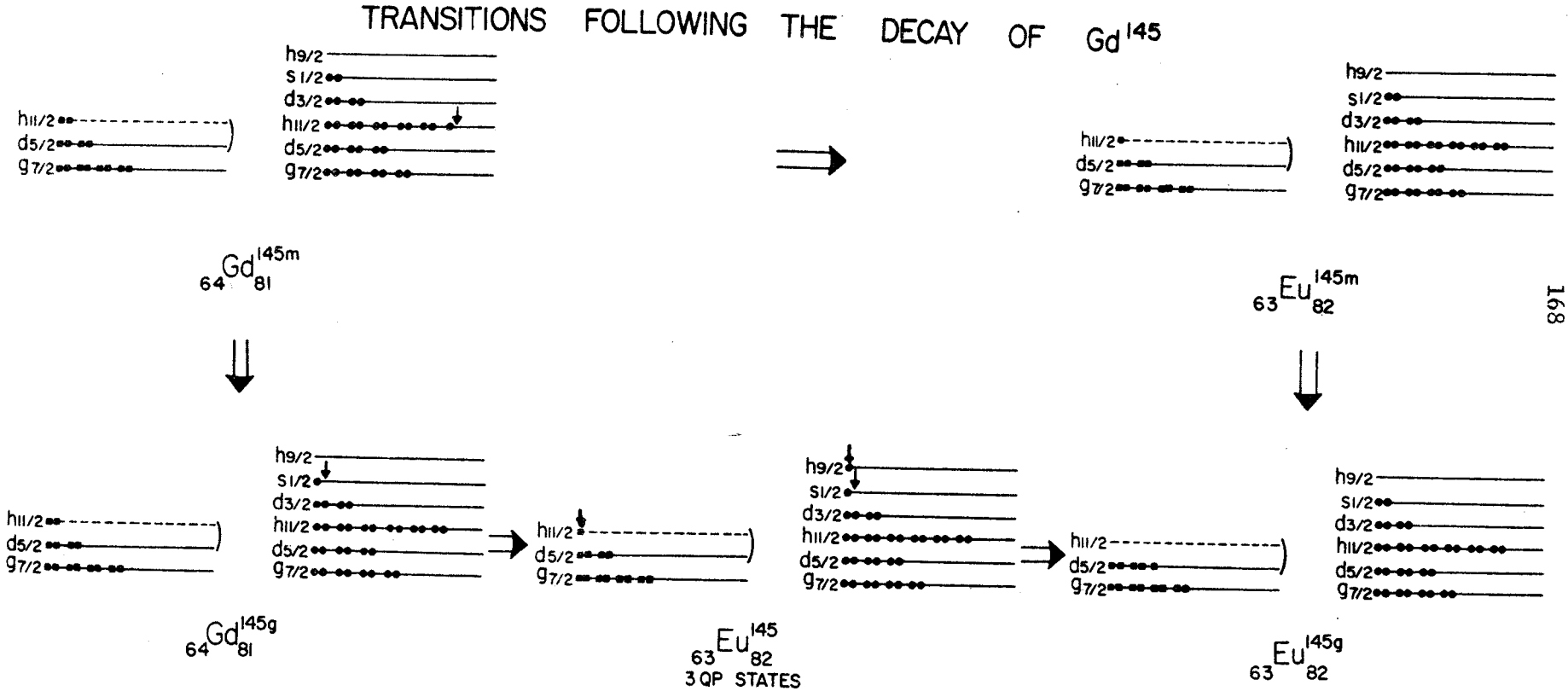

Figure 36. Schematic representation for transitions between states in Gd^{145} and Eu^{145}.

completely, $(\pi h_{11/2})^{2n}(\nu s_{1/2})^{-1} \rightarrow (\pi h_{11/2})^{2n-1}(\nu h_{9/2})(\nu s_{1/2})^{-1}$. This would make the 1757.8- and 1880.6-keV states three-quasiparticle states having the primary configuration, $(\pi h_{11/2})(\nu h_{9/2})(\nu s_{1/2})^{-1}$.

This model also explains the hindrance of the β^+/ϵ decay to the 808.5- $(s_{1/2})$ and 1041.9-keV $(d_{3/2})$ states in Eu^{145}. Each would require, in addition to the unfavorable transformation of a proton into an $s_{1/2}$ neutron, a promotion of the remaining proton into a higher orbit. Thus, these transitions probably proceed primarily through admixtures.

Appealing though it be, this explanation must at this time remain a hypothesis, for we have no direct proof of 1) the $(\nu s_{1/2})^{-1}$ nature of Gd^{145g} and 2) the fact that it is specifically the $\nu h_{9/2}$ orbit that participates in the three-quasiparticle states. Information would be useful concerning Dy^{147m+g}, the next member of the series, but it is far enough from stability to present formidable preparation difficulties (§4.5.). The same is true for Tb^{145}, which could populate states in Gd^{145}. Perhaps more promising would be the study of Gd^{145} states via the $Sm^{144}(\tau,2n\gamma)$ reaction.

4.3.5.C. The Remaining States.

Relatively little can be deduced about the remaining states at this time. The 953.4-keV state is anybodys guess. Although placed by reasonably convincing coincidence data, we have no clues as to its structure. The remaining states are all populated by transitions having log *ft*'s in the range of allowed or fast first-forbidden transitions. Thus, they are all probably 1/2 or 3/2 states, with the majority having even parity. One word about the 1599.9-keV state:

We observe its being populated by Gd^{145g} decay, which implies a 1/2 or 3/2 assignment. This is incompatible with the $7/2^+$ assignment made by Newman, et al., but they consider the statistics in their angular distribution for this state to be poor enough to make that assignment somewhat questionable.

4.3.5.D. ε/β^+ Ratios.

From our $\gamma^{\pm}$ gated spectrum (Figure 33) we obtained relative β^+ feedings to seven of the Eu^{145} states. The deduced ε/β^+ ratios for the transitions to these states are listed in Table 16, where they are compared with the theoretical ratios calculated by Zweifel's methods (Zwei57). We normalized the experimental values on the transition to the 1757.8-keV state, which we think is one of the two most straightforward transitions in the entire decay scheme. (If one normalizes to, say, the 808.5-keV state, then the β^+ feeding to the other states quickly exceeds 100%.) It can be seen that the ε/β^+ ratio appears to be a fairly sensitive test of the degree of hindrance of a transition, for it does not take much to depress the β^+ feeding per se. Unfortunately, the entire theoretical consideration of ε/β^+ ratios vs forbiddeness needs serious overhauling, so little can be said in a quantitative sense at this time.

Table 16. Comparison of Experimental and Theoretical $\varepsilon(tot)/\beta^+$ Ratios for Decay to States in Eu^{145}.

Energy[a] (keV)	$\varepsilon(tot)/\beta^+$	
	Experimental	Theoretical[b]
808.5	11	0.36
1041.9	1.6	0.65
1599.9	19	1.2
1757.8	≡1.4[c]	1.4
1880.6	1.7	1.7
2494.8	5.0	5.0
2642.2	12	7.1

[a]These are the only states in Eu^{145} that are measurably fed by β^+, as determined from the $\gamma^{\pm}$ gated coincidence spectrum.

[b]These values are anly as precise as can be read from the graphs in Ref. (TI67).

[c]The experimental ratios were normalized to the theoretical ratios by assuming that the transition to the 1757.8-keV states is allowed and unhindered, presumably yielding the expected ratio.

4.4. The Decay of Sm^{141m} and Sm^{141g}.

4.4.1. Introduction

Our interest in the decay of Sm^{141} was stimulated by the investigation of the decay of Nd^{139m} (Bee69d) which was carried out here at MSU. Six levels in Pr^{139} at relatively high energies are selectively populated by the isomeric decay of Nd^{139}. These levels have been characterized as three-quasiparticle excitations which decay predominantly to the $h_{11/2}$ state in Pr^{139}. Work on this nucleus led to the prediction (McH69j) that other $N = 77$ or 79 nuclei (specifically Sm^{141m} and Nd^{137m}) might possess similar states. Quite specific and stringent requirements must be met for the population of this type of state. The parent nust contain a high spin, low energy isomeric level which decays predominently via an ε/β^+ branch. In addition, the decay energy must be sufficient for the population of levels above the pairing energy gap of the daughter nucleus.

Prior to the present investigation very little work had been done on Sm^{141}. In fact, prior to 1967 it is doubtful whether it had been observed at all. In 1957 an activity, reported as Sm^{141}, was assigned a half-life of 17.5 to 22 days (Pav57) and then in 1966 there was a report (Lad66) concluding that Sm^{141} must have a much shorter half-life and, in fact, was probably less than 3 days. Correct identification of the Sm^{141} species seems to have first been made correctly at about the same time by a German group and a Russian group (Bley67 and Arl67). Their results

are summarized in Table 17. The principle disagreement between our data and theirs is the half-life for Sm^{141g}. As will be discussed in §4.4.8, this half-life is still somewhat uncertain (being a choice between 10.0 and 11.3 minutes). Our half-life value of 22.1 minutes for the Sm^{141m} decay is consistent with these other recently reported values. Hesse, in a more recent and more complete article(Hess69) on Sm^{141m}, has reported 32 γ rays as belonging to the decay of this species. These results are compared with ours in §4.4.4.

We have indeed found the decay of Sm^{141m} to exhibit similar characteristics to Nd^{139m}. Sm^{141m} seems also to have 6 states which have log ft values (average = 6.1) consistent with their being fed by allowed β transitions. Also, these states decay predominently through the 628.6-keV state which has been identified as the $h_{11/2}$. These states will be discussed in §4.4.11 in the light of what is known about three-quasiparticle states.

Table 17. Published Data for Sm^{141}

Authors	Half-life for Sm^{141m}	Half-life for Sm^{141g}	%M4[a] Transition	E_γ for M4
(Arl67)	21.5 min.	<10 min.	-	215 keV
(Bley67)	23.5 min	≈ 2 min.	<1%	≈ 200 keV

[a] Estimated Values

4.4.2. Source Preparation

The principle means of producing Sm^{141} has been by the $Nd^{142}(He^3,4n)Sm^{141}$ reaction (Q= -27.3 MeV), although Sm^{141} has also been produced indirectly by the $Sm^{141}(p,4n)Eu^{141}$ reaction (Q= -31.2 MeV). This second reaction was used primarily for the purpose of enhancing the Sm^{141g} species and also as an additional verification that the 438.2-keV transition is not associated with the Sm^{141g} decay. The results via this reaciton will be discussed in § 4.4.9.

For the He^3 runs 25 mg targets of separated isotope $Nd_2^{142}O_3$ (>90% Nd^{142}) were bombarded with a beam energy of 35 MeV and a current of 0.1-1.0 μa. Targets were bombarded for periods of 1-5 minutes. For the proton runs, 40 MeV beams of 0.5 μa were used in one minute bombardments.

Due to the short half-life of both Sm^{141g} and Sm^{141m} (11.3 minutes and 22.1 minutes, respectively) no attempt was made to chemically separate these species from unwanted contaminents.

The primary means of determining which γ rays are associated with the decay of each of the Sm^{141} species was by comparison of relative intensities of the γ rays in four consecutive spectra, each of which represented a 15 minute counting interval with the first spectrum starting two minutes after the end of each bombardment. These 4096-channel spectra were obtained by use of a routing circuit. This method allowed us to keep the four quadrants in the Sigma-7 memory simultaneously with no necessity of dumping the data between spectra. This also allowed us to accumulate data from several targets in each of the quadrants. In general, it was relatively

easy to pick out the Sm^{141m} transitions by this method. However, the Sm^{141g} transitions, with the exception of the 403.9-keV transition, are quite weak and considerably more difficult to ascertain. These determinations were complicated by several factors. Due to to both activities having short half-lives, it was necessary to begin counting the target material quite soon after bombardment. Thus, other short-lived activities could not be kept out of the spectra. Also, Sm^{141m} and Sm^{141g} have half-lives which are so comparable it is difficult to obtain a spectrum of Sm^{141m} (having the longer half-life) by waiting for the Sm^{141g} to decay. It is difficult to obtain meaningful statistics for some of the weakest observable transitions - a particularly acute problem for any short half-life species studied by off-line techniques. Many cyclotron bombardments must be made to complete a given experiment, and a compromise must be reached between using unlimited cyclotron time and minimum acceptable statistics for the experiment. This meant, for example, that the Sm^{141} 2-dimension coincidence data show quite low statistics for the gated spectra. Another problem is that as solid state detectors become more efficient and exhibit ever improving resolution, many very weak peaks become noticeable in the spectra. Many are too weak to obtain a measure of their half-lives and cannot easily be assigned to a specific activity. Still another problem with short half-life studies in general is the problem of competing activities. As the desired reaction takes one farther and farther from beta stability, reactions competing with (p,xn) and (He^3,xn) become a problem. Reactions such

as (p,αxn) and (He^3,α xn) begin to contribute measurably to the product activities.

All of the above mentioned problems were encountered in the Sm^{141m+g} investigations.

4.4.3. Half-Life Determinations for Sm^{141m} and Sm^{141g}

The half-lives for both Sm^{141m} and Sm^{141g} were determined with the help of a computer code called GEORGE (GEOR). This code has been described previously in §4.2.2. A pulser peak was included in each spectrum for determination of the proper dead-time correction. The net peak areas, corrected for dead-time, resulting from the analysis of the spectra, were used in the usual manner for the half-life determinations. The Sm^{141m} half-life was determined independently from the 196.6-keV, 43.9-keV and the 538.5-keV peaks. Series of spectra were obtained at two minute time intervals. The results of one analysis, using the 196.6-keV peak, are shown in Figure 37. The data points obtained were least-square fitted to a straight line (on a semi-log plot) to obtain the half-life value. The results for each of the above mentioned peaks were averaged to arrive at the value of 22.1±0.3 minutes for the half-life of Sm^{141m}. The Sm^{141g} half-life was determined from the 403.9-keV peak only, since this is the only intense peak in the ground state spectrum. The results of one of the analyses is shown in Figure 38. These data points were obtained from spectra taken at one minute intervals. An average of the least-squared results yields a value of 11.3±0.3 minutes for the half-life of Sm^{141g}.

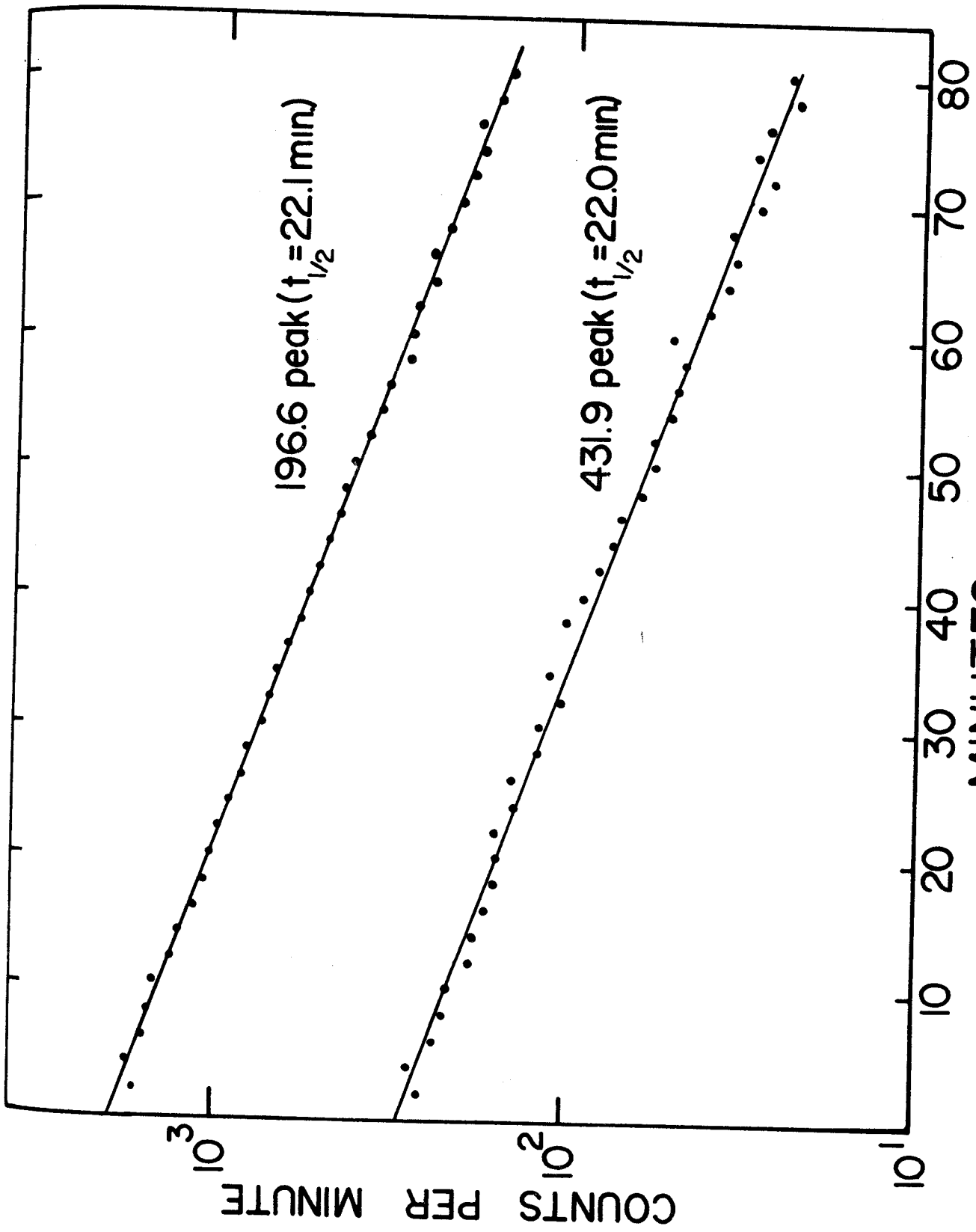

Figure 37. Half-life curves for Sm^{141m}.

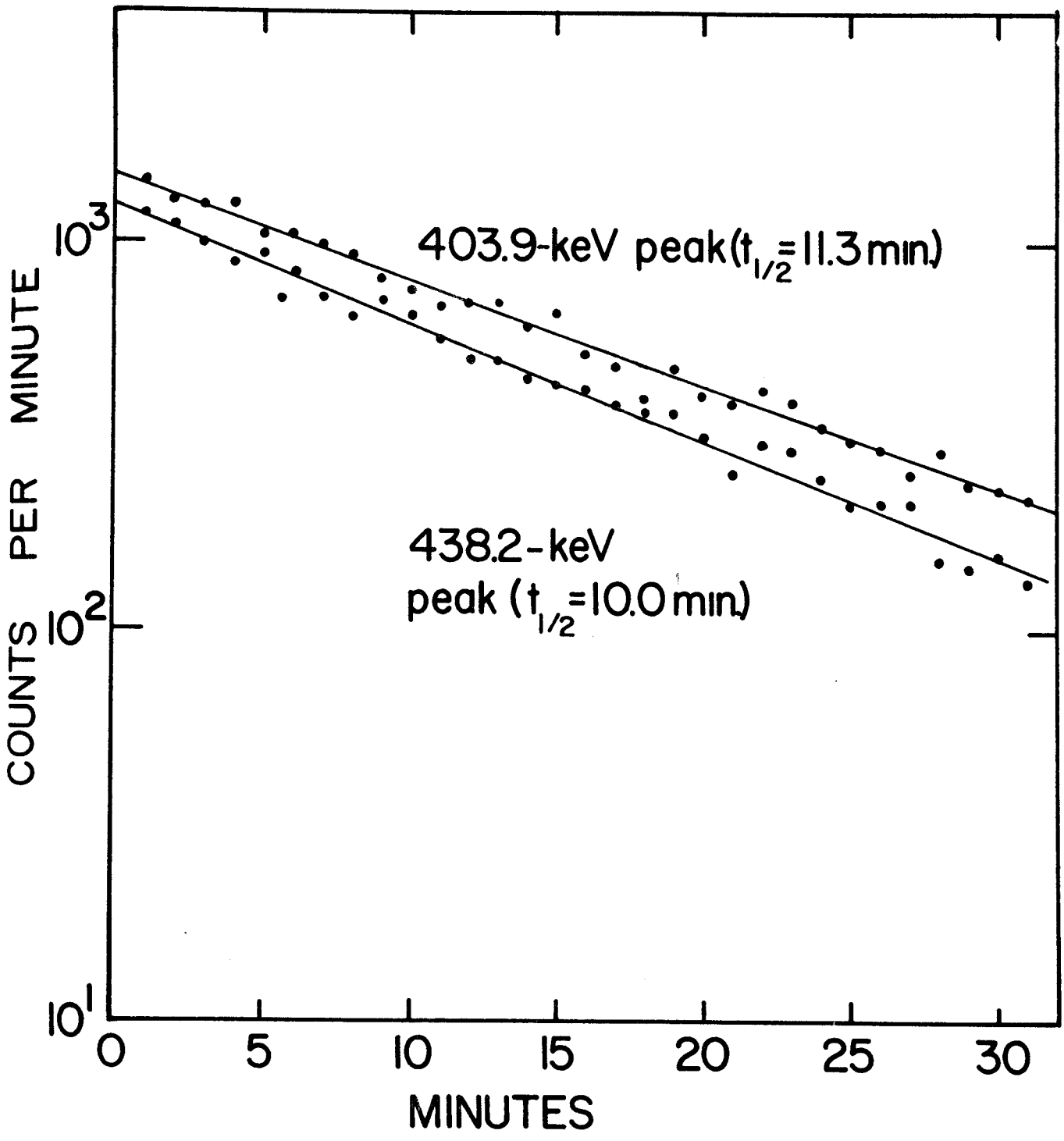

Figure 38. Half-life curves for the 403.9- and 438.2-keV peaks.

4.4.4. Sm^{141} γ-ray Spectra

4.4.4.A. Singles Spectra

The γ rays associated with the decay of Sm^{141m} were ascertained by their relative intensities in four 4096 channel spectra as described in § 4.4.2. These singles spectra were obtained with the 2.5% Ge(Li) detector as described in § 2.2.1. Figures 39 and 40 show the first and fourth of these spectra, respectively. Only the γ rays assigned to either Sm^{141m} or Sm^{141g} have energies shown on the figures. From their erratic intensity behavior many of the other peaks can be ruled out as belonging to Sm^{141}. These unclaimed γ rays are listed separately in § 4.4.12.

All of the data analysis was accomplished by use of either MOIRAE or SAMPO, both of which are described in § 3.1. γ-ray energies were determined from spectra taken by simultaneously counting with γ-ray standards which have been listed previously in Table 2. Various combinations of these standards were used in Sm^{141} spectra at different times and with different experimental setups. The centroids determined for the standard peaks were used to prepare energy calibration curves (generally quadratic) whereby energy determinations for the intense Sm^{141} peaks could be made. These intense peaks were then used as internal standards for the energy determinations for the remainder of the peaks in other spectra obtained in the absence of γ-ray standards.

Transition intensities were determined by correcting the net peak areas by use of detector efficiency curves which have been constructed for each detector.

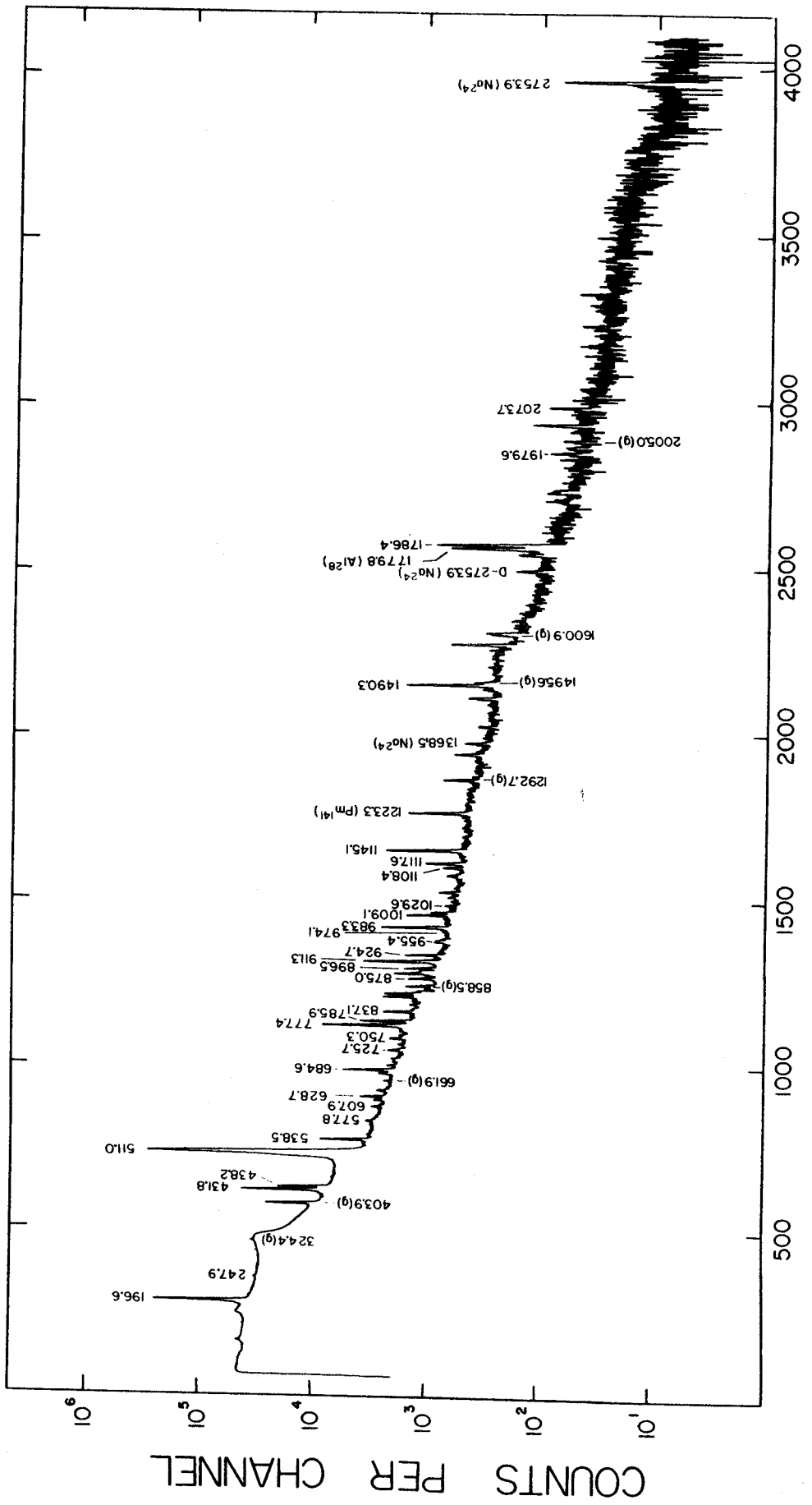

Figure 39. γ-ray singles spectrum for Sm^{141g+m} (Quad 1)

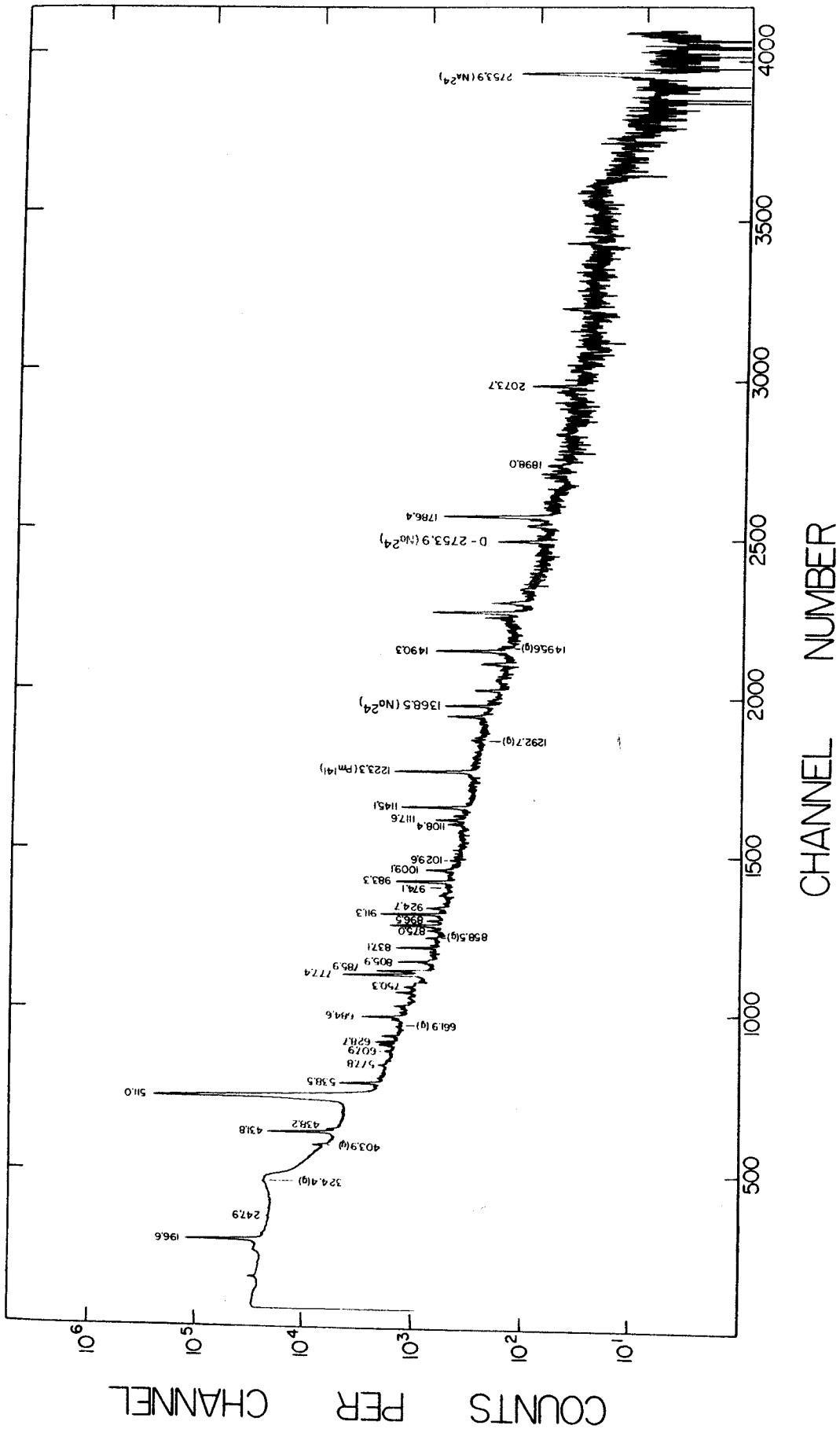

Figure 40. γ-ray singles spectrum for Sm^{141} (Quad 4)

By this technique we have assigned 32 γ rays as belonging to the decay of Sm^{141m}. The energies and relative intensities of these transitions are presented in Table 18 along with the recently published results by Hesse (Hess 69). These two sets of data are seen to be in substantial agreement with each other. We have included γ rays with energies of 247.9 keV, 577.8 keV, 607.9 keV, 955.4 keV, 974.1 keV, 1029.6 keV and 1108.4 keV which have not been reported by Hesse. Conversely, Hesse has reported γ rays with energies of 1136.6 keV, 1530.7 keV, 1879.9 keV, 1966.6 keV, 2281.1 keV, 2302.6 keV and 2582.3 keV which we do not include with the decay of Sm^{141m}. The 1136.6-keV, 1530.7-keV, 1966.6-keV, 2281.1-keV, 2302.6-keV and 2582.3-keV peaks do not show up in our spectra within the limits of our statistics. Therefore, we can say nothing about them. There is some question as to whether the reported 1879.0-keV peak is due to the daughter Pm^{141} activity.

4.4.4.B. Prompt Coincidence Spectra

Several types of prompt coincidence experiments have been carried out. These included 2-dimensional coincidence experiments, 511 keV coincidence experiments and anticoincidence experiments. More detail on the setup of these experiments is given in Chapter II.

The 2-dimensional coincidence experiments actually yield a 2-D (§ 2.1.D) array (4096×4096) of prompt coincidence events (2τ = 100 ns). For the Sm^{141} investigation, regions of the resulting x-axis integral spectrum were gated. All events in prompt coincidence (on the y-axis) with the events falling in the gate were assembled and output as a gated coincidence spectrum. Thus, the plots of the 2-dimensional coincidence data in Figure 41 show gated spectra

Table 18. Energies and Relative Intensities of γ Rays from the Decay of Sm^{141m}.

This Work		Hesse[a]	
Energy (keV)	Intensity	Energy (keV)	Intensity
196.6±0.3	184 ±18	196.5±0.5	260.±30
247.9±0.2	1.91±0.35		
431.8±0.1	100 ±5	431.7±0.5	100±10
538.5±0.3	20.9 ±1.4	538.0±0.5	18±5
577.8±0.3	2.24±0.60		
607.9±0.2	2.54±0.30		
628.7±0.1	6.62±0.20	628.3±0.5	6.8±1.0
684.6±0.2	19.6 ±1.5	684.2±0.5	21.8±2.6
725.7±0.5	3.59±0.60	726.3±0.7	9.9±1.7
750.3±0.3	3.94±0.60	749.5±0.8	4.6±1.0
777.4±0.3	50.3 ±2.0	777.1±0.5	58.2±7.0
785.9±0.1	16.9 ±1.0	785.8±0.5	20.7±2.5
805.9±0.1	8.80±1.6	806.0±0.6	10.8±1.6
837.1±0.2	8.87±0.30	836.7±0.7	11.5±3.0
875.0±0.1	3.09±0.10	874.6±0.7	4.6±1.0
896.5±0.1	3.59±0.40	896.2±0.7	5.6±1.5
911.3±0.3	22.8 ±0.60	911.1±0.5	26.5±3.5
924.7±0.1	5.67±0.80	924.4±0.7	6.9±1.3
955.4±0.5	1.67±0.10		
974.1±0.5	0.50±0.10		
983.3±0.3	18.0 ±0.80	982.9±0.5	21.6±3.5

Table 18, Continued.

This Work		Hesse[a]	
Energy (keV)	Intensity	Energy (keV)	Intensity
1009.1±0.4	7.23±0.60	1008.3±0.5	10.5±2.0
1029.6±0.6	1.25±0.30		
1108.4±0.2	3.07±0.25		
1117.6±0.2	8.04±0.60	1117.2±0.6	11.1±1.8
1145.1±0.2	21.6 ±0.80	1144.9±0.5	27.5±4.0
1463.4±0.6	4.47±0.80	1462.1±0.8	5.4±2.0
1490.3±0.1	22.9 ±1.5	1490.2±0.5	27.4±3.5
1786.4±0.4	27.1 ±1.10	1785.9±0.6	33.6±4.0
1898.0±1.0	0.94±0.15	1898.5±1.2	2.5±1.0
1979.6±0.2	0.99±0.12	1979.2±0.8	1.6±0.7
2073.7±0.2	3.53±1.2	2072.9±0.6	11.8±2.0
		1136.6[b]±0.8	5.2±1.5
		1530.7[b]±1.0	2±1
		1879.9[b]±0.8	6.3±1.5
		1966.9[b]±0.8	2.5±1.0
		2281.1[b]±1.0	1.5±0.5
		2302.6[b]±1.0	1.1±0.4
		2582.3[b]±1.0	2.9±0.8

[a] Ref (Hess 69).

[b] These transitions could not be identified in the present investigation.

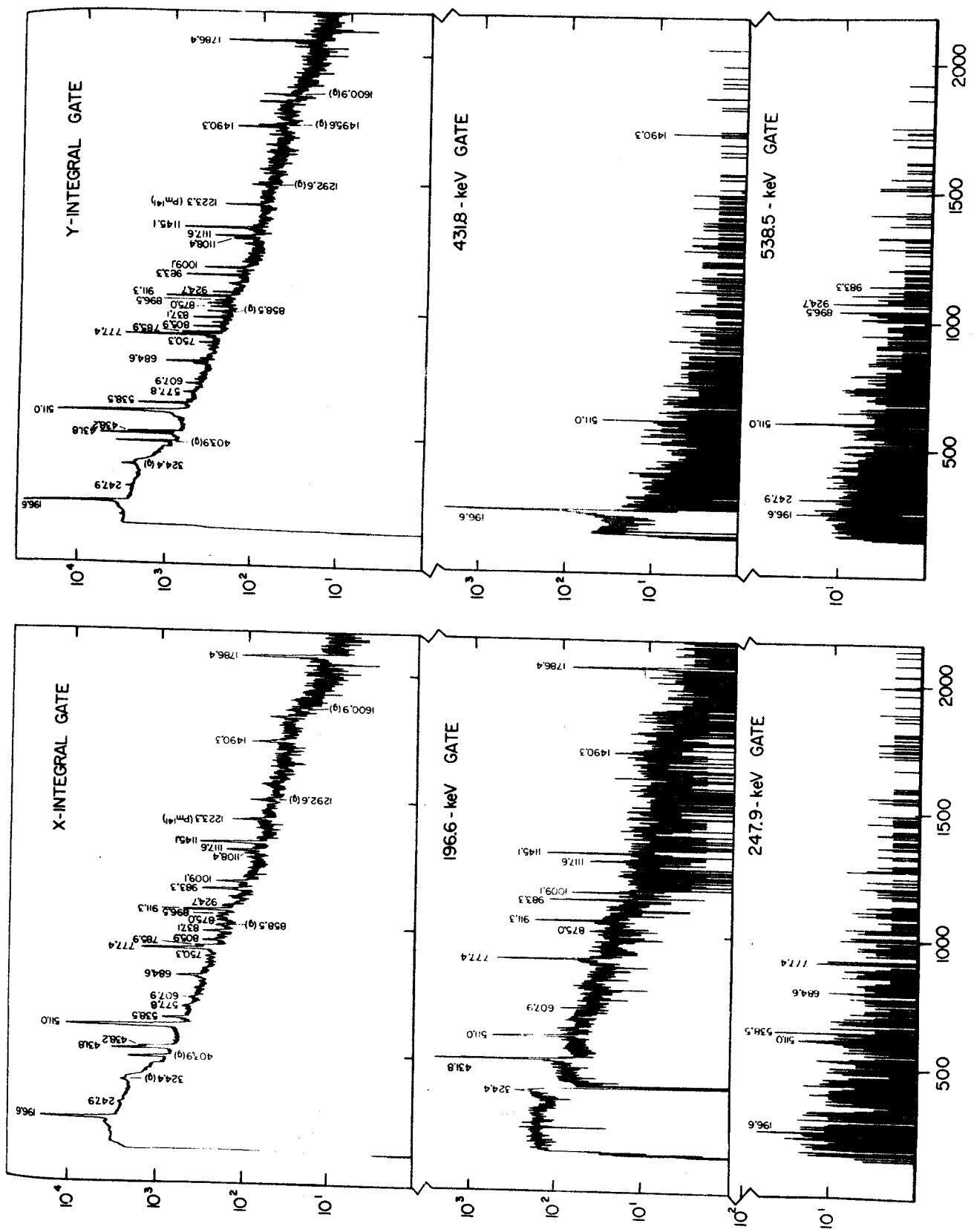

Figure 41. 2-dimensional coincidence spectra for Sm^{141m}.

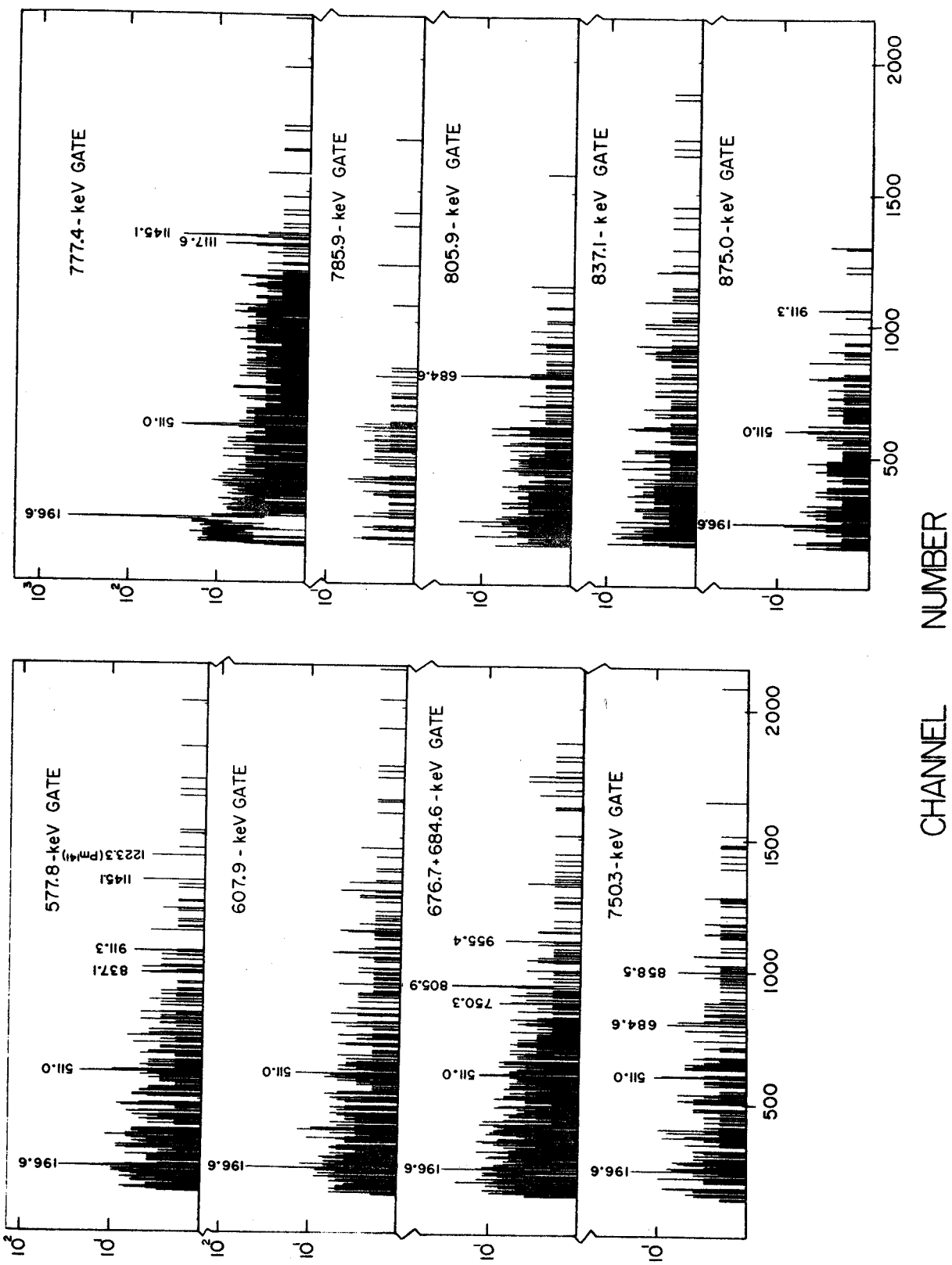

Figure 41. continued

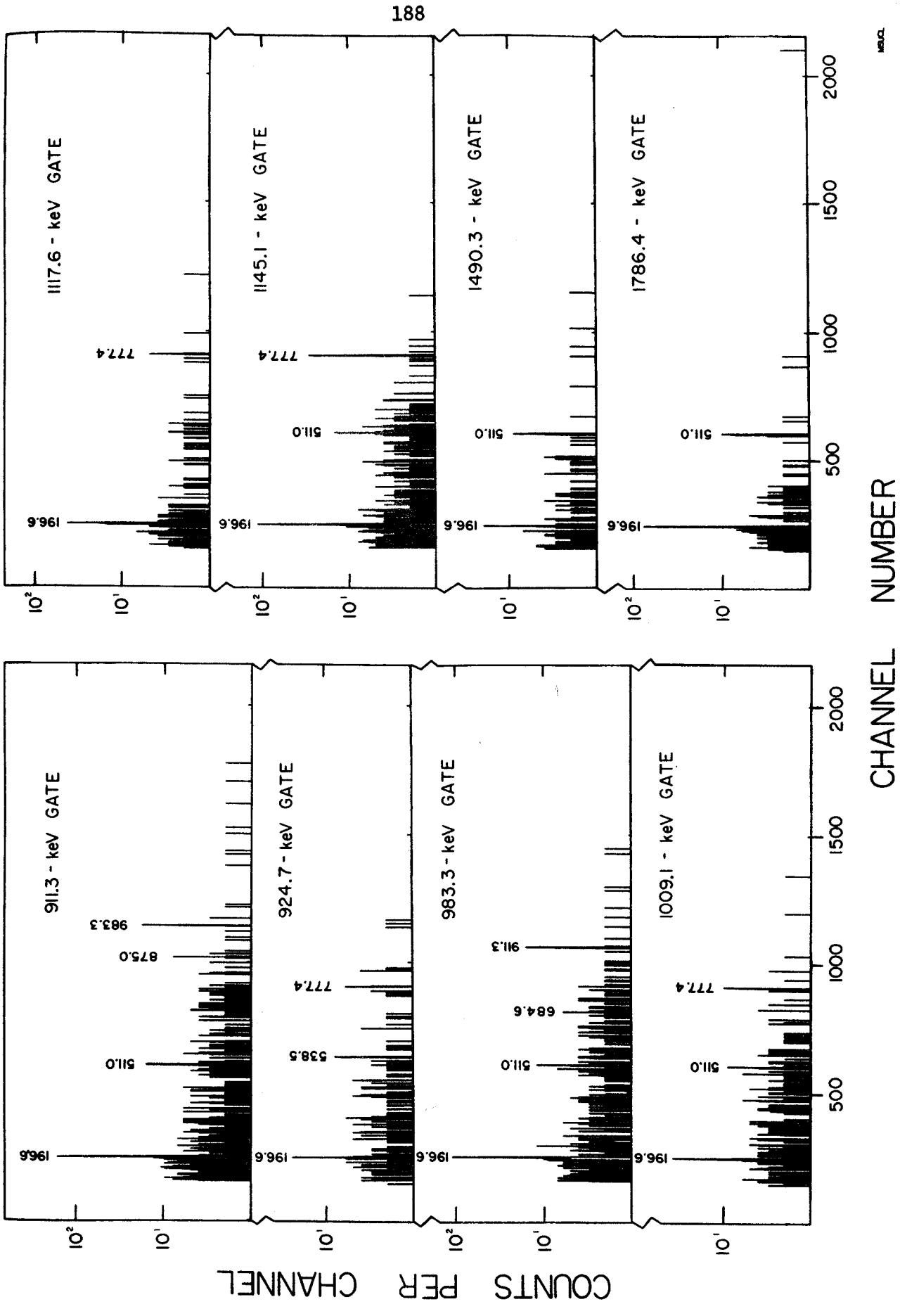

Figure 41. continued

resulting as subsets of the y-axis integral spectrum. In this figure the x-axis and y-axis integral spectra are shown in addition to 21 gated spectra. In spite of the low statistics exhibited by some of the gated spectra, much useful information has been gleaned from them. The implications of these spectra will be explored fully in §4.4.6.

The 511 keV-511 keV coincidence spectrum shown in Figure 42 was obtained with the NaI(Tl) split annulus and the 2.5% Ge(Li) detector in an arrangement described in 2.1.2.C. For this run, the single channel analyzers associated with the annulus had their windows adjusted to accept only the 511-keV peaks. Coincidence pulses (2_τ = 100ns) were required between each half of the annulus in order for the fast coincidence module to generate a gate signal. Thus, Figure 42 shows only those transitions associated with levels being fed by β^+ emission and those peaks due to the double escape process. The 511-keV annihilation peak in the spectrum is a measure of the chance contributions to the spectrum.

The anticoincidence set-up described in § 2.1.2.B. was used to obtain the spectrum in Figure 43. Anticoincidence spectra show enhanced those transitions which are not in prompt coincidence with other rays or with β^+ emission. This technique is particularly useful for placing single transitions to delayed states or to the ground state (when those states are not appreciably fed by β^+ emission).

The Sm^{141m} coincidence results for the anticoincidence, integral coincidence and 196.6-keV gated coincidence spectra are listed in Table 19. The 2-dimensional coincidence results for Sm^{141m} are summarized in Table 20. This information will be used further in the construction of the Sm^{141m} decay scheme (§4.4.6).

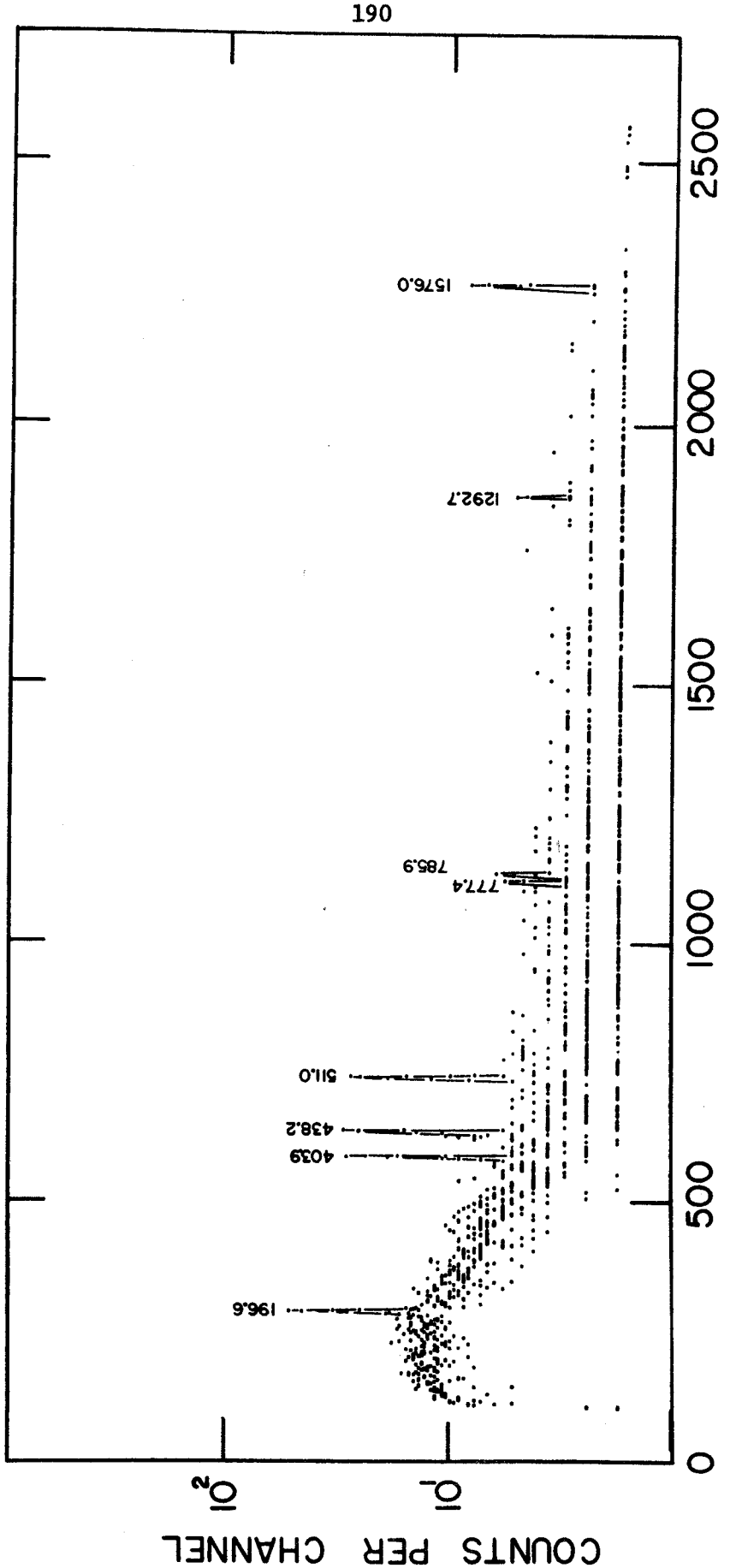

Figure 42. 511-511-keV gated coincidence spectrum for Sm^{144}.

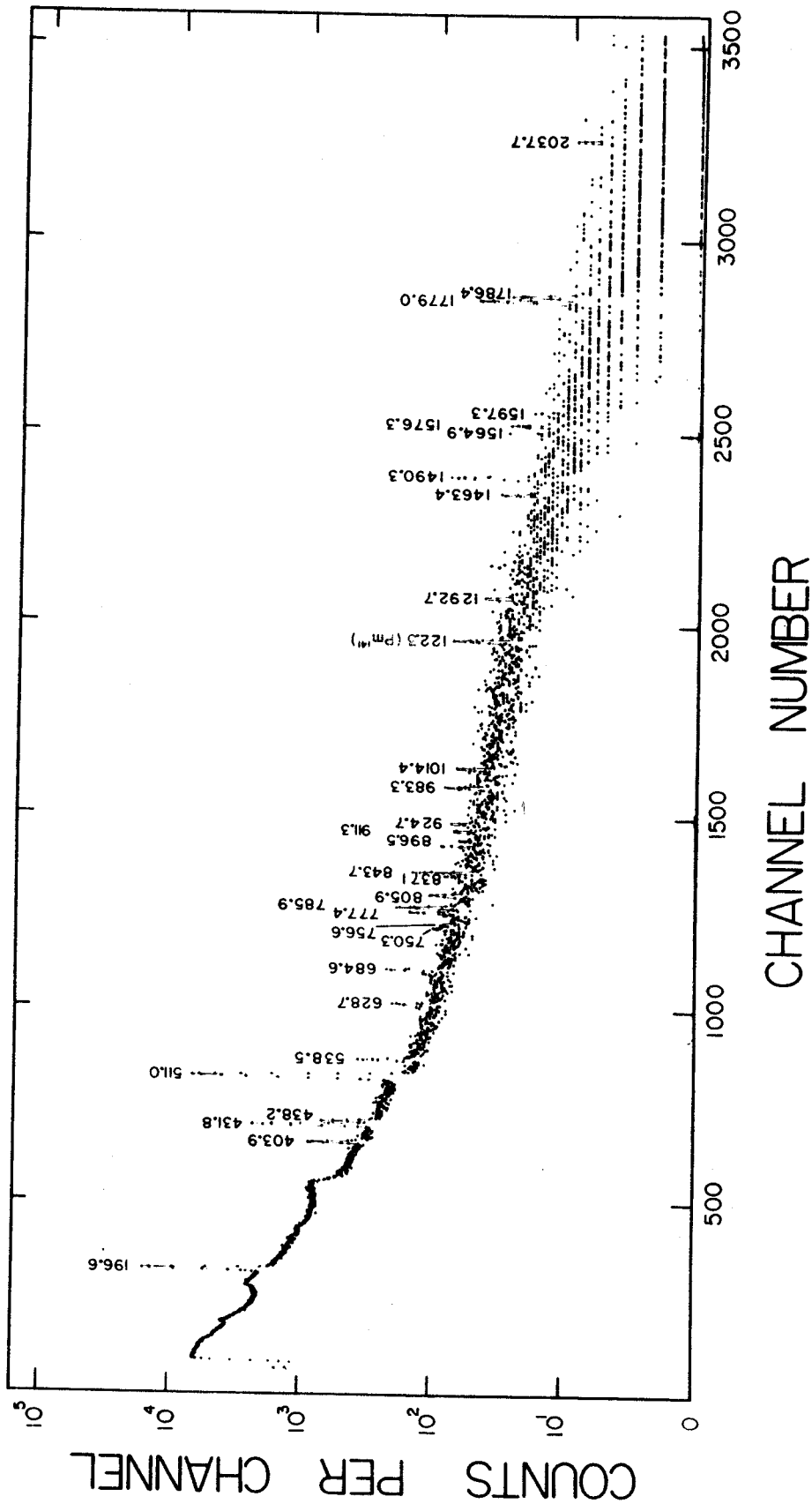

Figure 43. Anticoincidence spectrum for Sm^{141gm}.

Table 19. γ-Ray Intensities for Sm^{141m} Coincidence Experiments.

Energy (keV)[a]	Relative Intensities				
	Singles[a]	Anti-Coinc.	Integral Coinc.	196.6-keV Gate	Delayed Integral Coinc.
196.6	100	77.1	60.4		5.74
247.9	1.04	1.67	0.98		1.67
431.8	54.6	2.32	22.3	53.0	2.32
538.5	11.3	11.3	8.81		11.3
577.8	1.22		1.30		
607.9	1.38		1.79	1.90	
628.7	3.60				
684.6	10.6	8.32	7.30		8.32
725.7	1.95				
750.3	2.14	1.55	1.70		1.55
777.4	27.4		27.4	27.4	
785.9	9.20	10.2	4.99		10.2
805.9	4.78	4.50	3.45		4.50
837.1	4.82		3.99		
875.0	1.68		1.64	1.97	
896.5	1.95		1.33		
911.3	12.4		12.6	12.3	
924.7	3.08	1.67	2.06		1.67
955.4	0.91				
974.1	0.27				
983.3	9.80		8.03	7.96	

Table 19., Continued

Energy (keV)[a]	Relative Intensities				
	Singles[a]	Anti-Coinc.	Integral Coinc.	196.6-keV Gate	Delayed Integral Coinc.
1009.1	3.93		4.04	4.46	
1029.6	0.68				
1108.4	1.67		1.64		
1117.6	4.37		3.99	3.97	
1145.1	11.8		12.3	14.1	
1463.4	2.43				
1490.3	12.5	17.9	3.30		17.9
1786.4	14.6		9.78	17.0	
1898.0	0.51				
1979.6	0.54				
2073.7	1.92				

[a]The errors placed on these values are given in Table 18.

Table 20. Summary of γ-ray 2-dimensional coincidence results for Sm^{141m}.

Gate energy (keV)	γ's enhanced (keV)
Integral	196.6, 247.9, 538.5, 577.8, 607.9, 684.6, 750.3, 777.4, 805.9, 837.1, 875.0, 896.5, 911.3, 924.7, 983.3
196.6	431.8, 607.9, 777.4, 875.0, 911.3, 983.3, 1009.1, 1117.6, 1145.1, 1490.3, 1786.4
247.9	538.5
431.8	196.6, (1490.3)[a]
538.5	247.9, 896.5, 924.7
577.8	837.1 (weak)
607.9	196.6
676.7+684.6	(196.6)[a], 750.3, 805.9
750.3	(196.6)[a], 684.6, 858.5[b]
777.4	196.6, 1117.6, 1145.1
785.9	No coincidence in evidence
805.9	684.6
837.1	No coincidence in evidence
875.0	196.6, 911.3
911.3	196.6, 875.0, 983.3
924.7	(196.6)[a], 538.5, (777.4)[a]
893.3	196.6, 911.3
1009.1	196.6, 777.4

Table 20., continued

1117.6	196.6, 777.4
1145.1	196.6, 777.4
1490.3	(196.6)[a]
1786.4	196.6

[a]These intensities are less than expected for these transitions to be in coincidence. They are considered to be due to chance.

[b]This is not a Sm^{141m} transition.

4.4.4.C. Delayed Coincidence Spectra

Owing to the presence of the $h_{11/2}$ state at 628.6 keV in Pm^{141}, running delayed integral coincidence experiments proved to be very useful. As will be discussed in § 4.4.6., this state has an estimated half-life of 400 nsec, long enough to obtain useful information using a coincidence resolving time of 100 nsec.

Two types of spectra were obtained. In one case the gate signals were delayed 0.25 μsec with respect to the linear spectrum signals. The resulting spectrum should enhance those transitions proceeding from the delayed state. Such a spectrum is shown in Figure 44. The other case was that of delaying in the opposite direction. That is, the gate signal preceeded the linear spectrum signals by 0.25 μsec. This arrangement should enhance those transitions proceeding to the delayed state. This spectrum is shown in Figure 45.

4.4.5. Energy of the Sm^{141} Isomeric Level

As shown in Table 17, the isomeric transition energy for Sm^{141} has only been estimated. Based on a least-squares fit of experimentally measured $M4$ levels in other $N = 79$ nuclei we arrive at an energy of 171.6 keV for the expected $h_{11/2}$ level. A level of this energy would be expected to have a low $M4$ transition intensity (previously estimated to be <1% by (Bley 67)). The vicinity of 171 keV is a particularly unfortunate region for the observation of a weak γ ray since the annihilation quanta back-scatter peak is also 170 keV. We have looked for this transition both in γ-ray spectra and in electron spectra without success. An $M4$ transition of this energy should be

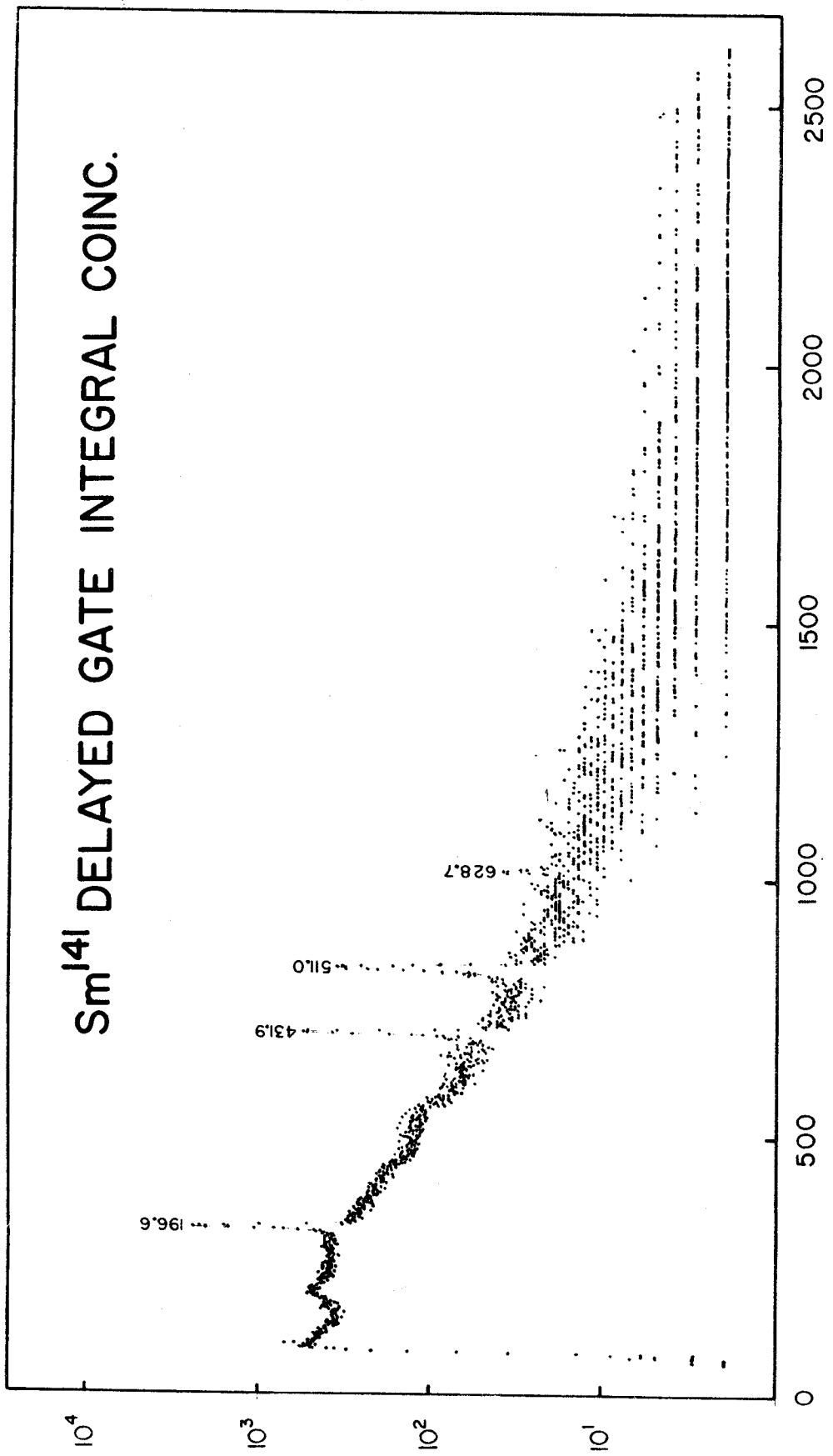

Figure 44. Delayed-gate integral coincidence spectrum for Sm^{141g+m}.

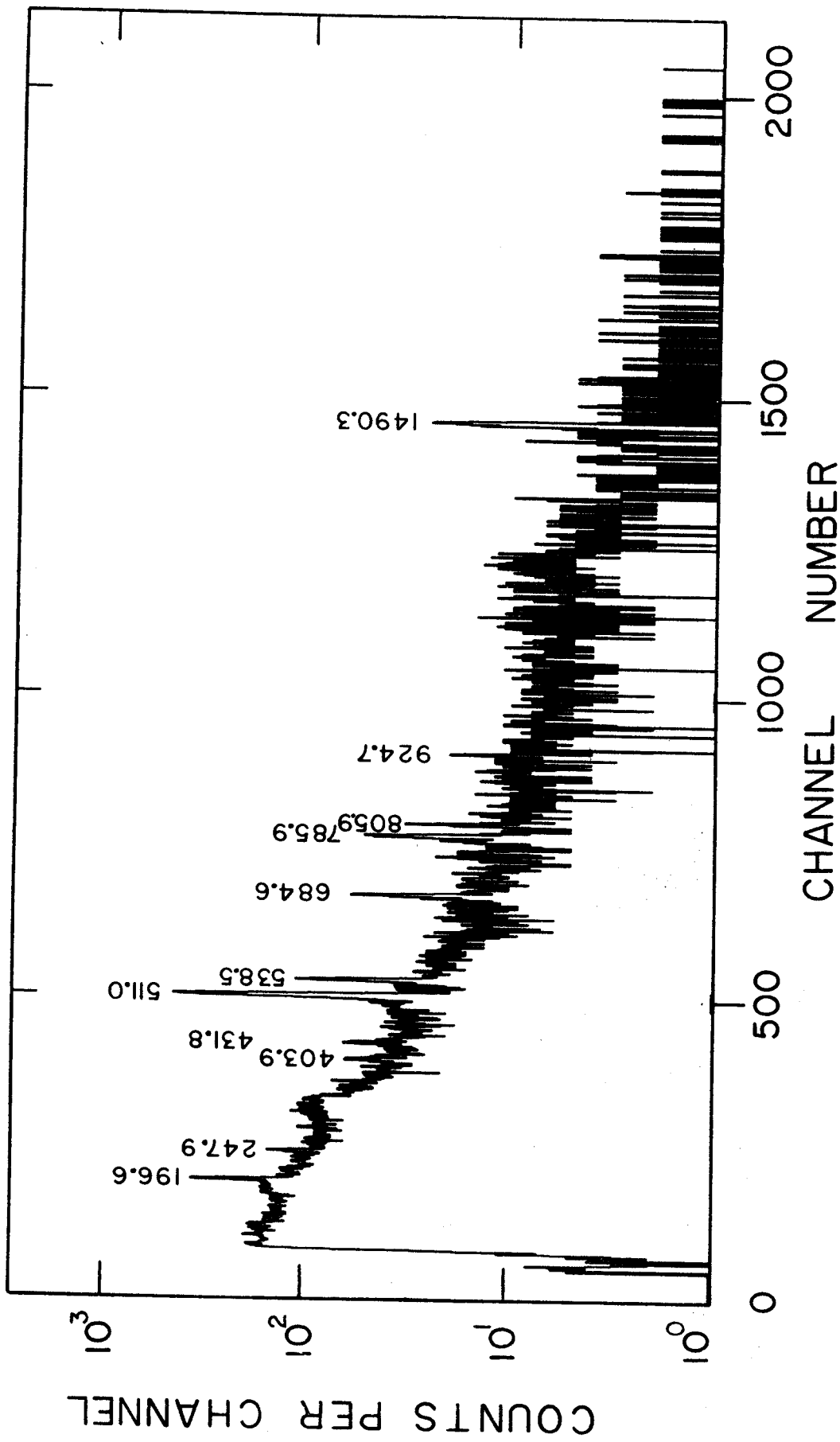

Figure 45. Delayed "spectrum" integral-coincidence spectrum.

prominent in an electron spectrum due to the large conversion coefficient; however, there is no evidence of any transition peaks above the continuum. These results demonstrate that such a transition is indeed very weak if not totally absent. Based on the statistics of our γ spectra, we place an upper limit of 0.2% of the total isomeric decay for this $M4$ process. The absence of an observable $M4$ trasition is interesting in the light of much experimental evidence which definitely shows the existence of an $h_{11/2}$ level in Sm^{141}.

4.4.6. Sm^{141m} Decay Scheme

A decay scheme for Sm^{141m} has been constructed from a combination of the above described prompt and delayed coincidence spectra and to a lesser extent from energy sums. This decay scheme is shown in Figure 46. Thirty-one of the thirty-two γ rays listed in Table 18 have been placed in the decay scheme, the 1979.6-keV transition being the only exception. The calculated ground state decay energy for Sm^{141} ($Q\varepsilon$) is 5.015 MeV (Myer 65). The γ-ray transition intensities are given in units of percent disintegration of the parent Sm^{141m}. The β^+ and ε intensities to each state are also calculated values (TI 67 and Zwei 57). The energy assigned to each level is a weighted average based on transitions out of that level.

The discussion of this decay scheme will be broken into two parts: a discussion of those levels which decay in a manner that bypasses the 628.6-keV level and those levels which decay primarily through the 628.6-keV level.

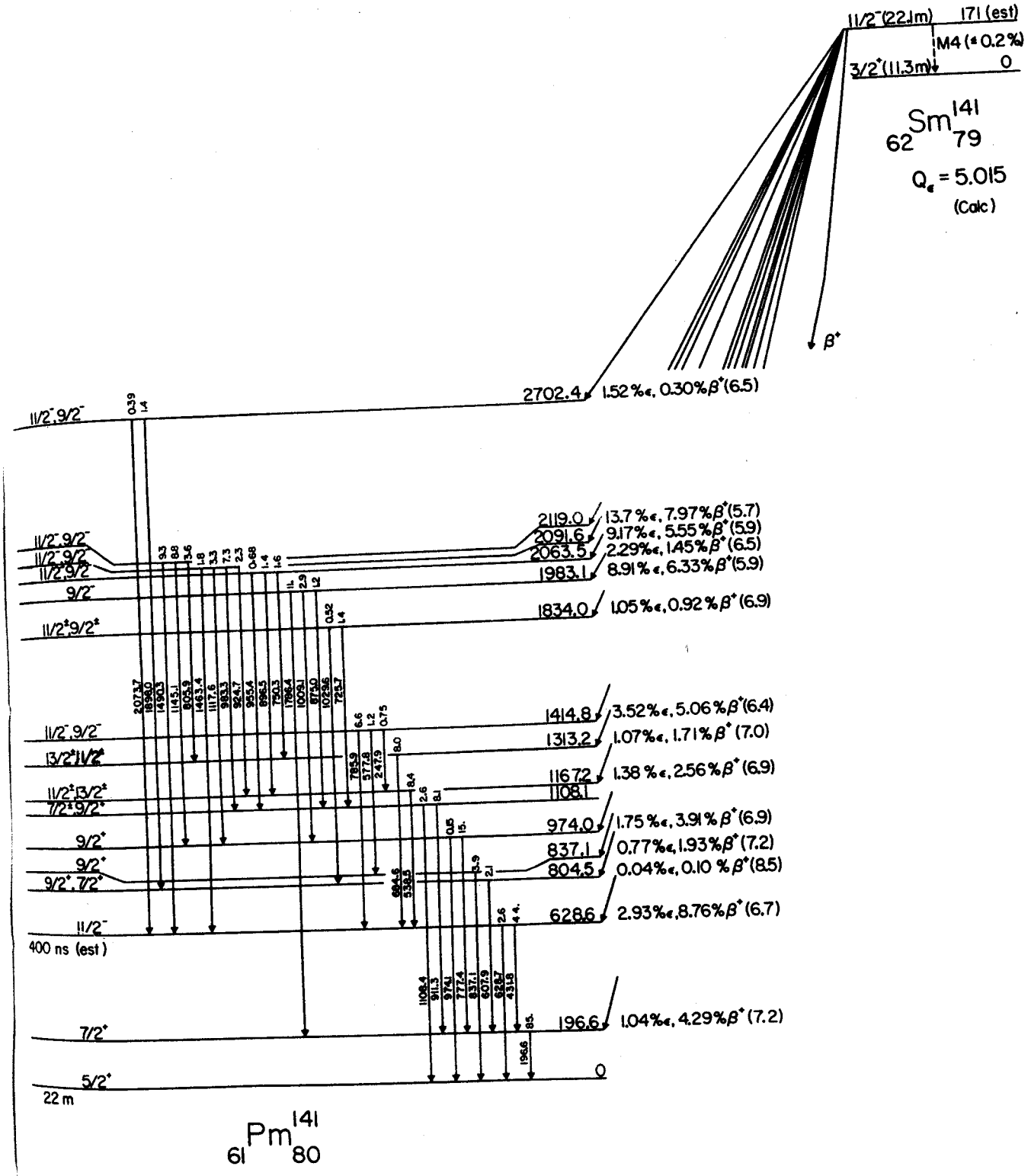

Figure 46. Decay scheme for Sm^{141m}.

4.4.6.A. The 196.6-keV and Related Levels

The 196.6-keV transition has been placed as proceeding from the first excited state of Pm^{141} on the basis of its being the most intense transition in the singles spectrum (Figure 39). This also seems reasonable from the systematics of the region. The levels at 804.5-keV, 837.1-keV, 974.0-keV, 1108.1-keV, 1834.0-keV, 1983.1-keV and 2702.4-keV bypass completely the 628.6-keV level, having de-excitations either through the 196.6-keV level or directly to ground. The 628.6-keV level has no choice but to decay to ground either directly or via a 431.9-keV transition to the first excited state. Both of these branches are observed. The level at 804.5-keV has been placed on the basis of a 196.6-keV and 607.9-keV coincidence as shown in the 2-dimensional spectra (Figure 41). Purely on the basis of sums, γ rays of 1029.6-keV and 1898.0-keV are placed as feeding this level. These are weak transitions and would not show up in the 607.9-keV gated coincidence spectrum due to the low statistics involved. Notice that there is an 805.9-keV γ ray. This transition is clearly in coincidence with the 684.6-keV transition (which feeds the 628.7-keV isomeric level) and is not to be confused with the 804.5-keV level. The 805.9-keV peak is clearly not a doublet (see Figure 39) and we must conclude that there is no appreciable ground state decay for the 804.5-keV level.

The level placed at 837.1 keV is somewhat of a puzzle. It is enhanced in the integral coincidence spectrum and attenuated in the anticoincidence spectrum. There is weak evidence for coincidence with the 196.6-keV transition on inspection of the 837.1-keV gated

spectrum. However, there is no enhancement of the 837.1-keV peak in the 196.6-keV gated spectrum. Possibly Compton events from other peaks (e.g. 875.0-keV) could account for the 196.6-keV peak appearing in the 837.1-keV gated spectrum. With this somewhat conflicting evidence the 837.1-keV transition has been placed as originating from a level of the same energy. The levels at 1834.0 keV and 2702.4 keV have been placed solely on the basis of sums. The 577.8-keV and 955.4-keV transitions have also been placed by energy sums. The placement of these two transitions does have the distinction of being accomplished without the introduction of any new levels. The remaining levels of this group, at 974.0-keV, 1108.1-keV, and 1983.1-keV are placed by the prompt coincidence data (Figure 41), energy sums, and relative intensities of the interconnecting γ rays.

4.4.6.B. The 628.6-keV and Spin-Related Peaks

The remaining levels can be divided into two sub-groups: those that decay exclusively through the 628.6-keV level and those that decay through both the 628.6-keV level and the 196.6-keV level. The levels at 1167.2-keV, 1313.2-keV and 1414.6-keV belong to the former sub-group while the levels at 2063.5-keV, 2091.6-keV and 2119.2-keV decay at least partly via the 196.6-keV level and thus belong to the latter group.

The 628.6-keV level is almost certainly an $h_{11/2}$ level. That this is, in fact, the high spin level is demonstrated by the results of the delayed coincidence spectra. In the delayed gated spectrum (Figure 45), only peaks at 196.6-keV and 431.9-keV are present. For this spectrum the gate was delayed for 0.25 μs. That these two

transitions are in coincidence is substantiated by spectra gated on these energies (Figure 41). This uniquely fixes an isomeric level at 628.6-keV. Further support for this conclusion is given from the enhancement of the 628.7-keV γ ray in the anticoincidence spectrum (Figure 43). This would be expected for a transition proceeding from an isomeric level. The γ rays which interconnect this group of levels can be placed using the delayed integral spectrum (Figure 45) as the basis. In this spectrum only those transitions feeding the 628.6-keV level should be enhanced. Additional placements and confirmations are obtained from the gated coincidence spectra (Figure 41) and the anticoincidence spectrum (Figure 43). The log *ft* values shown on the decay scheme have been computed using the electron-capture percentages to each level.

The ε/β^+ ratios calculated by the method of Zweifel (Zwei57) are not in good agreement with the results of the 511-keV-511-keV coincidence spectrum shown in Figure 42. This figure shows that the 196.6-keV, 403.9-keV and 438.2-keV transitions are the only transitions to receive significant β^+ decay. These results, then, are in disagreement with the theoretical values shown on the decay scheme. Table 21 compares the "normal" log *ft* values (obtained from calculated ε/β^+ ratios) versus the log *ft* values obtained on the assumption that all β-decay is via the ε-mode. The levels at lower energies are seen to be the most affected, although all of the values change less than one log *ft* unit. Either set can be used without significantly changing the conclusions drawn from them.

The only unplaced transition is the one of 1979.6-keV. This is a very weak transition and in no way affects the following discussion.

Table 21. Comparison of log ft's assuming either the theoretical ε/β^+ ratios or all ε-decay.

Level energy (keV)	Normal	ε-decay only
196.6	7.2	6.5
628.6	6.7	6.1
804.5	8.5	8.0
837.1	7.3	6.7
974.0	6.9	6.4
1167.2	6.9	6.5
1313.2	7.0	6.6
1414.8	6.5	6.1
1834.0	6.9	6.6
1983.1	5.9	5.7
2063.5	6.5	6.3
2091.6	5.9	5.7
2119.0	5.7	5.5
2702.4	6.5	6.4

4.4.7. Spin and Parity Assignments for the Decay of Sm^{141m}

Since no conversion-electron data are available for the transitions following the decay of Sm^{141}, multipolarity assignments cannot be made definite for these transitions. Because of this state of affairs no multipolarities are shown on the decay scheme (Figure 46)

4.4.7.A. The ground, 196.6-, and 628.6-keV States in Pm^{141}

The shell model predictions by Kisslinger and Sorensen (Kis 60) and systematics of this region suggest $5/2^+$ and $7/2^+$ configurations for the two lowest levels of Pm^{141}. As previously pointed out (Bee 69t), sixteen nuclei in this region have ground and first excited states which are well characterized (TI 67). For each of these nuclei, assignments of $7/2^+$ and $5/2^+$ are made for these two states. In the Pm isotopes there is a change of ground state spin between Pm^{145} and Pm^{147}. Pm^{147} and higher mass isotopes exhibit ground and first excited states of $7/2^+$ and $5/2^+$, respectively. Pm^{145} and Pm^{143} exhibit ground state and first excited states of $5/2^+$ and $7/2^+$, respectively. Similarly, looking at other $N = 79$ isotones shows a reversal in these spins in going from La^{137} to Pr^{139}. Pr^{139} is assigned ground and first excited state spins of $5/2^+$ and $7/2^+$, respectively. The lower mass $N = 79$ isotones exhibit ground and first excited state spins of $7/2^+$ and $5/2^+$. From these trends it seems reasonable to assign the value of $5/2^+$ for the ground state of Pm^{141} and to make the assignment of $7/2^+$ for the first excited state at 196.6 keV. Since the isomeric level

in Sm^{141} is undoubtedly the $h_{11/2}$ level, this would mean that a transition between this level and the ground state of Pm^{141} would have to be at least 2nd forbidden. Thus, it is assumed that this branch is negligibly small and is not considered in any calculation involving intensities. The β-branch to the 196.6-keV level, using $7/2^+$ as the J^π value for this level, must be at least 1st forbidden unique and very little β-feeding to this level would be expected. However, from γ-ray intensity balance for this state, it appears that 5.3% of the β-decay does go to this state, resulting in a log *ft* of 7.2. This compares with 3% decay to the first excited state of Pr^{139} (Bee 69d) with a log *ft* of 7.6. At first glance, it would seem reasonable to attribute at least a fraction of this decay to errors in γ-ray intensity determinations. However, the 511-511 keV coincidence spectrum (Figure 42), after correction for chance, shows that there is, in fact, β^+ decay to this level. Figure 37 shows the plot of the half-life curve for the 196.6-keV peak. In this plot there is no evidence of an 11.3 minute component, which means that any β^+/ε decay to this state must be from Sm^{141m}. In spite of this small β-branch to the 196.6-keV state, the bulk of evidence still suggests that it is the $7/2^+$ level.

That the 628.6-keV level is $11/2^-$ has already been discussed in §4.4.6. The log *ft* of 6.7 is on the high side for an allowed transition but still possible. As will be discussed in §4.4.12, this is an entirely reasonable value because of the particle rearrangement necessary for this $11/2^- \rightarrow 11/2^-$ transition. The half-life of the 628.6-keV state has been estimated from the 431.8-keV

*M*2 transition and the 628.7-keV *E*3 transition, resulting in values of 470 nsec and 323 nsec, respectively. These values are based on the measured value of 40 nsec for Pr^{139} (Bee 69d) and relating the two nuclides by the appropriate single-particle-transition equations (see Chapter 5).

4.4.7.B. The 804.5-, 837.1-, 974.0-, 1108.1-, 1834.0-, and 1983.1-keV Levels in Pm^{141}.

The γ transitions from these levels completely bypass the $h_{11/2}$ level at 628.6-keV. They exhibit log *ft*'s ranging from 5.9 to >8.

The 804.5-keV state (log *ft* = 8.5) appears to be fed by a 1st forbidden or 1st forbidden unique transition. Thus, positive parity states are possible with spins ranging from 15/2 to 7/2. Since there is only one transition, 607.9-keV, from this level, it is somewhat difficult to draw conclusions. From one point of view, the absence of a transition to the ground state would tend to rule out the $7/2^+$ assignment since that assignment should make an *M*1 ground state transition more favorable. A $9/2^+$ assignment would favor the transition to the $7/2^+$ level, as is observed. However, assuming the 804.5-keV level to be a vibrational level based on coupling the 2^+ level in Nd^{140} with the 196.6-keV state would explain the single γ de-excitation to this level. From this point of view, a $7/2^+$ assignment for the 804.5-keV level would also be reasonable. Hence, we feel that $9/2^+$ and $7/2^+$ must both be left as possible assignments for the 804.5-keV level, higher spins being ruled out by the single transition to the $7/2^+$ level at 196.6 keV.

The state at 837.1 keV, having a log ft of 7.2, is most likely fed by a 1st forbidden β branch, resulting in $13/2^+$, $11/2^+$, and $9/2^+$ as possibilities for the J^π assignment. An assignment of $13/2^+$ or $11/2^+$ should rule out the transition to ground. $9/2^+$ must remain as a possibility by the same arguments as for the 804.5-keV level. This level may also arise from vibrational coupling to the ground state.

The 974.0-keV level decays to both the ground state and the 1st excited state with γ intensities in the right ratio to be $M2$ and $E1$ transitions, respectively. The log ft of 6.9 for this level suggests a 1st forbidden nonunique β branch to this level, resulting in assignment possibilities of $13/2^+$, $11/2^+$, or $9/2^+$. The γ-ray intensities, coupled with the absence of any transition to the $11/2^-$ level at 628.6 keV, tend to rule out $13/2^+$ and $11/2^+$. Thus the assignment of $J^\pi = 9/2^+$ is made for this level.

Within the limits of our γ-ray statistics there is no feeding to the 1108.1-keV level. This leaves several possibilities for the J^π of this level. Spins higher than 9/2 can most likely be ruled out by the absence of a transition to the $h_{11/2}$ state at 628.6 keV and the presence of transitions to $7/2^+$ and $5/2^+$ states. This leaves 9/2 and 7/2 as possible candidates. The assignment of $9/2^-$ can be ruled out since this would mean an $M2$ 1108.4-keV transition and an $E1$ 911.3-keV transition, a very unlikely combination. Thus, we limit the assignment to $7/2^\pm$ being the most likely, with $9/2^+$ assignment being a possibility.

The 1834.0-keV level has a log ft (6.9) that puts it in that grey region between allowed and first forbidden transitions.

We feel that a $13/2^{\pm}$ assignment is improbable because of the fact that the only two transitions from this level are to levels with 9/2 and 7/2, 9/2 assignments. However, there is no way to limit the assignment beyond $11/2^{\pm}$ or $9/2^{\pm}$.

The low log ft value of 5.9 for the 1983.1-keV level suggests that it is one of the β-preferred three-quasiparticle levels. This is persued further in § 4.4.12. From the β decay, J^{π} values of $13/2^{-}$, $11/2^{-}$, and $9/2^{-}$ are the candidates. Here again, this level shuns the $11/2^{-}$ level at 628.6 keV, choosing instead to decay to levels having $7/2^{+}$ and $9/2^{+}$ assignments, with the 1786.4-keV γ ray (to the 196.6-keV level) being by far the most prominent. The only J^{π} assignment consistent with this information in $9/2^{-}$. This would mean that the three γ transitions from this level would probably all be $E1$'s, a conclusion which is qualitatively in agreement with the observed relative intensities of these γ rays.

4.4.7.C. The Levels which Decay through the Level at 628.6 keV

The remaining seven levels decay at least partially through the 628.6-keV level. Five of these levels, at 1414.8, 2063.5, 2091.6 2119.2, and 2702.4 keV, are proposed as being members of a three-quasiparticle multiplet (§ 4.4.12). The remaining levels, at 1167.2 and 1313.2 keV, have log ft values (6.9 and 7.0, respectively) too high to make them likely candidates for this preferred type of decay.

Considering these last two levels first, we see that they exhibit quite similar properties; the log ft's of 6.9 and 7.0

are almost identical and each one de-excites by a single transition to the 628.6-keV level. Again, these log ft values are of a magnitude which could mean the β branches are allowed or 1st forbidden nonunique. The possible J^{π} assignments would then be $13/2^{\pm}$, $11/2^{\pm}$, or $9/2^{\pm}$. Going on the assumption that there would be decay to several other states if the assignment were $9/2^{\pm}$, this value is ruled out. The J^{π} values of $13/2^{\pm}$ and $11/2^{\pm}$ are left as real possibilities with the $11/2^{\pm}$ assignment being the more likely. Without further information the choices for this level can not be narrowed any further.

The level at 1414.8 keV, having a log ft of 6.5, is most likely an allowed transition. Since this level has an appreciable de-excitation mode via the 577.8-keV transition to a $9/2^{+}$ level, a spin assignment of $13/2^{-}$ would mean that the multipolarity of the 577.8-keV transition would have to be $M2$. Such a transition should not compete favorably with $M1$ and/or $E1$ transitions. In addition, considering this to be a three-quasiparticle level would also make improbable an $M2$ transition, basing this statement on the fact that the three-quasiparticle levels in Pr^{139} de-excited exclusively via $E1$, $E2$, and $M1$ electromagnetic transitions, and that all transitions out of such a multiplet appear to be hindered. This means that an $M2$ should be very slow. Hence, we limit the assignments for this level to $11/2^{-}$ or $9/2^{-}$.

The remaining levels, at 2063.5, 2091.6, 2119.2, and 2702.4 keV, have log ft's ranging from 5.7 to 6.5. Each is assumed to be fed by an allowed β branch, resulting in J^{π} choices of $13/2^{-}$, $11/2^{-}$, or $9/2^{-}$. Using the same arguments as for the 1414.8-keV

level discussed above, the $13/2^-$ can be ruled out as being very likely. Neither the $11/2^-$ nor the $9/2^-$ assignments can be ruled out without more information.

4.4.8. Sm^{141g} γ-ray Spectra

Determining which γ rays constituted transitions resulting from the decay of Sm^{141g} has been a most difficult task, one that is still not completely settled. Originally, Sm^{141g} transitions were sought as ones maintaining a constant intensity relative to the 403.9-keV peak intensity, as measured in the four singles spectra described in §4.4.4.A. The 403.9-keV peak was picked as definitely belonging to the decay of Sm^{141g} both from its half-life and from the fact that it exhibits the same excitation threshold as do the peaks identified as coming from Sm^{141m} decay. The almost equally intense 438.2-keV peak still presents us with problems, as will be discussed in §4.4.9, but is tentatively placed as a level in Pm^{141}.

4.4.8.A. Singles Spectra

Obviously, because of Sm^{141g} having the shorter half-life, this species could never be viewed in the absence of Sm^{141m}. The Sm^{141g} peaks are therefore maximized relative to the Sm^{141m} peaks in spectra obtained immediately after bombardment. Such a spectrum is the one shown in Figure 39, which represents 15 minutes of counting beginning 2 minutes after the end of the bombardment.

It turned out that many of the observed transitions, aside from the ones assigned to the decay of Sm^{141m}, had eratically

behaving intensities. There are transitions present in the singles spectra having apparent half-lives ranging from less than 10 minutes to greater than 20 minutes. In the final analysis, only 2 or 3 peaks can definitely be said to have the same half-life as the 403.9-keV peak. In spite of the difficulties, 10 transitions were observed having decay properties near enough to the 403.9-keV peak to be placed tentatively as belonging to the decay of Sm^{141g}. These energies and relative intensities are listed in Table 22. Unfortunately, Table 23 shows why these transitions are only tentatively placed. In this figure the intensities, relative to the 403.9-keV trnsition intensity, are given as determined from the 4 spectra taken in four consecutive 15 minute periods. Only 2 or 3 of the peaks can be said really to follow the 403.9-keV half-life.

The $Sm^{144}(p,4n)Eu^{141}$ (Q= -36.8 MeV) $\rightarrow Sm^{141g}$ reaction was also used in an effort to enhance the Sm^{141g}/Sm^{141m} ratio, a result depending on the absence of a ß-emitting isomeric level in Eu^{141}. This indeed turned out to be the case as evidenced by the greatly increased 403.9/431.9-keV intensity ratio. Figure 47 shows the results from such a bombardment for the production of Eu^{141}. Each of the three spectra represents 5 minutes of counting time with the counting begun on the first spectrum 2 minutes after the end of a 30 second bombardment. The very intense peaks seen in the first spectrum have a common half-life of roughly 2.0±0.5 minutes and have not yet been positively identified as to their origin. This is still under investigation at MSU. Unfortunately the presence of all the short half-life activities precluded the attainment of better in-

Table 22. Energies and Relative Intensities of γ rays from the Decay of Sm^{141g}.

Energy	Intensity
196.6±0.3	(0.64)[a]
324.5±0.2	2.29
403.9±1.1	23.4
661.9±0.1	0.64
858.5±0.2	1.66
1292.7±0.1	3.67
1495.6±0.1	1.29
1600.9±0.3	2.07
2005.0±0.5	0.21

[a]This is a common energy level with the Sm^{141m} activity. Therefore, the intensity due only to the Sm^{141g} decay alone cannot be accurately determined and is assumed to be totally from feeding of this level by the 661.9-keV transition.

Table 23 Relative intensities of γ rays assigned to Sm^{141g} as measured in four consecutive 15 minute spectra.

Energy (keV)	Intensity			
	Quad 1	Quad 2	Quad 3	Quad 4
196.6	-[a]	-	-	-
324.5	9.8[b]	13	16	21
403.9	100	100	100	100
661.9	2.7	5.7	7.2	8.3
728.8	.77	-	-	-
858.5	7.1	16	16	28
1292.7	9.4	16	23	25
1495.6	5.5	11	8.9	14
1600.9	8.8	7.7	11	-
2005.0	0.90	-	-	-

[a] The 196.6-keV transition intensity cannot be measured directly because of the Sm^{141m} decay through this level.

[b] The intensity values from this first quadrant are used in the decay scheme construction.

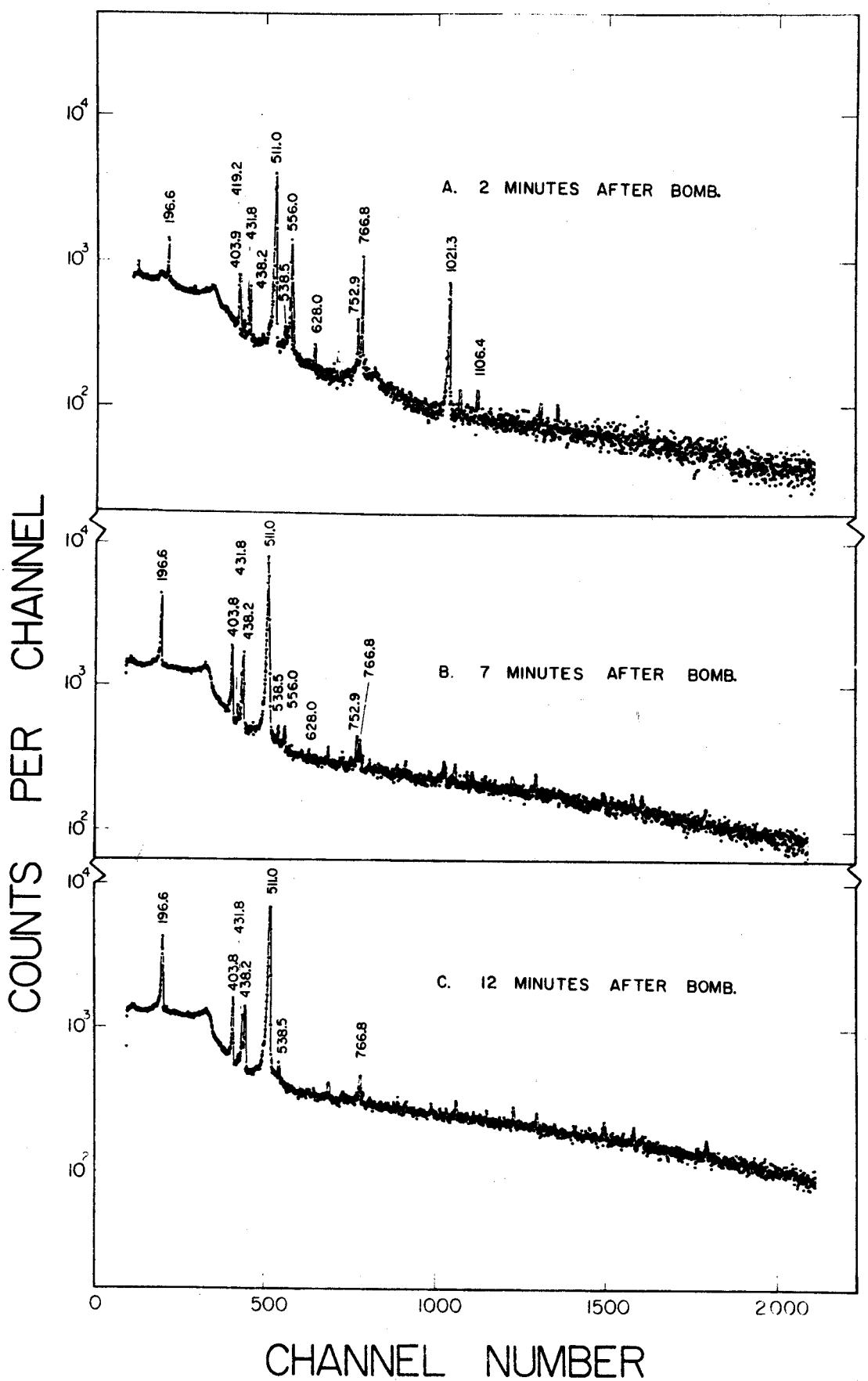

Figure 47. Eu^{141} γ-ray singles spectra.

tensity data for the Sm^{141g} decay. If anything, it was more difficult, via this reaction, to determine which transitions were due to the Sm^{141g} decay. An intriguing question, presently unanswered, pertains to the origin of the intense peak at 438.2-keV. In the early stages of this investigation it was supposed that this transition also came from the decay of Sm^{141g}. On closer examination, however, this assignment came into question on several counts. First, the 438.2-keV transition has a similar but different half-life. This was carefully measured by the computer program GEORGE (described in § 2.2), resulting in a value of 10.0±0.4 minutes. This was measured several times with quite good precision. Another interesting bit of information on the 438.2-keV transition is that there is no clear-cut evidence for transitions which are in coincidence with it. The consequence of this is that there is no way of relating the 438.2-keV transition with any other γ ray in the spectrum. This would indicate that if this transition is due to the decay of Sm^{141} it must be a ground state transition in Pm^{141} from a level of the same energy.

The $Sm^{144}(p,4n)Eu^{141}$ reaction was again called upon for the purpose of determining whether or not the 438.2-keV peak was produced in this manner and for the purpose of determining its relative intensity if it was produced. It is obvious from Figure 47 that this peak is indeed present with approximately the same intensity relative to the 403.9-keV peak as it has in Figure 39. An excitation function was run on the Sm^{144} target by changing the proton beam energy in increments of 5 MeV. The 403.9- and 438.2-keV

peaks, as well as the 196.6-keV, 431.9-keV and other Sm^{141m} peaks, first appear at the bombarding energy of 35 MeV. However, the 403.9 keV/438.2 keV intensity ratio is larger here than at higher energies. This could mean that the 438.2-keV transition originates from a species having a 2-3 MeV higher excitation threshold. An excitation function run on the Nd^{142} target (He^3 beam) shows similar behavior; that is, the 438.2-keV peak seems to have a slightly higher excitation threshold.

The above arguments could well be used to show that the 438.2-keV transition does not belong as a level in Pm^{141}. Our most recent experiment, however, can be used as a counter argument. This experiment was a 2-dimensional coincidence run using a γ-ray detector versus an x-ray detector. The γ-ray spectrum was subsequently used for setting gates on various γ-ray peaks. The resulting gated γ-ray spectra should show those x-rays which were in coincidence with the gated γ rays. In this manner γ-ray gates were set on the 196.6-, 403.9-, 431.8-, and 438.2-keV peaks. The results for each gated run were the same: all of the above γ rays were in coincidence with Pm x-rays. This makes certain that the 438.2-keV transition is from a level in a Pm isotope. That this level is in fact in Pm^{141} is suggested by the fact that no matter what reaction has been used for production, the 403.9- and 438.2-keV peaks always appear together - and in about the same ratio.

The bulk of the experimental evidence seems to be telling us that both the 403.9-keV and the 438.2-keV transitions must be from levels in Pm^{141} which are fed predominently from the

ground state of Sm^{141}. Bear in mind that we must still explain why the 403.9-keV and the 438.2-keV transitions have measurably different half-lives (10.0 and 11.3 minutes, respectively). A number of proposals have been offered in explanation of this puzzle, almost all of which seem to have serious defects. Two alternate proposals will be made for the Sm^{141g} decay in §4.4.9.

Also notice, just in passing, that there is an intense 538-keV peak (same energy as in Sm^{141m} decay) which exhibits the same 2 minute half-life as do the other intense peaks found in the first Eu^{141} spectrum.

4.4.8.B. Coincidence Spectra for Sm^{141g}.

As with the singles spectra, the Sm^{141g} coincidence peaks can only be observed amidst the Sm^{141m} peaks and other short-lived activity. Four relevant 2-dimensional coincidence spectra, gated on Sm^{141g} peaks, are shown in Figure 48. The original x- and y-axis integral coincidence spectra are shown in Figure 41. These gated spectra point up a difficulty in constructing the Sm^{141g} decay scheme. The ground state decay of Sm^{141} really seems to be lacking in coincidence transitions.

The 511-511-keV coincidence spectrum and the anticoincidence spectrum, both for Sm^{141g+m} are shown in Figures 42 and 43, respectively. Table 25 summarizes the principle coincidence intensity data obtained from these various spectra.

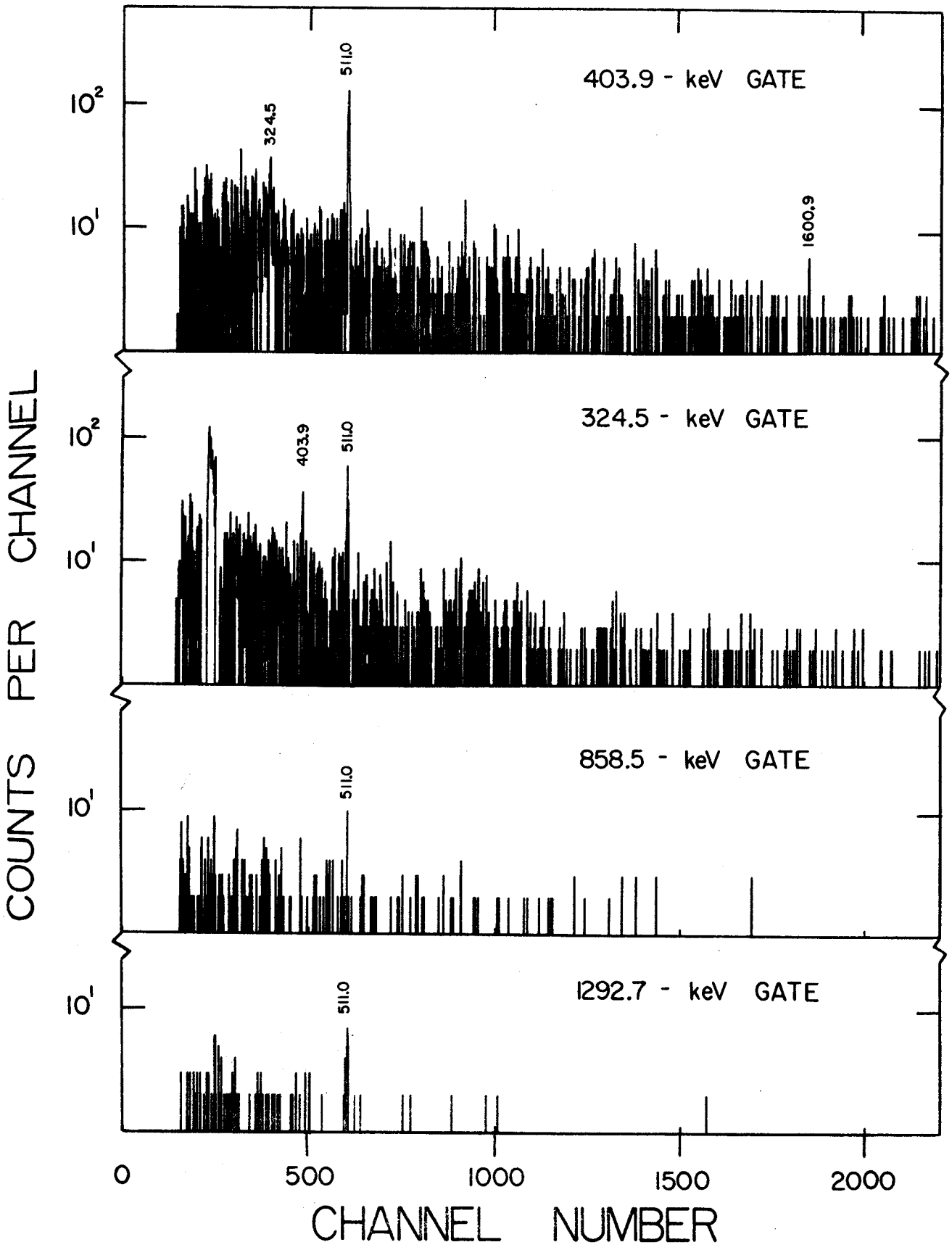

Figure 48. 2-dimensional gated coincidence spectra for Sm^{141g}.

Table 24. Coincidence Transition Intensity Summary for $Sm^{141}g$.

Energy (keV)	Relative Intensity		
	Singles	Integral-gate	Anti
324.5	2.29	4.60	
403.9	23.4	19.1	21.7
661.9	0.64		
858.5	1.66	3.10	
1292.7	3.67		3.36
1495.6	1.29	2.03	
1600.9	2.07	1.88	
2005.0	0.21		

4.4.9. Sm^{141g} Decay Scheme

The Sm^{141g} decay scheme, presented in Figure 49, has been constructed without consideration of the 438.2-keV transition, which cannot be placed definitely. This decay scheme is to be considered purely hypothetical at this time; the final word must await further investigation, particularily into the origin of the intense 438.2-keV peak. After a discussion of the decay scheme as presently envisioned, mention will be made of a possibility which may exist for the inclusion of the 438.2-keV peak in the Sm^{141g} decay scheme. The decay scheme in Figure 49 has been constructed from the available coincidence data, intensity balances and energy sums. As shown in Table 22, the 403.9-keV transition is by far the most intense transition resulting from the Sm^{141g} decay, accounting for 67% of the γ-ray intensity. From the 403.9-keV gated spectrum shown in Figure 48, one can see evidence for coincidences with the 324.4-keV and 1600.9-keV peaks, which suggests levels at 728.3 keV and 2005.0 keV. γ transitions have been observed at both of these energies. These 5 transitions, at 403.9, 324.4, 1600.9, 728.3 and 2005.0 keV, form the heart of the decay scheme. Weak evidence for a common level with that of Sm^{141m} can be found for the 196.6-keV level. Placing a level at 858.5 keV allows the placement of an 858.5-keV transition to ground and a 661.9-keV transition feeding the 196.6-keV level. These transitions are too weak to be seen in the coincidence spectra and can only be tentatively placed by energy sums. The remaining levels at 1292.7 keV and 1495.6 keV are placed

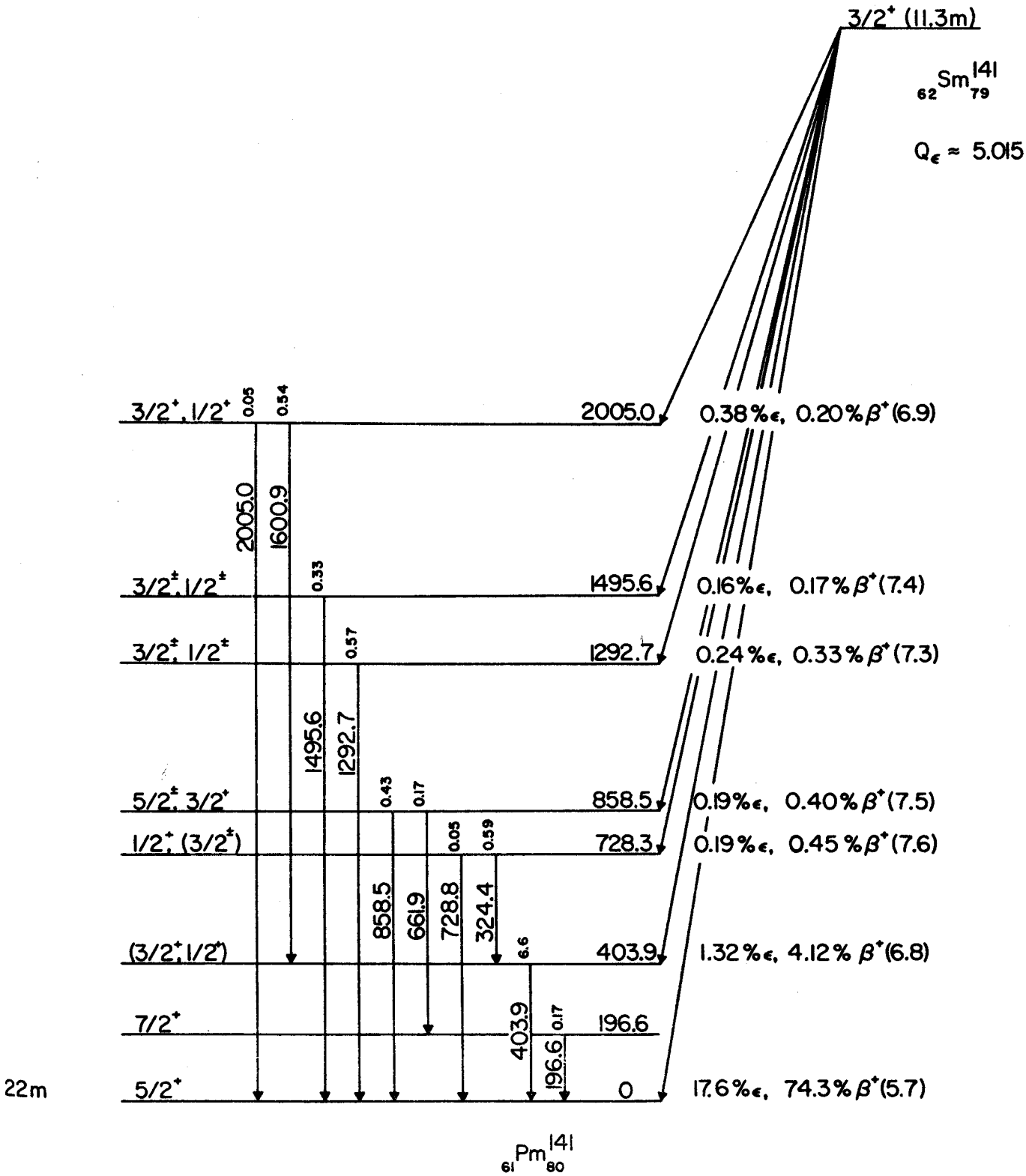

Figure 49. Tentative decay scheme for Sm^{141g}.

on the basis of single transitions at those energies. The 1292.7-keV peak is enhanced in the anticoincidence spectrum (see Table 24) and is thus placed as a ground state transition. This would be in keeping with the 1292-keV gated coincidence spectrum (Figure 48) which shows that only the 511.0-keV annihilation peak is in weak coincidence. The 1495.6-keV level is placed on a more tenuous basis. First of all, it has been kept as belonging to Sm^{141g} on the basis of having relatively similar decay characteristics. It was placed in the decay scheme even though no other peaks can be found that are in coincidence. The integral coincidence spectrum does indicate an enhancement of this transition. However, it cannot be gated due to the close lying 1490.3-keV peak. The integral coincidence enhancement could be due to β^+ feeding to this level, but at present the inclusion of this level is a very borderline situation.

The log ft values shown on the decay scheme have built-in assumptions on the percent β feeding to the ground state and the 196.6-keV state. In the proposed decay scheme only the 661.9-keV transition feeds this state. That the 196.6-keV state is only weakly fed by the Sm^{141g} decay (both γ- and β-decay) is supported by the visually absent 11.3 min component in the 196.6-keV half-life curve shown in Figure 37. We therefore make the assumption that there is no direct β feeding from Sm^{141g}. An upper limit on the amount of direct β feeding to the Pm^{141} ground state was set by reference to the 511-511-keV spectrum displayed in Figure 42. The levels fed by β^+ decay, other than any ground state feedings, are the 196.6-, 403.9-, and 438.2-keV levels. The intensities of these

peaks, after correction for chance, were normalized to the singles spectrum on the assumption that the 403.9-keV transition was allowed (or at most 1st forbidden nonunique). The resulting normalized intensities were subtracted from half of the annihilation peak intensity to arrive at this upper limit. This is an upper limit since we cannot determine the amount of 511.0-keV intensity arising from other ground state transitions (assumed to be low). This limit turns out to be 91.8%. That is, 91.8% of all ε/β^+ transitions from the decay of Sm^{141g} proceed directly to the ground state of Pm^{141}.

Total electromagnetic transition intensities are taken to be the same as the γ-ray intensities; conversion coefficients for the energies involved would be negligibly small. At this point only speculation can be made as to the placement of the 438.2-keV transition. If it must indeed be placed as a Pm^{141} level this would probably mean that the true Sm^{141g} half-life is 10.0 minutes (as opposed to the 11.3 minutes states in §4.4.3), the half-life measured for the 438.2-keV peak. To account for the longer half-life of the 403.9-keV peak would require a small amount of γ decay to this level from another Pm^{141} level which is populated by the 22.1 min Sm^{141m} decay. Folding in a 20% 22.1 min component could raise the 10 min half-life curve to one of over 11 minutes. This small amount of Sm^{141m} admixture would not be noticeable as a break in the 438.2-keV curve (Figure 38).

If this is in fact the real situation, the 728.3-keV level would have to be fed by a β branch from Sm^{141m}. The strongest transition from this level is the one at 324.4 keV which is situated on the 511.0-keV Compton knee. This makes an accurate determination of its intensity impossible. From the intensity data we do have it is conceivable that it does have a 22.1 minute half-life. It is only about 10% as strong a transition as the 403.9-keV transition and it is still questionable whether this is enough to account for the 11.3 minute half-life of the 403.9-keV transition. This would mean, of course, that the 728.3-keV level should rightly be included in the Sm^{141m} decay scheme.

4.4.10. Spin and Parity Assignments for Sm^{141g}

The spin and parity assignments for the Pm^{141} levels populated by the decay of Sm^{141g} are based on the log ft values and relative γ-transition intensities shown on the decay scheme presented in Figure 49.

In § 4.4.7 we have already discussed the evidence for assigning the ground and 1st excited states the J^{π} values of $5/2^+$ and $7/2^+$, respectively. This is seen to be consistent with a log ft of 5.7 for the ground state and a lack of feeding to the 1st excited state.

The 403.9-keV level exhibits a log ft of 6.8, which most likely means that it is an allowed transition. Since we have not observed transitions from this level to the $7/2^+$ level at 196.6 keV, it seems reasonable to eliminate the $5/2^+$ assignment from further consideration, although there is the possibility that 403.9-keV level is core coupled to the $5/2^+$ ground state. This could account for the single ground-state transition. Thus, we tentatively assign the values of $3/2^+$ or $1/2^+$.

The log ft of 7.6 for the 728.3-keV level is high for an allowed transition, although this remains a possibility. The spin of $5/2$ can be ruled out on the absense of any transition to the $7/2^+$ level at 196.6 keV. A spin of $3/2$ (with even or odd parity) cannot easily be ruled out, although an assignment of $1/2^+$ seems more reasonable. This assignment would indicate an $E2$ multipolarity for the de-exciting 728.8-keV transition and an $M1$ multipolarity for the 324.4-keV transition (an assignment of $1/2^-$ would mean $M2$ and $E1$

multipolarities for these transitions, clearly improbable). Thus, we assign a spin of $1/2^+$ for this level with $3/2^\pm$ being less likely but still possible choices.

For the 1292.7-keV level (log ft=7.3) we have a similar argument. The log ft value is ambiguous enough to allow us the liberty of assuming either an allowed or a first forbidden nonunique β transition. Here we have a 661.9-keV transition to the $7/2^+$ level and an 858.5-keV transition to the $5/2^+$ ground state (no transition to the low spin state at 403.9 keV). This situation most likely rules out a $1/2$ assignment. $3/2^-$ can also be ruled out since this would mean competing $M2$ and $E1$ transitions. This leaves the assignments of $5/2^\pm$ and $3/2^+$ as possibilities that cannot be easily ruled out without more information.

The two levels at 1292.7 keV and 1495.6 keV have log ft's of 7.3 and 7.5, respectively. Again, either allowed or 1st forbidden nonunique transitions. Since each of these levels has only a single transition to the ground state, not many conclusions can be drawn. Absence of transitions to the $7/2^+$ state at 196.6 keV is taken as *weak* evidence for the elimination of $5/2^+$ as possible assignments (the emphasis here is on *weak*).

The 2005.0-keV level prefers to decay to the ground and 403.9-keV levels rather than to the $7/2^+$ level at 196.6. This, coupled with the assumption tht the 2005.0-keV level is a β-allowed level (log ft=6.9), allows us to limit the assignments to $3/2^+$ or $1/2^+$.

At this point it should be re-emphasized that the Sm^{141g} decay scheme, including the spin and parity assignments for the proposed levels, is tentative. Further work is presently underway with a special emphasis on the characterization of the intense 438.2-keV transition. Properly placing this transition will help greatly in clearing up the uncertainties in this decay scheme.

4.4.11. Discussion

As mentioned in §4.1, the impetus for carrying out the investigation of Sm^{141} was the prediction (Bee 69d) that the isomeric level in this nucleus should populate three-quasiparticle states in Pm^{141} similar to those found in the decay of Nd^{139m}. The requirements for populating these levels are a parent nucleus containing a relatively low energy, high spin isomeric level and an electron-capture decay energy large enough to be able to populate levels above the pairing-energy gap in the daughter nucleus. The isomeric level in the parent should be low enough in energy such that the probability for the high multipolarity electromagnetic transition to ground is sufficiently low, thus allowing significant decay by the β process.

Since this nucleus has been predicted to be similar to Nd^{139} in its decay properties, it might be interesting to compare first the overall features of the isomeric decay in the two nuclei. The ground state decay for both Sm^{141} and Nd^{139} is principally via an allowed transition to the ground states of the daughter nuclei. Both are to a large degree straightforward decays. The β feeding in both Sm^{141m} and Nd^{139m} show remarkable similarities: very little feeding to the ground and 1st excited states, a somewhat more hindered decay to the lowest $11/2^-$ level than expected, and several states of relatively high energy which exhibit abnormally low log ft values. These two decays are, on the other hand, completely dissimilar in one basic feature. One of the quite remarkable characteristics of the Nd^{139m} decay is the large number of interconnecting transitions between the high-lying, three-quasiparticle levels. All of them seem to prefer decay to other members of the multiplet,

in spite of the low energies involved, rather than to other lower lying levels. Now, a look at the Sm^{141m} decay scheme (Figure 46) shows that none of the high lying levels have any interconnecting transitions. They are still levels preferred by Sm^{141m} for β feeding, as indicated by the low log ft values, but for some reason they remain independent of each other. In both nuclei, the conclusion is reached that there is no direct β population of the daughter ground state. There is some evidence, however, that there is some β feeding to the 1st excited state in each daughter (Pr^{139} and Pm^{141}). Beery (Bee 69d) places an upper limit of 3% on the ε decay from Nd^{139m} to the $7/2^+$ state at 113.8 keV in Pr^{139}. This would lead to a log ft value of 7.6. In the present case, there seems to be $\approx$5% β branch to the 1st excited state ($7/2^+$) in Pm^{141}. This yields a log ft of 7.2. In both cases, the log ft's are too low for what should be a 1st forbidden unique β transition. There is no satisfactory explanation for this state of affairs.

Both the Pr^{139} and Nd^{141} nuclei have $11/2^-$ levels fed by β branches having abnormally high log ft's (7.0 and 6.7, respectively) for what is presumably an allowed $11/2^- \rightarrow 11/2^-$ transition. As will be seen in the following discussion, this is explained by the particle rearrangement which must take place for this transition.

In each case, the proposed three-quasiparticle levels have similar log ft values. For the multiplet of 6 three-quasiparticle levels in Pr^{139} the average log ft is 6.0, while in Pm^{141} the 6 levels have an average log ft of 6.1.

Figure 50 shows a shell model representation for the

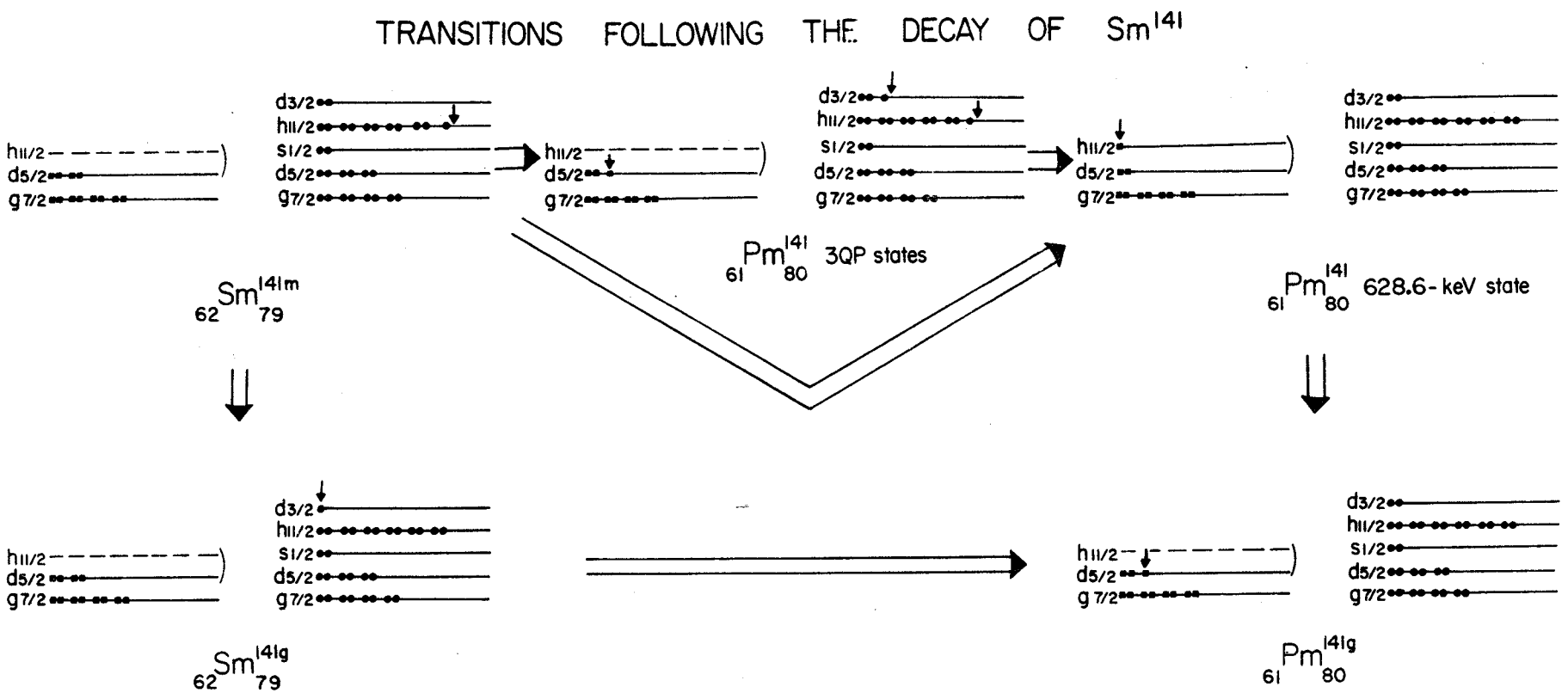

Figure 50. Shell model schematic representation of the reaction mechanism for the formation of three-quasiparticle states in Pm^{141}.

formation of the three-quasiparticle states in Pm^{141}. The ground state of Sm^{141} has 4 protons outside the $(g_{7/2})^8$ subshell. A major component of its wave function could be represented as being $(\pi d_{5/2})^{-2}(\nu d_{3/2})^1$. β^+/ε decay from this state can be considered simply to be the transformation of a $d_{5/2}$ proton into a $d_{3/2}$ neutron. This results in a Pm^{141} ground state configuration of $(\pi d_{5/2})^{-3}$ $(\nu d_{3/2})^2$. The isomeric state of Sm^{141} is formed by promoting an $h_{11/2}$ proton to the $d_{3/2}$ orbital, resulting in the Sm^{141m} configuration being $(\pi d_{5/2})^{-2}(\nu d_{3/2})^2(\nu h_{11/2})^{-1}$. Now, the Pm^{141} three-quasiparticle states are formed by converting a $d_{5/2}$ proton into a $d_{3/2}$ neutron, resulting in the quasiparticle configuration $(\pi d_{5/2})^{-3}$ $(\nu d_{3/2})^{-1}(\nu h_{11/2})^{-1}$. Since it is assumed that paired nucleons do not contribute to the spin of a state, we could just as easily rewrite the "effective" part of this configuration as $(\pi d_{5/2})^{-1}$ $(\nu d_{3/2})^{-1}(\nu h_{11/2})^{-1}$, the same configuration as given for the three-quasiparticle states in Pr^{141}.

Now we can consider why the allowed β transition $(11/2^-\rightarrow 11/2^-)$ between Sm^{141m} and Pr^{141} is hindered. From the diagram in Figure 50 it is seen that the transition requires not only the promotion of a $d_{5/2}$ proton to the $h_{11/2}$ state, but also the conversion of another $d_{5/2}$ proton to an $h_{11/2}$ neutron. This "double move" would certainly be expected to hinder the transition and is indeed the case for both Nd^{139} and Sm^{141}, as previously discussed.

The remaining states in the Pm^{141} nucleus, as seen both from Sm^{141m} and Sm^{141g} decay, are less easy to deal with. Viewing all of the Pm^{141} states as quasiparticle states would allow one to discuss these remaining states as probably best described as single-

quasiparticle states. They could be formed from fragmented single particle states or they could be described as vibrational states formed from core-coupling the lowest 2^+ state in Pm^{140} to a single-quasiparticle state. That this is possible at low energies is born out by noticing that the 2^+ level in Pm^{140} lies between 0.77 and 1.0 MeV (TI 67).

4.4.12: Remaining Peaks in the Sm^{141m+g} Singles Spectra

As already mentioned several times, many peaks in the Sm^{141m+g} spectra cannot be positively identified as originating from the decay of Sm^{141m} or Sm^{141g}. Some of these peaks are due to contaminant activities produced during the bombardments or to the daughter activities that build up. These peaks are listed in Table 25: those with half-lives under 20 minutes, those with half-lives over 20 minutes and those which occur only in quadrant 1 of the 4 quadrants mentioned in § 4.4.2. The intensities in each case are normalized to the Sm^{141m} 196.6-keV intensity. Those peaks recognized as belonging to contaminatnts have been labeled as such. The inclusion of this table is purely for future reference.

Table 25. Peaks in the singles spectra which have not been assigned to the decay of Sm^{141g} or Sm^{141m}

$t_{\frac{1}{2}}$ <20 min		$t_{\frac{1}{2}}$ >21 min			In Quad 1 only		
Energy (keV	Intensity	Energy (keV)		Intensity	Energy (keV)		Intensity
		114.4	(Nd^{139m})?	1.37			
		189.8		3.59			
438.2	19.8	208.9	(Nd^{139m})	0.29	648.6		0.13
549.2	0.39	424.9	(Nd^{139m})?	1.02	717.7		0.19
677.0	2.39	622.3	(Pm^{141})	1.33	753.4		0.81
693.8	0.87	641.6		1.44	756.6	(Pm^{141})	1.03
843.7 (Mg^{27})	5.10	708.1	(Nd^{139m})?	0.64	854.3		0.77
1014.6 (Mg^{27})	1.84	738.1	(Nd^{139m})	0.52	891.7		0.42
1057.1	1.47	764.1		0.30	958.4		0.26
1091.8	1.15	820.8		0.34	978.0		0.33
1482.4	0.40	886.4	(Pm^{141})	4.53	1046.9		0.42
1901.7	0.46	952.2		0.76	1094.9		0.27
2037.7	1.64	1037.7		0.24			
		1223.3	(Pm^{141})	7.79			
		1345.7	(Pm^{141})	2.76	1460.9		0.97
		1369.1	(Na^{24})	1.82	1479.8		0.23
		1403.5	(Pm^{141})	1.23	1482.4		0.40
		1564.9	(Pm^{141})	0.80	1768.2		0.63
		1576.0		6.28	1967.5		0.19
		1597.3	(Pm^{141}	1.70	2312.6		0.50
		1627.9	(Pm^{141})	0.40			
		1732.2		1.47			
		1765.5		0.99			
		2244.9		0.55			

4.5. The Search for Dy^{147}

4.5.1. Introduction

Our first observation of Gd^{145m} (§4.2.) along with the previously discovered $N = 81$ isomers led us to speculate on the existence of (and possibilities for producing) Dy^{147m}. It was felt that there would be a better chance for observing Dy^{147m} than there would be for observing Dy^{147g} since this latter species should ε/β^+ decay to Tb^{147} with quite a short half-life ($Q\varepsilon \approx 7.3$ MeV, (Myer 65)). Also, it should be easier to identify the $M4$ decay of the isomeric species by the internal conversion electron peaks, similar to the technique we used for Gd^{145m}.

The energy of the Dy^{147} isomeric level was estimated to be 604 ± 16 keV, based on a quadratic-least-squares extrapolation using the 7 $M4$ energies which were available for the other $N = 81$ isotones. The reduced $M4$ transition probability was estimated in the same fashion, and resulted in a value of 3.04 for the Dy^{147m} species. These values for the energy and the transition probability were then used to obtain an estimate for the $M4$ half-life of this state by relating them through the $M4$ single particle equation (see Chapter V). This procedure resulted in a value of 5 minutes for the $M4$ half-life of the Dy^{147} isomeric species.

These results were of such a nature that it seemed worthwhile to attempt a search for this species. This resulted in the performance of several experiments at Yale University using their Heavy Ion Linear Accelerator to furnish the required C^{12} beam.

During the course of these experiments we have obtained singles spectra for γ rays, x-rays, and positron decay. In addition, a γ-ray versus x-ray coincidence run was carried out by gating on the Tb K_β x-rays and observing coincidence γ rays.

The point at which we presently find ourselves does not allow us to make a positive statement on the nature of Dy^{147}. As will be brought out in the following sections, there is indirect evidence that we do, in fact, produce Dy^{147}. However, we cannot specifically identify those γ rays resulting from its decay.

4.5.2. Singles Experiments

All of the equipment used at Yale University is described in §2.2.4. In all cases it took a minimum of 2 - 3 minutes to retrieve the target at the end of the bombardment, transfer it to some suitable container for counting, and transport it to the counting area. Because of the short half-lives involved, no chemical separations of the target material were attempted.

4.5.2.A. γ-ray Singles Experiments

The logical reaction for the production of Dy^{147} (the one we started with, of course) is the $Nd^{142}(C^{12},7n)Dy^{147}$ reaction (Q = -78.9 MeV). Several spectra were obtained from $Nd_2^{142}O_3$ targets which had been bombarded with C^{12} beams ranging in energy from 80 to 120 MeV. In all of these spectra, we paid particular attention to the peaks in the 500-700 keV region, peaks which might be due to the predicted $M4$ transition. As it turned out, we were never lacking for possible candidates in this or in any other energy region.

During these runs we observed the two intense peaks at energies of 1757.8 and 1880.6 keV which belong to Gd^{145} (§ 4.3). We postulate that this activity was produced by the $Nd^{142}(C^{12},\alpha 5n)Gd^{145}$ reaction ($Q = -56.2$ MeV). From this observation we reasoned that this might also be a preferred type of reaction using Sm^{144} as the target. Thus, a set of runs was made over the same C^{12} energies with the expectation that the $Sm^{144}(C^{12},\alpha 5n)Dy^{147}$ reaction ($Q = -65.2$ MeV) would constitute a major reaction path. Figure 51 shows a typical γ-ray spectrum. This was obtained by counting a Sm^{144} target for 13 minutes beginning 2-3 minutes after the end of the bombardment. The bombardment was for 1 minute with the full energy (120-MeV) C^{12} beam. The energies shown on Figure 51, as well as on the other figures and tables in this section, were obtained from an energy calibration curve constructed from a separate Co^{56} standard spectrum at the same amplifier gain and same source position. Because of this the reported energies are only good to approximately ±1.0 keV.

Table 26 is a list of the γ-ray energies and net peak areas for the spectrum of Figure 51. Net peak areas must be reported (as opposed to relative transition intensities) because of the unavailability of detector efficiency curves for the detectors used at Yale.

Figure 52 is a spectrum from a Sm^{144} target obtained 4 days after a 1 hour bombardment at full beam energy (120 MeV). Energies are shown only for some of the more prominent peaks to save clutter on the spectrum. A listing of energies and net peak areas for most of the peaks on this spectrum will be found in Table 27. Notice on Figure 52 that peaks have been identified which prove the presence of Gd^{149}, Gd^{147}, and Eu^{147}. This is taken to be evidence of the

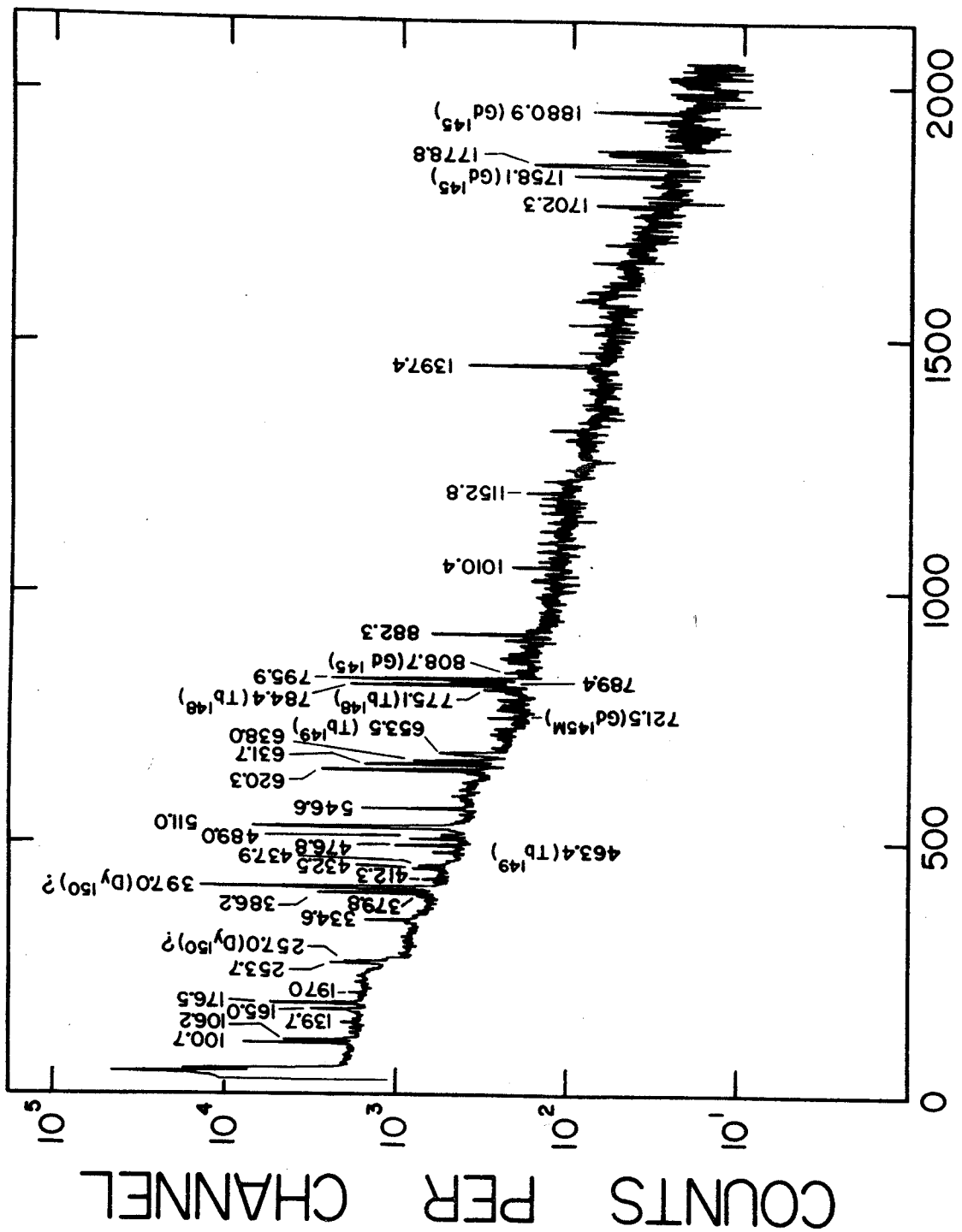

Figure 51. Spectrum resulting from a Sm^{144} target immediately after a 1 minute bombardment with a 120 MeV C12 beam.

Table 26. γ-ray energies and peak areas for transitions observed in a Sm^{144} target immediately after bombardment.

Energy (keV)	Peak Area	Energy (keV)	Peak Area
50.995	0.20 (5)	546.596	0.20 (4)
100.727	0.94 (4)	620.313	0.53 (4)
106.201	0.52 (4)	631.738	0.26 (4)
139.697	0.69 (3)	638.024	0.13 (4)
165.034	0.25 (4)	653.473	0.72 (3)
176.518	0.73 (4)	721.487	0.30 (3)
196.995	0.53 (3)	775.071	0.29 (3)
253.708	0.20 (4)	784.410	0.33 (4)
257.019	0.14 (4)	789.361	0.75 (3)
334.618	0.92 (3)	795.875	0.45 (4)
379.847	0.40 (3)	808.700	0.16 (3)
386.197	0.39 (4)	882.269	0.14 (4)
397.030	0.26 (5)	1010.372	0.30 (3)
412.295	0.37 (3)	1152.783	0.24 (3)
432.459	0.71 (3)	1397.440	0.11 (4)
437.941	0.55 (3)	1702.252	0.15 (3)
463.404	0.47 (3)	1758.145	0.23 (3)
476.839	0.16 (4)	1778.766	0.49 (3)
488.953	0.88 (3)	1880.932	0.19 (3)
510.959	0.12 (5)		

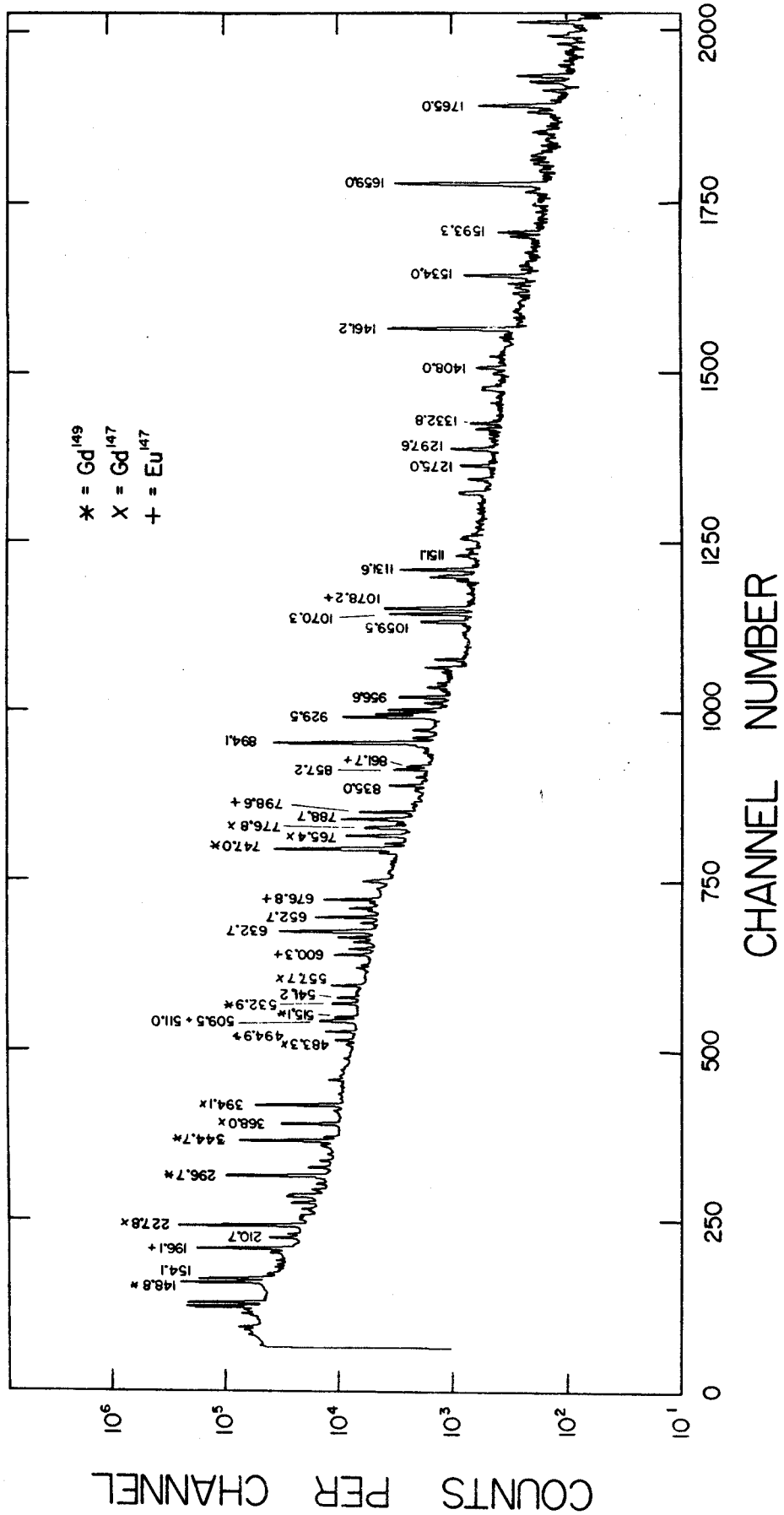

Figure 52. Spectrum resulting from a Sm^{144} target 4 days after being bombarded with a 120 MeV C^{12} beam.

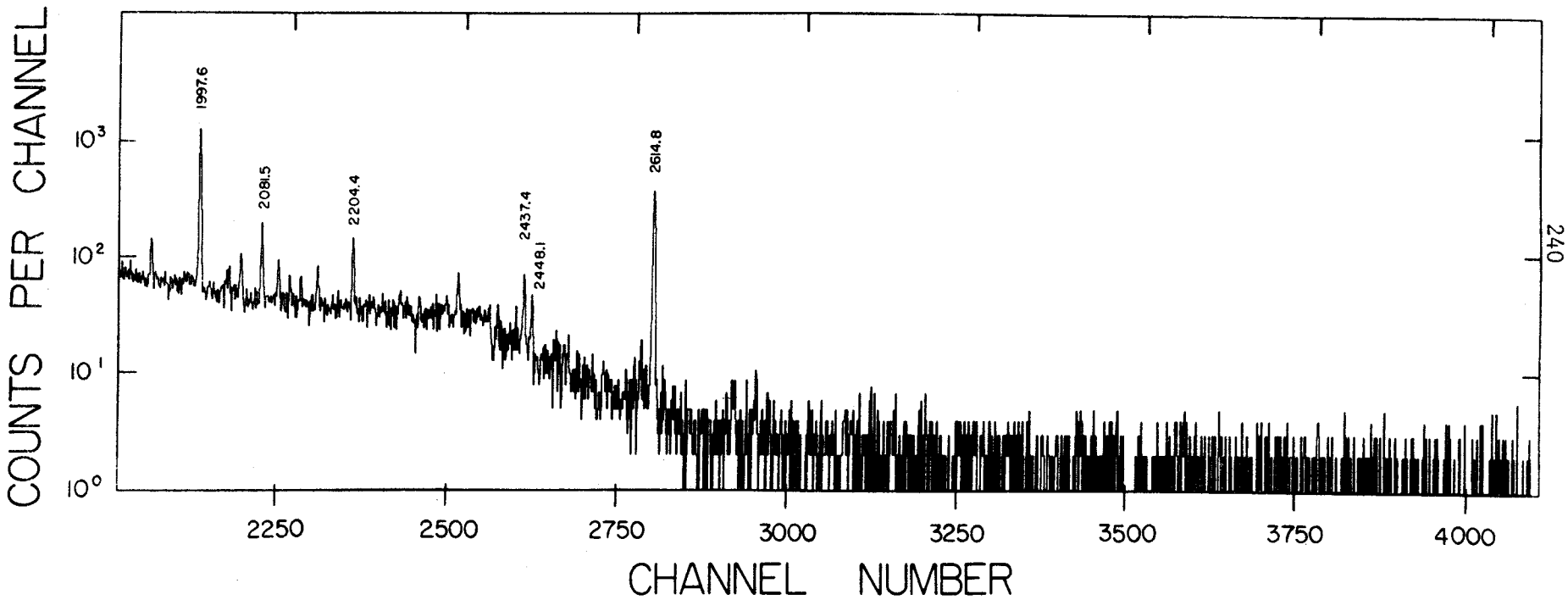

Figure 52, (con't). High-energy portion of spectrum resulting from a Sm^{144} target.

Table 27. γ-ray energies and peak areas for transitions observed in a Sm^{144} target four days after the bombardment.

Energy (keV)	Peak Area	Energy (keV)	Peak Area
138.052	0.17 (4)	337.758	0.59 (4)
148.829	0.37 (6)	244.737	0.13 (6)
154.141	0.28 (6)	350.037	0.66 (4)
169.806	0.53 (4)	367.983	0.53 (5)
173.913	0.91 (4)	386.001	0.31 (4)
179.154	0.13 (5)	394.075	0.98 (5)
189.890	0.21 (5)	409.015	0.19 (4)
196.057	0.29 (6)	420.083	0.96 (3)
210.665	0.40 (5)	428.642	0.64 (4)
215.580	0.11 (5)	434.439	0.16 (4)
227.782	0.46 (6)	442.036	0.15 (4)
236.752	0.10 (5)	458.174	0.21 (4)
241.176	0.96 (4)	477.166	0.26 (4)
250.255	0.82 (4)	483.250	0.78 (4)
259.233	0.23 (5)	494.858	0.12 (5)
269.937	0.28 (5)	509.501	0.17 (5)
277.202	0.65 (4)	515.115	0.67 (4)
285.404	0.64 (4)	532.910	0.11 (5)
296.746	0.20 (6)	541.234	0.80 (4)
307.910	0.15 (5)	557.723	0.11 (5)
316.582	0.72 (4)	581.941	0.29 (4)
325.821	0.31 (4)	586.213	0.17 (4)

Table 27. (Continued)

600.299	0.13 (5)	929.507	0.19 (5)
608.517	0.71 (4)	933.776	0.80 (4)
617.978	0.46 (4)	939.333	0.54 (4)
624.2.6	0.98 (4)	938.604	0.15 (4)
632.694	0.67 (5)	956.628	0.48 (4)
644.447	0.43 (4)	969.928	0.13 (4)
652.685	0.25 (5)	975.647	0.59 (3)
660.736	0.23 (4)	989.451	0.38 (3)
664.793	0.74 (4)	996.274	0.16 (4)
676.830	0.18 (5)	1007.357	0.11 (4)
692.274	0.12 (4)	1059.535	0.25 (4)
702.463	0.59 (4)	1070.312	0.59 (4)
726.527	0.57 (3)	1078.163	0.79 (4)
741.713	0.24 (4)	1116.643	0.53 (3)
747.034	0.83 (5)	1121.741	0.13 (4)
754.787	0.16 (4)	1131.624	0.47 (4)
765.397	0.15 (5)	1151.083	0.81 (3)
776.826	0.84 (4)	1160.404	0.31 (3)
788.677	0.15 (5)	1173.832	0.78 (3)
798.587	0.95 (4)	1177.014	0.67 (3)
835.001	0.40 (4)	1237.704	0.11 (4)
846.691	0.81 (3)	1256.340	0.81 (3)
857.173	0.40 (4)	1274.970	0.13 (4)
861.709	0.23 (4)	1297.552	0.18 (4)
880.552	0.41 (3)	1325.341	0.72 (3)
894.136	0.82 (5)	1332.755	0.96 (3)
911.326	0.20 (4)	1360.289	0.19 (3)

Table 27. (Continued)

1407.963	0.88 (3)	1804.775	0.55 (3)
1423.464	0.25 (3)	1858.433	0.19 (3)
1461.246	0.88 (4)	1877.228	0.60 (3)
1533.335	0.27 (3)	1931.645	0.26 (3)
1534.024	0.19 (4)	1997.581	0.31 (4)
1587.674	0.40 (3)	2053.078	0.20 (3)
1593.272	0.70 (3)	2081.450	0.41 (3)
1659.010	0.78 (4)	2103.933	0.17 (3)
1756.281	0.19 (3)	2204.446	0.34 (3)
1765.016	0.15 (4)	2437.360	0.17 (3)
1785.094	0.19 (3)	2448.057	0.10 (3)
1796.490	0.36 (3)	2614.826	0.13 (4)

original production of Dy^{147} at the time of bombardment. One could argue that the 147 mass chain was originally populated by a (formal) $Sm^{144}(Cl^{2},3p6n)Tb^{147}$ reaction and this certainly cannot be ruled out. However, as will be discussed in §4.4.2.C., there is other evidence that Dy^{147} is produced.

An interesting sidelight is that when using the Sm^{144} targets we were still able to observe Gd^{145g} in the resulting spectra. This suggests a reaction which could be written as $Sm^{144}(Cl^{2},2\alpha 3n)Gd^{145}$. Whether this product is produced via a compound nucleus (or possibly a stripping reaction) is uncertain.

4.5.2.B. Conversion-Electron Experiments

An $M4$ transition of 171 keV should have a K-conversion coefficient of ≈50. Both the Nd^{142} and the Sm^{144} targets were used to obtain β^{+} spectra with the Si(Li) surface barrier detector described in §2.2.2. At no bombarding energy (70-120 MeV) were we able to identify any conversion peak rising above the β^{+} continuum. Thus, if we are indeed producing Dy^{147m}, as we believe, it either has a half-life shorter than we are able to cope with or it decays predominently via an ε/β^{+} branch.

4.5.2.C. X-ray Experiments.

An x-ray detector (described in §2.2.4) became available for use during the experiments with Sm^{144}. Spectra were taken for Sm^{144} targets, bombarded at various energies, both immediately after the bombardments and at later periods. While x-ray peaks cannot show

the specific isotopes which are making contributions, they are very useful for confirmation of the elements being produced. In our case, we could verify that immediately after bombardment the Tb x-rays were the most intense ones present. This is what would be expected for the ground state decay of Dy. By following a given target versus time it was possible to watch the Tb dying away and the daughter x-rays (mostly Gd and Eu) increasing in intensity. The fact that there was no recognizable Dy peak is added evidence that we are not able to "see" the isomeric transition in Dy^{147}. We are undoubtedly also producing higher mass Dy species such as Dy^{148}, Dy^{149}, etc., but we cannot pin down the relative abundances from these experiments.

4.5.3. γ-ray versus x-ray Coincidence Experiments.

Since the x-ray detector had quite high resolution (275 eV @ 6.0 keV), it was practical to set up a γ-ray versus x-ray coincidence experiment with a coincidence gate set on the K_β x-ray of Dy. In this manner we could identify those γ rays which were in coincidence with the Dy x-rays.

Possibly a few comments are in order on some of the difficulties encountered with this type of experiment. First and foremost is the inherent differences in the timing characteristics of the x-ray and the γ-ray detectors. In this case the x-ray detector had a much greater "walk" problem than did the γ-ray detector. Therefore the dynamic range of the coincidence experiment for a given resolving time was much less than for other types of coincidence experiments which we have performed. Another problem is that of finding a

source having coincidence γ and x-rays which can be used for timing purposes. Since positron sources cause saturation and ringing problems in the x-ray detector, it is best to use a source decaying solely by electron capture. Since this "ideal" source was not available at Yale, we set up the electronics using the same source as for the experiment. Still another difficulty is detector geometry. Because of the large size difference between these two detectors it is difficult to obtain similar counting rates in each. The source must be placed by trial and error to maximize the count rate.

Our coincidence spectrum is shown in Figure 53 along with a self-gated singles spectrum taken at the same gain. The net relative peak areas for the coincidence spectrum are compared with their singles values in Table 28. From the analysis it is found that the peaks at 100.7, 176.5, 397.0 and 620.3 keV are clearly in coincidence with the Dy x-rays. As in the previous types of experiments, we are still not able to identify explicitly those peaks due to the decay of Dy^{147}.

4.5.4. Discussion

It has become obvious that more research will have to be done on this region in order to elucidate further the structure of Dy^{147}. In particular, more complete and detailed information for such species as Dy^{148}, Dy^{149}, Tb^{147}, Tb^{148}, Tb^{149}, etc., is needed. What little work has been reported on this region has been carried out with scintillation methods and lacks the detail which we need.

In summary, the research which we have conducted to date allows us to say that if Dy^{147m} exists for a period of time long enough for

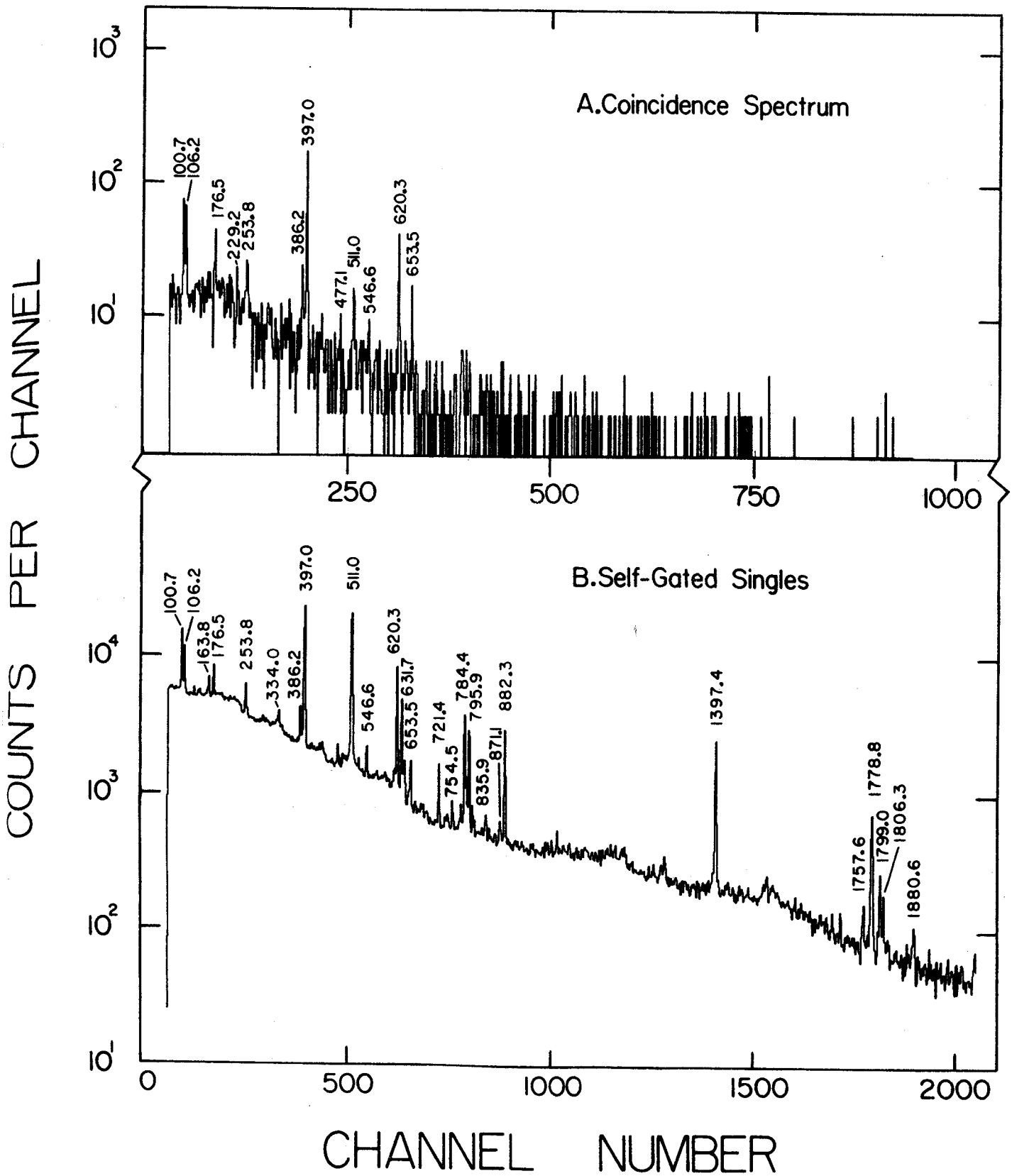

Figure 53. γ-ray versus x-ray coincidence spectrum from a Sm^{144} target compared to a self-gated singles spectrum at the same gain.

Table 28. Coincidence results from the γ-ray versus x-ray experiment performed on a Sm^{144} target.

Energy [a] (keV)	Peak Area [b]	
	Singles	Coincidence
100.7	39.8	41.3
106.2	20.5	29.6
176.5	13.1	15.8
253.8	10.8	17.4
386.6	8.42	14.2
397.0	≡100	≡100
477.1	?	3.6
511.0	108	13.0
547.1	3.09	4.45
620.3	26.5	26.7
652.5	4.75	7.69

[a] These energies were obtained by using an external Co^{56} standard spectrum. Hence, they should not be depended on to be closer than ±1.0 keV.

[b] No efficiency curve was available for the detector used in this experiment.

us to count it must decay predominantly via ε/β^+. x-ray spectra show us that the mass 147 chain is populated. The x-ray gated spectrum identifies the more prominent peaks in coincidence with Tb x-rays. Hopefully these results will be useful for further investigations in this region of nuclides.

CHAPTER V

MULTIPOLE RADIATION AND THE SINGLE PARTICLE MODEL

Nuclear reactions which are initiated by accelerated ions generally occur via a compound nucleus which, in turn, emits one or more neutrons (and frequently α particles o protons). This leaves the product nucleus on the neutron-deficient side of β stability. Consequently, the nuclei studied in this investigation, which were produced by cyclotron bombardments, are ε/β^+ emitters. To account theoretically for these processes of nuclear decay requires the adoption of a model of the nucleus with explicit mathematical relationships for the interactions among nucleons.

Almost all nuclear excited states decay at least occasionally by spontaneous emission of electromagnetic quanta, emission which can be characterized in a fashion analogous to the multipole description of atomic transitions. The intent of this chapter is to give the main steps on the way to obtaining numerically tractable equations expressing the matrix elements and transition probabilities arising when a single, unpaired nucleon changes its angular momentum state, i.e., by using a simple shell model picture of the nucleus. Since this type of model is particularly applicable to nuclei near closed shells, it will be of interest to compare these theoretical predictions with the experimental information available for the *M*4 transitions of the odd-mass nuclei near closed shells. These calculations have been used in § 4.2. and will be used in Chapter 6.

5.1. Multipole Radiation

γ rays were recognized to be electromagnetic in nature by von Laue in 1923. The description of this γ-ray process essentially uses the theory already developed for atomic transitions, that is, using the theory of multipoles. Several books (Jac62,Roy67,Mosz65, Blat52) describe this theory in varying detail. The notation used in this chapter is pretty much common to these texts.

The job at hand is to describe in some way the electromagnetic field that causes the emission of an energy quantum from a de-exciting nucleus. The source of the emitted quantum is then to be described in terms of a charge-current distribution confined to a small region of nuclear dimensions. The field and the source must then be connected and finally transformed into the equivalent quantum mechanical expressions.

This overall derivation is most eloquently expressed by the use of quantum electrodynamics; however, this requires more mathematical sophistication. It is therefore desirable to carry the derivation as far as possible in classical terms and then transform the result to the equivalent quantum mechanical expressions.

It will be seen that electromagnetic transition probabilities can be derived without invoking a specific nuclear model. The so-called "long-wavelength" approximation is used, the wave length of the

electromagnetic radiation being large relative to the nuclear dimensions. Finally, after the expressions are derived in general terms, a model must be introduced in order to obtain numerical results.

Before beginning the derivation, several mathematical results, which will be used along the way, must be considered.

5.1.1. Mathematical Paraphernalia

The theory of multipole radiation draws on a diverse set of mathematical techniques. A few definitions and results that will be needed later are given in this section.

5.1.1.A. Angular Momentum Operators

The orbital angular momentum operator is defined as

$$\vec{L} = \frac{1}{i}(\vec{r}x\vec{\nabla}) \ ,$$

or in cartesian coordinates,

$$\vec{L} = \vec{i}L_x + \vec{j}L_y + \vec{k}L_z .$$

These components can be regrouped as follows:

$$L_+ = L_x + iL_y = e^{i\phi}(\frac{\partial}{\partial\theta} + i\cot\theta\frac{\partial}{\partial\phi}) \qquad (1)$$

$$L_- = L_x - iL_y = e^{-i\phi}(-\frac{\partial}{\partial\theta} + i\cot\theta\frac{\partial}{\partial\phi}) \qquad (2)$$

$$L_z = i\frac{\partial}{\partial\phi} . \qquad (3)$$

Angular momentum identities which will be useful later on are:

$$L^2\vec{L} = \vec{L}L^2 \tag{4}$$

$$\vec{L}x\vec{L} = i\vec{L} \tag{5}$$

$$L_j\nabla^2 = \nabla^2 L_j \tag{6}$$

where $$\nabla^2 = \frac{1\partial^2}{r\partial r^2}(r) - \frac{L^2}{r^2} . \tag{7}$$

5.1.1.B. Spherical Harmonics

Spherical harmonics are solutions to the differential equation

$$L^2Y_{\ell m} = -\left[\frac{1}{\sin\theta}\frac{\partial}{\partial\theta}\left(\sin\theta\frac{\partial}{\partial\theta}\right) + \frac{1}{\sin^2\theta}\frac{\partial^2}{\partial\phi^2}\right]Y_{\ell m} = \ell(\ell+1)Y_{\ell m}, \tag{8}$$

where L is the total angular momentum, θ,ϕ are the spherical coordinate angles, and $Y_{\ell m}$ are the spherical harmonics. These solutions are usually written as

$$Y_{\ell m}(\theta,\phi) = \sqrt{\frac{(2\ell+1)(\ell-m)!}{4\pi(\ell+m)!}}\ P_{\ell m}(\cos\theta)e^{im\phi}, \tag{9}$$

where the first factor on the right side of the equation is for normalization. These functions form an orthonormal set with the orthogonality condition:

$$\int_0^{2\pi} d\phi \int_0^{\pi} \sin\theta\ d\theta\ Y^*_{\ell' m'}(\theta,\phi)Y_{\ell m}(\theta,\phi) = \delta_{\ell'\ell}\ \delta_{m'm} \tag{10}$$

The "P" functions in the expressions are called associated Lengendre functions and can be expressed as

$$P_{\ell m}(\cos\theta) = (-1)^m(1-\cos^2\theta)^{m/2}\frac{d^m}{(d(\cos\theta))^m}\ P_\ell(\cos\theta). \tag{11}$$

Retreating one more step, we have the Legendre functions defined by the recursion relationship

$$P_\ell(\cos\theta) = \frac{1}{2^\ell \ell!}\left[\frac{d^\ell}{(d(\cos\theta))^\ell}\right](\cos^2\theta-1)^\ell. \tag{12}$$

For our purposes, the vector spherical harmonics can be defined as

$$\vec{X}_{\ell m} = \left[\frac{1}{\sqrt{\ell(\ell+1)}}\right]\vec{L}\cdot Y_{\ell m}(\theta,\phi). \tag{13}$$

The first factor on the right arises from normalization. Operating on the spherical harmonics with the angular momentum operators of Equations 1, 2, 3 yields the results:

$$L_+ Y_{\ell m} = \sqrt{(\ell-m)(\ell+m+1)}\,Y_{\ell,m+1} \tag{14}$$

$$L_- Y_{\ell m} = \sqrt{(\ell+m)(\ell-m+1)}\,Y_{\ell,m-1} \tag{15}$$

$$L_z Y_{\ell m} = m\,Y_{\ell m} \tag{16}$$

5.1.1.C. Laplacian Operator

The Laplacian operator (∇^2) can be written in terms of spherical coordinates (r,θ,ϕ) as

$$\nabla^2 = \frac{1}{r^2}\frac{\partial}{\partial r}\left(r^2\frac{\partial}{\partial r}\right) + \frac{1}{r^2\sin\theta}\frac{\partial}{\partial\theta}\left(\sin\theta\frac{\partial}{\partial\theta}\right) + \frac{1}{r^2\sin^2\theta}\frac{\partial^2}{\partial\phi^2} \tag{17}$$

5.1.1.D. Bessel Functions

The differential equation

$$\frac{d^2R}{dx^2} + \frac{1}{x}\frac{dR}{dx} + \left(1-\frac{\nu^2}{x^2}\right)R = 0 \tag{18}$$

is called the Bessel equation. The two solutions are

$$J_\nu(x) = \left(\frac{x}{2}\right)^\nu \sum_{j=o}^{\infty}\frac{(-1)^j}{j!\Gamma(j+\nu+1)}\left(\frac{x}{2}\right)^{2j} \tag{19a}$$

$$J_{-\nu}(x) = \left(\frac{x}{2}\right)^{-\nu} \sum_{j=o}^{\infty}\frac{(-1)^j}{j!\Gamma(j-\nu+1)}\left(\frac{x}{2}\right)^{2j} \tag{19b}$$

These are Bessel functions of the first kind of order $\pm\nu$. These two solutions are linearly dependent when ν is an integer. A second solution which is always linearly independent with J_ν has been found to be

$$N_\nu(x) = \frac{J_\nu(x)\cos \nu\pi - J_{-\nu}(x)}{\sin \nu\pi} \tag{20}$$

This is known as the Newmann function or Bessel function of the second kind.

It is generally useful to combine Bessel and Neumann functions to form Bessel functions of the third kind. These are known as Hankel functions and are written as

$$H_\nu^{(1)}(x) = J_\nu(x) + iN_\nu(x) \tag{21a}$$

$$H_\nu^{(2)}(x) = J_\nu(x) - iN_\nu(x) \tag{21b}$$

Hankel functions are still valid solutions to Bessel's equation and are frequently the form of the solutions that are used in problems. Now that the Bessel functions have been defined in their most general form, we need to consider specific cases which will be of use in the present derivation. If we redefine the equations as spherical Bessel functions and let $\nu = \ell + \frac{1}{2}$, the following formulas result:

$$j_\ell(x) = \left(\frac{\pi}{2x}\right)^{\frac{1}{2}} J_{\ell+\frac{1}{2}}(x) \tag{22a}$$

$$n_\ell(x) = \left(\frac{\pi}{2x}\right)^{\frac{1}{2}} N_{\ell+\frac{1}{2}}(x) \tag{22b}$$

$$h_\ell^{(1,2)}(x) = \left(\frac{\pi}{2x}\right)^{\frac{1}{2}} [J_{\ell+1/2}(x) + iN_{\ell+1/2}(x)]. \tag{22c}$$

It is often difficult to evaluate expressions numerically containing these functions. Under certain circumstances asymptotic values can be used. In particular, it is useful to look at the expressions which result when x<<1 and for when x>>1.

Asymptotic limit for x<<1

This would be an appropriate approximation for working atomic and nuclear problems. In these cases the wavelengths of the emitted quanta are large compared to the size of the source (nucleus). In this limit the results are:

$$j_\ell(x) \longrightarrow \frac{x^\ell}{(2\ell+1)!!} \tag{23a}$$

$$n_\ell(x) \longrightarrow \frac{-(2\ell+1)!!}{x^{\ell+1}} \tag{23b}$$

Asymptotic limit for x>>1

A useful application for this asymptotic limit (wave-zone approximation) would be in describing fields far from the source such as problems dealing with angular distributions. The appropriate expressions are:

$$j_\ell(x) \rightarrow \frac{1}{x} \sin\left(x - \frac{\ell\pi}{2}\right) \tag{23c}$$

$$n_\ell(x) \rightarrow -\frac{1}{x} \cos\left(x - \frac{\ell\pi}{2}\right) \tag{23d}$$

$$h_\ell^{(1)}(x) \rightarrow (-i)^{\ell+1} \frac{e^{ix}}{x} \tag{23e}$$

5.1.2. Maxwell's Equations

All of electromagnetism is contained in the Maxwell equations. It has been said about electrostatics (a subset of these equations) that "···there is nothing to the subject; it is just a case of doing complicated integrals over three dimensions···" (Feyn64). This is just as true for the full set of Maxwell equations. The catch is knowing how to solve the integrals.

In a source-free region, Maxwell's equations can be written as

$$\vec{\nabla} \times \vec{E} = -\frac{1}{c}\frac{\partial \vec{B}}{\partial t} \qquad \vec{\nabla} \times \vec{B} = \frac{1}{c}\frac{\partial \vec{E}}{\partial t}$$

$$\vec{\nabla}\cdot\vec{E} = 0 \qquad \vec{\nabla}\cdot\vec{B} = 0 \tag{24}$$

In the quantized case, the frequency is proportional to the energy, and thus has a definite value. In this manner, by assuming a sinusoidal time dependence of the fields, the fields may be written as

$$\vec{E}(\vec{r},t) = \mathrm{Re}[\vec{E}(\vec{r})e^{-i\omega t}] \tag{25a}$$

$$\vec{B}(\vec{r},t) = \mathrm{Re}[\vec{B}(\vec{r})e^{-i\omega t}] \tag{25b}$$

where ω is the angular frequency, related to the propagation vector $\vec{k}$ by $\omega = kc$, where $k = 2\pi/\lambda$.

This assumption allows the rewriting of the equations thus:

$$\vec{\nabla} \times \vec{E} = ik\vec{B}\,, \quad \vec{\nabla} \times \vec{B} = -ik\vec{E} \tag{26}$$

This set of equations can be reduced in number by solving for $\vec{E}$ or $\vec{B}$ in terms of the other. Thus, on elimination of $\vec{E}$

$$(\nabla^2 + k^2)\vec{B} = 0$$

$$\vec{\nabla}\cdot\vec{B} = 0\,, \quad \vec{E} = \frac{1}{k}\vec{\nabla} \times \vec{B} \tag{27}$$

On elimination of $\vec{B}$, an equivalent set of equations can be written as

$$(\vec{\nabla}^2 + k^2)\vec{E} = 0 \qquad \vec{\nabla} \cdot \vec{E} = 0$$
$$\vec{B} = -\frac{1}{k}\vec{\nabla} \times \vec{E}. \tag{28}$$

In each of these sets the first equation is seen to be a vector Helmoholtz equation. It is now necessary to determine the multipole solutions of the functions $\vec{E}$ and $\vec{B}$.

5.1.3. Multipole Expansion of the Radiation Field

For a time varying EM field we need an expansion in terms of vector spherical waves. It is easiest to consider first the scalar wave function, which can be written as $\psi(\vec{r},t)$ and which satisfies the wave equation,

$$\nabla^2\psi - \frac{1}{c^2}\frac{\partial^2\psi}{\partial t^2} = 0$$

A Fourier analysis in time yields:

$$\Psi(\vec{r},t) = \int_{-\infty}^{\infty}\Psi(\vec{r},\omega)e^{-i\omega t}\,d\omega \tag{29}$$

where $\omega = kc$ and k is the propagation vector. Each component of the above transform satisfies the Helmholtz wave equation

$$(\nabla^2 + k^2)\psi(\vec{r},\omega) = 0.$$

∇^2 is the Laplacian operator as given in equation 17. Assuming the nucleus to be symmetrical about its orgin, solutions can be found to the Helmholtz equation in terms of spherical harmonics. Therefore, solutions are sought of the form

$$\psi(\vec{r},\omega) = \sum_{\ell,m} f_\ell(r)Y_{\ell m}(\theta,\phi) \tag{30}$$

in terms of the spherical harmonics as defined in equation 9. The functions $f_e(r)$ are related to the Bessel functions of equation 19 by

$$f_\ell(r) \approx \frac{1}{r^{\frac{1}{2}}} J_{\ell+\frac{1}{2}}(x) = \frac{1}{r^{\frac{1}{2}}}\left(\frac{2x}{\pi}\right) j_\ell(x), \text{ where } x \equiv kr. \tag{31}$$

Equation 30 can be written because of the assumptions made in arriving at equation 25. This is just the familiar separation of variables technique, separating the radial and angular parts of the function. Utilizing the Hankel function (22c), a more general statement (30) is

$$\psi(\vec{x}) = \sum_{\ell,m} \left[\vec{A}^{(1)}_{\ell,m} h^{(1)}_\ell(x) + \vec{A}^{(2)}_{\ell m} h^{(2)}_\ell(x) \right] Y_{\ell m}(\theta,\phi) \tag{32}$$

The $\vec{A}$'s must be determined from the imposed boundary conditions.

Since each component of $\vec{B}$ satisfies the Helmholtz equation (27), it can be written in an analogous fashion to (30) as

$$\vec{B} = \sum_{\ell,m} \left[\vec{A}^{(1)}_{\ell m} h^{(1)}_\ell(kr) + \vec{A}^{(2)}_{\ell m} h^{(2)}_\ell(kr) \right] Y_{\ell m}(\theta,\phi) \tag{33}$$

The condition $\vec{\nabla}\cdot\vec{B}=0$ must now be considered. This condition must hold separately for each term in (33); for example, the $\vec{A}$'s must satisfy the requirement

$$\vec{\nabla} \cdot \sum_{\ell,m} h_\ell(kr)\, \vec{A}_{\ell m}\, Y_{\ell m}(\theta,\phi) = 0. \tag{34}$$

Using the spherical coordinate expression for the gradient

$$\vec{\nabla} = \frac{\vec{r}}{r}\frac{\partial}{\partial r} - \frac{i}{r^2}\vec{r} \times \vec{L} \tag{35}$$

yields

$$\vec{r} \cdot \sum_{\ell} \left[\frac{\partial h_\ell}{\partial r} \sum_{m} \vec{A}_{\ell m} Y_{\ell m} - \frac{ih_\ell}{r} \vec{L} \times \sum_{m} \vec{A}_{\ell m} Y_{\ell m} \right] = 0 \quad (36)$$

The recursion formula for the spherical Bessel functions dictates the requirement

$$r \cdot \sum_{m} \vec{A}_{\ell m} Y_{\ell m} = 0 \quad (37)$$

in order for the $\vec{A}$'s to be uncoupled. Equation 34 also requires the condition

$$\vec{r} \cdot (\vec{L} \times \sum_{m} \vec{A}_{\ell m} Y_{\ell m}) = 0 \quad (38)$$

to hold. These two conditions (37 and 38) are all that are necessary to determine a unique set of functions.

It turns out that a solution fulfilling all requirements is

$$\sum_{m'} \vec{A}_{\ell' m'} Y_{\ell' m'} = \sum_{m} a_{\ell m} \vec{L} Y_{\ell m} \quad (39)$$

(37) is satisfied since $\vec{r} \cdot \vec{L} = 0$

(38) is satisfied since

$$\vec{r} \cdot (\vec{L} \times \vec{A}_{\ell m} Y_{\ell m}) = \vec{r} \cdot (\vec{L} \times a_{\ell m} \vec{L} Y_{\ell m}) = a_{\ell m} \vec{r} \cdot (i\vec{L} Y_{\ell m}) \equiv 0 \quad (40)$$

again since $\vec{r} \cdot \vec{L} = 0$.

By assumption (37) we now have a special set of functions, fulfilling the Schrödinger equation, and forming a set of electromagnetic fields.

$$\vec{B}_{\ell m} = f_\ell(kr)\,\vec{L}\,Y_{\ell m} \tag{41}$$

$$E_{\ell m} = \frac{i}{k}\nabla \times \vec{B}_{\ell m}$$

$$f_\ell(r) = A^{(1)}_\ell h^{(1)}_\ell(kr) + A^{(2)}_\ell h^{(2)}_\ell(kr).$$

Any linear combination of this special set of functions will satisfy the Maxwell equations. They also exhibit the property that the radius vector is perpendicular to the magnetic field,

$$\vec{r}\cdot\vec{B}_{\ell m} = 0.$$

The reduced set of Maxwell equations (28) could have been used equally well to arrive at the expansion

$$\vec{E}_{\ell m} = f_\ell(kr)\,\vec{L}\,Y_{\ell m}$$

$$\vec{B}_{\ell m} = -\frac{i}{k}\nabla \times \vec{E}_{\ell m} \tag{42}$$

The expressions $\vec{L}\cdot Y_{\ell m}$, in equations (41) and (42) are the vector spherical harmonics which were defined in (13). Using this expression, together with the most general combination of equations (41) and (42), a solution to the Maxwell equations can be written as:

$$\vec{E} = \sum_{\ell,m}\left[\frac{i}{k}\,a_E(\ell,m)\vec{\nabla} \times f_\ell(kr)\,\vec{X}_{\ell m} + a_M(\ell,m)g_\ell(kr)\,\vec{X}_{\ell m}\right] \tag{43}$$

$$\vec{B} = \sum_{\ell,m}\left[\,a_E(\ell,m)\,f_\ell(kr)\,\vec{X}_{\ell m} - \frac{i}{k}\,a_M(\ell,m)\vec{\nabla} \times g_\ell(kr)\,\vec{X}_{\ell m}\right] \tag{44}$$

The coefficients $a_E(\ell,m)$ and $a_M(\ell,m)$ are the magnitudes of each field component. These are to be determined later.

5.1.4. Sources of Multipole Radiation

Once the description is obtained for the multipole radiation field, it remains to describe similarly the source of these fields. The usual procedure is to assume that these fields arise from three localized distributions in the nucleus: The charge density $(\rho(\vec{r},t)$ current density $\vec{J}(\vec{r},t)$, and the intrinsic magnetization $\vec{M}(\vec{r},t)$. Assuming harmonically varying quantities, these distributions can be written as

$$\rho(\vec{r})e^{-i\omega t},\ \vec{J}(\vec{r})e^{-i\omega t},\ \text{and}\ \vec{M}(\vec{r})e^{-i\omega t},\ \text{respectively.}$$

In the presence of these sources, Maxwell's equations in vacuum can be written as

$$\vec{\nabla}\times\vec{E} = ik\vec{B},\quad \vec{\nabla}\cdot\vec{B} = 0 \tag{45}$$

$$\vec{\nabla}\times\vec{H} + ik\vec{E} = \frac{4\eta}{c}\vec{J},\ \vec{\nabla}\cdot\vec{B} = 4\pi\rho$$

along with the continuity equation

$$\vec{\nabla}\cdot\vec{J} - i\omega\rho = 0.$$

It is desirable to have the solutions in the same form as for the source-free case. Consequently, to obtain a vanishing divergence for the $\vec{E}$ field it is rewritten as

$$\vec{E}' = \vec{E} + \frac{4\pi i}{\omega}\vec{J}\ .$$

With this substitution, reduced sets of Maxwell's equations can be written similar to (27) and (28).

For E-radiation

$$(\nabla^2 + k^2)\vec{B} = -\frac{4\pi}{C}\left[\vec{\nabla}\times\vec{J} + C\,\vec{\nabla}\times\vec{\nabla}\times\vec{M}\right] \tag{46}$$

$$\vec{\nabla}\cdot\vec{B} = 0,\quad \vec{E}' = \frac{i}{k}(\vec{\nabla}\times\vec{B} - 4\pi\vec{\nabla}\times\vec{M})$$

For M-radiation

$$(\nabla^2 + k^2)\vec{E}' = -\frac{4\pi ik}{c}\left[c\vec{\nabla} \times M + \frac{1}{k^2}\vec{\nabla} \times \vec{\nabla} \times \vec{J}\right] \qquad (47)$$

$$\vec{\nabla} \cdot \vec{E}' = 0, \quad \vec{B} = \frac{-i}{k}(\vec{\nabla} \times \vec{E}' - \frac{4\pi i}{\omega}\vec{\nabla} \times \vec{J})$$

Outside the source these equations reduce to (27) and (28). Inside the source $\vec{B}$ and $\vec{E}$ still have vanishing diverguences and thus can be solved for with the preservation of the general form (44) which has already been derived. The sole difference arises in the form of the radial functions, $f_{\ell m}(kr)$ and $g_{\ell m}(kr)$. For example, the magnetic induction is written as:

$$\vec{B} = \sum_{\ell,m}\left[f_{\ell m}(r)\ \vec{X}_{\ell m} - \frac{i}{k}\vec{\nabla} \times g_{\ell m}(r)\ \vec{X}_{\ell m}\right] \qquad (48)$$

We need to determine the equations satisfied by the electric multipole function $f_{\ell m}(r)$ and the magnetic multipole function $g_{\ell m}(r)$. To do this, the above expression for $\vec{B}$ is substituted into the first equation of (46), the scalar product of both sides with some $\vec{X}_{\ell m}$ is taken, and the result integrated over all angles. In this fashion an inhomogeneous differential equation results. By substituting an equivalent expression for $\vec{E}'$ into the first equation of (47), and following an analogous procedure, the same type of differential equation results. Both of these equations can then be solved by means of a Green's function technique. More details on this procedure are given in several texts, for example (Jac62) and (Ray67). The solution of the equations for $f_{\ell m}(r)$ and $g_{\ell m}(r)$ allow the identification of the multipole coefficients. Since, as has already been mentioned, the

long-wavelength approximation is used ($kr_{max} << 1$), the asymptotic limit (equations 23) can be used for the Bessel functions that arise. On keeping only the lowest order terms involving kr, the approximate solutions are

E-Coefficients

$$a_E(\ell,M) = \frac{4\pi k^{\ell+2}}{i(2\ell+1)!!} \left(\frac{\ell+1}{\ell}\right)^{1/2} (Q_{\ell m} + Q'_{\ell m}) \tag{49a}$$

where the Q's are multipole moments defined as

$$Q_{\ell m} = \int r^{\ell} Y^*_{\ell m} \rho d^3x \tag{49b}$$

$$Q'_{\ell m} = \frac{-ik}{\ell+1} \int r^{\ell} Y^*_{\ell m} \vec{\nabla} \cdot (\vec{r} \times \vec{M}) \, d^3x \tag{49c}$$

M-Coefficients

$$a_M(\ell,m) = \frac{4\pi i k^{\ell+2}}{(2\ell+1)!!} \frac{\ell+1}{\ell} (M_{\ell m} + M'_{\ell m}) \tag{50a}$$

where,

$$M_{\ell m} = -\frac{1}{\ell+1} \int r^{\ell} Y^*_{\ell m} \vec{\nabla} \cdot \left(\frac{\vec{r} \times \vec{J}}{c}\right) d^3x \tag{50b}$$

$$M'_{\ell m} = -\int r^{\ell} Y^*_{\ell m} \vec{\nabla} \cdot M \, d^3x \tag{50c}$$

In equation (49c), the expression for $Q'_{\ell m}$ is usually much smaller in magnitude and can be dropped from further consideration. In equations (50b) and (50c), both the moment $M_{\ell m}$ and the intrinsic moment $M'_{\ell m}$ are of similar magnitudes and must be retained in further calculations.

5.1.5. Transition Probabilities

The total power radiated by a pure multipole over all angles is given by

$$P(\ell,m) = \frac{c}{8\pi k^2} |a(\ell,m)|^2 \tag{51}$$

where P is the total power radiated and the a's are the multipole coefficients. In quantum mechanical terms, the transition probability is given as

$$T = \frac{1}{\tau} = \frac{P}{\hbar\omega} \tag{52}$$

where T is the transition probability and τ is the mean life of the species. This allows transition probabilities to be written as

$$T_M(\ell,m) = \frac{2\pi c}{\hbar\omega[(2\ell+1)!!]^2} \frac{\ell+1}{\ell} k^{2\ell+2} |M_{\ell m} + M'_{\ell m}|^2 \tag{53a}$$

$$T_E(\ell,m) = \frac{2\pi c}{\hbar\omega[(2\ell+1)!!]^2} \left(\frac{\ell+1}{\ell}\right) k^{2\ell+2} |Q_{\ell m} + Q'_{\ell m}|^2 \tag{53b}$$

The expressions for the multipole moments must be changed from the classical expressions for charge and current densities, as given by equations (49) and (50), to their quantum mechanical equivalent. That is,

$$\rho(\vec{r}) \longrightarrow 2\, e\, \psi_f^*(\vec{r})\, \psi_i(\vec{r}) \tag{54}$$

and

$$j(\vec{r}) \longrightarrow 2\frac{e}{m} \psi_f^*(\vec{r})\, \vec{p}\, \psi_i(\vec{r}) = \frac{-ieh}{m}\left[\psi_f^* \nabla\psi_i - (\nabla\psi_f)\psi_i\right] \tag{55}$$

where ψ_i and ψ_f are the initial and final states of the transforming

nucleon. The results of these transformations are

$$\mathcal{Q}_{\ell m} = e \langle f | r^{\ell} Y^{*}_{\ell m} | i \rangle \tag{56a}$$

$$\mathcal{Q}'_{\ell m} = -\frac{iek\hbar}{2(\ell+1)M} \langle f | \mu_n \vec{\sigma} \times \vec{r} \cdot \vec{\nabla}(r^{\ell} Y^{*}_{\ell m}) + 2r^{\ell} Y^{*}_{\ell m} \frac{\vec{r} \cdot \vec{p}}{\hbar} | i \rangle \tag{56b}$$

$$M_{\ell m} = \frac{e\hbar}{(\ell+1)M} \langle f | \vec{\nabla}(r^{\ell} Y^{*}_{\ell m} \cdot \vec{L}) | i \rangle \tag{56c}$$

$$M'_{\ell m} = \tfrac{1}{2}\mu_n \frac{e\hbar}{M} \langle f | \vec{\sigma} \cdot \vec{\nabla}(r^{\ell} Y^{*}_{\ell m}) | i \rangle \tag{56d}$$

This is about as far as the equations for the electric and magnetic multipole transition probabilities can be carried without first introducing a specific nuclear model.

5.2. Single Particle Transition Probabilities

Numerical evaluation of these multipole expressions can be obtained most easily by resorting to the shell model (humorously called "simple"). This model provides expressions for the wave functions and subsequently the radial matrix elements. It assumes that the structure of the nuclear excited states is due entirely to the last single, unpaired nucleon in the nucleus, either a proton or a neutron. The nuclear spin is determined solely by the angular momentum of this unpaired nucleon. γ transitions from the excited nuclear states are viewed as changes in the state of the odd nucleon under the influence of spherically symmetric potential created by the remainder of the nucleons in the nucleus.

The usual procedure for formulating the single-particle transition probabilities is to assume the odd particle to be a proton. Neutron transitions can then be expressed by slightly modifying these expressions. The expressions for the proton transition probabilities are derived in (Mosz65).

Considering transitions of a proton in a central velocity independent well, equations (53) and (56) can be simplified and expressed as

$$T_{i\to f}^{(EL)} = \frac{2(\ell+1)}{\ell[(2\ell+1)!!]^2}\,\omega\left(\frac{e^2}{\hbar c}\right)\left(\frac{\omega a}{c}\right)^{2\ell}\cdot\left(\int_0^\infty R_f\left(\frac{r}{a}\right)^{\ell} R_i r^2 dr\right)^2 S(j_i,\ell,j_f) \qquad (57a)$$

$$T_{i\to f}^{(ML)} = \frac{2(\ell+1)}{\ell[(2\ell+1)!!]^2}\omega\frac{e2}{\hbar c}\left(\frac{\omega a}{c}\right)^{2\ell}\left(\frac{h}{mca}\right)^2\cdot\left(\mu_p\ell - \frac{\ell}{\ell+1}\right)\left(\int_0^\infty R_f\left(\frac{r}{a}\right)^{\ell-1} R_i\, r^2 dr\right)^2 \cdot S(j_i,\ell,j_f) \qquad (57b)$$

In these equations, ℓ is the angular momentum carried away by the emitted quantum.

R_i, R_f = Radial wave functions of the initial and final states, respectively.

$\omega = (E_i - E_f)/\hbar$

c = velocity of light

a = nuclear radius

μ_p = proton magnetic moment

S = statistical factor

The statistical factor, S, represents the angular dependance of the transition probability and can be derived as

$$S(j_i,\ell,j_f) = (2j_f + 1)[\langle j_i \tfrac{1}{2} j_f \tfrac{1}{2} | j_i j_f \ell 0\rangle] \tag{58}$$

where the bracketed term is a Clebsch-Gordan coefficient. For the special case where $|j_i - j_f| = \ell$, the results are comparatively simple. For example, the statistical factor for the *M*4 transitions considered in this thesis is

$$S(11/2,4,3/2) = 15/11.$$

The radial integrals can be evaluated only after substitution of explicit forms for the nuclear wave functions.

On the basis of a constant density model, where the wave function is constant over nuclear dimensions and zero outside the nucleus, the radial integral can be evaluated as

$$\int_0^\infty R_f \left(\frac{r}{a}\right)^\ell R_i \, r^2 dr^2 = \frac{3}{(\ell+3)} \tag{59}$$

Using this assumption, along with $a = 1.2\times10^{-13}$ cm and $\mu_p = 2.79$, we can simplify the transition probabilities to a point where they can be evaluated numerically. Several of them are listed in Table 29 for reference. Again, it must be remembered that these equations apply to a very specific case, that of a single proton in a spherical well, considering the wavefunctions to be constants, and for particular fixed values for a and μ_p.

As explained in (Mosz65), magnetic transition probabilities in odd-neutron nuclei are expected to be smaller than odd-proton nuclei by the factor

Table 29. Expressions for single-proton transition probabilities.

$E1 = 1.0\times10^{14} \cdot A^{2}/_{3} \cdot E_{\gamma}^{3}$	S
$E2 - 7.4\times10^{7} \cdot A^{4}/_{3} \cdot E_{\gamma}^{5}$	S
$E3 = 3.4\times10^{1} \cdot A^{2} \cdot E_{\gamma}^{7}$	S
$E4 = 1.1\times10^{-5} \cdot A^{8}/_{3} \cdot E_{\gamma}^{9}$	S
$E5 = 2.5\times10^{-12} A^{10}/_{3} E_{\gamma}^{11}$	S
$M1 = 2.9\times10^{13} \cdot A^{0} \cdot\cdot E_{\gamma}^{3}$	S
$M2 = 8.4\times10^{7} \cdot A^{2}/_{3} \cdot E_{\gamma}^{5}$	S
$M3 = 8.7\times10^{1} \cdot A^{4}/_{3} \cdot E_{\gamma}^{7}$	S
$M4 = 4.8\times10^{-5} \cdot A^{2} \cdot\cdot E_{\gamma}^{9}$	S
$M5 = 1.7\times10^{-11} A^{8}/_{3} \cdot E_{\gamma}^{11}$	S

These equations are approximations for proton transitions, assuming constant nuclear wave functions, $\mu_p = 2.79$ and $a = 1.2\times10^{-13}$cm.

$$\left[\frac{\mu_n}{\mu_p-(\ell+1)^{-1}}\right]^2 \qquad (60)$$

The *M*4 transition probabilities calculated for the present investigation have included this factor. Particular use has been made of the resulting *M*4 expression in § 4.2 and will be used further in Chapter VI.

These single particle estimates are the ones most generally used when estimates are sought for transition probabilities. Hence it is important to have a feeling for the method used in deriving these equations and the approximations used along the way. Hopefully this chapter contributes to that understanding.

CHAPTER VI

SYSTEMATICS OF THE Z=63 AND N=82 NUCLEI AND DISCUSSION OF SOME $M4$ ISOMERS

As mentioned in Chapter I, this thesis project began as a study of the decay properties of the neutron-deficient, odd-mass Gd isotopes. In this vein we studied Gd^{149} and Gd^{145m+g} (§ 4.1, § 4.2, and § 4.3, respectively). The first part of this chapter is a brief look at these results along with previously published data on the decay of Gd^{147} and Gd^{151}. The levels in Eu^{145} will then be considered in relationship to levels in other N=82, odd-mass nuclei. The second part of this chapter compares the trends in several series of $M4$ isomers. The energies and reduced transition probabilities are plotted.

6.1. Levels in Neutron-deficient, Odd-mass Eu Isotopes

The neutron-deficient Eu levels can be traced only over four Eu isotopes with any certainty: Eu^{145}, Eu^{147}, Eu^{149}, and Eu^{151}. Eu^{143} has not as yet been studied in enough detail for levels to be placed, however, it is reported (Mal66 and Kot65) to have a half-life of 2.3-2.6 minutes, with no strong γ rays having been observed. At the other end of the scale, Eu^{153} exhibits rotational structure and thus is of limited use for our purpose. Figure 54 is a plot of those Eu levels which have been assigned spins and parities. The

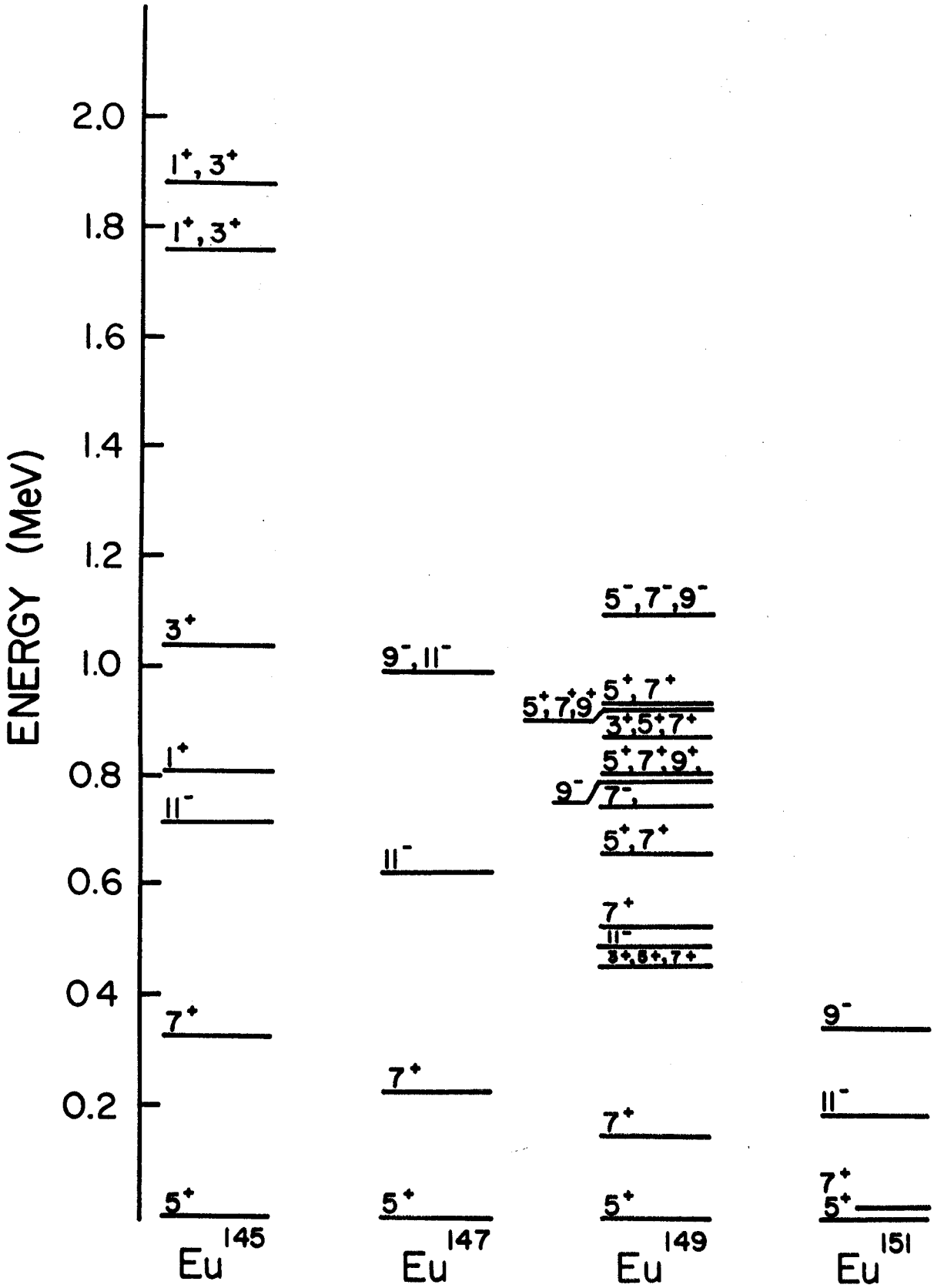

Figure 54. Levels in Eu nuclei which are populated by β decay. Spins are shown in units of 2J. Only three levels are shwon for which spin assignments have been made.

Eu^{145} levels are taken from § 4.3. and (New70), the Eu^{149} levels from § 4.1, and the Eu^{147} and Eu^{151} levels from (Ti67). In all cases the ground state is $5/2^+$ and the first excited state is 7/2+, as would be expected from a simple shell model picture. The only other states that can be followed with any regularity are an $11/2^-$ and a $9/2^-$ state. In all cases these states drop in enrgy as one moves from the closed shell at Eu^{145} toward the rotational systems.

6.2. Levels in Odd-mass, *N*=82 Nuclei

The odd-mass, *N*=82 nuclei are much better characterized than are the odd-mass, *Z*=63 nuclei. For the *N*=82 series, extending from I^{135}, experimental information is known both from β-decay studies and from stripping reactions. Some of this information is summarized in Figures 55 and 56. The levels having assigned spin and parities as determined from β decay are shown in Figure 55 and the levels known from stripping reactions are shown in Figure 56. This latter figure is complements of Wildenthal, et al., and, in addition to showing the energies of the levels which are excited by the stripping reactions, it shows the magnitudes of the spectroscopic factors by the width of the lines marking each level. The lines connecting the various levels trace the energy centroids of the single particle orbits in the "*gdhs*" shell ($1g_{7/2}$,$2d_{3/2}$,$2d_{5/2}$,$3s_{1/2}$, and $1h_{11/2}$). From these stripping reactions the 5 single-particle states can be traced in all of the species from Cs^{137} to Eu^{145}. The $d_{3/2}$, $s_{1/2}$, and $h_{11/2}$ states decrease in energy with increasing proton number over the series. Notice that the $g_{7/2}$ and $d_{5/2}$ states cross each other in

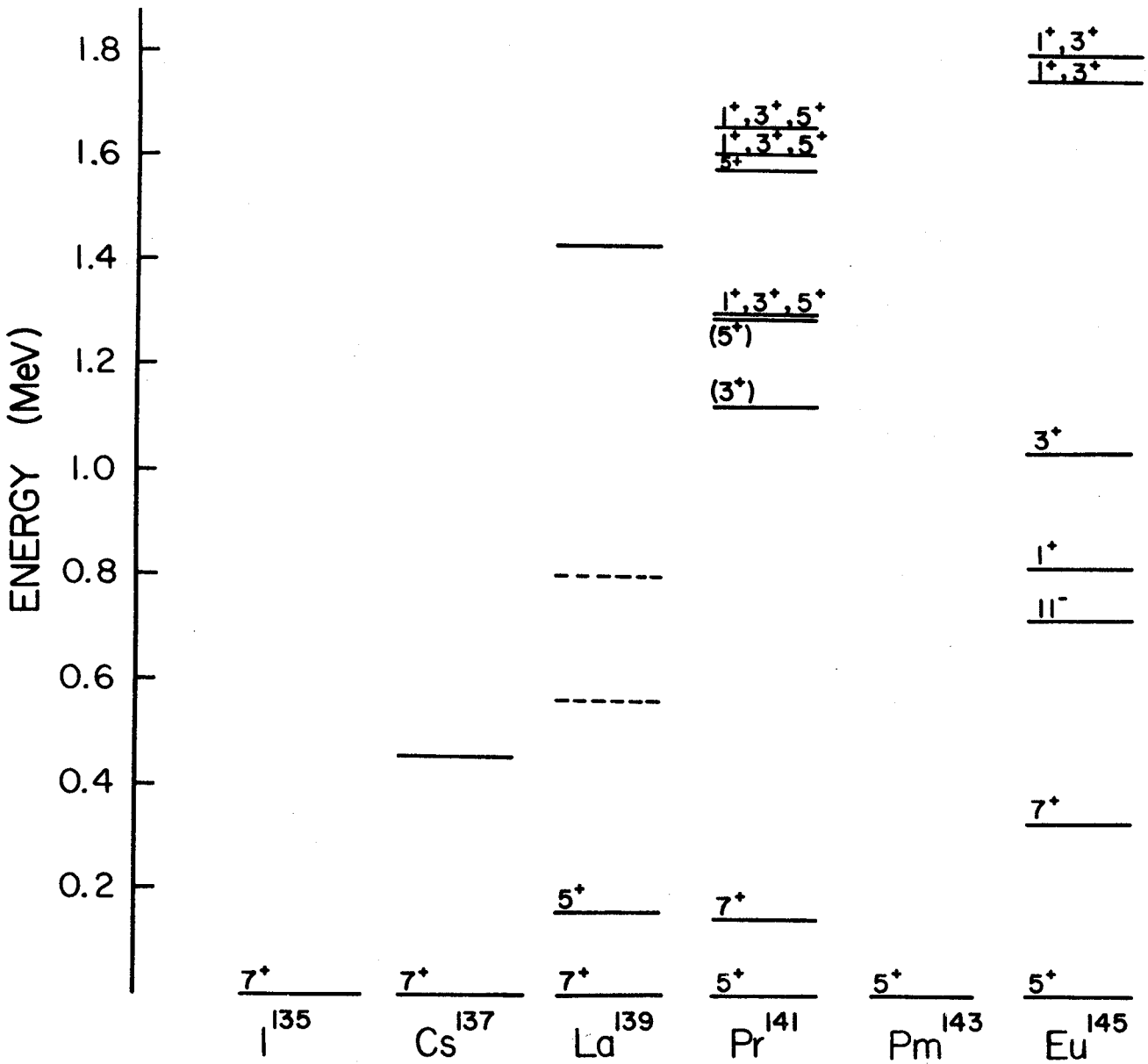

Figure 55. Levels in odd-mass, N=82 nuclei which are populated by β decay. Spins are shown in units of 2J. Only those levels are shown for which spin assignments have been made.

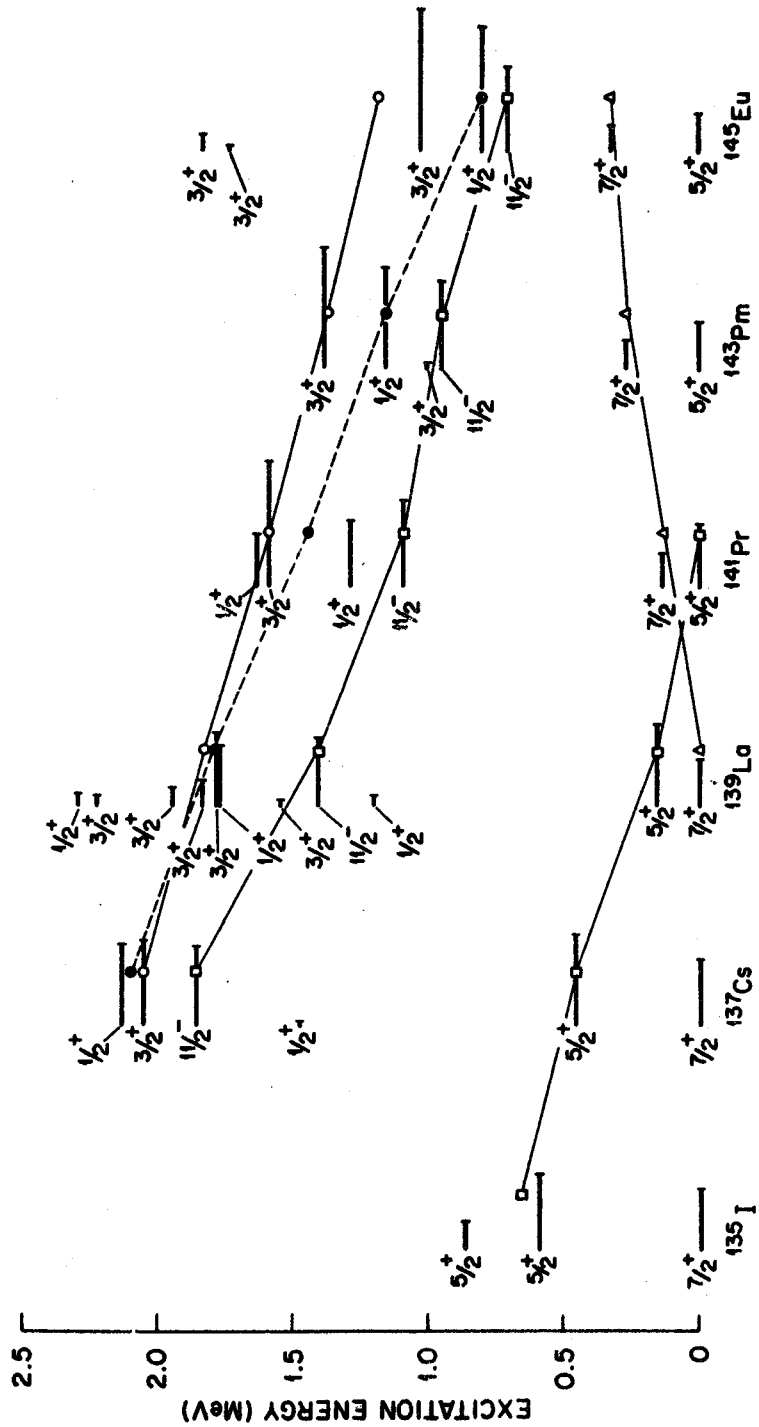

Figure 56. Levels in odd-mass, N=82 nuclei which are populated in stripping (τ,d) reactions.

going from La^{139} to Pr^{141}. As mentioned in §4.2, this makes the $7/2^+$ assignment for the 329.5-keV level in Eu^{145} quite certain even though there appears to be a small β branch to this level from the β decay of Gd^{145g} $(1/2^+)$.

6.3. Survey of a Few *M*4 Isomeric Series

Study of *M*4 electromagnetic transitions continues to hold a special interest for the testing of nuclear theories. In particular, the high multipolarity electromagnetic transitions from such excited states are considered the best candidates for being relatively "pure" single particle transitions. A considerable effort has been expended on the study of these isomers, particularly the *M*4 isomers found in the odd-mass, *N*=81 nuclei. This series was discussed at some length in § 4.2. in conjunction with the decay of Gd^{145m} and its associated 721.4-keV *M*4 transition. Figure 57 shows the experimentally measured isomeric transition energies for this *N*=81 $(11/2^- \rightarrow 3/2^+)$ series and also for the *N*=79 series for comparison. The experimental reduced transition probabilities, $|M|^2$, are also shown on the figure. These probabilities were calculated by using experimental energies and half-lives in equation (57b) of § 5.2. and solving for the factor

$$\left(\int_0^\infty R_f \left(\frac{r}{a}\right)^\ell R_i r^2 dr \right)^2$$

which is defined in the same section. Partial half-lives for the *M*4 branches were determined from the experimental half-life values and dividing by the percent decay via the *M*4 branch. γ-ray half-lives were then computed by multiplying the *M*4 half-lives by the factor

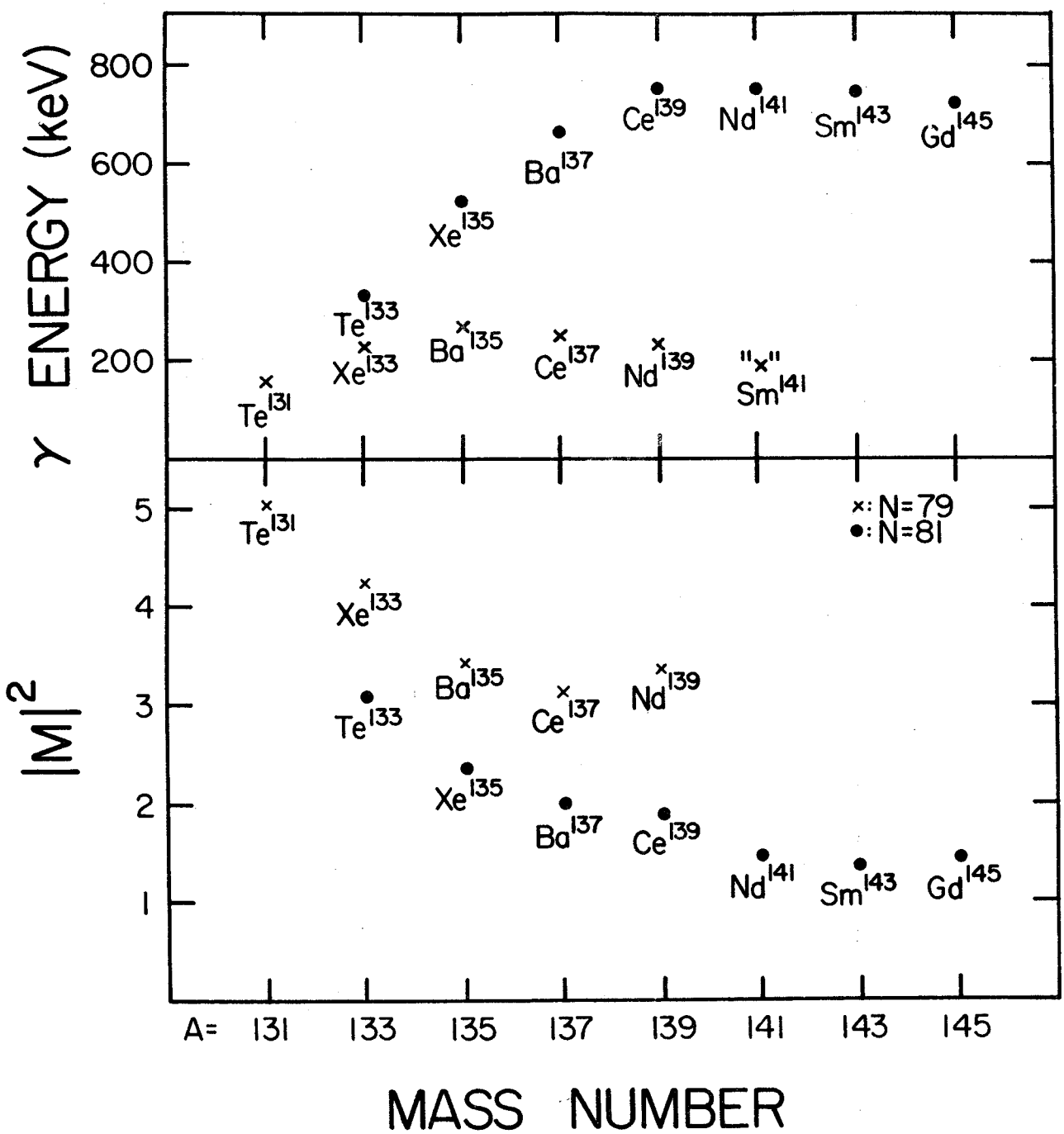

Figure 57. Upper: *M*4 transition energies for the *N*=79 and *N*=81 isotones. The Sm^{141} point is predicted (see §4.4.5). Lower: Values of the squared matrix elements for the single-neutron isomeric transitions in the same nuclei.

$(1+\alpha_{tot})$, where α_{tot} is the total theoretica ρ conversion coefficient as determined from the tables of Hager and Seltzer (Hag68). As can be seen in this figure, there is a pronounced "bow" to the probability curve. On assuming constant density wave functions in the above expression, $|M_r|^2$ for neutrons comes out to be 14.6 (see § 4.2.3.). Not only does this yield a constant probability for the series, but also is substantially larger in magnitude than are the experimental values. Much better experimental-theoretical agreement has been obtained by Jansen, Morinaga, and Signorini (Jan69). They recalculated the N=81 radial matrix elements using a "realistic" potential consisting of a Woods-Saxon part and a spin-orbit part. In addition, the calculation included a configuration mixing term as calculated by Harie and Oda (Hor64). In this manner much of the Z dependence was removed, although the theoretical values still remain the layer for all reasonable values of R_o.

The reduced transition probabilities for the Z=82 isomers, which are shown in Figure 58, are remarkably constant over the whole range from Pb^{197m} to Pb^{207m}. This is so in spite of the large range of energies envolved. The $|M_r|^2$ values are ones reported by Doebler, McHarris, and Gruhn (Doeb68). The value for Pb^{205m}, reported as 18±2, has been omitted from the figure. This value is probably inaccurate because of an unresolved doublet in the spectrum.

This notable difference in the probability trends between the N=81 and Z=82 series of nuclei piqued our curiosity as whether other $M4$ isomers followed one or the other of these two types of

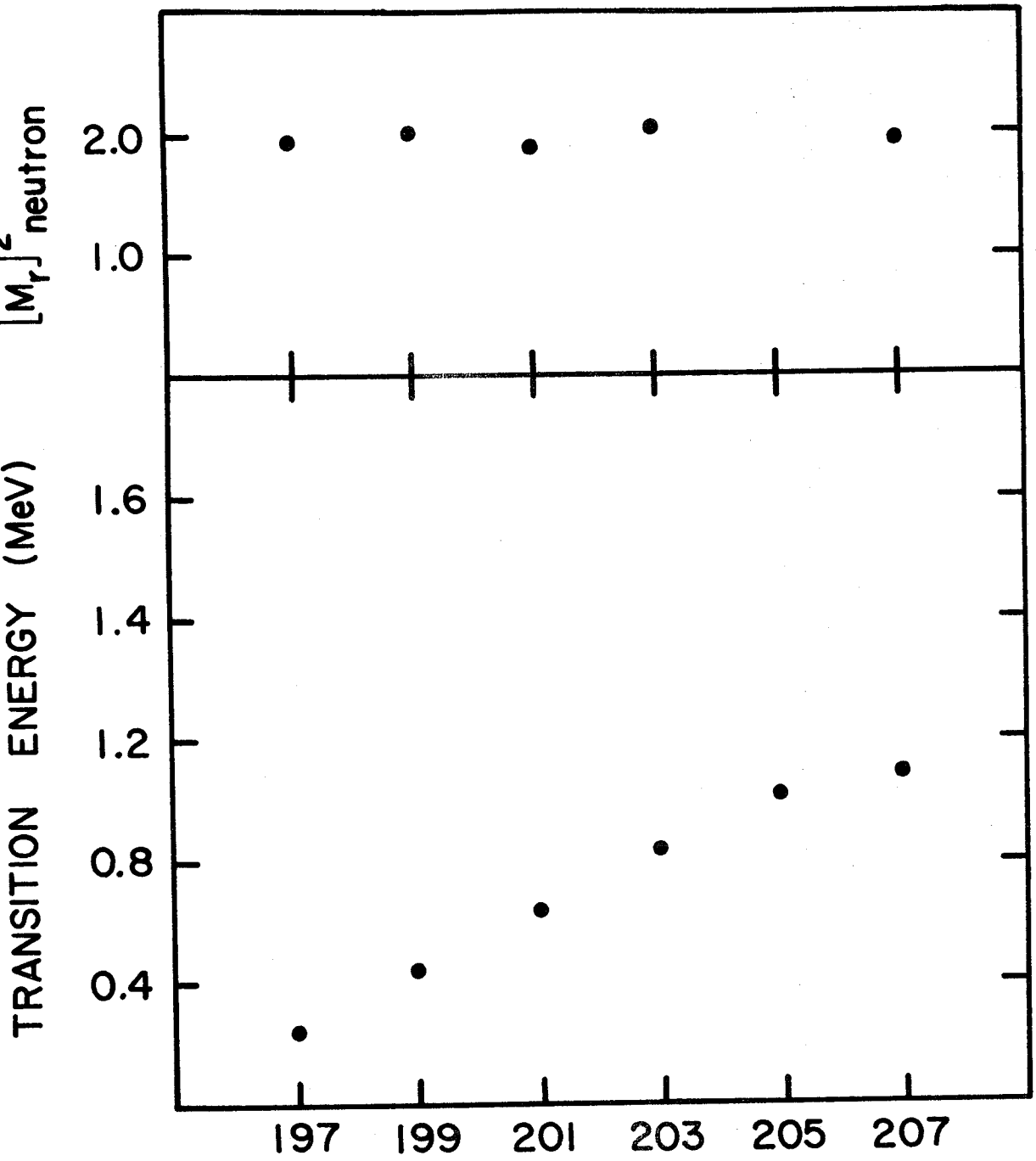

Figure 58. Upper: Values for the squared matrix elements for the *M*4 transitions in the Z=82 isotopes. The value for Pb^{205}has been omitted because of an inaccuracy in in the intensity measurement caused by an unresolved doublet.
Lower: Isomeric transition energies for the above nuclei.

trends. Consequently, we plotted the energies and experimentally determined reduced transition probabilities for the N=49 (Figure 59) series of isomeric transitions, the Z=49 (Figure 60) series of isomers and the Z=50 (Figure 61) series. These are $1/2^- \rightarrow 9/2^+$, $1/2^- \rightarrow 9/2^-$, and $11/2^- \rightarrow 3/2^+$ transitions, respectively. All data for these transitions have been taken from the Table of Isotopes (TI67). As it turns out, little can be said about the Z=50 series since only two isotopes, Sn^{117m} and Sn^{119m}, have reported electromagnetic branches from the isomeric level. We calculate that these reduced transition probabilities are 3.5 and 5.3 for Sm^{117m} and Sm^{119m}, respectively, although they have not been plotted on Figure 61. The N=49 isomers, whose energies and reduced transition probabilities are plotted in Figure 59, show a "bow" in the series of probabilities, but one that is less pronounced than found for the N=81 series. There is no value for Se^{83m} since this species decays exclusively by β^- emission. As a contrast, the series of Z=49 isomers (Figure 60), show a marked curvature in the plot of their γ-emission probabilities. The value for In^{117m} is noticeably out of line, possibly due to an inaccurate value for the percentage of decay via the γ branch.

It undoubtedly would be useful to carry out "realistic" calculations for these series analogous to the N=81 calculations. At this point about the only conclusion that can be drawn is that even for these high multipolarity transitions, in nuclei adjoining closed shell, there are residual interactions contributing with significant strength. Because of the deviations from the ideal shell model picture, the $M4$ isomers seem assured of providing a source of continued interest and study.

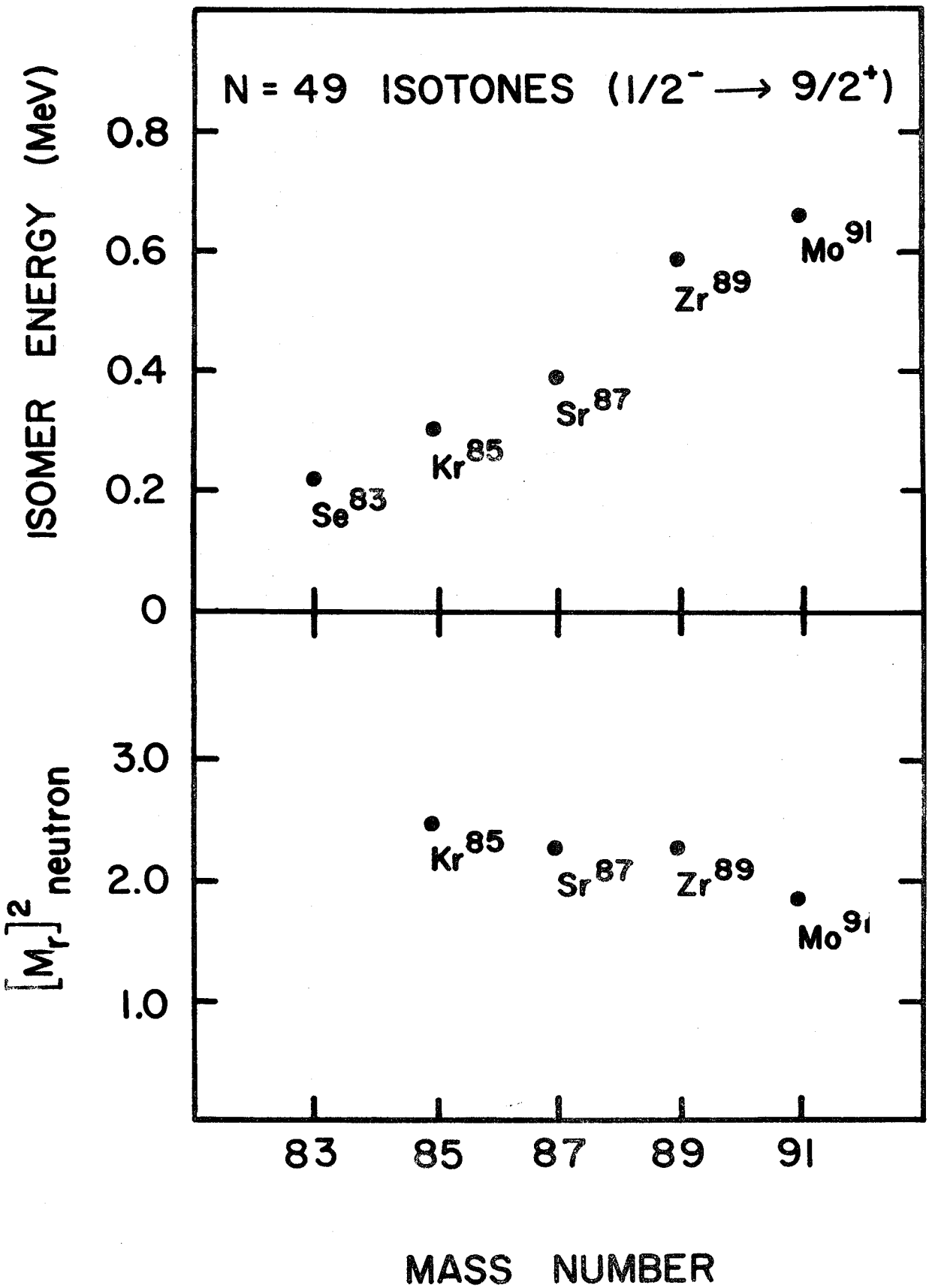

Figure 59. Upper: Isomeric transition energies for odd-mass, N=49 isotones.
Lower: Values of the squared matrix elements for the isomeric transitions in the above nuclei.

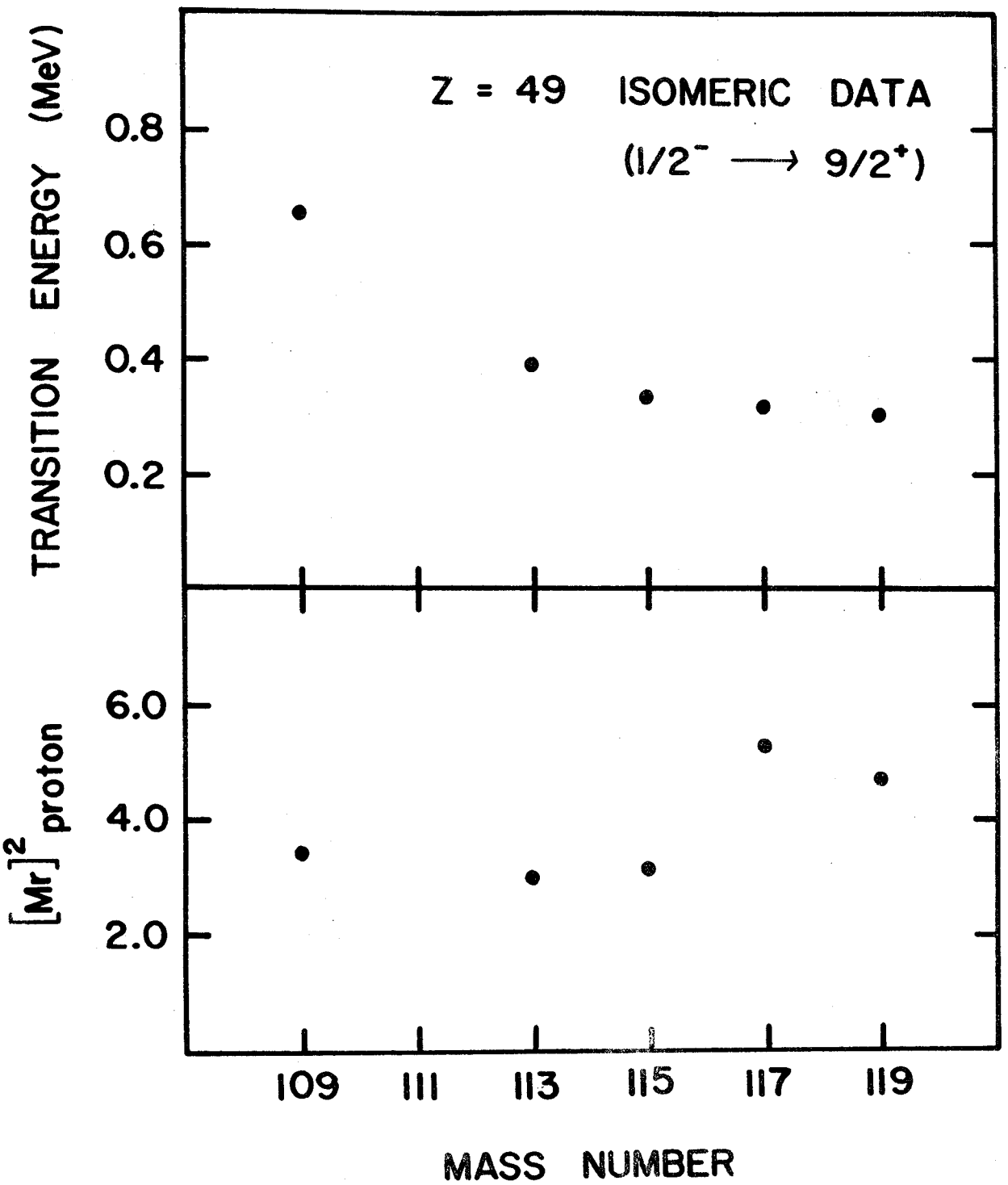

Figure 60. Upper: Isomeric transition energies for odd-mass, Z=49 isotopes. No isomer is reported for In^{111}.
Lower: Values of the squared matrix elements for the isomeric transitions in the above nuclei.

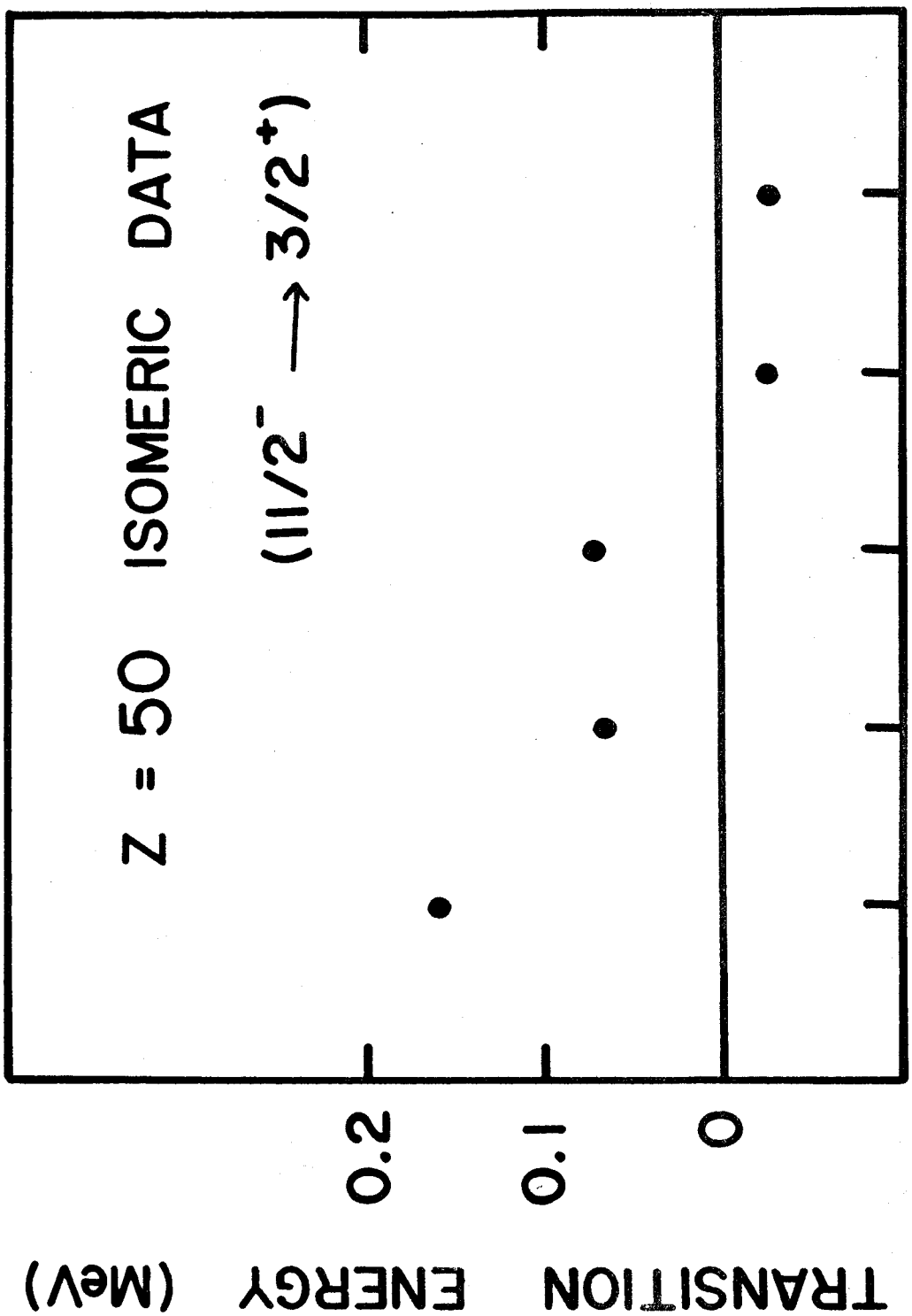

Figure 61. Isomeric transition energies for the Sn isotopes.

BIBLIOGRAPHY

BIBLIOGRAPHY

(Adam58) V. K. Adamchuck, A. A. Bashilov, and B. K. Preobrazhenskii, Izv. Akad, Nauk SSSR, Ser. Fiz. 22, 919 (1958).

(Adam68) I. Adam, K. S. Toth, and R. A. Meyer, Nucl. Phys. A106, 275 (1968).

(Adam68a) I. Adam, K. S. Toth, and M. F. Roche, A121, 289 (1968).

(Alex64a) P. Alexander, F. Boehm, and E. Kankeleit, Phys. Rev. 133, B284 (1964).

(Alex64b) P. Alexander, Phys. Rev. 134, B499 (1964); T. Cretzu, K. Holmuth, and G. Winter, Nucl. Phys. 56, 415 (1964).

(Ann69) Michigan State University Nuclear Chemistry Annual Report for 1969. COO-1779-13.

(Anto58) N. M. Anton'eva, A. A. Bashilov, B. S. Dzhelepov, and B. K. Preobrazhenskii, Izv. Akad, Nauk SSSR, Ser. Fiz. 22, 895 (1958).

(Ar167) R. Art'1, B. Baier, G. Muziol, L. K. Peker, G. Pfrepper, Kh.Shtrusnyi, and D. Khristov, JINR, Dubna (USSR), Report 21 (1967).

(Aub167) R. L. Auble, D. B. Beery, G. Berzins, L. M. Beyer, R. C. Etherton, W. H. Kelly, and Wm. C. McHarris, Nucl. Instr. Methods 51, 61 (1967).

(Avot67) M. P. Avotina, as quoted in ref. 7.

(Baba63) C. V. K. Baba, G. T. Ewan, and J. F. Suárez, Nucl. Phys. 43, 264, 285 (1963).

(Bee68) B. Beery, W. H. Kelly, and Wm. C. McHarris, Phys. Rev. 171, 1283 (1968).

(Bee69d) D. B. Beery, W. H. Kelly, and Wm. C. McHarris, Phys. Rev. 188, 185 (1969).

(Bee69e) D. B. Beery, Ph.D. Thesis, Michigan State University, Cyclotron Laboratory (1969).

(Ber161) E. Ye. Berlovich, V. N. Klementyev, L. V. Krasnov, M. K. Nikitin, and I. Yursik, Nucl. Phys. 23, 481 (1961).

(Ber162) E. E. Berlovich, Yu. K. Gusev, V. V. Ilin, V. V. Nikitin, and M. K. Nikitin, Zh. Eksper. i Teor. Fiz. 42, 967 (1962).

(Bir63) E. I. Biryukov, V. T. Novikov, and N. S. Shimanskaya, Izv. Akad. Nauk SSSR, Ser. Fiz. 27, 1412 (1963).

(Blat52) John M. Blatt and Victor F. Weisskopf, *Theoretical Nuclear Physics*, John Wiley and Sons, New York, (1952).

(Bley67) H. J. Bleyl, H. Münzel and G. Pfinning, Radiochem. Acta 8, 200 (1967).

(Brau63) G. Bauer, *Handbook of Preparative Inorganic Chemistry*, (Academic Press, New York, 1963), Vol. 1, 2nd edition.

(Cho56a) G. R. Choppin, B. G. Harvey, and S. G. Thompson, J. Inorg. Nucl. Chem. 2, 66 (1956).

(Cho56b) G. R. Choppin and R. J. Silva, J. Inorg. and Nuclear Chem. 3, 153 (1956).

(Cle49) R. Clement, Z. Anorg. Allg. Chem. 260, 267 (1949).

(Dan62) H. Daniel and H. Schmidt, Z. Phys. 168, 292 (1962).

(Def68) DeFrenne, K. Heyde, L. Dorikens-Vanpraet, M. Dorikens and J. Demuynck, Nucl. Phys. A110, 273 (1968).

(Doeb68) R. E. Doebler, Wm. C. McHarris, and C. R. Gruhn, Nucl. Phys. A120, 489 (1968).

(Doeb70) R. E. Doebler, G. C. Giesler, and K. L. Kosanke unpublished results (1970).

(Don68) D. P. Donnelly and M. L. Wiedenbeck, Nucl. Inst. and Meth. 64, 26 (1968).

(Epp70a) R. E. Eppley, Wm. C. McHarris, and W. H. Kelly, to be published (1970); also in Michigan State University Nuclear Chemistry Annual Report for 1969, COO-1779-13, p. 55.

(Epp70b) R. E. Eppley, Wm. C. McHarris, and W. H. Kelly, Bull. Am. Phys. Soc. 13, 1467 (1968).

(EVENT) A program written for the MSU Cyclotron Laboratory Sigma-7 computer by D. Bayer, D. B. Beery and G. C. Giesler.

(Fel70) J. Felsteiner and B. Rosner, Phys. Lett. 31B, 12 (1970).

(Feyn64) Richard P. Feynman, *The Feynman Lectures on Physics*, Vol II. Robert B. Leighton and Mathew Sands, Addison - Wesley, Reading, (1964).

(Geig65) J. S. Geiger, R. L. Graham, I. Bergström, and F. Brown, Nucl. Phys. 68, 352 (1965).

(Geor) GEORGE, a data-taking code with live oscilloscope display developed by P. Plauger for use on the MSU Cyclotron Laboratory Sigma-7 computer.

(Gie70) G. C. Giesler, Wm. C. McHarris, R. A. Warner, and W. H. Kelly, Nucl. Instr. Methods, accepted for publication (1970).

(Hag68) R. S. Hager and E. C. Seltzer, Nucl. Data 4A, 1 (1968).

(Harm11) Ref. 11, using the results of P. A. Seeger, Nucl Phys. 25, 1 (1961).

(Harm61) B. Harmatz, T. H. Handley, and J. W. Mihelich, Phys. Rev. 123, 1758 (1961).

(Harm66) B. Harmatz and T. H. Handley, Nucl. Phys. 81, 481 (1966).

(Hess69) K. Hesse, Z. Phydik 220, 328 (1969).

(Hise67) J. R. Van Hise, G. Chilosi, and N. J. Stone, Phys. Rev. 161, 1254 (1967).

(Hoff51) R. W. Hoff, J. O. Rasmussen, and S. G. Thompson, Phys. Rev. 83, 1068 (1951).

(Hor64) H. Horie and T. Oda, Prog. Theor, Phys. (Japan) 32, 65 (1964).

(Hult61) S. Hultberg, D. J. Horen, and J. M. Hollander, Nucl. Phys. 28, 471 (1961).

(Jac62) J. D. Jackson, *Classical Electrodynamics*, John Wiley and Sons, Inc., New York (1962).

(Jac66) J. M. Jaklevic, E. G. Funk, and J. W. Mihelich, Nucl. Phys. 84, 618 (1966).

(Jan69) G. Jansen, H. Morinaga, and C. Signorini, Nucl. Phys. A128, 247 (1969).

(Kel61) R. N. Keller, reported in P. C. Stephenson and W. E. Nervik, *The Radiochemistry of the Rare Earth, Scandium, and Actinium*, NAS-Ns 3020 (1961).

(Kot63) K. Kotajima, Nucl. Phys. 46, 284 (1963).

(Kot65) K. Kotajima, K. W. Brockman, Jr. and Gerda Wolzak, Nucl. Phys. 65, 109 (1965).

(Lad66) I. M. Ladenbauer-Bellis, Radiochim. Acta 6, 215 (1966).

(Mal66) H. P. Malan, H. Münzel and G. Pfenning, Radiochim. Acta 24 (1966).

(Mat65) J. H. E. Matlauch, W. Thiele, and A. H. Wapstra, Nucl Phys. 67, 1, 32, 73 (1965).

(McH69a) Wm. C. McHarris, D. B. Beery, and W. H. Kelly, Phys. Rev. Lett. 22, 1191 (1969).

(Moir) MOIRAE, an oscilloscope code developed primarily by R. Au and G. Berzins for use on the MSU Sigma 7 Computer in the Cyclotron Laboratory.

(Mosz51) S. A. Moszkowski, Phys. Rev. 82, 35 (1951).

(Mosz63) S. A. Moszkowski, in *Alpha-, Beta- and Gamma-Ray Spectroscopy*, ed. by K. Siegbahn (North-Holland Publ. Co., Amsterdam, 1965); S. A. Moszkowski, Phys. Rev. 89, 474 (1953).

(Mosz65) S. A. Moszkowski, *The Theory of Multipole RAdiation, in Alpha-, Beta-, and Gamma-Ray Spectroscopy*, ed. by Kai Siegbahn, North-Holland Publishing Co., Amsterdam (1965).

(Myer65) W. D. Myers and W. J. Swiatecki, UCRL-11980 (1965).

(Nem61) L. Nemet, Izv. Akad, Nauk SSSR, Ser. Fiz. 25, 681 (1961).

(New70) E. Newman, K. S. Toth, R. L. Auble, R. M. Gaedke, M. F. Roche, and B. H. Wildenthal, Phys. Rev. C 1, 1118 (1970).

(NST59) A. H. Wapstra, G. J. Nijgh and R. van Lieshout, *Nuclear Spectroscopy Tables*, North Holland Publishing Co., Amsterdam (1959).

(Olk59) J. Olkowsky, M. LePepe, I. Gratot, and L. Cohen, J. Phys. Rad. 20, 549 (1959).

(Pav57) F. I. Pavlotskaya and A. K. Lavrukhina, J. Nucl. Energy 5, 149 (1957).

(Pras62) H. J. Prask, J. J. Reidy, E. G. Funk, and J. W. Mihelich, Nucl. Phys. 36, 441 (1962).

(Rou69) J. T. Routti and S. G. Prussin, Nucl. Inst. Methods 72, 125 (1969). We used a variant of this code adapted for the MSU Cyclotron Laboratory Sigma-7 Computer.

(Roy67) R. R. Roy and B. P. Nigam, *Nuclear Physics*, John Wiley and Sons, Inc., New York (1967).

(Shir57) V. S. Shirley, W. G. Smith, and J. O. Rasmussen, Nucl. Phys. 4, 395 (1957).

(Shir63) V. S. Shirley and J. O. Rasmussen, Phys. Rev. 109, 2092 (1958); E. Steinchele, and P. Kienle, Z. Phys. 175, 405 (1963).

(Siiv65) A. Siivola and G. Graeffe, Nucl. Phys. 64, 161 (1965).

(Stev60) P. C. Stevenson and W. E. Nervick, *The Radiochemistry of the Rare Earths, Scandium, Yttrium, and Actinium*, UCRL-5923 (1960).

(Thom54) S. G. Thompson, B. G. Harvey, G. R. Choppin, and G. T. Seaborg, J. Am. Chem. Soc. 76, 6229 (1954).

(TI67) C. M. Lederer, J. M. Hollander, and I. Perlman, *Table of Isotopes*, 6th Ed., Wiley, (1967).

(Toth69) See, e.g., K. S. Toth, E. Newman, B. H. Wildenthal, R. L. Auble, R. M. Gaedke, and M. F. Roche, in *Proceedings of the International Conference on Radioactivity in Nuclear Spectroscopy*, Vanderbilt University, *August 11-15, 1969* (Gordon and Breach, N. Y., to be published, 1970), and the comments following.

(UPM) Utility Programs, Programmers Reference Manuals, Advanced Software System, DEC-9A-GUAA-D, Digital Equipment Corporation, (1967).

(Way54) K. Way and M. Wood, Phys. Rev. 94, 119 (1954).

(Wild70) B. H. Wildenthal, MSU, private communication (1970).

(Wild70a) B. H. Wildenthal, MSU, private Communication (1970).

(Yap70) F. Yap, R. R. Todd, W. H. Kelly, and Wm. C. Mcharris, to be published (1970).

(Zwei57) P. F. Zweifel, Phys. Rev. 107, 329 (1957).